Neutrinos From the Milky Way

Neutrinos From the Milky Way

Erwin Visser

ISBN 978-90-8593-219-2

Casimir PhD series 2015-11

Erwin Visser

Propositions associated with the dissertation

Neutrinos From the Milky Way

1. A neutrino telescope on the Northern Hemisphere will have a better chance of observing the neutrino flux from cosmic ray interactions with interstellar matter than one on the Southern Hemisphere.

   CHAPTER 2.

2. The main difficulty of reconstructing the muon direction from the timing information of Čerenkov light is the non-linearity of the problem. By using a grid of predefined directions this problem can be overcome and some particle identification can be achieved at the same time.

   CHAPTER 4.

3. Thanks to the rotation of the Earth, it is straightforward to create systematically equivalent background regions.

   CHAPTER 5.

4. The limit set by the AMANDA-II experiment is quantitatively better, but scientifically less meaningful than the limit set in this dissertation.

   CHAPTER 5.

5. The IceCube experiment has observed a cosmic neutrino flux with a significance of more than 5σ, which is enough to claim a discovery, but surprisingly not enough to assess its origin.

   M.G. Aartsen et al. *Phys. Rev. Lett.*, 113(101101), 2014.

6. Rather than assuming a single power-law energy spectrum for the full sky, a distinction should be made between Galactic and extragalactic contributions to the cosmic neutrino flux.

   M.G. Aartsen et al. *Phys. Rev. D*, 91(022001), 2015.

7. Although the cosmic neutrino flux has been discovered in the ice of the South Pole, the origin of the flux can better be determined in the water of the Mediterranean Sea.

   A. Margiotta. *Geosci. Instrum. Method. Data Syst.*, 2:35–40, 2013.

8. In a sky-map produced by a next-generation neutrino telescope, the Milky Way will be clearly distinguishable.

   M. Spurio. *Phys. Rev. D*, 90(103004), 2014.

9. A unique aspect of neutrino detection is that it allows for the study of completely different topics in science.

10. Even when optimising a set of parameters does not quantitatively improve the sensitivity of an analysis, the optimisation could still be meaningful.

Leiden, May 12th 2015
Erwin Visser

Neutrinos From the Milky Way

Neutrinos From the Milky Way

Proefschrift

ter verkrijging van
de graad van Doctor aan de Universiteit Leiden,
op gezag van Rector Magnificus prof. mr. C.J.J.M. Stolker,
volgens besluit van het College voor Promoties
te verdedigen op dinsdag 12 mei 2015
klokke 16:15 uur

door

Erwin Lourens Visser
geboren te Hoorn
in 1987

Promotiecommissie:

Promotor:	Prof. dr. M. de Jong
Co-promotor:	Dr. D.F.E. Samtleben
Overige leden:	Dr. A.J. Heijboer (Nikhef, Amsterdam)
	Prof. dr. M. Kadler (Universität Würzburg, Würzburg, Germany)
	Prof. dr. P.M. Kooijman (Universiteit van Amsterdam)
	Prof. dr. E.R. Eliel
	Prof. dr. J.W. van Holten

Casimir PhD series, Delft-Leiden 2015-11
ISBN 978-90-8593-219-2
First published in print format 2015
An electronic version of this thesis can be found at https://openaccess.leidenuniv.nl

The work described in this thesis is part of the research programme of the Foundation for Fundamental Research on Matter (FOM), which is part of the Netherlands Organisation for Scientific Research (NWO).

The cover shows a panoramic image of the Milky Way over Lake Tekapo, New Zealand, after sunset with the zodiacal light visible.

This document was typeset using the typographical look-and-feel `classicthesis` developed by André Miede. The style was inspired by Robert Bringhurst's seminal book on typography "*The Elements of Typographic Style*". `classicthesis` is available for both LaTeX and LyX:
http://code.google.com/p/classicthesis

Printed in the Netherlands by Ipskamp Drukkers B.V.

Aan mijn ouders

CONTENTS

1 INTRODUCTION

The Milky Way Galaxy is one of billions of galaxies in the universe we call home. It appears like a dim "milky" band arching across the night sky, see figure 1.1. This band is actually only a part of our Galaxy; all stars in the night sky that are visible to the naked eye are part of the Milky Way Galaxy. Our Galaxy is disk shaped, and since we ourselves are inside it, we see a lot of matter when we look in the plane of our Galaxy and less matter when we look perpendicular to it. The milky band corresponds to the Galactic plane and is commonly referred to as the Milky Way, although also the whole Galaxy is called the Milky Way, which can be confusing. In this work, the meaning will be clear from the context. To emphasize that the Milky Way is our home Galaxy, it is referred to with a capital 'G' to distinguish it from the billions of other galaxies.

Figure 1.1: The Milky Way over the 3.6 metre telescope of the European Southern Observatory (ESO) at La Silla. Image credit ESO/S. Brunier.

In Greek mythology, the Milky Way is formed when Hermes, the messenger of the gods, brought Hercules to suckle at the breast of Zeus's sleeping wife Hera in order to gain immortality. When Hera woke up and found she was feeding the child of

Zeus and a mortal woman, she pushed the baby away. This made her breast milk spray into the heavens, thus creating the Milky Way [Walter and Hodge, 2003]. It is thought that this legend is also the origin of the name *Milky Way*. The Latin *Via Lactea* is adapted from the Greek *Galaxias Kuklos*, meaning milky circle. It is interesting to note that the root of the word "galaxy" means simply "milk".

It was also the Greeks that made the first written scientific explanations about the Milky Way. In his book *Meteorologica*, the Greek philosopher and scientist Aristole wrote that fellow Greek philosopher Democritus proposed that the Milky Way consists of distant stars, although Aristotle himself did not share that view. He instead thought that the Milky Way was caused by the ignition of the fiery exhalation of some stars that were large, numerous and close together. It wasn't until 1610 that Galileo Galilei resolved the issue when he used his telescope to observe that the Milky Way consists of a huge number of faint stars.

Democritus: *c. 460 BC; † c. 370 BC

Galileo Galilei: *1564; † 1642

In the 1780s, Sir William Herschel and his sister used a larger reflecting telescope, which allowed them to carefully count the stars as a function of location in the sky. Sir William used these measurements to create a map of our Galaxy, in which he placed our solar system near the centre. In the 1920s American astronomer Harlow Shapley realised that the Sun is not at the centre of the Galaxy. He studied globular clusters, which we now know are spherical collections of stars orbitting the core of a galaxy. He noticed that they formed a spherical halo around a point several thousands of lightyears away and realised that this point must coincide with the centre of our Galaxy [Pasachoff, 1979].

Sir William Herschel: *1738; † 1822

Harlow Shapley: *1885; † 1972

In 1931, Karl Jansky, an engineer of Bell Labs, performed experiments with a radio antenna to determine the possible sources of noise that could pose a problem for short-wave radiotelephones [Pasachoff, 1979]. He recorded a signal of unknown origin that peaked about every 24 hours. At first he thought the signal originated from the Sun, but upon more careful analysis, it turned out that the signal appeared 4 minutes earlier each day. He realised that after exactly one sidereal day the signal repeated itself and that it thus originated from outside the solar system. Later it turned out that he had observed radiation from the centre of our Galaxy. After publishing his results [Jansky, 1933], he wanted to study the Milky Way in more detail. However Bell Labs reassigned him, and he didn't do any further work on radio astronomy. The measurements of Jansky mark the birth of a new field of research: radio astronomy.

Karl Guthe Jansky: *1905; † 1950

A sidereal day is the time it takes for a distant star to be at the same position on the sky again after one rotation of the Earth. It is 23 hours, 56 minutes and 4 seconds and is slightly shorter than a solar day due to the rotation of the Earth around the Sun.

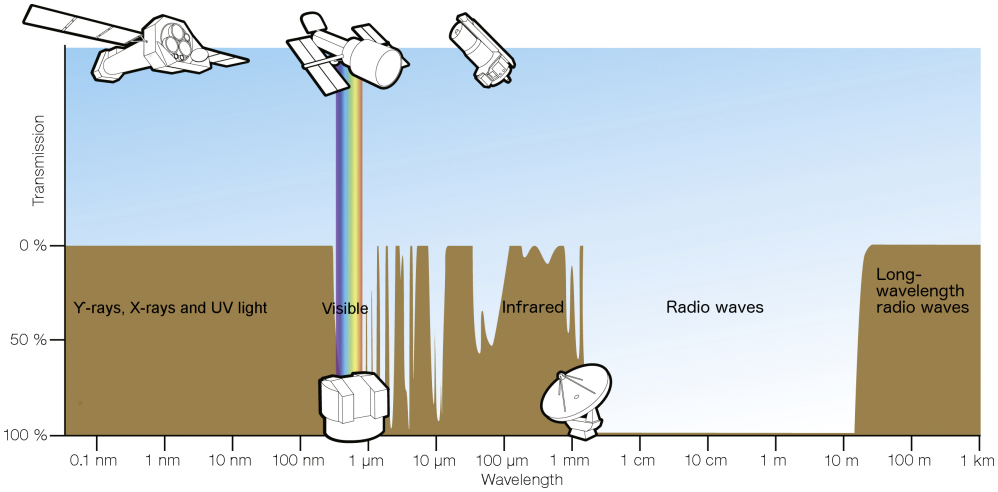

Figure 1.2: The atmospheric transmission versus wavelength and the methods used to observe the different parts of the electromagnetic spectrum. Image credit ESA/Hubble (F. Granato).

Professor Jan Oort was particularly interested in the measurements of Jansky. He was interested in determining the structure of the Milky Way and radio astronomy could help him with this, since absorption is negligible at radio wavelengths. However, the featureless spectrum measured by Jansky was of little use. A spectral line would be much more helpful, since it reflects the dynamics of its source. Since Oort knew hydrogen is a very abundant element, he asked his student Hendrik van de Hulst to find out if hydrogen could have any radio spectral lines. Van de Hulst predicted that neutral hydrogen should have a prominent line at 21 cm, caused by the hyperfine splitting of its ground state [van de Hulst, 1945]. In 1951, the now famous 21 cm line was indeed detected and the spiral structure of our Galaxy became visible [Ewen and Purcell, 1951; Muller and Oort, 1951].

JAN HENDRIK OORT:
** 1900; † 1992*

HENDRIK CHRISTOFFEL VAN DE HULST:
** 1918; † 2000*

Radio astronomy opened a new window on the universe, since it allowed for the observation of objects that were not detectable with "normal" optical astronomy, like quasars and radio galaxies [Burke and Graham-Smith, 2010]. In the same manner, by observing other parts of the electromagnetic spectrum, a lot of new things can be learned [Kambič, 2010]. However, to perform observations at other wavelengths, the telescopes have to be placed outside of the Earth's atmosphere, since it absorbs or reflects these wavelengths. This can be seen in figure 1.2, in which the atmospheric transmission of the electromagnetic spectrum is shown.

Quasars, or quasi-stellar radio sources, are extremely luminous sources at the centres of galaxies.

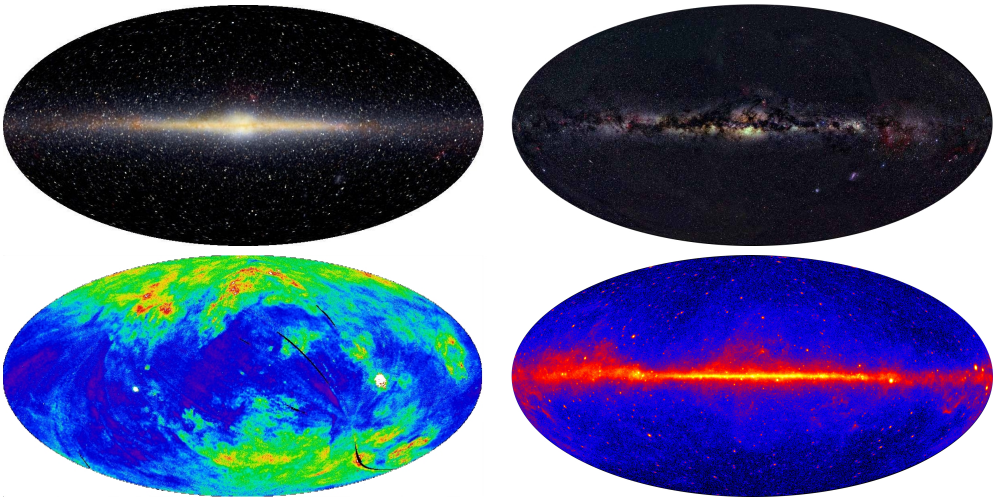

Figure 1.3: The Milky Way observed with photons at different wavelengths. TOP LEFT: in near-infrared. Image credit E.L. Wright (UCLA), The COBE project, DIRBE, NASA. TOP RIGHT: in visible light. Image credit Alex Mellinger. BOTTOM LEFT: in X-rays (between 0.1 keV and 0.3 keV). Image credit Snowden et al. [1995]. BOTTOM RIGHT: in γ-rays (above 1 GeV). Image credit NASA/DOE/International LAT Team.

At infrared wavelengths the sky looks quite different than at visible wavelengths. The dust that blocks the view of the centre of our Galaxy at visible wavelengths, becomes transparent in the near-infrared. This can be seen by comparing the top left and top right sky-maps in figure 1.3. These sky-maps show the flux of photons observed for each direction, and they are made using Galactic coordinates, with the Galactic Centre (GC) in the middle of the plot (see also figure 2.9).

Also, at infrared wavelengths, cooler, redish stars which do not radiate in visible light show up. At longer infrared wavelengths, the dust is no longer transparent and cold clouds of gas and dust become visible [Glass, 1999]. Examples of infrared telescopes include ESA's Herschel Space Observatory and the DIRBE experiment aboard NASA's COBE satellite, which was used to produce the top left sky-map in figure 1.3.

DIRBE: Diffuse InfraRed Background Experiment

COBE: COsmic Background Explorer

The bottom left sky-map in figure 1.3 shows a sky-map in X-rays (with energies from 0.1 keV to 0.3 keV) produced by the ROSAT satellite [Snowden et al., 1995]. The sky-map looks completely different than the infrared and visible sky-maps. Most of the emission actually comes from outside the Galactic plane. The low flux of X-rays from the Galactic plane is caused by the efficient photoelectric absorption of X-rays at these energies by

ROSAT: short for Röntgensatellit, named after Wilhelm Röntgen (1845; † 1923).*

neutral hydrogen [McCammon and Sanders, 1990]. This form of hydrogen is located mainly in the disk of our Galaxy. The strongest emission comes from the Vela pulsar (the big white dot on the right side in the X-ray sky-map). X-ray satellites currently in orbit are, among others, NASA's Chandra X-ray Observatory and ESA's XMM-Newton.

XMM-Newton: X-ray Multi-mirror Mission - Newton

Photons that are even more energetic than X-rays are called γ-rays and are produced by objects such as supernova explosions, pulsars like the one in the Vela constellation and blazars. The γ-ray sky-map (shown in the bottom right in figure 1.3), created by the LAT instrument of the Fermi Gamma-ray Space Telescope using 5 years of data, looks again similar to the infrared and optical sky-maps. The Galactic plane is clearly visible, which is caused by the interaction of high energy charged particles (cosmic rays (CRs), see next section) with the interstellar matter in the Galaxy. Another bright source of γ-rays is the Cygnus region (located on the left of the Galactic centre). This signal is a combination of several pulsars and cosmic rays interacting with the matter present in the Cygnus region [Abdo et al., 2007; Ackermann et al., 2012a]. Besides the earlier mentioned Vela pulsar (which is also a strong source in γ-rays), the famous Crab pulsar is visible (located on the right end of the picture, slightly below the Galactic plane).

Blazars are galaxies which, like quasars, have an extremely bright central nucleus containing a supermassive black hole.

LAT: the Large Area Telescope, the main instrument aboard the Fermi satellite.

The supernova explosion that created the Crab pulsar was widely observed on Earth in 1054.

It should be noted that although the γ-ray sky-map looks similar to the optical sky-map, there is an important difference. In the optical sky-map, the sources outside of the Galactic plane are mostly stars in our own Galaxy, while in the γ-ray sky-map they are mainly extragalactic sources, such as blazars. Blazars are an important field of research in astronomy, since they can for instance be used to study the environment in which high-energy γ-rays travel [Aleksić et al., 2015].

Recently, some interesting new features were discovered in the Fermi data: two giant γ-ray bubbles extending 50° above and below the Galactic centre and with a width of about 40° [Su et al., 2010]. They are now called the Fermi bubbles, and are almost not visible in the γ-ray sky-map, but show up at higher photon energies, see also section 2.3. The mechanism creating these bubbles is not known yet.

1.1 THE ADVENT OF ASTROPARTICLE PHYSICS

Before 1912 the general consensus was that the ionisation of the air was a consequence of radiation of radioactive elements in the Earth's crust. This would imply lower ionisation rates for higher

*Victor Francis Hess: *1883; † 1964*

altitudes, since the emitted photons would be absorbed by the air. To test this hypothesis, Victor Hess embarked on seven balloon flights carrying three enhanced-accuracy Wulf electrometers. Instead of finding a uniform decrease, he found that the intensity of the radiation at his highest obtained altitude (about 5 km) was a factor of about 2 higher than at ground level [Hess, 1912]. From this he concluded that there was a "radiation of great penetrating power" entering our atmosphere from outside. He ruled out the Sun as a source by also performing measurements at night-time and during an eclipse. For his discovery, Victor Hess obtained the Nobel Prize in physics in 1936.

*Pierre Victor Auger: *1899; † 1993*

Hess's discovery marked the birth of the field of astroparticle physics and the so-called cosmic rays were studied extensively. In the late 1930s Pierre Auger measured coincidences between Geiger counters over 300 metre apart and concluded that they were caused by extensive air showers from cosmic ray interactions with the atmosphere of the Earth. From the size of the air showers he estimated that the energy spectrum of the interacting cosmic rays extends above 10^{15} eV [Auger et al., 1939].

The extensive air showers are still used to study the highest energy cosmic rays, since big instrumented areas are needed to measure the low fluxes. At energies around 10^{20} eV for instance, the flux of particles is only about 1 event per km^2 per century. Examples of experiments are the Telescope Array Project in Utah, USA and the Pierre Auger Observatory in Argentina. The latter has a detection area of about 3000 km^2 [Abraham et al., 2004]. These experiments are hybrid detectors consisting of a large number of surface detectors and some fluorescence telescopes. The surface detectors measure the interaction products of the cosmic rays that reach the ground. The fluorescence detectors measure the air fluorescence light emitted by the shower in the air.

The cosmic rays are mainly composed of nuclei (99%), consisting of protons (about 85%) and α-particles (the nucleus of the helium atom, about 12%), with elements of $Z \geqslant 3$ making up only about 3% [Grupen, 2005]. The remaining fraction of the cosmic rays consists mostly of electrons, and a very small part is made up of positrons and antiprotons [Beringer et al., 2012].

The origin of cosmic rays is still unknown. It is thought that cosmic rays with energies lower than 10^{10} eV are mostly produced by the Sun, since the solar wind acts as a shield for protons from outside of the solar system at those energies [Anchordoqui et al., 2003]. Cosmic rays with energies up to 10^{18} eV are thought to be of Galactic origin, with supernova remnants being the

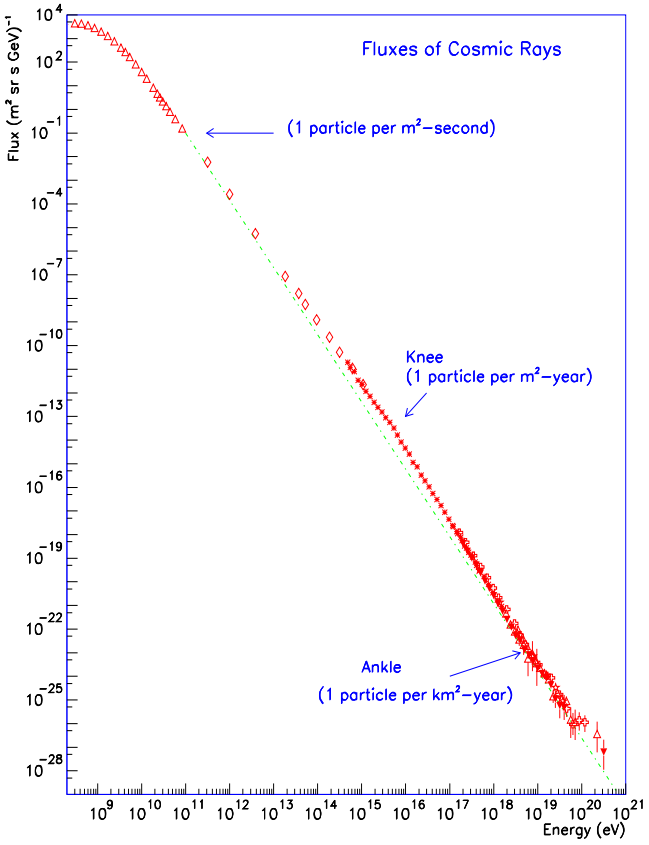

Figure 1.4: The cosmic ray energy spectrum, showing the knee and the ankle. Figure reproduced from Anchordoqui et al. [2003].

main producers. The so-called *knee* in the cosmic ray spectrum (see figure 1.4) is thought to be a combination of two factors, namely [Beringer et al., 2012]:

A. Most cosmic accelerators have reached their maximum energy.

B. Leakage of cosmic rays from the Milky Way.

Cosmic rays with energies above 10^{18} eV are thought to be of extragalactic origin.

So far, no sources of cosmic rays could be uniquely identified, which is partly due to the fact that cosmic rays are charged particles. This causes the cosmic rays to be deflected by the (extra)galactic magnetic fields, so that they do not point back to their source. Only at the highest energies (above 10^{19} eV) are

cosmic rays not significantly deflected, although this depends on the charge of the particle. An iron nucleus at this energy will still be substantially deflected [Grupen, 2005]. If sources, either Galactic or extragalactic, are identified, it would give information concerning the physical processes taking place. More information about cosmic rays and their candidate sources can be found in section 2.1.4.

Neutrinos

Cosmic rays are not the only particles studied in astroparticle physics. Another particle, which recently opened a new window on the universe, is the neutrino. Neutrinos are not charged and interact only very weakly with matter, making them the perfect cosmic messenger since they can be used to probe the interior of their source, travel in a straight line and are not absorbed on their way to the Earth.

IMB: Irvine-Michigan-Brookhaven detector

The first cosmic neutrinos were measured by the Kamiokande and IMB experiments in 1987 [Hirata et al., 1987; Bienta et al., 1987]. The neutrinos were created by the supernova explosion of the blue supergiant Sanduleak, which created an estimated total of 10^{58} neutrinos [Hirata et al., 1987]. Even though only 20 neutrinos have been observed (12 by Kamiokande and 8 by IMB), some interesting astrophysical conclusions can be drawn. It allowed the estimation of the energy of the supernova explosion and also has been used to set a limit on the neutrino mass [Arnett and Rosner, 1987].

One of the advantages of using neutrinos as cosmic messengers is the fact that they only interact very weakly with matter. This is, however, also their main disadvantage. Since the neutrinos interact very weakly, they are very hard to detect, as the numbers above also illustrate. For this reason, huge instrumented volumes are needed. Neutrino telescopes, which use neutrinos in the same way as traditional telescopes use light, make use of one of two detection media: water or ice. The medium is used to measure the interaction products of the neutrino interactions, which generally emit Čerenkov light. Neutrino telescopes are different from normal telescopes, in that they look down through the Earth instead of up at the sky. This is done to reduce the main background, which consists of muons created in the air showers discussed before. These muons cannot traverse the Earth; the only particle that is able to this is the neutrino.

The first initiative to build a neutrino telescope was the DUMAND project [Hanada et al., 1998], which was planned to be located in the water off the coast of Hawaii. In December 1993 the first string with PhotoMultiplier Tubes (PMTs, used to measure the Čerenkov light) was deployed, but after just 10 hours of operation a leak occured, resulting in short circuits. In 1996 the funding was stopped, which lead to the cancellation of the project.

DUMAND: Deep Underwater Muon And Neutrino Detection

The first working neutrino telescope was the Baikal neutrino telescope [Aynutdinov et al., 2006]. It is located in the southern part of the Siberian lake Baikal, which is the deepest fresh water lake in the world. The first stage, called NT200, was completed in 1998 and consists of 8 strings with in total 192 PMTs. The strings are arranged in an umbrella-like frame and are located at a depth of about 1100 m. In 2005 the setup was extended by the deployment of 3 additional string placed 100 m from the centre of NT200. This upgraded setup is called NT200+ and increased the sensitivity of Baikal by a factor of about 4. Currently the Baikal neutrino telescope is still operating, and the collaboration is working on a successor called GVD, which will consist of several NT200 building blocks [Avrorin et al., 2011].

GVD: Gigaton Volume Detector

The AMANDA experiment [Andres et al., 2000] is the first neutrino telescope built in ice. It has been build near the Amundsen-Scott South Pole Station and construction of the final phase, called AMANDA-II [Wischnewski, 2002], was completed in 2000. The detector consisted of 677 PMTs distributed over 19 strings, located $1500 - 2000$ m below the Antarctic ice. In 2005 it stopped operation and was succeeded by the IceCube neutrino telescope [Halzen and Klein, 2010], which is constructed at the same location. IceCube consists of 5160 PMTs deployed on 86 strings located at a depth from 1450 to 2450 metre. IceCube is currently the largest neutrino telescope in the world, encompassing a cubic kilometre of ice. Being located at the South Pole, the complete Northern sky is visible for 100% of the time.

AMANDA: Antarctic Muon And Neutrino Detection Array

The first operational undersea neutrino telescope is the ANTARES detector, located in the Mediterranean Sea off the coast of France at a depth of 2475 metre [Ageron et al., 2011]. It consists of 12 strings, the last of which was connected in 2008, and a total of 885 PMTs. Since the ANTARES detector is located in the Northern Hemisphere, it has a high visiblity of the Milky Way and the Galactic centre. The ANTARES experiment will be discussed in greater detail in chapter 3.

ANTARES: Astronomy with a Neutrino Telescope and Abyss environmental RESearch

The successor of ANTARES, called KM3NeT , has recently completed its qualification phase with the deployment of a prototype

KM3NeT: KiloMetre cubed Neutrino Telescope

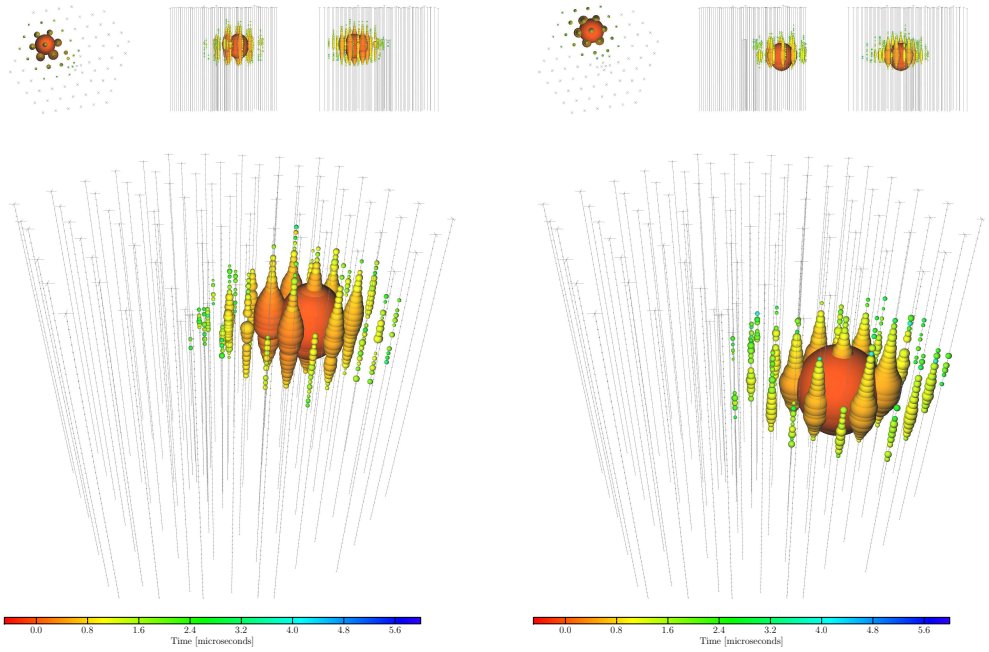

Figure 1.5: The first two PeV-energy neutrinos measured by IceCube. Figures reproduced from Aartsen et al. [2013b]. LEFT: "Bert", with an energy of (1.04 ± 0.16) PeV. RIGHT: "Ernie", with an energy of (1.14 ± 0.17) PeV.

detection unit in the night from the 6th to the 7th of May 2014. The plan of the KM3NeT collaboration is to build a neutrino telescope with an instrumented volume of about $5\,\mathrm{km}^3$ distributed over three sites in France, Greece and Italy. More information about KM3NeT can be found in chapter 6.

One of the scientific goals of neutrino telescopes is to find point sources of neutrinos. The observation of neutrinos from a source would also tell where cosmic rays are accelerated [Grupen, 2005]. There are several source candidates, such as SNRs and AGNs, but no sources have been found yet. For a recent overview see Bogazzi [2014]. Other analyses include searches for a diffuse flux [Aguilar et al., 2011b] and searches for neutrinos from dark matter annihilation in, for instance, the Sun [Lim, 2011].

SNR: SuperNova Remnant, the structure resulting from a supernova explosion.

AGN: Active Galactic Nucleus, the centre of a galaxy hosting a supermassive black hole. Blazars and quasars are types of AGN.

Recently two extremely high energy neutrinos have been observed by the IceCube detector [Aartsen et al., 2013a], corresponding to a 2.8σ excess. The events were named after muppet characters from the children's television show *Sesame Street*, see figure 1.5. These events, which have an energy around one PeV, were the highest energy neutrinos ever measured at the

time. Using a more sensitive analysis, 26 more events have been found [Aartsen et al., 2013b], increasing the significance to about 4σ. Recently, the analysis has been updated with one more year of data, finding in total 37 events (including a third PeV neutrino) where 15 ± 7.2 background events are expected, giving a significance of 5.7σ [Aartsen et al., 2014]. This marks the discovery of the first high-energy cosmic neutrinos and the birth of neutrino astronomy.

Most of the events are so-called shower events, in which the neutrino interaction creates a hadronic and/or electromagnetic shower (see chapter 3 for more details). These events have a poor angular resolution, making it difficult to pinpoint their origin. Because of this, the source of these cosmic neutrinos is unknown at the time of writing, and a wide range of explanations have been brought forward. These range from Galactic sources, such as the Fermi bubbles [Lunardini et al., 2013] to extragalactic sources such as AGNs [Waxman, 2014]. See Anchordoqui et al. [2014] for a nice overview.

1.2 THESIS GOALS AND STRUCTURE

This thesis will focus on neutrinos created by cosmic ray interactions with the interstellar matter in the Milky Way. This signal of neutrinos is guaranteed, since both cosmic rays and the interstellar matter are known to exist and the corresponding diffuse γ signal has been observed [Ackermann et al., 2012b]. Measuring this diffuse Galactic neutrino flux will open a new view on our Galaxy and can give better insight into the cosmic ray and matter distribution in our Galaxy.

So far, only an upper limit on the diffuse Galactic neutrino flux is published, which has been set using the AMANDA-II detector. This experiment has measured the number of neutrinos coming from a region extending 4.4° above and below the Galactic plane and extending from 33° to 213° in Galactic longitude [Kelley et al., 2005]. This longitude range has been used, since it is the part of the Galactic plane which is visible from the South Pole. The advantage of a neutrino telescope in the Mediterranean Sea is that the inner Galactic plane is visible, from which the highest signal is expected (see also the γ-ray sky-map in figure 1.3).

The flux upper limit obtained by AMANDA-II is:

$$\Phi_{\nu_\mu + \overline{\nu}_\mu} < 4.8\, E_\nu^{-2.7}\, \mathrm{GeV}^{-1}\, \mathrm{m}^{-2}\, \mathrm{sr}^{-1}\, \mathrm{s}^{-1}, \tag{1.1}$$

in the energy range from 0.2 TeV to 40 TeV, with E_ν the neutrino energy in GeV. IceCube has not published any updates of the

AMANDA-II analysis so far and according to Tchernin et al. [2013] it will take IceCube around 20 years to detect the neutrino flux of cosmic ray interactions in the Cygnus region. Other parts of the Galactic plane will require even longer exposures.

It is interesting to note that the most recent parameterisation of the flux measured by IceCube [Aartsen et al., 2015] gives a best-fit spectral index that is close to that expected from the diffuse Galactic neutrino flux and is softer than that typically expected from neutrino point sources [Waxman and Bahcall, 1998]. The neutrino flux measured by IceCube could thus be caused by the interaction of cosmic rays in our Galaxy. For instance, Neronov et al. [2014] propose that they are created by a multi-PeV cosmic ray source at the edge of the Norma arm/tip of the Galactic Bar, which could also explain the arrival directions of the neutrinos observed by IceCube. However, other theoreticians discard this hypothesis and point out that the matter density in our Galaxy is about a factor of 100 too low to explain the IceCube flux [Joshi et al., 2014; Kachelrieß and Ostapchenko, 2014]. The possible origin of the IceCube signal will be discussed in more detail in section 5.4.1.

This thesis will be organised as follows. In chapter 2 different models are described to estimate the diffuse Galactic neutrino flux. Two ways to determine this neutrino flux are presented: using theoretical models and using the γ-ray measurement performed by the Fermi satellite. The signal is also compared to the background, which for neutrino telescopes consists mainly of atmospheric neutrinos (which are produced by cosmic rays interacting with our atmosphere).

The ANTARES neutrino telescope, used to perform a measurement of the diffuse Galactic neutrino flux, is introduced in chapter 3. ANTARES is well suited to perform this measurement, since it has a high visibility of the Galactic plane. Several algorithms used to select interesting physics events, as well as the reconstruction strategies currently available within ANTARES, will be described in more detail in chapter 4.

The analysis follows the flow of defining an *on-source* region (a rectangular area centred around the Galactic centre) and a number of comparable *off-source* regions (which are used to obtain an estimate of the background from the data). The number of events from the *on-source* and *off-source* regions are then compared to detect a possible signal.

The Galactic plane region is in any case an interesting region to consider, since besides the diffuse neutrino emission considered here, also sources reside there that are expected to emit neutrinos.

For example, the flux measured by IceCube could also be caused by these sources. The measurement can thus give an idea of the total number of neutrinos (diffuse and otherwise) that originate from the Galactic plane. In chapter 5 the analysis and the optimisations performed to remove the background are described in detail and the results are presented. Furthermore, the results are discussed, also in light of the flux measured by IceCube.

Chapter 6 gives a description of the next generation neutrino telescope, KM3NeT. In this chapter the sensitivity and discovery potential of KM3NeT for the diffuse Galactic neutrino flux are presented.

Finally, the conclusions and outlook are presented in chapter 7.

2

NEUTRINO FLUXES FROM COSMIC RAY INTERACTIONS IN THE MILKY WAY

In this chapter two different approaches for estimating the diffuse Galactic neutrino flux are described. The first approach is based on a theoretical modelling of the problem. This requires assumptions about the sources of cosmic rays and their energy spectrum. Also assumptions need to be made about the matter distribution and composition in the Milky Way, since this constitutes the target with which the cosmic rays interact. Finally, assumptions need to be made about the magnetic field in our Galaxy, because the cosmic rays are charged particles and they are influenced by this field. An overview of the relevant properties of the Milky Way and cosmic rays is given in section 2.1. Three different theoretical models are used and these are described and compared in section 2.2.

The second approach to calculate the diffuse Galactic neutrino flux is based on the γ-ray spectrum that is measured by the Fermi satellite. As noted in the previous chapter, these high energy photons are partly created from cosmic ray interactions. The advantage of this approach compared to the theoretical models is that less assumptions have to be made. Only the fraction of the observed photons originating from cosmic ray interactions with the interstellar matter needs to be estimated. This approach is described in section 2.3, and the fluxes obtained in this way are compared to the theoretical fluxes.

Finally, the signal is put into context by comparing it to the main background, which for neutrino telescopes consists of neutrinos produced by cosmic ray interactions in our atmosphere. These so-called atmospheric neutrinos are described in more detail in section 2.4. Finally, the signal fluxes for a neutrino telescope located in the Mediterranean Sea are compared to one located on the South Pole.

2.1 MODEL INGREDIENTS

Before discussing the theoretical models and the underlying assumptions, an overview is given of what is known about the Milky Way and the model ingredients: the interstellar matter, the Galactic magnetic field and cosmic rays.

2.1.1 *The Milky Way*

*Edwin Powell Hubble: *1889; †1953*

Galaxies are classified by their Hubble type [Hubble, 1926], introduced in 1925 by Edwin Hubble. It is normally represented as a tuning-fork diagram, as can be seen from figure 2.1. Most of the galaxies that we know are elliptical, which are denoted by the letter *E* followed by a number that represents the ellipticity, where 0 is nearly circular and 7 is the most ellipse-like. Most of the remaining galaxies are spiral galaxies, of which there are two types: those with a bar (about one-third of the spirals) and those without. The spiral galaxies are denoted by the letter *S* and a second letter (*a*, *b* or *c*) that denotes how tightly wound the spiral arms are, with type *Sa* having the most tightly wound arms. The barred spiral galaxies are denoted with an extra *B* inserted. A few percent of galaxies do not show any regularity. These irregular galaxies are classified as *Irr*. Examples of irregular galaxies are the Magellanic Clouds [Pasachoff, 1979].

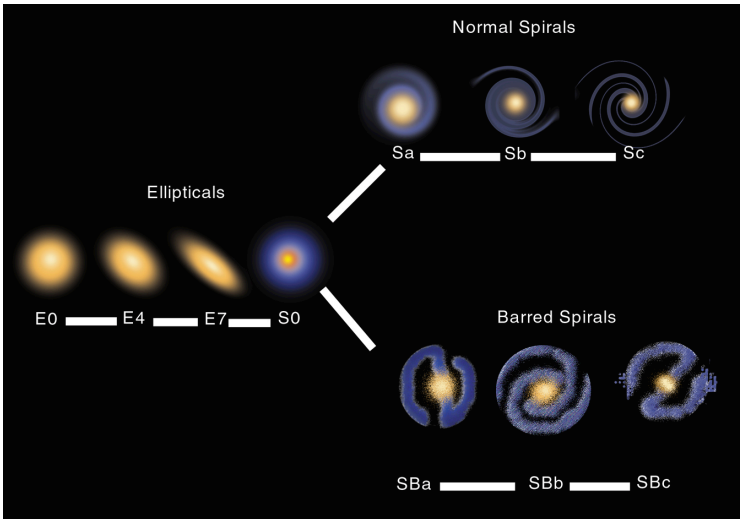

Figure 2.1: The Hubble classification of galaxies. Image credit NASA.

Since the Earth is situated within the Milky Way, it is difficult to classify the Milky Way precisely. It is known that we live in a barred spiral galaxy, but not exactly how tightly wound the spiral arms are. It is thought to be between type *SBb* and *SBc*, also denoted by *SBbc* [Jones and Lambourne, 2004].

The Milky Way, like other galaxies, consists of stars, gas, dust and some form of dark matter. For (barred) spiral galaxies these are organised into a disk (containing the spiral arms), a bulge

and a halo. For elliptical galaxies the disk is not present, they only consist of a bulge and a halo. In the following, the structural components are described in more detail.

The dark-matter halo

The main structural component is the dark-matter halo. The mass of the dark matter is about $10^{12} M_\odot$ (where $M_\odot$ denotes the mass of our Sun: $2 \cdot 10^{30}$ kg). It is primarily the gravity of the dark matter that is responsible for holding the Galaxy together [Pasachoff, 1979]. The dark-matter halo is thought to have the form of a flattened sphere, specifically an oblate spheroid. It is difficult to cite the exact size of the dark-matter halo, since it has not been observed directly. By looking at its effect on the Magellanic Clouds, its diameter is estimated to be at least 100 to 120 kpc.

A parsec (symbol: pc) is the distance from the Sun to an astronomical object having a parallax of one arcsecond and is equal to 3.262 ly.

The disk

Most of the luminous matter is contained in a thin disk, which also contains the Sun and the Earth. Its mass is only one-tenth of the mass of the dark-matter halo ($10^{11} M_\odot$). It consists of stars and the InterStellar Medium (ISM). The ISM contains gas and dust (see section 2.1.2), magnetic fields (section 2.1.3) and cosmic rays (section 2.1.4). Since we are located within the Galactic disk, it appears as a band of diffuse light on the sky.

It is difficult to define *the* radius of the Galactic disk. The stellar disk has an apparent radius of 15 kpc, but the gas and in particular the atomic hydrogen disk extends to about 25 kpc, although the density decreases considerably beyond 15 kpc [Jones and Lambourne, 2004]. The total height of the Galactic disk is about 1 kpc. For an edge-on view of our Galaxy see figure 2.2.

From a bird's-eye view of the Galaxy, the spiral structure is visible, see figure 2.3 for an artist's impression. The spiral arms stand out not because they contain a higher number of stars, but rather since very hot and luminous stars are concentrated there. Our solar system is located near the inner edge of the local Orion-Cygnus arm (Local Arm) at about 8.5 kpc from the Galactic centre and about 15 pc above the midplane [Ferrière, 2001].

The bulge

The density of stars increases towards the centre of the Galaxy and their distribution is more spherical than in the disk. This region is called the bulge and it is thought to have an elongated

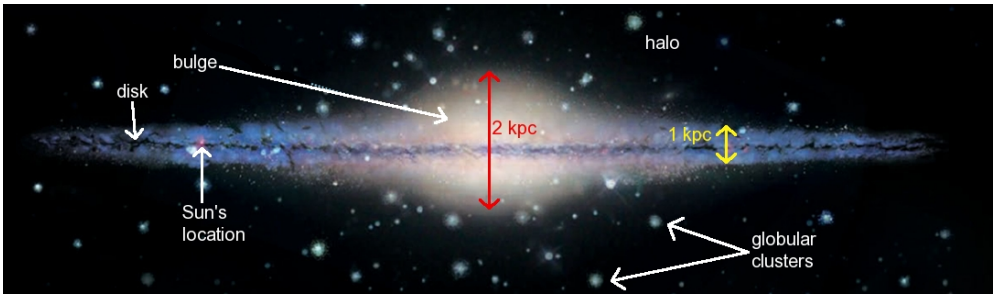

Figure 2.2: Edge-on view of the Milky Way. Figure reproduced after http://woodahl.physics.iupui.edu/Astro105/milkyonedge.jpg.

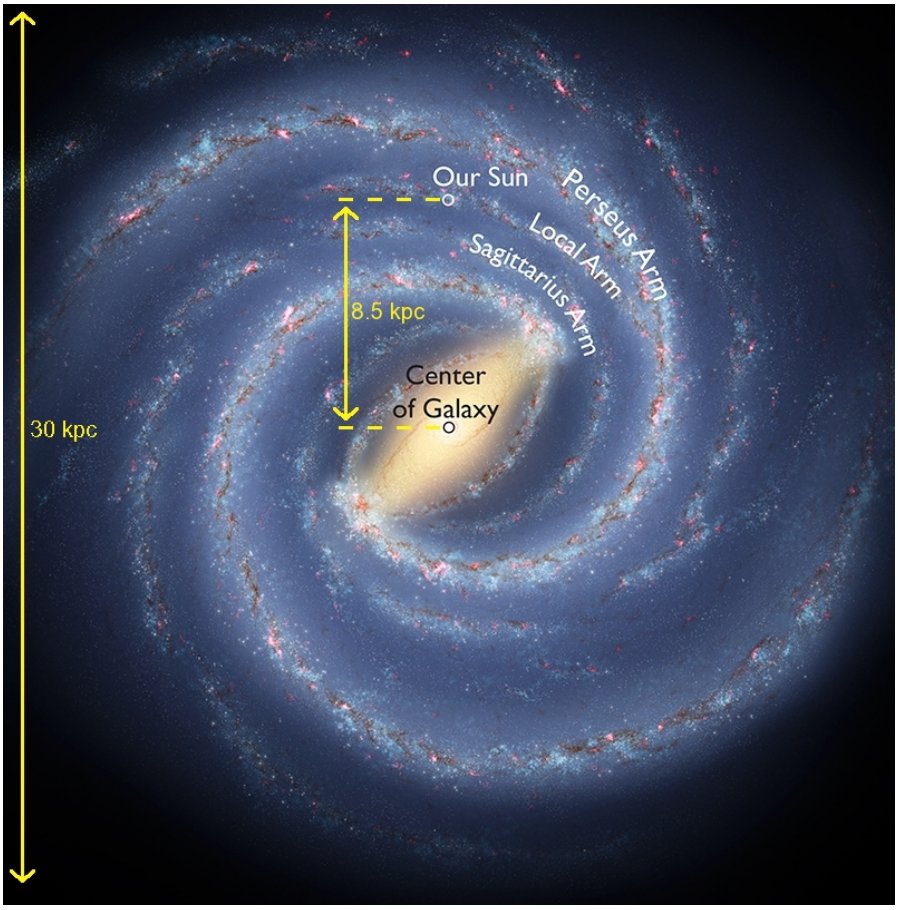

Figure 2.3: Bird's-eye view of the Milky Way. Image credit Robert Hurt, IPAC; Bill Saxton, NRAO/AUI/NSF.

shape, making the Milky Way a barred spiral galaxy. The bulge extends to about 3 kpc on either side of the Galactic centre and has a height (and width) of about 2 kpc.

2.1.2 *The interstellar matter*

The matter in the ISM is made up of gas (in atomic, ionised and molecular forms) and dust. It is concentrated near the Galactic plane (typically found within 150 pc [Jones and Lambourne, 2004] above/below the plane) and in the spiral arms. It has a total mass of about $10^{10} M_{\odot}$. About half of the interstellar mass is confined to clouds which only occupy $1 - 2\%$ of the interstellar volume [Ferrière, 2001]. The chemical composition of the interstellar matter is mainly hydrogen (70.4% by mass, 90.8% by number). Helium makes up 28.1% of the mass (9.1% by number) and the remaining 1.5% of the mass consists of heavier elements (referred to as metals by astronomers). The different forms of matter will now be described separately (for a thorough description of the subject see the lecture notes of Pogge [2011] and the references cited therein).

Neutral atomic gas

The main method of detecting neutral atomic hydrogen (denoted by H I) is via the observation of the 21-cm line, as described in the previous chapter. Only hydrogen is mentioned here since it is the most abundant element in the interstellar matter. The reader should keep in mind the chemical composition described above (see also figure 2.4). The H I is present in two thermal phases:

A. A cold phase with temperatures between 50 and 100 K, located in dense clouds (also called H I regions), with a hydrogen density of $20 - 50\,\mathrm{cm}^{-3}$.

B. A warm phase with temperatures between 6000 and 10000 K, located in the so-called *intercloud medium*, with a hydrogen density of $\sim 0.3\,\mathrm{cm}^{-3}$.

The H I density in the immediate vicinity of the Sun is lower than the values quoted above. It turns out that our solar system is located inside an H I cavity, called the Local Bubble. The Local Bubble has a width of about 100 pc in the Galactic plane and is elongated along the vertical. It is filled with ionised hydrogen (see next section), which has a very low density of only $\sim 0.005\,\mathrm{cm}^{-3}$,

but which has temperatures[1] of nearly 10^6 K. The Local Bubble is carved out by a series of past supernovae [Galeazzi et al., 2014].

As noted before, most of the atomic gas is located in the Galactic disk and is concentrated near the Galactic plane. The exponential scale height of the cold phase is about 100 pc. For the warm phase, two vertical scale height components are seen, one is Gaussian with a scale height of about 300 pc, the other is exponential with a scale height of about 400 pc. However, the disk in which the neutral atomic gas is located is not completely flat. It is only flat and centred around the Galactic plane to distances of about 12 kpc from the Galactic centre, but at greater distances it is tilted, with the gas reaching heights above/below the plane of 1 to 2 kpc [Jones and Lambourne, 2004].

[1] *Actually our solar system is not directly surrounded by the hot gas of the Local Bubble. It is instead located in a warm interstellar cloud, called the Local Cloud, with temperatures of about 6700 – 7600 K and a hydrogen density of about 0.18 – 0.28 cm^{-3}.*

Ionised gas

Ionised hydrogen (denoted by H II) can be detected using the Hα line, which has a wavelength of 656.28 nm. It is one of the Balmer lines and is created when the electron of a hydrogen atom changes its excitation state from $n = 3$ to $n = 2$. The ionised hydrogen is also present in two thermal phases:

*The Balmer lines or Balmer series are named after Johann Jakob Balmer (*1825; †1898), who discovered an empirical formula to calculate them.*

A. A warm phase with temperatures between 6000 and 10000 K, mainly located in the intercloud medium (90%), with a hydrogen density of about 0.1 cm^{-3}, but also partly in H II regions (10%).

B. A hot phase with temperatures above 10^6 K which extends into the Galactic halo, with a very low hydrogen density below about 0.003 cm^{-3}.

The H II regions are created by the UV radiation emitted by hot O and B stars (the most massive and hottest stars in the Milky Way). Inside the H II region, the ions and free electrons continuously recombine, after which the newly created neutral hydrogen will be ionised once more. The size of the region is thus determined by the equilibrium of the recombination rate with the photo-ionisation rate. For an artist's impression of the H I and H II regions see figure 2.4.

The H II regions are highly concentrated along the Galactic plane, with an exponential scale height of about 70 pc, while the diffuse component located in the intercloud medium has an exponential scale height around 1 kpc. For the radial dependence, Cordes et al. [1991] used several different measurements to come to a Gaussian dependence on distance to the Galactic

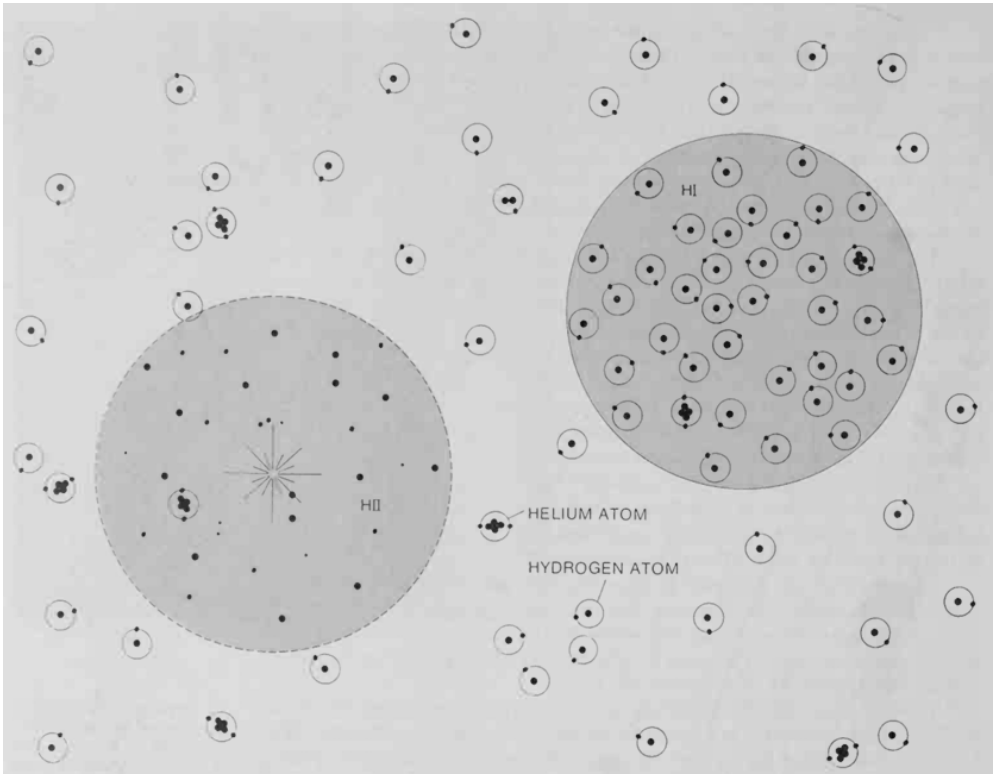

Figure 2.4: Schematic represention of H I and H II regions. Figure reproduced from Pasachoff [1979].

centre with a scale length of 20 kpc, which peaks around 4 kpc, and then decreases again towards the Galactic centre.

The hot interstellar gas is generated by supernova explosions and stellar winds from the progenitor stars. The hot gas is very buoyant and is located in bubbles (like the Local Bubble described above) and fountains that rain back gas on the Galactic disk. Because of this it has a large exponential scale height of about 3 kpc, although the uncertainty on this value is quite large.

Molecular gas

Molecular gas is expected at places where the density is high (as there is a higher chance of atoms meeting each other), the temperature is low (below about 100 K, which avoids collisional disruption) and the UV flux is low (which avoids UV-induced disruption). These are the conditions found in cool dense clouds, which are thus called molecular clouds.

The molecular clouds themselves are organised in complexes with typical sizes between 20 and 100 pc and a mean hydrogen number density between 100 and 1000 cm^{-3}. Cloud complexes are mostly located along the spiral arms and are particularly numerous at distances between 4 and 7 kpc from the Galactic centre.

The most abundant interstellar molecule is H_2. It is difficult to observe this molecule directly, since it has no permanent electric dipole moment and only a very small moment of inertia. Most of what is known about molecular interstellar gas is by the use of so-called *tracers*. The main tracer is the CO molecule (the second most abundant interstellar molecule), which can be observed in its $J = 1 \rightarrow 0$ rotational transition at a radio wavelength of 2.6 mm [Glover and Mac Low, 2011]. The advantage of using radio wavelengths is that the molecular gas itself is transparent to it, so that measurements can be made from the inside of molecular clouds.

Dust

Dust consists of tiny lumps of solid compounds made predominantly of carbon, oxygen and silicon. The typical size of a dust particle is about 0.1 to 1 μm, which makes it comparable in size to the wavelength of visible light. Dust is therefore a very efficient absorber and scatterer of visible light, resulting in the dark lines seen in the top right plot of figure 1.3.

The total mass of the dust is only about 0.1% of the total mass of the stars, but dust is still very important for a number of processes. It serves as a catalyst in the formation of molecular hydrogen and also shields the H_2 against UV light. It is also thought to be important for the formation of planets, since the formation of a planetary system can start with the coagulation of dust grains into planetesimals, which can eventually turn into planets.

Discussion

For the work carried out in this thesis, the H I and H_2 components are the most important constituents of the ISM, with the H II component contributing to a lesser extent. The dust can safely be neglected due to its low density. The hot ionised gas phase can also be neglected, because even though it extends far from the Galactic plane, it has a very low density. It should be noted that according to Taylor et al. [2014], the neutrinos measured by

IceCube might actually originate from PeV cosmic ray interactions in the Galactic halo, after they escape from the Galactic disk.

2.1.3 *The magnetic field*

The observation of the polarisation of starlight from distant stars was the first evidence for the presence of magnetic fields in the ISM [Hiltner, 1949; Hall, 1949]. The polarisation is caused by dust grains, the short axis of which aligns with the local magnetic field. Radiation with the electric field vector parallel to the long axis of the dust grain is mostly absorbed, leading to polarisation along the direction of the magnetic field.

Polarisation measurements only tell us about the direction of the Galactic magnetic field. The strength of the magnetic field can be inferred through other means, such as Zeeman splitting of the 21 cm H I line and Faraday rotation of light from pulsars. See the article of Brown [2011] for an overview of detection techniques.

The magnetic field at our location in the Galaxy has a strength of $3 - 5\,\mu$G [Jansson and Farrar, 2012a], which is very small compared to the typical magnetic field strength at the equator of the Earth of 0.31 G. The Galactic magnetic field consists of two components. A large scale field (also called the regular or uniform component) which evolves slowly and has a local strength of about $1.4\,\mu$G and a small scale field (also called the irregular or random component) representing the fluctuations on the large scale field. These two field components will be described separately.

The regular field

While it is relatively easy to measure the local magnetic field, since it can be measured directly using magnetometers aboard spacecraft, the magnetic field further away in the Galaxy is much more difficult to measure. For this reason there is still some controversy about the exact topology and strength of the magnetic field, but a few properties are widely accepted.

The regular magnetic field component in the disk has a strong azimuthal component and a smaller radial component of which the magnitude is not known. As viewed from the North Galactic pole, the direction of the regular field is clockwise while the direction in the Sagittarius Arm is counter-clockwise. This is the only field reversal that is generally agreed upon, however, it is also possible that there are more magnetic field reversals. There is also still uncertainty about the topology of the regular

field in the disk, and both axisymmetric and bisymmetric spiral configurations (see figure 2.5) are plausible [Haverkorn, 2014]. The strength of the regular field increases smoothly toward the Galactic centre, reaching about 4.4 μG at a radial distance of 4 kpc [Beck, 2008].

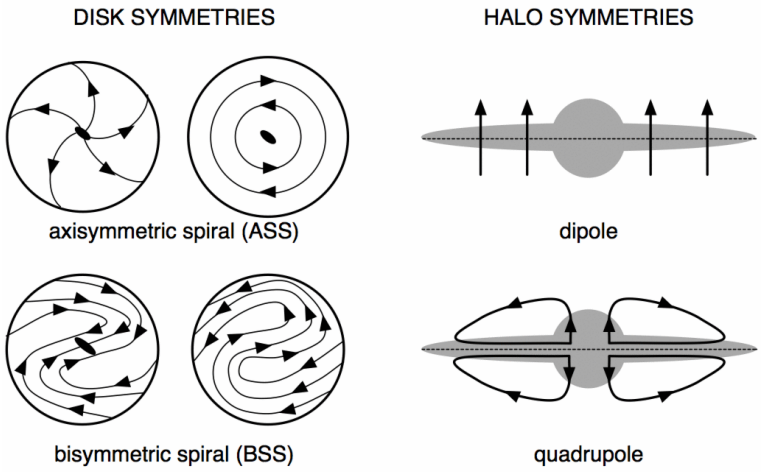

Figure 2.5: The possible configurations of the regular magnetic field in the disk. Figure reproduced from Brown [2011].

The regular field consists of two separate field layers, with one being localised in the disk and the other, which is an order of magnitude weaker than the field in the disk, extending into the Galactic halo. The transition between the layers takes place at a typical distance of 0.4 kpc above/below the Galactic plane [Jansson and Farrar, 2012b]. The exponential scale height of the halo field is about 1.4 kpc. It is not known if the magnetic field in the halo is symmetric above and below the Galactic plane (dipole), or anti-symmetric (quadrupole), see also figure 2.5.

The random field

The random magnetic field, which is associated with the turbulent interstellar plasma, has a local strength of about 5 μG and is also thought to consist of both a disk and a halo component. The strength of the disk component varies per spiral arm and decreases as $1/r$ (with r being the radial distance to the Galactic centre) for radii larger than 5 kpc [Jansson and Farrar, 2012a]. The halo component decreases as an exponential with the radius and is a Gaussian in the vertical direction, with a scale height comparable to the halo component of the regular magnetic field.

The random field has a typical coherence length scale of the order of 100 pc [Prouza and Šmída, 2003].

Discussion

Even though the magnetic field in the halo is an order of magnitude weaker than that in the disk, it is of more importance for the propagation of cosmic rays, since it extends much further in height. Since the strength and scale height of the uniform and random components are of the same order, the transport of cosmic rays in the Galaxy takes place under highly turbulent conditions [Evoli et al., 2007].

2.1.4 *Cosmic ray flux*

As described in the introduction, cosmic rays are charged particles, consisting primarily of protons. The major part of the observed cosmic rays is produced in Galactic sources [Ptuskin, 2012], although there is no consensus yet as to what their origin is. The prime candidates and the acceleration mechanism of cosmic rays are described below. After that, the propagation of cosmic rays through the Galaxy and their interactions with the matter and magnetic fields previously described will be discussed. Some more details will also be given about the cosmic ray fluxes measured at the Earth.

Sources of cosmic rays

SNRs, and the supernova explosions that create them, are the main candidate sources for cosmic rays. There are two types of supernovae: Type I and Type II. Type I supernovae arise when old low-mass stars accrete enough matter from their companion to create a thermonuclear instability. Type II supernovae arise from young stars with a mass of at least $8M_{\odot}$, which go through gravitional core-collapse after all their fuel is exhausted. In both cases a total amount of energy of the order of 10^{46} J is released, of which about 99% is released in the form of neutrinos. The remaining 1% goes into acceleration of interstellar material and electromagnetic radiation (0.01%) [Goobar and Leibundgut, 2011].

There are several theoretical grounds to assume that SNRs are sources of cosmic rays. The relative overabundance of iron points to very evolved early-type stars, which then release the cosmic rays into the ISM in the supernova explosion [Ferrière, 2001]. Also, the shockwaves created by the supernovae are able to accelerate the cosmic rays to higher energies over a broad energy

range and produce the observed power-law energy spectrum (see later in this section). Finally, the amount of energy released in supernova explosions is high enough to maintain a steady cosmic ray energy density [Grupen, 2005].

Recently, the Fermi collaboration claimed the proof that cosmic rays originate from the molecular clouds IC443 and W44, by looking for the characteristic pion-decay feature in the γ-ray spectra [Ackermann et al., 2013] (see also section 2.3.2 for more information). The measurement by Fermi could be the first experimental proof that cosmic rays are indeed accelerated in SNRs.

Concerning the rates of supernovae, there exist big uncertainties. Ferrière [2001] gives a Type I supernova frequency of:

$$f_{\mathrm{I}} \approx \frac{1}{250\,\mathrm{year}}, \tag{2.1}$$

and a Type II supernova frequency of:

$$f_{\mathrm{II}} \approx \frac{1}{60\,\mathrm{year}}, \tag{2.2}$$

in our Galaxy, giving a total rate of about 2 supernovae per century. Other estimates range from 1 to 4 supernova explosions per century.

The spatial distribution of SNRs has also big uncertainties, and various methods exist which yield different results. Besides performing direct measurements of the SNRs, it is also possible to use tracers of supernova explosions. For instance, Type I supernovae are thought to follow the distribution of old disk stars. Pulsars, which result from Type II supernovae, or H II regions, which are produced by the progenitor stars, can be used as tracers of Type II supernovae.

Concerning the radial distribution, Ferrière [2001], gives a distribution for Type II SNRs which consists of a rising Gaussian with a scale length of 2.1 kpc for $r < 3.7$ kpc and a standard Gaussian with a scale length of 6.8 kpc for $r \geqslant 3.7$ kpc. This radial distribution is shown in figure 2.6 as the blue dotted line, together with several other distributions. The differences between the distributions gives a measure for the uncertainty. The vertical distribution of Type II SNRs is given by the superposition of a thin disk with a Gaussian scale height of 0.2 kpc containing 55% of the SNRs and a thick disk with a Gaussian scale height of 0.6 kpc containing the remaining 45%.

For the Type I SNRs, a distribution with an exponential scale length of 4.5 kpc in radius and an exponential scale height of

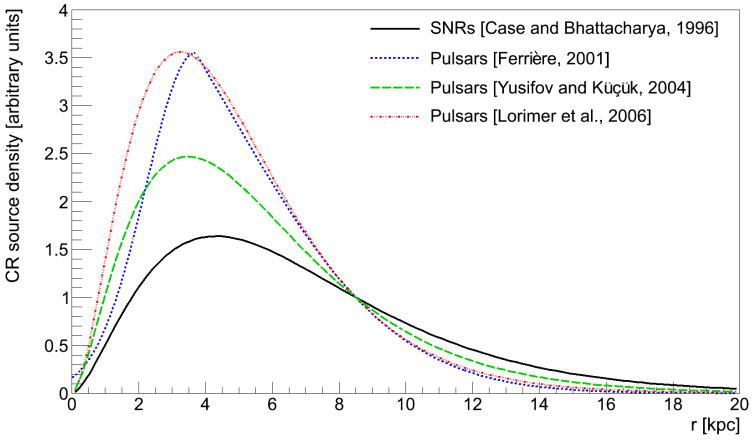

Figure 2.6: Several radial Type II SNR distributions, the legend shows the type of tracer that is used and the reference.

0.3 kpc is obtained from measurements of old disk stars. Although the rate of Type I supernovae is about 4 times lower than that of Type II (compare equations 2.1 and 2.2), the former is more important in the inner Galaxy.

Even though SNRs are the main candidate for the sources of (Galactic) cosmic rays, they might not be the only source. Other cosmic ray candidate sources include pulsars and (for extragalactic cosmic rays) AGNs and GRBs.

GRB: Gamma-Ray Burst, a short but extremely energetic burst of γ-radiation. It is the brightest electromagnetic event known.

Acceleration mechanism

It is generally accepted that primary cosmic rays (those produced in the source) are accelerated further by scattering off moving magnetic field irregularities, regardless of the injection site. This acceleration can happen via the mechanism as proposed by Enrico Fermi, in which cosmic rays interact with magnetic clouds [Fermi, 1949].

*ENRICO FERMI: *1901; †1954*

When a particle of mass m and velocity v is reflected from a magnetic cloud moving with velocity u, the energy gain of the particle is:

$$\Delta E_{\pm} = \frac{1}{2}m(v \pm u)^2 - \frac{1}{2}mv^2, \tag{2.3}$$

where the $+$ $(-)$ sign should be taken when v and u are parallel (anti-parallel). The average net gain of energy is then:

$$\Delta E = \Delta E_{+} + \Delta E_{-} = mu^2, \tag{2.4}$$

which gives a relative energy gain of:

$$\frac{\Delta E}{E} = 2\frac{u^2}{v^2}. \tag{2.5}$$

Since the relative energy gain in equation 2.5 (which is also valid for relativistic velocities) is quadratic in the cloud velocity, this mechanism is called the 2nd order Fermi mechanism. Acceleration by the 2nd order Fermi mechanism will take a very long time, since the cloud velocity is low compared to the particle velocity. Furthermore, the mechanism only works above ~200 MeV, since the energy losses below this energy are larger than the energy gain by the 2nd order Fermi mechanism.

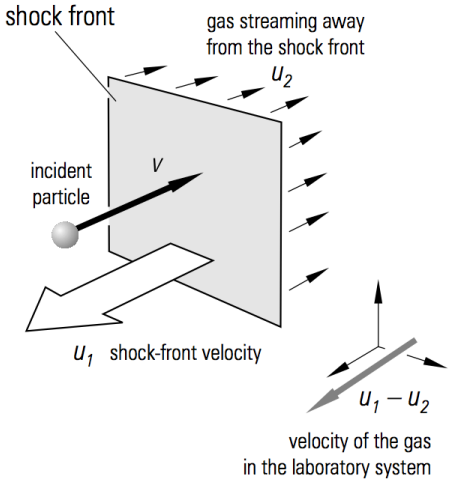

Figure 2.7: Schematic representation of shock acceleration. Figure reproduced from Grupen [2005].

A different mechanism was proposed by Axford et al. [1978], who considered particles colliding with shock fronts (which can be produced by supernova explosions).

Consider a particle colliding with and scattering off a shock front moving with a velocity u_1. Behind the shock front, the gas recedes with a velocity u_2, meaning that the gas has a velocity of $u_1 - u_2$ in the laboratory frame (see figure 2.7). The energy gain of the particle is now:

$$\Delta E = \frac{1}{2}m(v + (u_1 - u_2))^2 - \frac{1}{2}mv^2, \tag{2.6}$$

$$= \frac{1}{2}m(2v(u_1 - u_2) + (u_1 - u_2)^2). \tag{2.7}$$

When considering large particle velocities ($v \gg u_1, u_2$), the first term dominates and the relative energy gain becomes:

$$\frac{\Delta E}{E} = 2\frac{u_1 - u_2}{v}, \tag{2.8}$$

which is linear in the relative velocity, and is thus called the 1st order Fermi mechanism. A relativistic calculation, taking variable scattering angles into account, gives the same dependence on the relative velocity, see Grupen [2005]:

$$\frac{\Delta E}{E} = \frac{4}{3}\frac{u_1 - u_2}{c}. \tag{2.9}$$

The Fermi mechanisms can also explain the observed power-law dependence of the cosmic ray energy spectrum. After one collision/reflection, the particle will have an energy E_1:

$$E_1 = E_0(1 + \epsilon), \tag{2.10}$$

where E_0 is the initial energy and ϵ is the relative energy gain. After n collisions the energy will then be:

$$E_n = E_0(1 + \epsilon)^n. \tag{2.11}$$

Assume now that the probability that the particle escapes (and is not further accelerated) is P_{esc}. After n collisions there will then be:

$$N_n = N_0(1 - P_{\text{esc}})^n, \tag{2.12}$$

particles remaining which have an energy E_n. This results in an energy spectrum given by:

$$\frac{dN}{dE} \propto E^{\frac{\ln(1-P_{\text{esc}})}{\ln(1+\epsilon)}-1}. \tag{2.13}$$

Using the fact that the energy gain per cycle and the escape probability are small (i. e. ϵ, $P_{\text{esc}} \ll 1$) [Grupen, 2005], equation 2.13 can be written as:

$$\frac{dN}{dE} \propto E^{\frac{-P_{\text{esc}}}{\epsilon}-1}. \tag{2.14}$$

An elegant feature of the 1st order Fermi mechanism is that it yields a universal prediction for the spectral index [Baring, 1997]. From kinetic theory, the escape probability for non-relativistic plasma shocks can be written as [Bustamante et al., 2009]:

$$P_{\text{esc}} = \frac{4}{3}\frac{u_1 - u_2}{c}, \tag{2.15}$$

which is identical to the relative energy gain per cycle (equation 2.9), so that equation 2.14 becomes:

$$\frac{dN}{dE} \propto E^{-2}. \tag{2.16}$$

The 2nd order Fermi mechanism also results in a power-law in the energy spectrum, but the spectral index cannot be uniquely determined in this case [Baring, 1997].

It is generally thought that the 1st order Fermi mechanism accelerates particles to a sufficiently high energy, after which they are further accelerated by the 2nd order mechanism.

Transport of cosmic rays

After acceleration, the cosmic ray particles propagate through the interstellar medium under the influence of the interstellar magnetic field. This field confines the cosmic rays to the Galaxy, since they are forced to gyrate about the magnetic field lines, following a circular orbit with radius:

$$r_L = \frac{p}{qB}, \tag{2.17}$$

called the Larmor radius, where B is the magnetic field strength, p is the particle momentum and q its charge. It is useful to rewrite equation 2.17 using $q = Ze$, with Z the atomic number and $e = 1.602 \cdot 10^{-19}\,\mathrm{C}$:

$$r_L = 1.08 \cdot 10^{-6}\,\mathrm{pc}\,\frac{p\,[\mathrm{GeV}/c]}{ZB\,[\mu\mathrm{G}]}, \tag{2.18}$$

in which different units, which are more suited for the situation at hand, are used for the variables.

Inserting the average strength of the magnetic field in the Milky Way of about 3 μG in equation 2.18 gives a Larmor radius of 0.36 pc for a proton ($Z = 1$) with an energy[2] of 10^6 GeV, and 360 pc for a proton with an energy of 10^9 GeV. From these considerations it can be seen that cosmic rays with energies up to at least about 10^7 GeV are contained in the Galaxy.

[2] *At the given energies, energy and momentum are approximately the same, since* $E = \sqrt{p^2c^2 + m^2c^4} \approx pc$ *for a proton mass of* $0.938\,\mathrm{GeV}/c^2$.

In the direction parallel to the magnetic field lines, the cosmic ray particles diffuse through the Galaxy due to the random component of the magnetic field. This component is coherent over length scales of about 100 pc, which is small compared to the size of the Milky Way. This explains the isotropy and relatively long confinement time in the Galaxy (which is inferred from unstable isotopes, see below). Besides diffusion, convection can also play

a role in the transport of cosmic rays, which is inferred from the observation of galactic winds in many galaxies [Strong et al., 2007].

During propagation through the Galaxy, cosmic rays can interact with constituents of the Milky Way in several ways. Some cosmic rays interact with the interstellar matter and produce secondary particles in inelastic collisions. This is the process responsible for the photon and neutrino production, which will be described in detail in sections 2.2 and 2.3. Cosmic ray nuclei can also break up in lighter nuclei like Li, Be and B (referred to as the *light elements*) in collisions with the interstellar gas. This process is known as spallation. As a result, the abundance of light elements in cosmic rays exceeds the average solar system abundances of these elements. The spallation process is the main way in which these light elements are produced [Lemoine et al., 1998] and most of the knowledge about cosmic ray propagation comes from measurements of their abundances. In addition, unstable secondary nuclei are produced, such as ^{10}Be, which is used to deduce the average cosmic ray lifetime.

Spallation is so named because 'spall' is produced: flakes of a material broken off a large solid body due to impact or stress.

Besides losing energy, the cosmic ray particles can also gain energy by scattering off shock fronts or randomly moving magnetic waves. This process can be represented as diffusion in momentum space, and is known as diffusive reacceleration.

In the most general form, the cosmic ray transport can be formulated as [Strong et al., 2007]:

$$\frac{\partial \Phi(\vec{r}, p, t)}{\partial t} = Q(\vec{r}, p, t) + \vec{\nabla} \cdot \left(\mathbb{D}_{xx} \vec{\nabla} \Phi \right) - \vec{\nabla} \cdot \left(\vec{V} \Phi \right) + \frac{\partial}{\partial p} \left(p^2 D_{pp} \frac{\partial}{\partial p} \frac{\Phi}{p^2} \right) - \frac{\partial}{\partial p} \left[\frac{\partial p}{\partial t} \Phi - \frac{p}{3} \left(\vec{\nabla} \cdot \vec{V} \right) \Phi \right] - \frac{\Phi}{\tau_f} - \frac{\Phi}{\tau_d}, \tag{2.19}$$

where $\Phi(\vec{r}, p, t)$ is the cosmic ray density at position $\vec{r}$ at time t for a particle with momentum p, $Q(\vec{r}, p, t)$ is the source term (representing the cosmic ray sources and including production by spallation and decay), $\mathbb{D}_{xx}$ is the spatial diffusion tensor, $\vec{V}$ is the convection velocity, D_{pp} is the diffusion coefficient in momentum space (representing diffusive reacceleration), τ_f is the timescale for loss by fragmentation and τ_d is the timescale for radioactive decay.

The cosmic ray transport equation introduced above can be solved by starting with the solution for the heaviest primary (since it can only be produced at the source, and not via spallation or decay) and using this solution to compute the solutions for the lighter primaries in an iterative way. Because of the complexity,

this can best be done numerically, such as is done in the GALPROP code [Moskalenko et al., 2011].

Considering the fate of the cosmic rays, several things can happen. It is generally believed that they eventually disappear; either by diffusing to the edge of the Galaxy where they then have a finite chance to leak out into intergalactic space, or by means of convection. It is also possible however, that they lose all their energy by inelastic collisions with the interstellar matter. And of course, some of the cosmic rays end up in the atmosphere of the Earth, where they interact and can be observed.

Convection is the movement of particles in a gas or fluid due to differences in density, for instance the rising of warmer air.

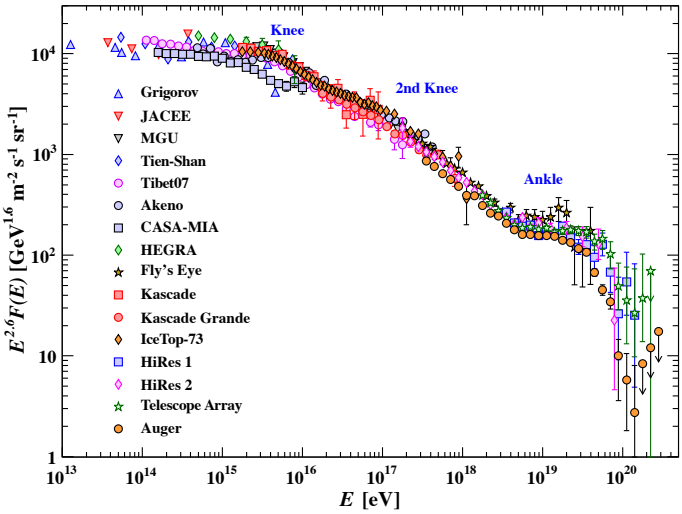

Figure 2.8: All-particle spectrum of cosmic rays as a function of energy-per-nucleus. Figure reproduced from Beringer et al. [2012].

Local cosmic ray flux

As noted before, the cosmic ray flux that is measured at the Earth exhibits a power-law behaviour in its energy spectrum:

$$\Phi_{\mathrm{CR}} \propto E^{-\gamma}, \tag{2.20}$$

where γ is the so-called spectral index. Below an energy of about $5 \cdot 10^6$ GeV it has a value of about 2.7. Above this energy, the spectrum steepens and the spectral index changes to about 3.0. This transition, called the knee, is thought to be due to cosmic ray sources not accelerating protons to beyond this energy and an increase in the escape probability of particles from the Galaxy [Beringer et al., 2012]. At an energy of about $5 \cdot 10^8$ GeV

the spectrum steepens once more ($\gamma \approx 3.3$), a feature which is called the 2nd knee, for which there is no explanation yet. The spectrum hardens again at an energy of about $5 \cdot 10^9$ GeV, a feature called the ankle, and the spectral index changes to about 2.7 again. The ankle is explained either by an extragalactic flux component or by energy losses from cosmic rays interacting with the cosmic microwave background radiation. The different parts of the spectrum can be seen in figure 2.8.

2.2 THEORETICAL MODELS FOR THE NEUTRINO FLUX

Now that the ingredients for the calculation of the diffuse Galactic neutrino flux have been introduced, three theoretical models considered in this work will be discussed. Some assumptions are used in the models to solve the equations analytically. Other approaches exist, such as using GALPROP to solve the cosmic ray transport equation numerically, which is descibed by Jouvenot [2005].

The focus of this work is to perform a measurement of the diffuse Galactic neutrino flux with ANTARES and to determine the sensitivity of KM3NeT. For this goal the theoretical models used here are suitable, since they incorporate the main ingredients. By considering different models, the influence of the assumptions can be checked. Besides using a pure theoretical modelling, experimental observations of high energy γ-rays are used to determine the neutrino fluxes. This will be described in section 2.3.

The names of the models and the references to the papers from which they are obtained are given in table 2.1. The reason for the names of the models will become clear after discussing the assumptions that are made in each of them.

MODEL NAME	REFERENCE
NoDrift_simple	Ingelman and Thunman [1996]
NoDrift_advanced	Candia and Roulet [2003]
Drift	Candia [2005]

Table 2.1: References for the three theoretical models.

2.2.1 *Assumptions*

As input for the determination of the neutrino fluxes, two distributions are needed. These are the matter density and the cosmic ray density as a function of location in the Galaxy. Using cylindrical symmetry, a point in the Galaxy can be identified using two coordinates: the height above/below the Galactic plane z (with $z > 0$ above the Galactic plane) and the distance from the Galactic centre r (in the plane where $z = 0$). The coordinate system is shown in figure 2.9.

Matter distribution

In the two NoDrift models it is assumed that the matter density is constant and has a value of $1\,\text{nucleon/cm}^3$ in the Galactic plane, which has a radius R of 12 kpc. Out of the plane the matter density falls off exponentially, so that it can be parameterised as:

$$\rho_{\text{ISM}}(r, z) = \rho_0 \cdot e^{-|z|/(0.26\,\text{kpc})}, \tag{2.21}$$

with $\rho_0 = 1\,\text{nucleon/cm}^3$.

For the Drift model, a more realistic matter distribution is used which takes into account the higher matter density around the Galactic centre. The radial distribution is taken from the paper from Berezinsky et al. [1993], where it is given in tabular form. The radius of the Galaxy R is taken to be 20 kpc for this model. To avoid steps and ensure a smooth distribution, a function has been fitted to the tabulated values:

$$n(r) = 18.8\,\text{nucleon/cm}^3\ \ (1 - \text{erf}(15.4r\,[\text{kpc}] - 3.5)) + 2.3e^{-0.166r\,[\text{kpc}]}, \tag{2.22}$$

which provides for an accurate parameterisation, see Visser [2013].

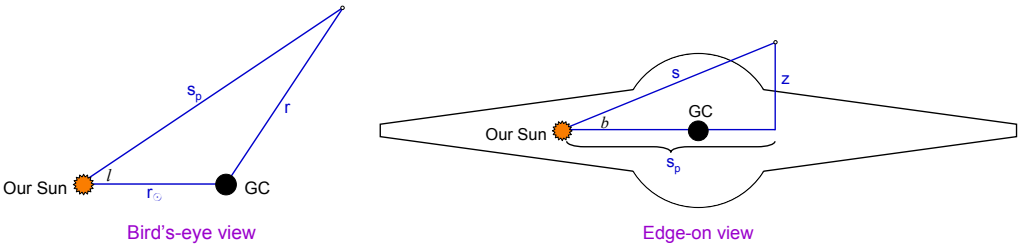

Figure 2.9: Coordinate system used to represent a point in the Galaxy, see the text for details.

Also a different exponential scale height is used[3], so that the matter density as a function of location in the Galaxy becomes:

$$\rho_{\mathrm{ISM}}(r, z) = n(r) \cdot e^{-|z|/(0.5\,\mathrm{kpc})}, \tag{2.23}$$

with $n(r)$ given by equation 2.22. The matter density as seen from outside the Galaxy (in a slice through the Galactic centre) is shown in figure 2.10 (where $r = |x|$).

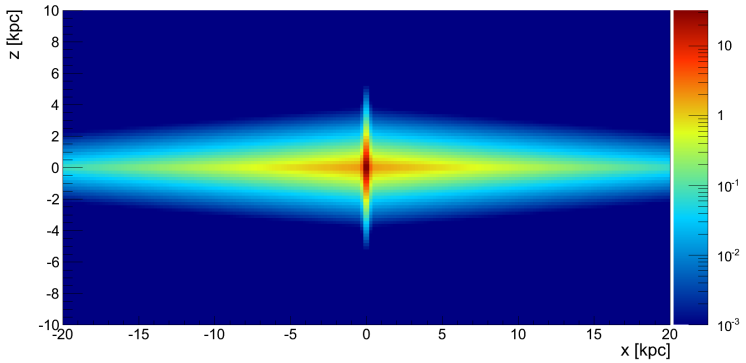

Figure 2.10: Matter density in the Galaxy in nucleon/cm^3 as used in the Drift model.

A useful (and in astronomy often used) quantity is the column density, which is the mass substance (or number of particles) per unit of area as seen from the Earth, integrated along a straight path. For this the Galactic coordinate system is used, where the direction to an object in the sky is expressed in terms of its Galactic longitude l and Galactic latitude b (see also figure 2.9). In this coordinate system, the direction with $l = 0°$ and $b = 0°$ marks the location of the Galactic centre[4]. The column density N is a function of l and b and is given by:

$$N(l, b) = \int \mathrm{d}s\, \rho_{\mathrm{ISM}}(r, z), \tag{2.24}$$

where s is the integration variable (with $s = 0$ at the location of the Earth). Using some geometry, the coordinates used earlier (r and z) can be written in these new coordinates as (see figure 2.9):

$$r(l, b, s) = \sqrt{s^2 \cos^2 b + r_\odot^2 - 2 r_\odot s \cos b \cos l}, \tag{2.25}$$

and:

$$z(l, b, s) = s \sin b, \tag{2.26}$$

[3] *The exponential scale height used by Candia [2005] is not the same as that given in the paper from which the matter distribution is taken [Berezinsky et al., 1993], in which the exponential scale height is ~0.21 kpc for $r < 8$ kpc and ~0.26 kpc for larger values of r. Even though the value of 0.5 kpc is a bit higher than generally assumed (see section 2.1.2), it is compatible with measurements, and the model is used as given by Candia [2005].*

[4] *Actually, the radio source Sagittarius A*, which is the best physical marker of the Galactic centre, is located at $l = 359.94°$ and $b = -0.046°$.*

where $r_\odot$ is the distance from the Earth to the Galactic centre (taken to be 8.5 kpc).

A typical value of the column density is $1\,\mathrm{kpc} \cdot 1\,\mathrm{nucleon/cm^3} \approx 0.3 \cdot 10^{22}\,\mathrm{nucleon/cm^2}$. A plot of the column density for the matter density used in the NoDrift models can be found in figure 2.11 and for the one used in the Drift model in figure 2.12.

Cosmic ray flux

For the NoDrift models, the cosmic ray flux is assumed to be constant throughout the Galaxy and equal to the flux measured locally on Earth. No cosmic ray transport equation is solved and no particle propagation is done, hence the name 'NoDrift', since no drift of cosmic ray particles is considered.

In the NoDrift_simple model the cosmic ray flux is parameterised as:

$$\Phi_\mathrm{N}(E_\mathrm{N}) = \begin{cases} 1.7 \cdot 10^4\, E_\mathrm{N}^{-2.7}\,\mathrm{GeV^{-1}\,m^{-2}\,sr^{-1}\,s^{-1}} & E_\mathrm{N} < 5 \cdot 10^6\,\mathrm{GeV} \\ 174 \cdot 10^4\, E_\mathrm{N}^{-3}\,\mathrm{GeV^{-1}\,m^{-2}\,sr^{-1}\,s^{-1}} & E_\mathrm{N} \geqslant 5 \cdot 10^6\,\mathrm{GeV} \end{cases} \tag{2.27}$$

where Φ_N is the cosmic ray nucleon flux as a function of the nucleon energy E_N and the break represents the knee in the cosmic ray spectrum.

In the NoDrift_advanced model, each nuclear component in the cosmic ray spectrum is modelled separately and the following parameterisation is used for the cosmic ray flux Φ_CR:

$$\Phi_\mathrm{CR}(E) = \sum_Z \frac{\Phi_Z^< \cdot \Phi_Z^>}{\Phi_Z^< + \Phi_Z^>}, \tag{2.28}$$

where $\Phi_Z^<$ ($\Phi_Z^>$) is the CR flux for the component with charge Z and energy E below (above) the knee, which is given by:

$$\begin{Bmatrix} \Phi_Z^< \\ \Phi_Z^> \end{Bmatrix} = f_Z\,\Phi_0 \left(\frac{E}{E_0}\right)^{-\alpha_Z} \cdot \begin{Bmatrix} 1 \\ \left(\frac{E}{ZE_k}\right)^{-2/3} \end{Bmatrix}, \tag{2.29}$$

where $\Phi_0 = 3.5 \cdot 10^{-4}\,\mathrm{GeV^{-1}\,m^{-2}\,sr^{-1}\,s^{-1}}$ is the total CR flux at an energy of $E_0 = 1\,\mathrm{TeV}$, E_k is a parameter fixing the position of the knee, which is taken to be $3.1 \cdot 10^6\,\mathrm{GeV}$ and f_Z and α_Z are the CR fractions and spectral indices per nuclear component for

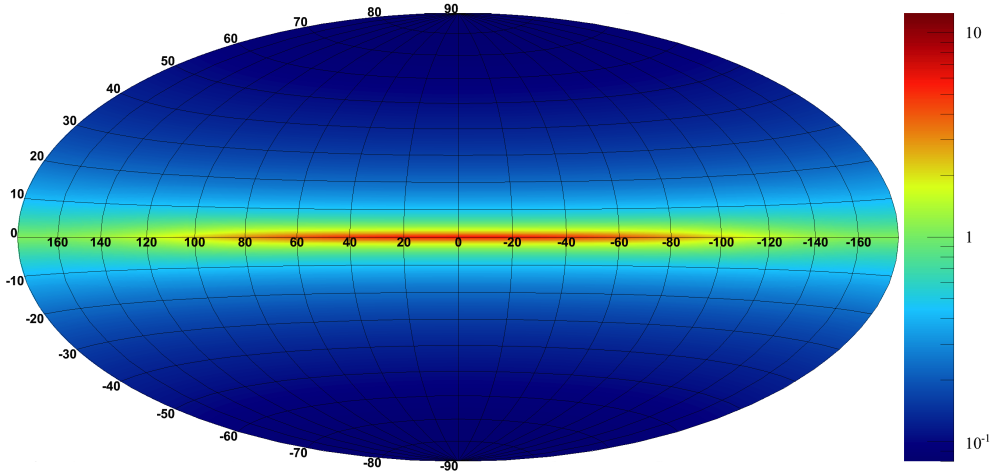

Figure 2.11: Column density in units of 10^{22} nucleon/cm^2 used in the NoDrift models.

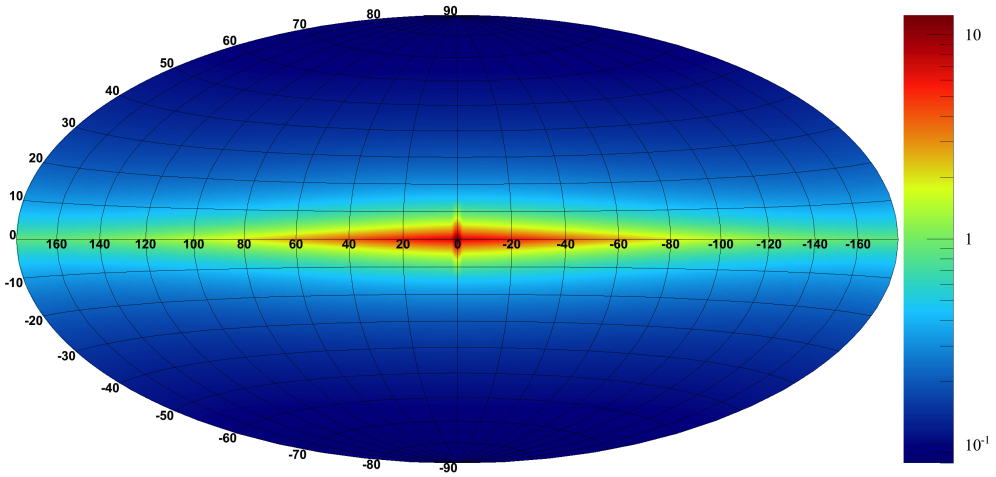

Figure 2.12: Column density in units of 10^{22} nucleon/cm^2 used in the Drift model.

cosmic rays with an energy E_0 respectively. The values of f_Z and α_Z can be found in the paper from Candia and Roulet [2003] and are not repeated here.

In addition to the Galactic component, there is also an extragalactic component, which is assumed to consist only of protons and to permeate the Milky Way homogeneously:

$$\Phi_{XG}(E) = 0.68\, E^{-2.4}\,\mathrm{GeV}^{-1}\,\mathrm{m}^{-2}\,\mathrm{sr}^{-1}\,\mathrm{s}^{-1}, \tag{2.30}$$

with E in GeV.

The cosmic ray flux given by equation 2.28 is the CR particle flux, but for the calculation of the neutrino fluxes, the CR nucleon flux is needed. The particle flux can be converted to a nucleon flux using the following equation[5]:

[5] *Note that the energy in the particle flux is the energy per nucleus, while the energy in the nucleon flux is the energy per nucleon.*

$$\Phi_N(E_N) = \sum_Z A^2\, \Phi_Z(A \cdot E_N), \tag{2.31}$$

where $\Phi_Z(E)$ is the CR particle flux for a single component and A is the average mass number of the element with atomic number Z.

The total cosmic ray nucleon flux can thus be obtained by substituting equation 2.31 in equation 2.28 and adding the extragalactic component from equation 2.30. Since this involves more steps (and assumptions), this model is called the 'NoDrift_advanced' model, while the other NoDrift model is called 'NoDrift_simple'. Since the cosmic ray flux is constant over the Milky Way, the neutrino flux for the NoDrift models will be directly proportional to the column density shown in figure 2.11.

The Drift model is the most advanced model considered here. In it, the cosmic ray transport equation is solved. The steady-state solution is required, so all the time dependence drops out of equation 2.19, which, when also neglecting convection, reacceleration, energy-loss processes and spallation, can be written as:

$$Q(r, z, E) = \vec{\nabla} \cdot \left(\mathbb{D}_{xx} \vec{\nabla} \Phi \right), \tag{2.32}$$

with $Q(r, z, E)$ the source term. This model is also called the *plain-diffusion* model and is generally considered a good description of cosmic ray transport through the Galaxy (at least for energies up to $10^8 \cdot Z$ GeV) [Ptuskin, 2012].

The sources of cosmic rays are assumed to be SNRs, which are distributed within a thin disk with a height h_s, with a radial profile given by:

$$q(r) = \begin{cases} \left(\frac{r}{r_\odot}\right)^{1.69} e^{-3.33\cdot(r-r_\odot)/r_\odot} & r \geqslant 3\,\mathrm{kpc} \\ q(r = 3\,\mathrm{kpc}) & 0\,\mathrm{kpc} < r < 3\,\mathrm{kpc} \end{cases} \tag{2.33}$$

with the part for $r \geqslant 3\,\mathrm{kpc}$ corresponding to the Type II SNR distribution shown as the black line in figure 2.6.

The source term in equation 2.32 can then be written as:

$$Q(r, z, E) = 2h_s q(r)\delta(z)E^{-\beta}, \tag{2.34}$$

where β is the spectral index of the source energy spectrum. In this, it is assumed that the sources lie in a thin disk so that the delta function approximation can be applied.

Concerning the magnetic field, it is assumed that only an azimuthal component with opposite directions above and below the Galactic plane exists (i. e. an anti-symmetric field). The spatial diffusion tensor $\mathbb{D}_{xx}$ can then be written as:

$$\mathbb{D}_{xx} = \begin{pmatrix} D_\perp & 0 & D_A\,\mathrm{sgn}(z) \\ 0 & D_{||} & 0 \\ -D_A\,\mathrm{sgn}(z) & 0 & D_\perp \end{pmatrix}. \tag{2.35}$$

The coefficients $D_{||}$, $D_\perp$ and D_A in equation 2.35 are the diffusion coefficients describing diffusion parallel to the magnetic field lines, diffusion transverse to the magnetic field lines and collective macroscopic diffusion (drift) respectively. The parallel and transverse diffusion coefficients depend on the magnetic field energy density and are assumed to be proportional to $E^{1/3}$, whereas the macroscopic diffusion is proportional to E. This stronger energy dependence of D_A is used by Candia [2005] to explain the knee and the second knee in the cosmic ray energy spectrum as a transition from the transverse diffusion dominated regime to the drift dominated regime.

The drift velocities in the radial and vertical direction can be written as:

$$v_r = -\frac{\partial(D_A\,\mathrm{sgn}(z))}{\partial z} = -2D_A\delta(z), \tag{2.36}$$

$$v_z = \frac{1}{r}\frac{\partial(rD_A\,\mathrm{sgn}(z))}{\partial r} = \frac{2D_A}{r}\mathrm{sgn}(z), \tag{2.37}$$

where the simplifying assumption $D_A(r, z) = D_{A0} \cdot r$ and the relation $\frac{\mathrm{d}(\mathrm{sgn}(z))}{\mathrm{d}z} = 2\delta(z)$ have been used.

The effect of the assumed (anti-symmetric) magnetic field configuration is a radial drift that is directed towards the Galactic centre, as can be seen from equation 2.36. In the case of a symmetric magnetic field there is no radial drift. From equation 2.37 it can be seen that the drift in the vertical direction is removing the CRs from the Galactic plane.

The solution to equation 2.32 (for a single nuclear component), which is set to be unity at $r = r_\odot$ and which is flat at low E is given by[6]:

[6] *For a more detailed derivation of the solution to equation 2.32, see Visser [2013] and Candia [2005].*

$$\Psi(E, r, z) = E^{-2/3} \frac{1 - e^{-w(1-|z|/H)}}{1 - e^{-w}} \int_1^{R/r} \mathrm{d}y \, q(yr) \, y^{-1-2/(e^w-1)}, \tag{2.38}$$

where $H = 2\,\mathrm{kpc}$ is the height of the Galactic disk in which the cosmic ray transport takes place, y is the integration variable which goes from 1 to R/r and

$$w = 0.85 \left(\frac{E}{3 \cdot 10^6\,\mathrm{GeV}} \right)^{2/3}. \tag{2.39}$$

The analytical solution to equation 2.38 can be found in Visser [2013].

Analogously to equation 2.28, the contributions of the separate nuclear components have to be added, so that the total cosmic ray particle flux for the Drift model can be written as:

$$\Phi_{\mathrm{CR}}(E, r, z) = \Phi_0 \sum_Z f_Z \left(\frac{E}{E_0} \right)^{-\alpha_Z} \Psi(E/Z, r, z), \tag{2.40}$$

where Φ_0, E_0, f_Z and α_Z are the same as in equation 2.29.

Like for the NoDrift_advanced model, an extragalactic cosmic ray component is also considered, which is in this case given by:

$$\Phi_{\mathrm{XG}}(E) = 1.3\, E^{-2.4}\,\mathrm{GeV}^{-1}\,\mathrm{m}^{-2}\,\mathrm{sr}^{-1}\,\mathrm{s}^{-1}, \tag{2.41}$$

with E again in GeV. The total cosmic ray nucleon flux can be obtained by adding this result to the Galactic part obtained by applying equation 2.31 on equation 2.40.

The cosmic ray nucleon fluxes for the three models are compared in figure 2.13. It can be seen that the fluxes at the Earth are similar (as they should be, since they have to match the observations), and that the Drift model predicts an increased flux at

MODEL NAME	MATTER DENSITY	R	COSMIC RAY FLUX
NoDrift_simple	Constant (ESH = 0.26 kpc)	12 kpc	Constant
NoDrift_advanced	Constant (ESH = 0.26 kpc)	12 kpc	Constant
Drift	r-dependent (ESH = 0.5 kpc)	20 kpc	Drift of CRs to GC

Table 2.2: Assumptions made by the three theoretical models considered in this work (ESH stands for exponential scale height).

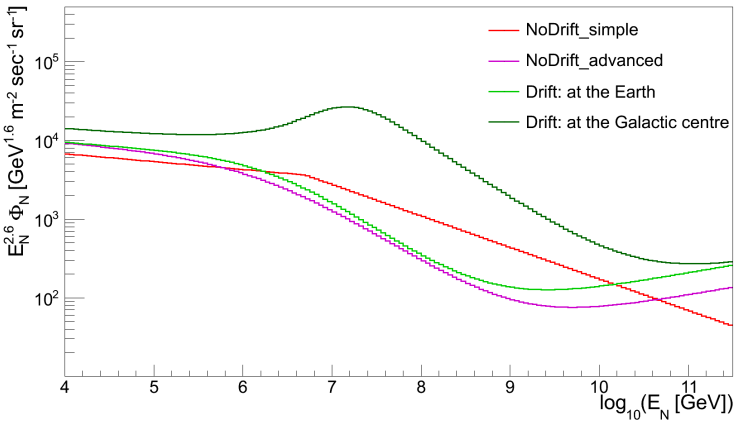

Figure 2.13: Cosmic ray nucleon fluxes predicted by the three theoretical models considered in this work as a function of energy per nucleon.

the Galactic centre. The main difference between the two NoDrift models is the predicted flux at high nucleon energies. This is mainly caused by the fact that no extragalactic component is used in the NoDrift_simple model, so that the ankle in the CR spectrum is not reproduced.

Table 2.2 summarises the assumptions made about the different model components for each of the three models.

2.2.2 *Calculation of $\nu_\mu + \overline{\nu}_\mu$ fluxes*

The matter density and the cosmic ray nucleon fluxes can now be used to calculate the neutrino fluxes. The different processes contributing to neutrino production are described first, after which the neutrino flux calculation is presented. In this, neutrino oscillations are taken into account.

Production mechanisms

Proton-proton interactions can be divided in three different types [Arneodo and Diehl, 2005], see figure 2.14:

A. Non-diffractive (or elastic), in which both protons emerge intact in the final state.

B. Single diffractive, in which one of the protons breaks up and the other one remains intact.

C. Double diffractive, in which both protons break up.

Single and double diffractive interactions are also called inelastic collisions. At the energies considered in this work, a substantial fraction of the total proton-proton cross section is due to inelastic collisions (about 80%, which is then nearly energy independent [Candia, 2005]).

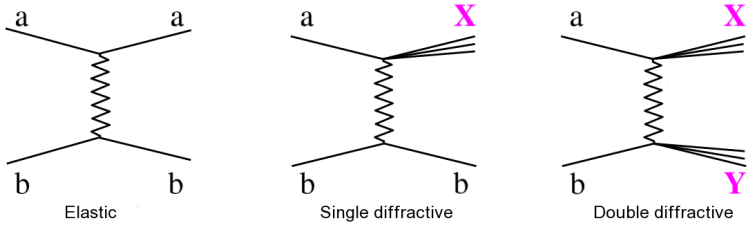

Figure 2.14: The three different types of hadron-hadron interactions. Figure reproduced from Arneodo and Diehl [2005].

Neutrinos are only indirectly produced in inelastic collisions, via the decay of a myriad of leptons and mesons (particles containing a quark and an anti-quark). Since the matter density in the Milky Way is very low, the mesons and leptons that are produced will decay before interacting with another interstellar matter particle. As a result, the maximum energy is transferred to the neutrinos. This sharply contrasts the production of leptons and mesons in cosmic ray interactions in the Earth's atmosphere, see section 2.4.

The main production mechanism is via the decay of charged pions [Huang and Pohl, 2008]:

Pions are the lightest mesons and consist of up and down (anti-)quarks: $\pi^+ = u\bar{d}$, $\pi^- = d\bar{u}$, $\pi^0 = (u\bar{u} - d\bar{d})/\sqrt{2}$.

$$\pi^+ \rightarrow \mu^+ + \nu_\mu, \tag{2.42}$$

and the subsequent decay of the muon:

$$\mu^+ \rightarrow e^+ + \nu_e + \overline{\nu}_\mu, \tag{2.43}$$

where reaction 2.42 happens in about 99.99% of the charged pion decays and reaction 2.43 in almost 100% of the muon decays [Beringer et al., 2012]. The same reactions hold for the anti-particles (by changing particles to anti-particles and vice versa).

Kaons can also decay into neutrinos, where the charged kaon can decay via:

$$\begin{aligned} K^+ &\to \mu^+ + \nu_\mu && (63.55\%) \\ K^+ &\to \pi^0 + e^+ + \nu_e && (5.07\%) \\ K^+ &\to \pi^0 + \mu^+ + \nu_\mu && (3.35\%) \end{aligned} \tag{2.44}$$

and the same again for the K^-. The neutral kaon decays into neutrinos via:

$$\begin{aligned} K^0_L &\to \pi^\pm + e^\mp + \nu_e && (40.55\%) \\ K^0_L &\to \pi^\pm + \mu^\mp + \nu_\mu && (27.04\%) \end{aligned} \tag{2.45}$$

Using the PYTHIA event generator [Sjöstrand et al., 2008] version 8.162, it has been calculated that the contribution of kaon decays to the neutrino production is of the order of 10%, independent of the neutrino energy. The reason that the kaons contribute less than the pions is that the kaon is a factor of about 3.5 heavier than the pion.

The decay of (anti-)neutrons also contributes, but only to the electron-neutrino flux:

$$n \to p + e^- + \overline{\nu}_e, \tag{2.46}$$

which happens in 100% of the decays.

Even heavier mesons, like the charmed mesons $D^\pm$ and D^0, which are important for atmospheric neutrino production (see section 2.4), have a negligible contribution compared to the pion decays [Huang and Pohl, 2008].

So far only muon- and electron-neutrinos[7] have been discussed, since most of the neutrinos that are produced have one of those two flavours[8]. However, tau-neutrinos are also produced, but since lepton number conservation requires a tau-neutrino to be accompanied by a τ-particle (with a mass of $1.78\,\mathrm{GeV}/c^2$), the number of tau-neutrinos is much lower than the number of electron- and muon-neutrinos, see also figure 2.15.

Kaons are the second-lightest mesons and contain a strange (anti-) quark: $K^+ = u\bar{s}$, $K^- = \bar{u}s$, $K^0 = d\bar{s}$, $\overline{K}^0 = \bar{d}s$. The neutral kaons combine into a long-lived and a short-lived state, called K^0_L and K^0_S respectively.

[7] *The subsequent discussions focus on neutrinos, but also hold for anti-neutrinos.*

[8] *Roughly twice as many muon-neutrinos as electron-neutrinos are produced, as can be inferred from reactions 2.42 and 2.43.*

Neutrino yield in proton-proton interactions

The neutrino flux can be calculated from the cosmic ray flux and matter distribution as:

$$\Phi_\nu(E_\nu, l, b) = \int_{E_\nu}^{\infty} \mathrm{d}E_\mathrm{N}\, Y_\nu(E_\mathrm{N}, E_\nu)\, \Phi_\mathrm{T}(E_\mathrm{N}, l, b), \tag{2.47}$$

where $\Phi_\nu(E_\nu, l, b)$ is the neutrino flux (either ν_e, ν_μ or ν_τ) for a given direction, $Y_\nu(E_N, E_\nu)$ is the neutrino yield, i.e. the number of neutrinos produced in the interval E_ν to $E_\nu + \delta E_\nu$ per proton-proton interaction (see Engel [2008] for an overview) and $\Phi_T(E_N, l, b)$ is the cosmic ray nucleon flux times the number of proton-proton interactions per metre, integrated along the line of sight:

$$\Phi_T(E_N, l, b) = \int \mathrm{d}s \; \Phi_N(E_N, r, z)\, \rho_{ISM}(r, z)\, \sigma_{pp}(E_N), \quad (2.48)$$

where $\sigma_{pp}(E_N)$ is the total proton-proton cross section. For the NoDrift models, the cosmic ray flux does not depend on position in the Galaxy, so that the integral along the line of sight in equation 2.48 reduces to the product of the cosmic ray nucleon flux, the total cross section and the column density (equation 2.24).

The neutrino yield is calculated by simulating fixed target proton-proton collisions with the PYTHIA event generator. It is important to point out that only proton-proton interactions are simulated; however the interstellar medium also consists of a small fraction of helium (having two neutrons in addition to two protons) and cosmic rays also contain particles with neutrons. Since PYTHIA cannot simulate these neutron-proton and neutron-neutron interactions, they are not included. However, at the energies of interest, the interactions that take place are mainly gluon-gluon interactions and the neutron and proton can be considered identical. The error arising from only simulating proton-proton interactions is thus small, see also Kamae et al. [2005].

The interactions are simulated in the Centre Of Momentum (COM) frame and the result is then Lorentz boosted to the universal frame. It is important to force the pions and muons to decay in order to produce neutrinos, since they are normally considered stable for collider experiments.

The muon-neutrino yield is shown in the top left plot of figure 2.15; the result for anti-muon-neutrinos is similar. It can be seen that in order to produce a neutrino with an energy of for instance 10 TeV, nucleons with an energy of at least 10 TeV are needed, as expected. Cosmic ray nucleons with an energy of $E_N \approx 10 \cdot E_\nu$ contribute the most to the neutrino flux at an energy of E_ν [Kachelrieß and Ostapchenko, 2014]. This results from the interplay of the neutrino yield, which rises with cosmic ray energy, the proton-proton cross section, which also rises with energy and the cosmic ray flux, which falls off as $E^{-2.7}$.

The electron- and tau-neutrino yields are shown in the top right and bottom plot of figure 2.15 respectively. The electron-neutrino

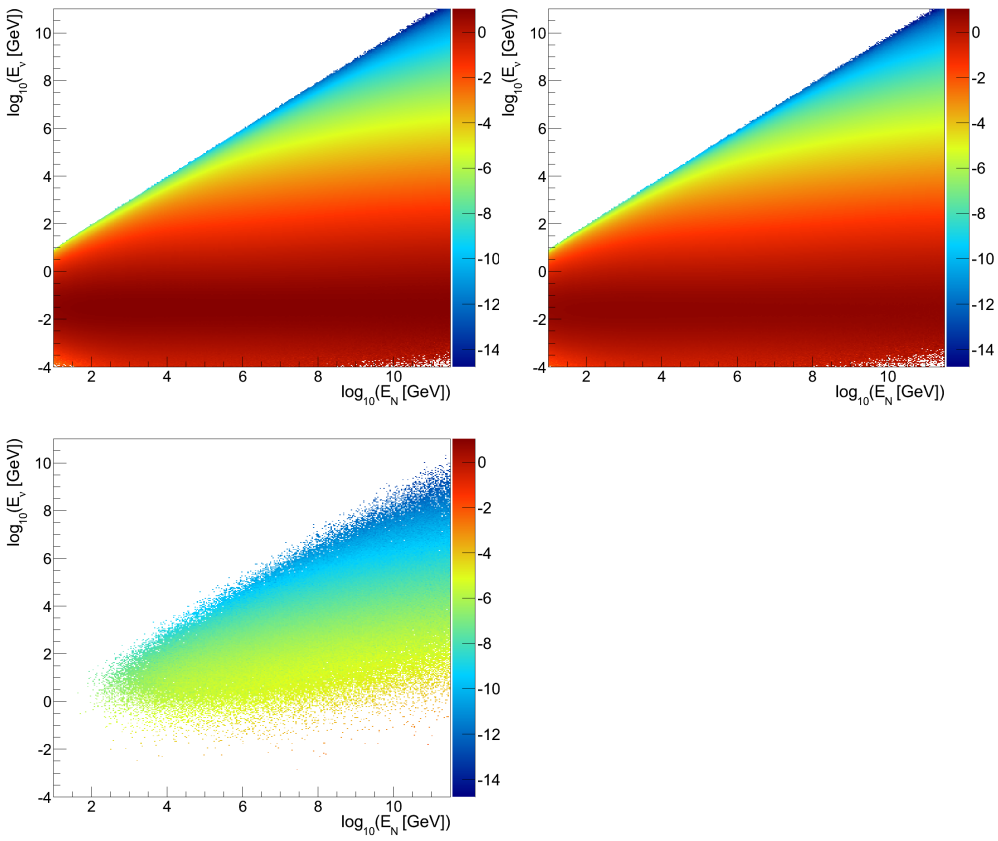

Figure 2.15: Logarithm of the neutrino yield in units of GeV^{-1} versus energy of the incoming proton and neutrino energy. TOP LEFT: for muon-neutrinos. TOP RIGHT: for electron-neutrinos. BOTTOM LEFT: for tau-neutrinos.

yield is similar to the muon neutrino yield, just about a factor of 2 lower. The tau-neutrino yield is much lower than the electron- and muon-neutrino yield, as expected.

Neutrino oscillations

In the late 1960s the Homestake Experiment used to observe solar neutrinos to study the nuclear fusion reactions in the Sun. However, the detector recorded less electron-neutrinos than theoretically predicted, leading to the so-called *solar neutrino problem* [Grupen, 2005]. With the SNO detector, which was sensitive to all three neutrino flavours, one could observe that the total neutrino flux from the Sun (i. e. including muon- and tau-neutrinos)

SNO: Sudbury Neutrino Observatory

was in accordance with theoretical predictions, but that electron-neutrinos disappeared. The solar neutrino problem was solved! The explanation is that the electron-neutrinos oscillate into muon- and tau-neutrinos on their way to the Earth.

Neutrino oscillations imply that neutrinos are not massless, as was previously assumed, but that at least two of the neutrino flavours have a mass. Oscillations occur when the flavour eigenstates are not the same as mass eigenstates, but a linear superposition of them, e. g.:

$$\begin{pmatrix} \nu_e \\ \nu_\mu \\ \nu_\tau \end{pmatrix} = \begin{pmatrix} c_{12}c_{13} & s_{12}c_{13} & s_{13}e^{-i\delta} \\ -s_{12}c_{23} - c_{12}s_{13}s_{23}e^{i\delta} & c_{12}c_{23} - s_{12}s_{13}s_{23}e^{i\delta} & c_{13}s_{23} \\ s_{12}s_{23} - c_{12}s_{13}c_{23}e^{i\delta} & -c_{12}s_{23} - s_{12}s_{13}c_{23}e^{i\delta} & c_{13}c_{23} \end{pmatrix} \begin{pmatrix} \nu_1 \\ \nu_2 \\ \nu_3 \end{pmatrix}, \tag{2.49}$$

where the abbreviations $s_{ij} \equiv \sin\theta_{ij}$ and $c_{ij} \equiv \cos\theta_{ij}$ are used, and where ν_i are the mass eigenstates, ν_α are the flavour eigenstates, θ_{ij} are the mixing angles and δ is the complex phase, which allows for CP violation in the neutrino sector [Martin and Shaw, 2008].

The oscillation of a neutrino of flavour α to flavour β (which can be the same as α) is given by [Anchordoqui et al., 2014]:

$$P_{\nu_\alpha \to \nu_\beta} = \delta_{\alpha\beta} - 4\sum_{i>j} \Re(U^*_{\alpha i} U_{\beta i} U_{\alpha j} U^*_{\beta j}) \sin^2 \Delta_{ij} + 2\sum_{i>j} \Im(U^*_{\alpha i} U_{\beta i} U_{\alpha j} U^*_{\beta j}) \sin(2\Delta_{ij}), \tag{2.50}$$

where $U_{\alpha i}$ etc. denote elements from the matrix as given in equation 2.49 and the oscillation phase Δ_{ij} is given by:

$$\Delta_{ij} = \frac{\Delta m^2_{ij} L}{4E_\nu} \approx 1.27 \frac{\Delta m^2_{ij}\,[\mathrm{eV}^2] L\,[\mathrm{km}]}{E_\nu\,[\mathrm{GeV}]}, \tag{2.51}$$

where $\Delta m^2_{ij} \equiv m^2_i - m^2_j$ is the mass squared difference between mass eigenstates and L is the distance the neutrino has travelled.

With the recent measurement of θ_{13} by the Daya Bay experiment, the values of all three mixing angles are now known [Weiler, 2013]: $\theta_{12} \simeq 35°$, $\theta_{23} \simeq 43°$ and $\theta_{13} \simeq 9°$. Nothing is known yet about the complex phase δ.

A good approximation is to adopt maximal mixing for $\nu_\mu \leftrightarrow \nu_\tau$ (so $\theta_{23} = 45°$) and neglect terms with θ_{13} [Anchordoqui et al., 2014]. Furthermore, since the focus is here on neutrinos travelling from anywhere in the Milky Way to Earth, L is large and

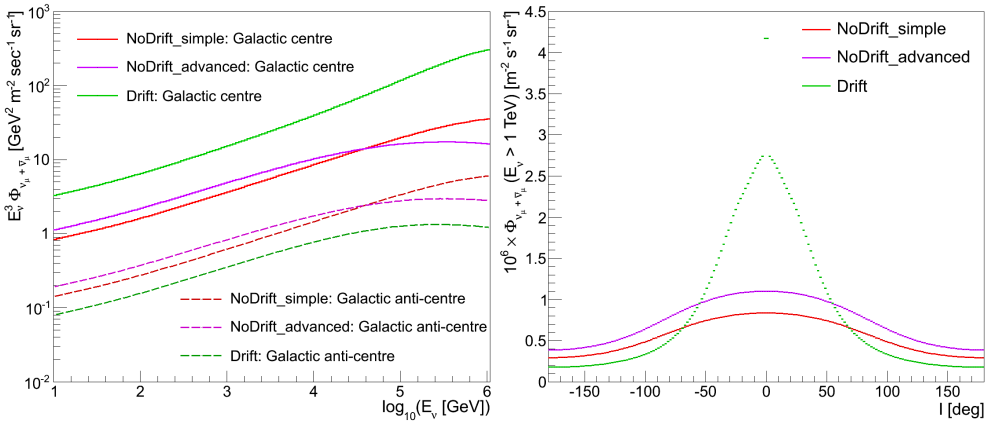

Figure 2.16: Neutrino fluxes for the three theoretical models. LEFT: versus neutrino energy. RIGHT: versus Galactic longitude.

varies for each neutrino, so that $\sin^2 \Delta_{ij}$ can be averaged over and equation 2.50 can be written as:

$$P_{\nu_\alpha \to \nu_\beta} = \sum_i U_{\alpha i} U_{\beta i}, \tag{2.52}$$

or in matrix form as[9]:

$$\begin{pmatrix} \hat{\nu}_e \\ \hat{\nu}_\mu \\ \hat{\nu}_\tau \end{pmatrix} = \begin{pmatrix} 1 - \frac{1}{2}\sin^2 2\theta_{12} & \frac{1}{4}\sin^2 2\theta_{12} & \frac{1}{4}\sin^2 2\theta_{12} \\ \frac{1}{4}\sin^2 2\theta_{12} & \frac{1}{2} - \frac{1}{8}\sin^2 2\theta_{12} & \frac{1}{2} - \frac{1}{8}\sin^2 2\theta_{12} \\ \frac{1}{4}\sin^2 2\theta_{12} & \frac{1}{2} - \frac{1}{8}\sin^2 2\theta_{12} & \frac{1}{2} - \frac{1}{8}\sin^2 2\theta_{12} \end{pmatrix} \begin{pmatrix} \nu_e \\ \nu_\mu \\ \nu_\tau \end{pmatrix}, \tag{2.53}$$

where $\hat{\nu}_\alpha$ represent the flavour eigenstates after oscillation. The same equation holds for anti-neutrinos.

[9] *A useful trigonometric identity is* $cos^4 x + sin^4 x = 1 - \frac{1}{2} sin^2 2x$.

Neutrino fluxes

The neutrino fluxes obtained for the three theoretical models including oscillations are compared in figure 2.16. These and all following plots show the sum of muon-neutrino and anti-neutrino fluxes, unless stated otherwise. The electron- and tau-neutrino fluxes are not shown, since these neutrinos are not used in the analysis, due to the signatures they leave in the detector, see chapter 3.

The left plot in figure 2.16 shows the fluxes versus energy for two directions, whereas the right plot shows the fluxes versus Galactic longitude, averaged over Galactic latitude ($|b| < 4.5°$) and integrated above a neutrino energy of 1 TeV.

It can be seen that the fluxes for the different models agree with each other to within a factor of about 3. The models consistently show that the flux peaks in the direction of the Galactic centre. The Drift model predicts a higher flux around the Galactic centre than the NoDrift models, and a lower flux near the Galactic anti-centre ($l = 180°$). This is caused by the drift of cosmic rays from the outer parts of the Milky Way towards the GC.

The three theoretical models used here only constitute a small subset of all possible models, and other assumptions can be made that would result in slightly different predictions, see for instance the paper by Evoli et al. [2007]. The models used here give a good general idea about the flux. Instead of calculating neutrino fluxes by using more theoretical models, the neutrino flux is also determined in a different way, which will be described in the next section.

2.3 CALCULATION OF NEUTRINO FLUXES FROM FERMI γ-RAY FLUX

To get an independent estimate for the neutrino flux, the γ-ray flux measured by the Fermi satellite is used and converted into a neutrino flux. It is widely accepted that part of the γ-ray flux is of hadronic origin, i. e. comes from π^0-decays (see below), at least for the emission from the Galactic plane (see also the paper by Kamae et al. [2005] and the references therein). The main assumption made in this method of estimating the neutrino flux, is the fraction of the γ-ray flux coming from π^0-decays.

The MILAGRO (meaning miracle in Spanish) experiment was a ground based water Čerenkov telescope.

A similar procedure has been applied in the paper by Taylor et al. [2009], in which the γ-ray data measured by MILAGRO in combination with EGRET data are used. The procedure applied in this paper uses some simplifying assumptions. It is assumed that all photons are of hadronic origin and the flux in the inner Galaxy ($-40° < l < 40°$ and $-2° < b < 2°$) is obtained by scaling the MILAGRO results (which only measures the part of the inner Galaxy between a longitude of 30° and 40°) with the help of the EGRET results.

EGRET: Energetic Gamma Ray Experiment Telescope: one of the experiments aboard the Compton Gamma Ray Observatory (CGRO) satellite.

Here instead, the Fermi data are used, which cover the full sky with much higher statistics and show a good angular resolution (see below). Although the data do not extend to energies of 10 TeV like the MILAGRO data, it extends far enough in energy (~600 GeV) to give a reliable estimate of the expected neutrino fluxes.

2.3.1 *Photon flux measured by Fermi*

The LAT instrument aboard the Fermi satellite detects photons, with energies that range from about 20 MeV to over 300 GeV, by recording the electron-positron pairs created by individual γ-rays [Ackermann et al., 2012c]. Since the focus of this thesis is on the diffuse Galactic neutrino flux, point sources of photons are not important, and it is the diffuse γ-ray flux as measured by the Fermi collaboration that is used. The Fermi collaboration provides these data on their website[10] in the form of a .fits file (`gal_2yearp7v6_v0.fits`), in which they have subtracted the fluxes of all known point sources. The diffuse photon sky-map at an energy of 3.4 GeV is shown in Galactic coordinates in figure 2.17. This figure is similar to the bottom right plot of figure 1.3, except for the fact that the point sources of γ-rays have been subtracted.

[10] *See* `fermi.gsfc.nasa.gov/ssc/data/access/lat/BackgroundModels.html`

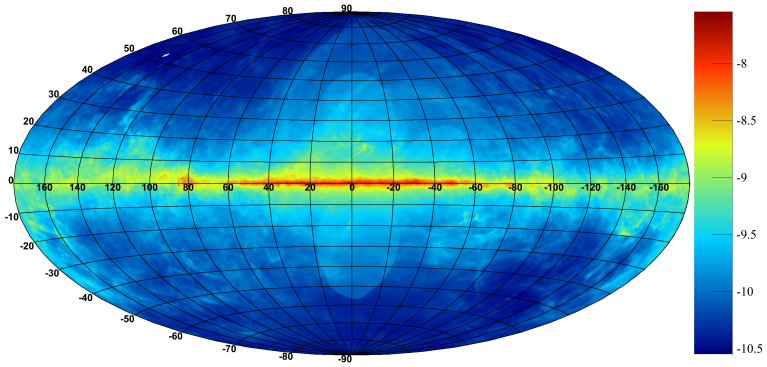

Figure 2.17: Sky-map of the diffuse γ-ray flux in units of $\mathrm{GeV}^{-1}\,\mathrm{m}^{-2}\,\mathrm{sr}^{-1}\,\mathrm{s}^{-1}$ at an energy of 3.4 GeV.

The Fermi diffuse flux is binned in 30 bins in energy (going from 50 MeV to 600 GeV), and the sky-map contains 2880 pixels in Galactic longitude and 1441 in Galactic latitude. Only the last 17 of the energy bins (from 3.4 GeV to 600 GeV) will be used. A simple single power law describes well the data above 3.4 GeV. The photon flux for each of the pixels is parameterised as:

$$\Phi_\gamma(E_\gamma) = A\,E_\gamma^{-B}, \tag{2.54}$$

where Φ_γ is the photon flux and E_γ is the photon energy. A and B are the flux constant and spectral index respectively, which will be fitted.

In general the fit works very well, as can be seen from the left plot in figure 2.18, which shows a typical γ-ray spectrum

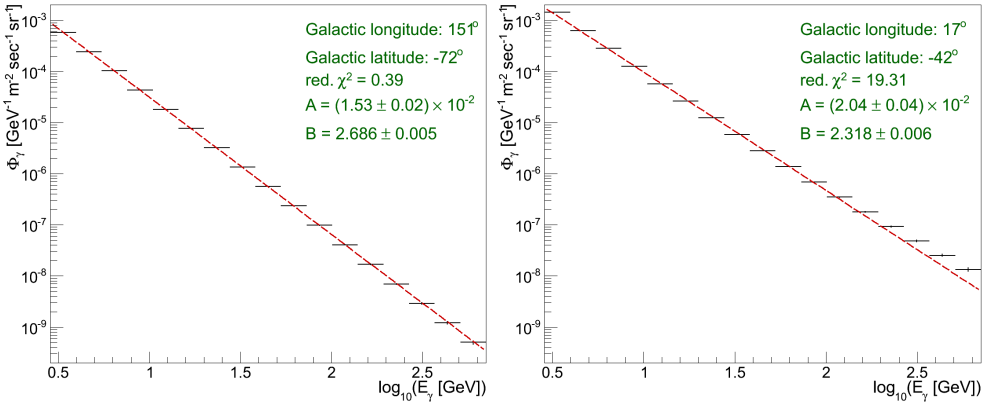

Figure 2.18: The photon flux versus energy, fitted with equation 2.54. LEFT: an example of a good fit. RIGHT: an example of a bad fit.

together with the fit. Sometimes the fit does not work so well (see the right plot in figure 2.18), which can be attributed to the Fermi bubbles. It can be seen from the figure that the distribution cannot be described by a single power law. It appears to consist of two separate contributions, the standard diffuse flux and some contribution becoming dominant at higher energies. It is possible to correct for this and also get an estimate for the flux from the Fermi bubbles in this way, but since this is beyond the scope of this work it has not been pursued and the Fermi bubble region has been omitted altogether.

The reduced χ^2 value of the fit (i. e. the χ^2 divided by the number of degrees of freedom) is typically between 0.3 and 2.0, except for the Fermi bubbles, which can be clearly distinguished in the sky-map of the reduced χ^2 shown in figure 2.19. Also the spectral index (parameter B in equation 2.54) is different for the Fermi bubbles, as can be seen in figure 2.20, which shows a sky-map of the spectral indices obtained in the fit. The spectral index is generally found to be between about 2.6 and 2.7, but is significantly lower for the Fermi bubbles, namely around 2.2. It should be noted though, that the spectral index in the Fermi bubbles is not correct and should be even lower than the one obtained here, see also the right plot in figure 2.18. The spectral index in the inner Galactic plane[11] is found to be slightly lower (between about 2.5 and 2.6) than in the rest of the sky, as also found by Taylor et al. [2009]. This can be seen in figure 2.21, in which the distributions of the fitted spectral indices in the inner Galaxy and the rest of the sky are shown.

[11] *Defined as* $|l| < 40°$ *and* $|b| < 4°$.

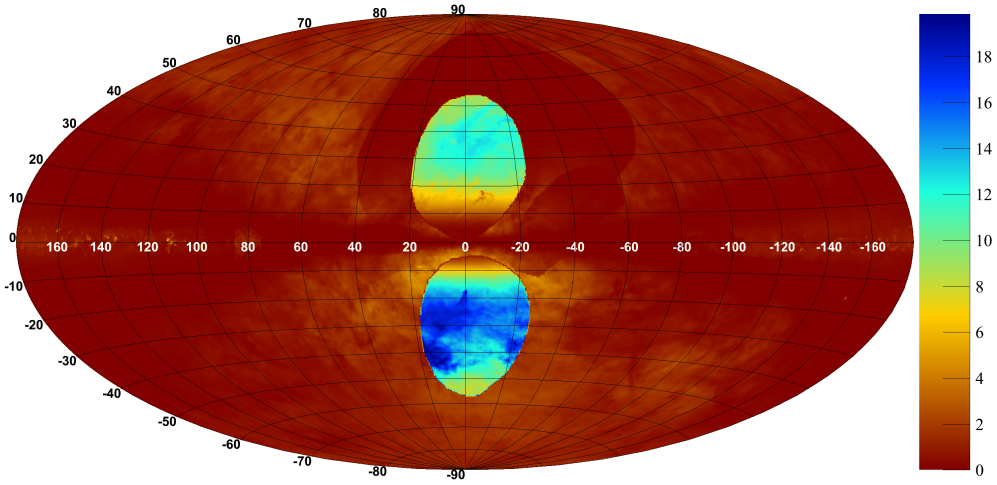

Figure 2.19: Sky-map of the reduced χ^2 value of the fit.

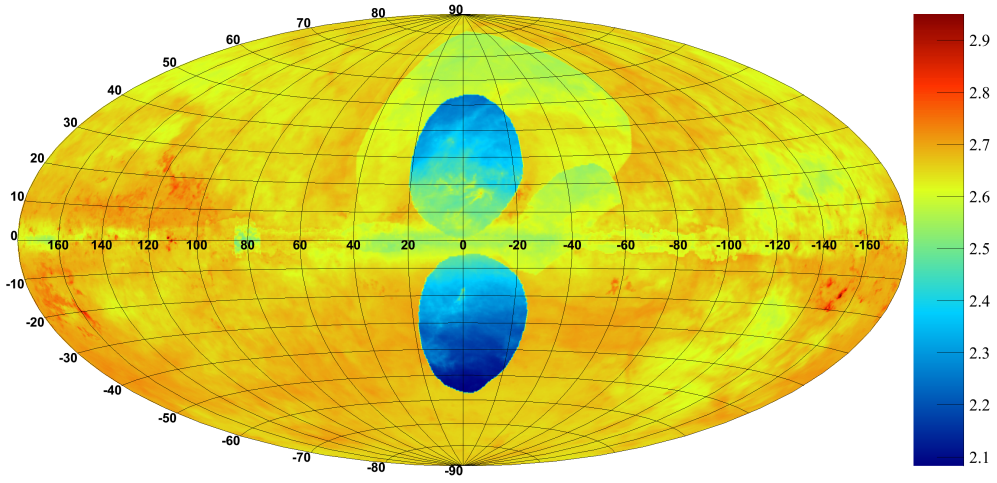

Figure 2.20: Sky-map of the spectral index obtained in the fit.

Lower spectral indices are not only found in the inner Galactic plane, but also in some structure above the upper Fermi bubble and in a structure that starts near $l = 30°$, $b = 10°$ and extends towards smaller longitude and larger latitude values. The first of these structures corresponds to the North Polar Spur associated with Loop I [Su et al., 2010]. There is no explanation for the second structure, but a template has been developed by the Fermi collaboration[12] in order to remove it. However, since the focus lies here on the Galactic plane (with $|b| < 5°$), this correction is not applied here.

[12] *Which can be found at* `fermi.gsfc.nasa.gov/ssc/data/access/lat/Model_details/Pass7_galactic.html`

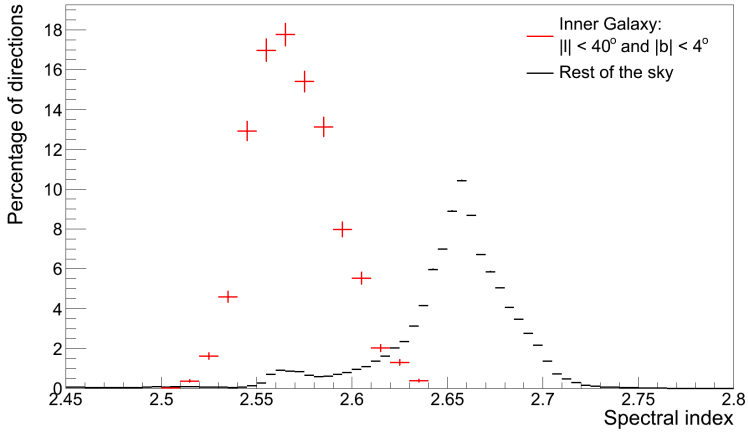

Figure 2.21: Distributions of the spectral index obtained in the fit.

The errors obtained from the fit are of the order of 1.5% for the flux constant and of the order of 0.2% for the spectral index in the cases where the fit worked well (i. e. had a reduced χ^2 around 1) and are not taken into account as part of the systematic error. This is justified since the systematic error from the uncertainty in the effective area of the Fermi-LAT instrument is about a factor of 10 bigger. This error is 14.4% at 3.4 MeV and 20% above 10 GeV, with linear interpolation in logartithm of energy in between [Ackermann et al., 2012b].

2.3.2 *Photon flux from π^0-decays*

Several mechanisms can produce γ-rays, see also figure 2.22:

A. Synchrotron radiation, which occurs when a charged particle is deflected in a magnetic field.

B. Bremsstrahlung, which is similar to synchrotron radiation, but in this case the charged particle is deflected in the Coulomb field of a nucleus instead of in a magnetic field.

C. Inverse Compton (IC) scattering, in which a low energy photon (for instance from the cosmic microwave background) is blueshifted by the collision with an energetic electron.

D. Matter-antimatter annihilation, mostly electron-positron and proton-antiproton annihilations.

E. Decay of subatomic particles, like the π^0 or the η^0, see below.

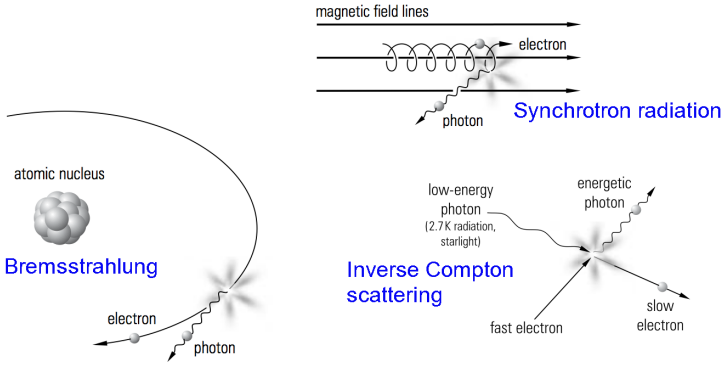

Figure 2.22: Some of the mechanisms that can produce γ-rays. Figure reproduced from Grupen [2005].

Concerning the decay of subatomic particles, almost all of them have one or more decay modes involving photons, but for the current discussion only the neutral pion and the η^0-particle are important, since they are the lightest neutral unflavoured mesons. Photons are produced from these particles via:

The η^0-meson is a combination of up, down and strange (anti-)quarks: $\eta^0 = \frac{u\bar{u} + d\bar{d} - 2s\bar{s}}{\sqrt{6}}$.

$$\begin{aligned} \pi^0 &\rightarrow \gamma + \gamma \qquad (98.82\%) \\ \pi^0 &\rightarrow e^+ + e^- + \gamma \qquad (1.17\%) \end{aligned} \tag{2.55}$$

and:

$$\begin{aligned} \eta^0 &\rightarrow \gamma + \gamma \qquad (39.31\%) \\ \eta^0 &\rightarrow \pi^+ + \pi^- + \gamma \qquad (4.60\%) \end{aligned} \tag{2.56}$$

Both of these mesons are commonly produced in proton-proton interactions and will contribute to the number of observed γ-rays.

However, since about a factor of 10 more π^0 particles than η^0 particles are produced and the η^0 only decays to photons in about 44% of the cases, the contribution from π^0 particles will be the dominant one. Using the PYTHIA event generator, it has been calculated that the contribution of η^0-decays to photon production is of the order of 10%, independent of photon energy. The contribution of η^0-decays is not taken into account, leading to an overestimation of the π^0-flux and thus of the neutrino fluxes of the order of 10%.

Of the mechanisms described above, IC scattering and π^0-decay are the most important at photon energies $\gtrsim 10\,\mathrm{GeV}$, see also figure 2.23. The relative importance of these two processes depends on the density of electrons and photons compared to the density of CRs and interstellar matter. In the Galactic plane, where the density of protons is maximal, the main contribution will thus come from π^0-decays, while at high latitudes the IC scattering contribution is higher.

The contributions of these two processes (and also bremsstrahlung) have been determined by the Fermi collaboration for several regions in Galactic coordinates. The region with $-80^\circ \leqslant l \leqslant 80^\circ$ and $-8^\circ \leqslant b \leqslant 8^\circ$ (referred to as region 1) encompasses the (inner) Galactic plane. This is the region of most interest in this work. Also the region with $80^\circ < l < 280^\circ$ and $-8^\circ \leqslant b \leqslant 8^\circ$ (referred to as region 2) is important, since it encompasses the signal region used by the AMANDA-II experiment. In order to obtain neutrino flux predictions for the whole sky, also the region with $0^\circ \leqslant l < 360^\circ$ and $8^\circ < |b| \leqslant 90^\circ$ is considered.

Several different models are used by the Fermi collaboration to fit the diffuse γ-ray flux, which differ in the CR source distribution, the size of the volume in which the CRs can propagate and the distribution of interstellar matter. The models are constrained to reproduce the locally observed CR fluxes and the predicted γ-ray flux is compared to data using a maximum-likelihood fit. In this fit, the fluxes and spectra of an isotropic γ-ray background component and of known point sources, the strength of the infrared and optical radiation field and a parameter relating to the matter composition can be varied. As an example, figure 2.23 shows the fit results for region 2 for four different models. For more details, see the paper from Ackermann et al. [2012b].

Since neutrinos are produced (mainly) from charged pion decays, the contribution of π^0-decays to the total diffuse γ-ray flux is needed for the determination of the neutrino fluxes. This contribution (which is energy dependent, as can be seen from figure 2.23), together with its uncertainty, is estimated from the models used

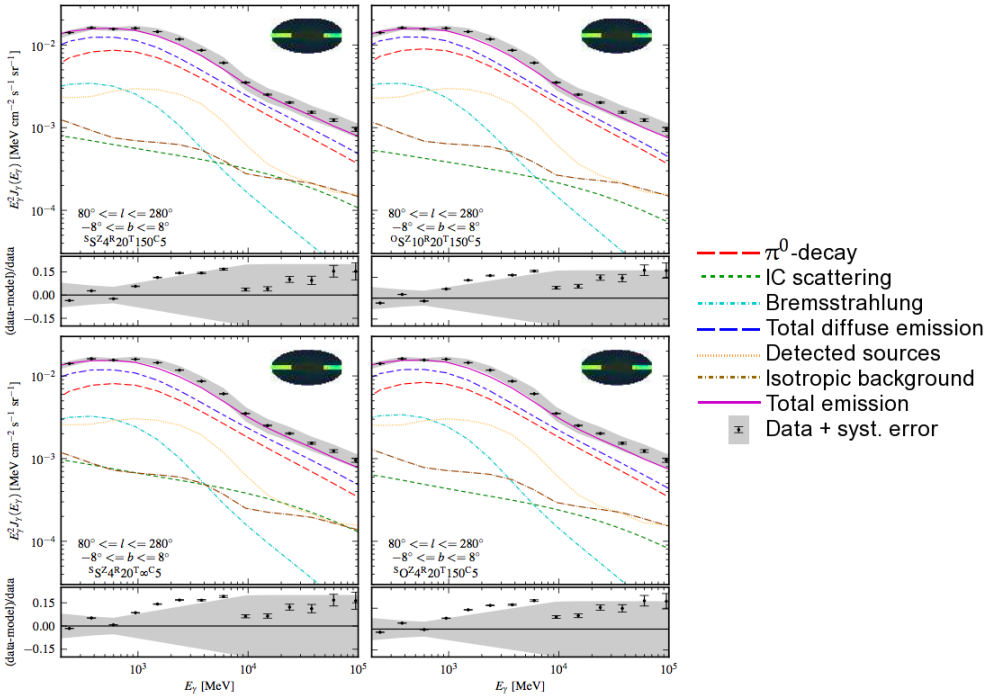

Figure 2.23: Fermi γ-ray data for the region with $80^\circ < l < 280^\circ$ and $-8^\circ \leqslant b \leqslant 8^\circ$ (i. e. region 2), with the contribution from the several components obtained from the fit for four different models. Figure reproduced from Ackermann et al. [2012b].

by the Fermi collaboration. The percentage of all photons originating from neutral pion decays is around 70% for region 2 and is independent of photon energy. For region 1 the percentage varies from about 70% at 10 GeV to an extrapolated 45% at 1 PeV. The difference between the models gives a systematic error of about 15% over the whole energy range.

An important aspect that should be mentioned is the attenuation of photons, since it could lead to a wrong (too low) estimate of the neutrino flux. However, since attenuation only plays a role for photon energies above about 10 TeV for the (Galactic) distances considered here it is not important [Moskalenko et al., 2006].

2.3.3 *Determination of pion fluxes*

By using PYTHIA, the γ-ray flux from π^0-decays can be converted into the π^0-flux, which can in turn be converted into the $\pi^\pm$-fluxes.

The π^0-flux

Analogously to computing the neutrino flux from the cosmic ray flux, the γ-ray flux can be computed from the π^0-flux as:

$$\Phi_\gamma(E_\gamma) = \int_{E_\gamma}^{\infty} \mathrm{d}E_{\pi^0}\, Y_\gamma(E_{\pi^0}, E_\gamma)\, \Phi_{\pi^0}(E_{\pi^0}), \tag{2.57}$$

where $\Phi_{\pi^0}(E_{\pi^0})$ is the neutral pion flux as a function of energy of the neutral pion E_{π^0}. This equation is very similar to equation 2.47, but does not contain a cross section term, since the probability is 100% that the π^0 will decay at some point. It has been assumed that the π^0 does not interact before decaying (which would cause it to lose energy), which is justified since the matter density in the Milky Way is very low and the π^0 decays rapidly.

Equation 2.57 can also be written in matrix-vector form as:

$$\begin{pmatrix} \Phi_\gamma(E_{\gamma,1}) \\ \Phi_\gamma(E_{\gamma,2}) \\ \Phi_\gamma(E_{\gamma,3}) \\ \vdots \end{pmatrix} = \begin{pmatrix} Y_{\gamma,11}\mathrm{dE}_{\pi^0,1} & Y_{\gamma,12}\mathrm{dE}_{\pi^0,2} & \cdots \\ Y_{\gamma,21}\mathrm{dE}_{\pi^0,1} & Y_{\gamma,22}\mathrm{dE}_{\pi^0,2} & \cdots \\ Y_{\gamma,31}\mathrm{dE}_{\pi^0,1} & Y_{\gamma,32}\mathrm{dE}_{\pi^0,2} & \cdots \\ \vdots & \vdots & \ddots \end{pmatrix} \begin{pmatrix} \Phi_{\pi^0}(E_{\pi^0,1}) \\ \Phi_{\pi^0}(E_{\pi^0,2}) \\ \Phi_{\pi^0}(E_{\pi^0,3}) \\ \vdots \end{pmatrix}, \tag{2.58}$$

which can then be inverted to obtain the π^0-flux from the γ-ray flux:

$$\begin{pmatrix} \Phi_{\pi^0}(E_{\pi^0,1}) \\ \Phi_{\pi^0}(E_{\pi^0,2}) \\ \Phi_{\pi^0}(E_{\pi^0,3}) \\ \vdots \end{pmatrix} = \mathbb{Y}_\gamma^{-1} \begin{pmatrix} \Phi_\gamma(E_{\gamma,1}) \\ \Phi_\gamma(E_{\gamma,2}) \\ \Phi_\gamma(E_{\gamma,3}) \\ \vdots \end{pmatrix}, \tag{2.59}$$

where $\mathbb{Y}_\gamma^{-1}$ is the inverse of the matrix in equation 2.58.

To obtain the inverted matrix, PYTHIA is used again. However, instead of simulating proton-proton interactions, PYTHIA is used in the so-called *single-particle gun* mode. In this mode, an unstable particle with a certain energy is given as input, which is then forced to decay.

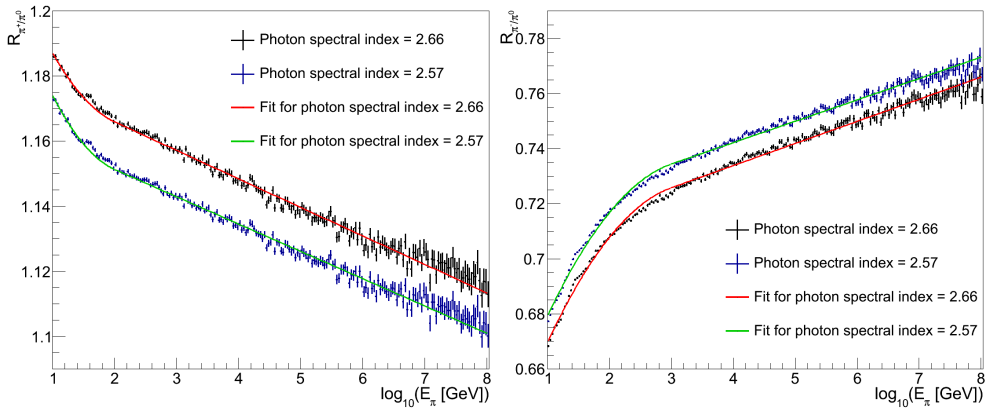

Figure 2.24: Ratios of the charged to neutral pion fluxes versus pion energy. LEFT: R_{π^+/π^0}. RIGHT: R_{π^-/π^0}.

The $\pi^{\pm}$-flux

To obtain the π^+- and π^--fluxes corresponding to a given π^0-flux, proton-proton interactions have been simulated in PYTHIA and the π^+-, π^-- and π^0-fluxes are obtained using the same method as for obtaining the neutrino fluxes:

$$\Phi_\pi(E_\pi) = \int_{E_\pi}^{\infty} \mathrm{d}E_\mathrm{N}\, Y_\pi(E_\mathrm{N}, E_\pi)\, \Phi_\mathrm{N}(E_\mathrm{N})\, \sigma_\mathrm{pp}(E_\mathrm{N}). \quad (2.60)$$

Then, the ratios of the π^+- to the π^0-flux (named R_{π^+/π^0}) and the π^-- to the π^0-flux (named R_{π^-/π^0}) are determined as a function of the pion energy. The $\pi^{\pm}$-fluxes are obtained from the π^0-fluxes by multiplying the latter by the corresponding ratio. This can be done, since the mass of the neutral and charged pions is nearly identical (139.6 MeV/c^2 for the charged pions compared to 135.0 MeV/c^2 for the neutral pion), so that $E_{\pi^+} \approx E_{\pi^-} \approx E_{\pi^0} = E_\pi$.

Two different proton spectra are used (i. e. $\Phi_\mathrm{N}(E_\mathrm{N})$ in equation 2.60), which have been chosen to reproduce a γ-ray flux with a spectral index corresponding to the average spectral index obtained in the fit to the photon flux. A proton spectrum with a spectral index of 2.63 gives a γ-ray spectrum with a spectral index of about 2.56, i. e. reproducing the photon flux in the inner Galaxy. A proton spectrum with a spectral index of 2.72 gives a γ-ray spectrum with a spectral index of about 2.66, i. e. reproducing the photon flux in the rest of the sky (see also figure 2.21).

The ratios R_{π^+/π^0} and R_{π^-/π^0} are shown as a function of pion energy in figure 2.24. It can be seen that these ratios are energy

dependent. The higher the pion energy is, and thus the energy of the proton that created the pion, the closer the ratio to unity. This can be understood from the fact that the higher the COM energy of the interaction is, the more likely it is that a gluon-gluon interaction takes place (as opposed to a gluon-quark or quark-quark interaction), in which it is equally likely to produce a charged or a neutral pion.

The ratios also depend on the spectral index of the proton flux; the higher the spectral index is, the higher R_{π^+/π^0} and the lower R_{π^-/π^0}. This is caused by the fact that a higher spectral index results in a softer energy spectrum[13], so that relatively less gluon-gluon interactions take place and more positively charged pions are created compared to negatively charged pions. The latter comes from the fact that the proton has a positive charge. The shape of the ratio however, is invariant under the variation of the spectral index.

[13] *In a softer energy spectrum there are relatively more low energy events than in a harder spectrum.*

The ratios have been fitted with a parabolic function in the logarithm of the pion energy from 1 to 2 (1 to 3) and with a straight line in the logarithm of the pion energy from 2 to 8 (3 to 8) for R_{π^+/π^0} (R_{π^-/π^0}). By comparing the left and right plots in figure 2.24, it can be seen that the difference in the ratio is only about 1% for the two different spectral indices. The inner Galaxy and the rest of the sky are treated separately, i. e. different ratios are used, but the variation of the spectral index within the region (see figure 2.21) is ignored. This is justified, since the error made in this way is of the order of a tenth of a percent, and can thus be ignored compared to the other sources of systematic error.

2.3.4 *Obtained $\nu_\mu + \overline{\nu}_\mu$ fluxes*

To obtain the neutrino fluxes from the π^+- and π^--fluxes is again straightforward:

$$\Phi_\nu(E_\nu) = \int_{E_\nu}^{\infty} \mathrm{d}E_{\pi^\pm}\; Y_{\nu,\pm}(E_{\pi^\pm}, E_\nu)\, \Phi_{\pi^\pm}(E_{\pi^\pm}), \qquad (2.61)$$

where $Y_{\nu,\pm}(E_{\pi^\pm}, E_\nu)$ is the neutrino yield from $\pi^\pm$-decays. The yields for postively charged and negatively charged pions are determined separately, so to obtain the total neutrino or anti-neutrino flux the contributions have to be added. The yields are again determined using PYTHIA in the *single-particle gun* mode.

For the calculation of the neutrino fluxes, it has been assumed that all neutrinos are created through $\pi^\pm$-decay (and the subsequent μ-decay). However, neutrinos can also be produced via $K^\pm$- or K^0_L-decays, see reactions 2.44 and 2.45. This contribution

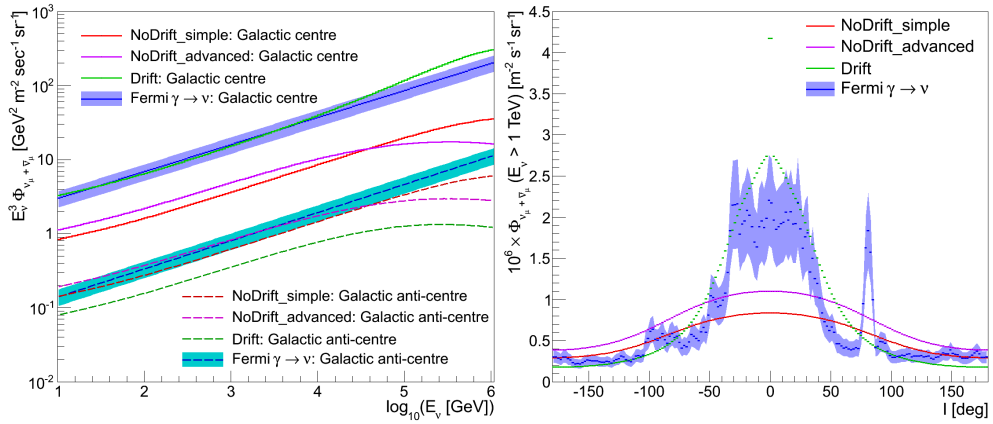

Figure 2.25: Neutrino fluxes for all models. LEFT: versus neutrino energy. RIGHT: versus Galactic longitude.

has not been taken into account and leads to an underestimation of the neutrino fluxes of the order of 10% (see section 2.2.2). Since the overestimation of the neutrino fluxes by not considering η^0-decays is of the same size, the combined effect is expected to be small compared to the total systematic error.

The result of the calculations can be seen in figure 2.25, in which the fluxes calculated in this way are compared to the theoretical fluxes calculated earlier (figure 2.16). The fluxes calculated in this way will be referred to as the 'Fermi $\gamma \rightarrow \nu$' model. Neutrino oscillations have been taken into account using equation 2.53. The blue band around the flux calculated from the Fermi data represents the total systematic error which consists of the combination of the uncertainty on the Fermi-LAT effective area and the uncertainty in the π^0-decay contribution. The systematic error is about 25% and is independent of the neutrino energy.

The agreement between the theoretical fluxes and the flux calculated here is reasonable. The flux from the Fermi $\gamma \rightarrow \nu$ model is similar to the flux from the Drift model, as can be seen from the left plot in figure 2.25. When comparing the longitudinal distribution, it can be seen that the Fermi $\gamma \rightarrow \nu$ fluxes are higher than the NoDrift fluxes in the inner Galactic plane and lower outside of it. The flux is less smooth than the theoretical predictions, due to the simplifying assumptions (such as cylindrical symmetry) made in the latter. In addition, the Cygnus region, which is a known source of diffuse γ-ray emission, is visible at a longitude of 80°.

The spectral indices obtained by the four models are similar. The spectral index of the diffuse Galactic neutrino flux is comparible to that of the cosmic ray flux, ranging from about 2.6 to 2.7, see also table 2.3 in section 2.4.3.

2.4 SIGNAL FLUX COMPARISONS

There are two types of background that are important for this analysis, which are, just like the signal, created in cosmic ray interactions. The target in this case is not the interstellar matter, but the atmosphere of the Earth. In these interactions, a so-called air shower is created, which contains pions, kaons, muons and a myriad of heavier hadrons. Muons are the dominant charged component at sea level, followed by protons [Grupen, 2005]. Some of these (higher energy) atmospheric muons also reach the detector, in which they can generate a signal. However, since muons cannot pass through the entire Earth, this background can be efficiently reduced by looking through the Earth. More details on this concept can be found in chapter 4.

The second type of background are neutrinos produced in the air showers, which are called atmospheric neutrinos. These neutrinos constitute the main background and will be described in more detail first.

2.4.1 *Atmospheric neutrinos*

Even though the mechanism that produces the atmospheric neutrinos is the same as that producing the diffuse Galactic neutrino flux, the neutrino fluxes are quite different. The atmosphere of the Earth consists mainly of nitrogen and its density is substantially higher than that of the Galaxy. Because of the low density in the Galaxy, all pions and muons produced there will decay and contribute to the diffuse Galactic neutrino flux. For atmospheric neutrinos, the main contribution comes from the pions and kaons, since most muons will reach the Earth before decaying. Furthermore, because of the higher density, most created particles will interact before decaying, thereby losing some of their energy. This results in a softer energy spectrum for the atmospheric neutrino flux compared to the diffuse Galactic neutrino flux. The spectral index of the former is about 3.7, compared to the 2.6 to 2.7 for the diffuse Galactic neutrino flux.

The atmospheric neutrino flux consists primarily of two contributions. For energies below about 50 TeV the conventional flux

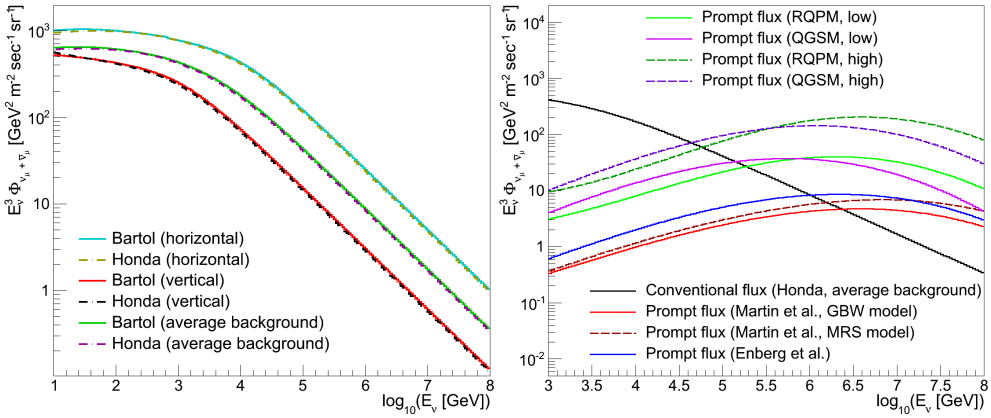

Figure 2.26: The atmospheric neutrino flux versus energy. LEFT: the conventional flux for several zenith angles. RIGHT: several models for the prompt flux.

(produced by pions and kaons as in reactions 2.42, 2.44 and 2.45) is the dominant component. For higher energies the prompt contribution takes over, which is due to charm-pair production ($D^{\pm}$, D^0, etc.). For an overview of the atmospheric neutrino flux, see the thesis of Palioselitis [2012].

The conventional flux depends on the zenith angle, since the path length through the atmosphere changes. It can be seen from the left plot in figure 2.26, in which the conventional neutrino flux is shown versus neutrino energy, that the horizontal (zenith $= 90°$) flux is higher than the vertical (zenith $= 0°$ and zenith $= 180°$) flux. The average background expected for the diffuse Galactic neutrino flux coming from the inner Galactic plane is also shown (the average zenith angle is about $110°$). The fluxes are shown for two frequently used models: the flux calculated by Honda et al. [2007] (called the *Honda*-flux) and that calculated by Barr et al. [2004] (called the *Bartol*-flux, named after the institute where two of the authors are affiliated to). The model predictions are very similar; the largest difference is about 6%. In the following the *Honda*-flux model is used as the conventional component of the atmospheric neutrino flux. The uncertainty on this conventional flux is about 7% at 10 GeV, 14% at 100 GeV and 25% at 1 TeV [Palioselitis, 2012].

Different models for the prompt neutrino flux are shown in the right plot of figure 2.26. The models from Martin et al. [2003]

and Enberg et al. [2008] are in agreement with each other within a factor of two, but there are also models that predict significantly higher fluxes (the RQPM and QGSM models in the figure, see [Palioselitis, 2012] for details). Recent results from the IceCube experiment, in which the prompt component is fitted using the observed neutrino events, seem to favour a low prompt neutrino flux [Aartsen et al., 2014].

The prompt contribution is not so important for this work, since the conventional flux constitutes the main background and the uncertainty on it contributes more than the difference between the prompt models. The flux model from Enberg et al. [2008] is used as the prompt component.

Concerning neutrino oscillations, a slightly different calculation has to be performed than for Galactic fluxes. Starting again from equation 2.50, the $\sin^2 \Delta_{ij}$ term can now not be averaged over. However, since $\Delta m^2_{32} \simeq 2.5 \cdot 10^{-3}\,\mathrm{eV}^2/c^4$ is substantially larger than $\Delta m^2_{21} \simeq 0.8 \cdot 10^{-4}\,\mathrm{eV}^2/c^4$, the latter mass splitting can be neglected, and the so-called two-flavour approximation can be used. The probability that a muon-neutrino stays a muon-neutrino can then be written as [Beringer et al., 2012]:

$$P_{\nu_\mu \to \nu_\mu} = 1 - \sin^2(2\theta_{23}) \sin^2 \left(1.27 \frac{\Delta m^2_{32}\,[\mathrm{eV}^2] L\,[\mathrm{km}]}{E_\nu\,[\mathrm{GeV}]} \right). \quad (2.62)$$

For energies above a few hundred GeV and neutrino travel distances of at most two times the Earth's radius ($2r_\oplus \approx 13000\,\mathrm{km}$), which are typical values of interest for this work, the muon-neutrino flux reduction is negligible.

2.4.2 *Signal compared to the background*

The diffuse Galactic neutrino flux is compared to the average atmospheric neutrino background in figure 2.27. The atmospheric neutrino background dominates over the signal for most of the energy range. In the direction of the Galactic centre, the diffuse Galactic neutrino flux rises above the background at an energy of about 40 TeV for the Drift and Fermi $\gamma \to \nu$ models, at about 250 TeV for the NoDrift_simple model and at about 1 PeV for the NoDrift_advanced model. For the other directions this happens for higher energies, since the signal flux is lower in these directions.

From figure 2.27 and the right plot in figure 2.25 it can be concluded that the optimal region to look for the diffuse Galactic

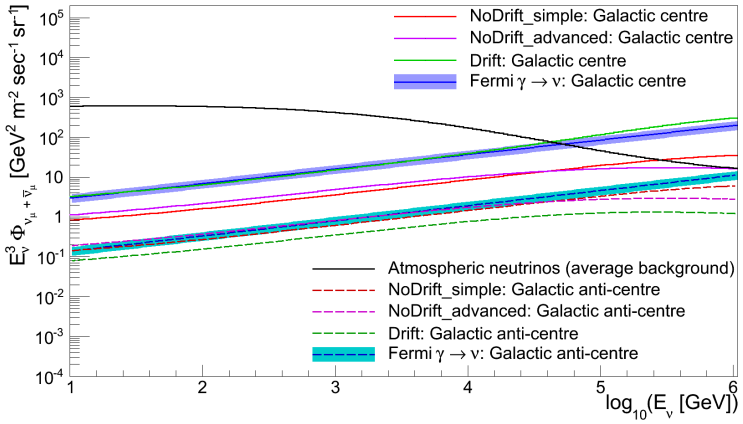

Figure 2.27: The diffuse Galactic neutrino flux for two different directions compared to the (average) atmospheric neutrino background versus neutrino energy.

neutrino flux will consist of the inner part of the Galactic plane and only events with energies above a few TeV should be selected.

2.4.3 *The Mediterranean sea versus the South Pole*

From the previous discussion it is clear that it is best to have a detector with a high visibility of the Galactic centre, or more generally the inner Galactic plane. The visibility $\mathcal{V}$ is defined as the percentage of time a given direction can be observed. Since neutrino telescopes use the Earth as a shield, this means that the source has to be below the horizon (i. e. only directions with $\theta \geqslant 90^\circ$ are considered). Using the fact that a given direction in Galactic coordinates will have the same local detector coordinates after exactly one sidereal day has passed, the visibility can be calculated as:

$$\mathcal{V} = \frac{\int_0^T \mathrm{d}t \; v(l, b, t)}{\int_0^T \mathrm{d}t}, \tag{2.63}$$

where $T = 23.9345\,\mathrm{day}$ is one sidereal day and with:

$$v(l, b, t) = \begin{cases} 1 & \theta(l, b) \geqslant 90^\circ \\ 0 & \theta(l, b) < 90^\circ \end{cases} \tag{2.64}$$

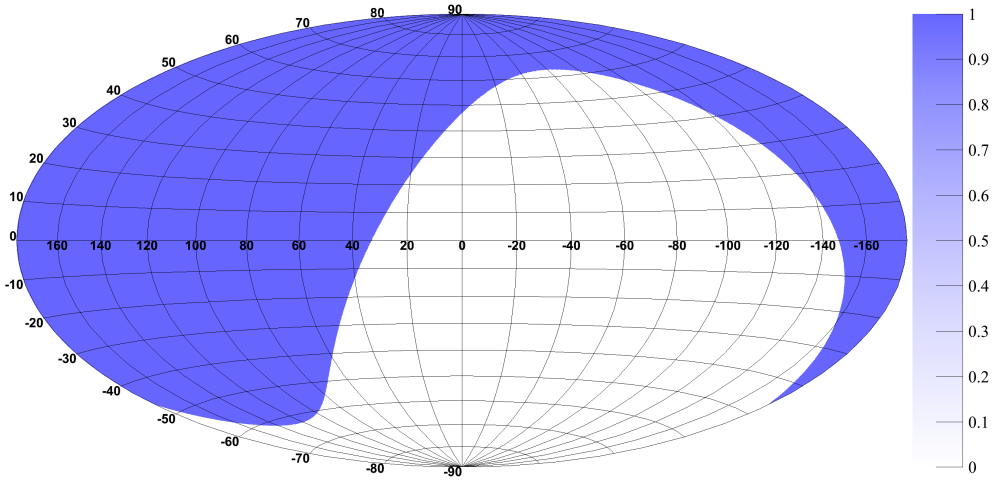

Figure 2.28: Sky-map of the AMANDA/IceCube visibility.

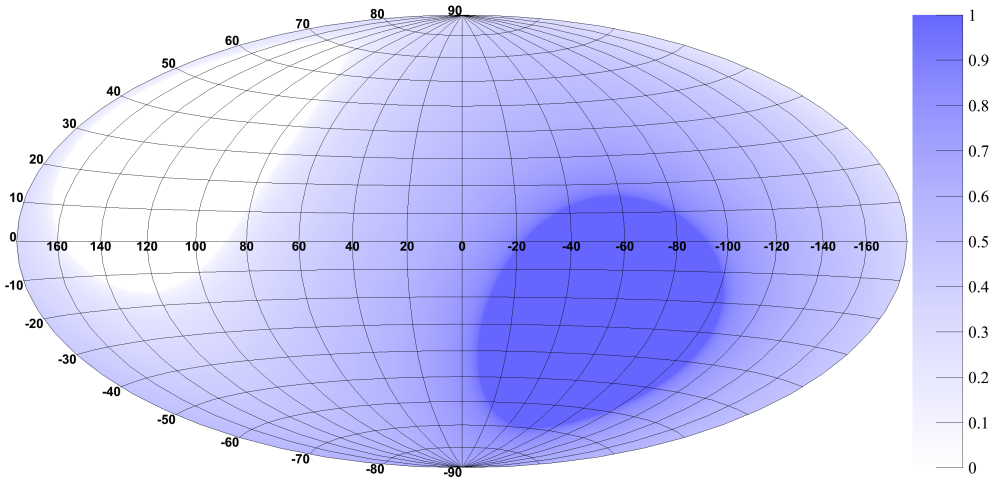

Figure 2.29: Sky-map of the ANTARES/KM3NeT visibility.

The visibility of AMANDA (and of IceCube[14]) is 100% for the Northern sky, which corresponds to Galactic longitudes between 33° and 213° for $b = 0°$. A sky-map of the visibility of AMANDA/IceCube is shown in Galactic coordinates in figure 2.28. The visibility of ANTARES[15] is diluted and is shown in Galactic coordinates in figure 2.29. The visibility sky-maps display one of the advantages of a detector in the Mediterranean sea compared to one on the South Pole for measuring the diffuse Galactic neutrino flux: the Galactic centre has a high visibility for the former (about 68% for ANTARES).

The diffuse Galactic neutrino fluxes averaged over the region $33° < l < 213°$; $-4.4° < b < 4.4°$, i. e. the region used by the AMANDA-II experiment to set their limit, are plotted in figure 2.30 versus neutrino energy. For comparison, the fluxes in the region $-39° < l < 39°$; $-4.5° < b < 4.5°$ are also shown, which is the region of interest for ANTARES[16]. The average flux in the ANTARES region is about a factor of 3 higher than in the AMANDA region, although this differs per model. In table 2.3 the average flux integrated above 1 TeV in the ANTARES region compared to that in the AMANDA region is summarised for the four models.

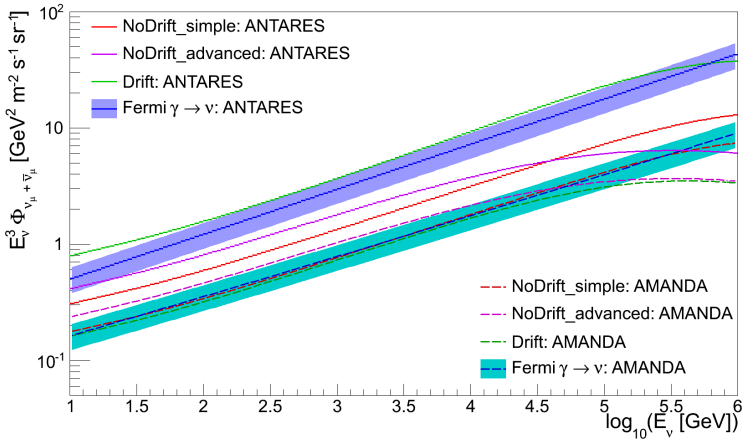

Figure 2.30: Average diffuse Galactic neutrino fluxes versus energy for the ANTARES and AMANDA regions.

Also shown in table 2.3 are the spectral indices for the four models, that have been obtained from a fit to the fluxes shown in figure 2.30 for a neutrino energy between $E_\nu = 100\,\text{GeV}$ and $E_\nu = 100\,\text{TeV}$. The spectral index for the NoDrift models is identical in both regions, since these fluxes just scale with the column density. For the other two models, the spectrum in the

[14] *Using the veto-technique, IceCube is also able to observe the Southern sky, which results in a different visibility than shown in figure 2.28. However, since IceCube can only observe very high energy neutrinos ($\gtrsim 100\,\text{TeV}$) coming from the Southern sky, this is not relevant for the current discussion.*

[15] *The visiblity of the future KM3NeT detector will be very similar.*

[16] *This is the region that is found to be optimal, see chapter 5.*

MODEL NAME	AVERAGE FLUX ANTARES REGION TO AMANDA REGION	SPECTRAL INDEX ANTARES REGION	SPECTRAL INDEX AMANDA REGION
NoDrift_simple	1.8	2.63	2.63
NoDrift_advanced	1.8	2.69	2.69
Drift	4.5	2.61	2.65
Fermi $\gamma \rightarrow \nu$	4.0	2.61	2.65

Table 2.3: Average flux above 1 TeV in the ANTARES region compared to that in the AMANDA region and spectral indices for the average fluxes from $E_\nu = 100\,\text{GeV}$ to $E_\nu = 100\,\text{TeV}$.

ANTARES region is slightly harder than that in the AMANDA region.

To complete the comparison of ice and water, it is important to mention the detection media themselves. More on this, and the optical properties (which are also different for the two detection media) can be found in the next chapter.

3 THE ANTARES NEUTRINO TELESCOPE

In this chapter a description of the whole detection process is given, starting from a neutrino interacting in the vicinity of the detector, to the arrival of the data at the shore station. The ANTARES detector uses the so-called *all-data-to-shore* concept, which means that all signals that are recorded by the PMTs are sent to shore and could in principle be stored. Since this would require too much storage space, non-interesting signals are directly filtered out in a process called *triggering*. This procedure, and the reconstruction of the neutrino interaction from the signals measured by the PMTs are described in chapter 4.

First the neutrino interactions and light production by the interaction products are described in section 3.1. A description is also given of the sources of optical background present in the deep sea. Following this, the ANTARES detector is introduced in section 3.2, and details of its components are given. For an exhaustive description of the detector, see the paper by Ageron et al. [2011].

3.1 NEUTRINO SIGNATURES

Neutrinos only interact via the weak interaction by exchanging a weak boson with a target nucleus in the water around or the rock below the ANTARES detector. If a charged W-boson is exchanged the interaction is called a Charged Current (CC) interaction; if a neutral Z-boson is exchanged it is called a Neutral Current (NC) interaction, see figure 3.1. In a NC interaction, the neutrino interaction may break up the nucleus, which induces a hadronic shower with a size depending on its energy (a typical size being a few metres). Not all of the energy of the neutrino is transferred to the nucleus, and the outgoing neutrino carries away an (unknown) part of the total energy, depending on the elasticity of the interaction. Because of this, the energy resolution of these interactions is very poor. About 1 in 4 neutrino interactions proceeds via the neutral current (see the right plot in figure 3.2).

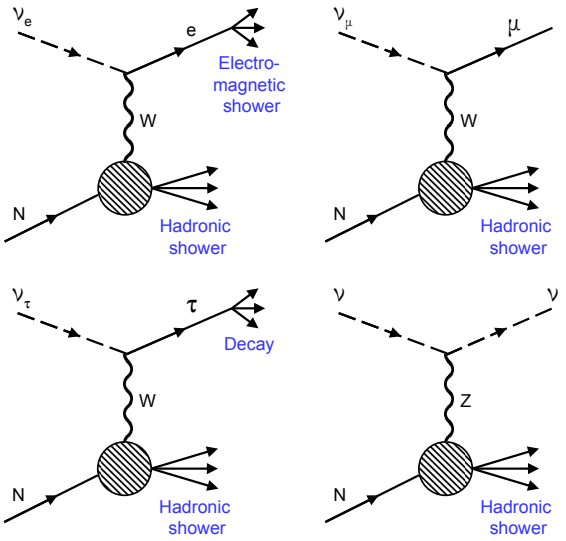

Figure 3.1: The different neutrino interactions. TOP LEFT: CC electron-neutrino. TOP RIGHT: CC muon-neutrino. BOTTOM LEFT: CC tau-neutrino. BOTTOM RIGHT: NC.

In a CC interaction, in addition to a hadronic shower, the exact signature produced depends on the neutrino flavour, see figure 3.1. In a CC interaction of an electron-neutrino[17] an electron is produced, which in turn produces an electromagnetic shower due to bremsstrahlung and pair production. The size of this shower again depends on its energy. In a CC muon-neutrino interaction a muon is produced, which has a much larger mass, meaning that the energy losses due to bremsstrahlung and pair production are reduced. Due to its relatively long mean life time of about 2.2 µs, the muon travels a considerable distance before decaying. Finally, in a CC tau-neutrino interaction a tau is produced, which has a much shorter mean life time τ_τ of about $2.9 \cdot 10^{-7}$ µs.

[17] *An anti-electron-neutrino will create a positron, but the interaction will otherwise look the same.*

The average distance d between the interaction and the decay vertex for the tau is given by:

$$d = \frac{E_\tau \tau_\tau}{m_\tau c}, \tag{3.1}$$

where E_τ and m_τ are the energy and mass of the tau particle respectively. Using $m_\tau = 1.78\,\mathrm{GeV}/c^2$ gives $d = 4.9$ m for a 100 TeV tau particle. Except for energies above 100 TeV, the interaction vertex and the decay vertex cannot be separated in ANTARES sufficiently well to detect a tau-neutrino signature.

The tau can decay in various ways:

$$\begin{aligned} &\text{A. } \tau^- \to \text{Hadrons} && (\sim 65\%) \\ &\text{B. } \tau^- \to e^- + \overline{\nu}_e + \nu_\tau && (17.85\%) \\ &\text{C. } \tau^- \to \mu^- + \overline{\nu}_\mu + \nu_\tau && (17.36\%) \end{aligned} \tag{3.2}$$

where A will create a hadronic shower and B an electromagnetic shower. In ANTARES, the muonic decay (C) cannot be distinguished from the muon-neutrino CC interaction and will therefore contribute to the CC muon channel.

Since neutrinos only interact via the weak interaction, their cross section is low compared to other processes. The neutrino-nucleon CC cross section is given by [Connolly et al., 2011]:

$$\sigma_{\nu N}^{CC} = \frac{2 G_F m_N E_\nu}{\pi} \int_0^1 \int_0^1 dx\, dy \left(\frac{M_W^2}{Q^2 + M_W^2} \right)^2 \left[q + (1-y)^2 \overline{q} \right], \tag{3.3}$$

where G_F is the Fermi coupling constant, m_N and M_W are the nucleon and W-boson mass respectively, $-Q^2$ is the square of the four-momentum transfer between the neutrino and the nucleon, q and $\overline{q}$ are the corresponding parton distribution functions for quarks and anti-quarks, x is the parton momentum fraction and y is the inelasticity. The neutrino-nucleon NC cross section is very similar:

$$\sigma_{\nu N}^{NC} = \frac{2 G_F m_N E_\nu}{\pi} \int_0^1 \int_0^1 dx\, dy \left(\frac{M_Z^2}{Q^2 + M_Z^2} \right)^2 \left[q^0 + (1-y)^2 \overline{q}^0 \right], \tag{3.4}$$

where M_Z is the Z-boson mass and q^0 and $\overline{q}^0$ are the sum of all parton distribution functions, since the Z-boson can interact with any quark.

The neutrino-nucleon cross sections are shown in figure 3.2. The left plot shows the CC cross section for both muon-neutrinos and anti-muon-neutrinos, from which it can be seen that the former is about a factor of two higher. This is due to the fact that neutrinos are predominantly left-handed, so that scattering on (right-handed) anti-quarks is suppressed compared to scattering on (left-handed) quarks and by the larger momentum fraction carried by quarks [McFarland, 2008]. The right plot in the figure shows the muon-neutrino CC and NC cross sections versus energy. The NC cross section is about a factor three lower than

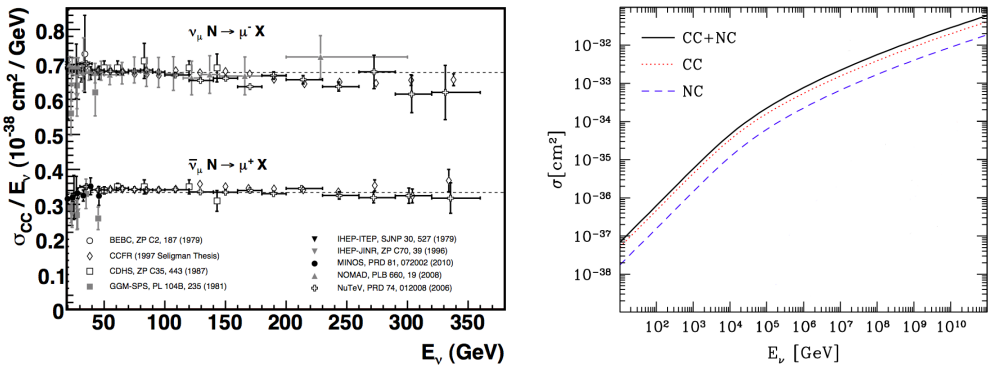

Figure 3.2: The neutrino-nucleon cross section versus neutrino energy. LEFT: the CC for muon-(anti-)neutrinos (divided by neutrino energy) up to 350 GeV. Figure reproduced from Formaggio and Zeller [2013]. RIGHT: both CC and NC for the average of muon-neutrinos and anti-neutrinos. Figure reproduced from Ahlers et al. [2006].

the CC cross section due to the difference in the W- and Z-boson mass and couplings [Paschos, 2002].

As pointed out before, only muon-(anti-)neutrinos are used for this work, and more specifically the CC interaction in which an (anti-)muon is produced. The average distance travelled by a muon with initial energy E_0 is given by:

$$R_\mu = \frac{1}{b(E_\mu)} \ln\left(1 + \frac{b(E_\mu)}{a(E_\mu)} E_0\right), \tag{3.5}$$

with $a(E_\mu)$ representing the ionisation losses and $b(E_\mu)$ the radiative losses. For water $a(E_\mu) \simeq 2.67\,\mathrm{MeV/cm}$ and $b(E_\mu) \simeq 3.4 \cdot 10^{-6}\,\mathrm{cm}^{-1}$. Above 100 GeV, the range of the muon exceeds 350 m. The muon thus has enough energy to traverse the detector (see figure 3.6), even if it is produced outside.

3.1.1 *Muon propagation*

While passing through the water or rock, the muon loses its energy by ionisation and radiative processes. The radiative processes, which consist of electron-positron pair production, bremsstrahlung and photonuclear contributions, are characterised by large energy fluctuations and become the dominant energy loss mechanism above several hundred GeV [Beringer et al., 2012]. The direction of the muon is subject to multiple Coulomb scattering off atomic nuclei.

Since the muon is a charged particle, and at the energies of interest has a velocity higher than the phase velocity of light,

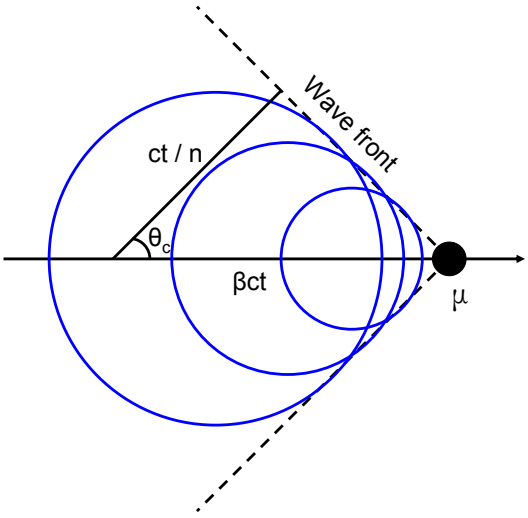

Figure 3.3: Schematic view of Čerenkov radiation.

Čerenkov radiation is produced [Čerenkov, 1937]. The charged particle polarises the atoms in the medium, resulting in the emission of dipole radiation at a specific angle θ_c (see also figure 3.3):

$$\cos\theta_c = \frac{1}{\beta n(\lambda)}, \tag{3.6}$$

where $\beta = v/c$ is the ratio between the velocity of the muon and the speed of light (in vacuum) and $n(\lambda)$ is the refractive index, which depends on the wavelength λ. Between 400 and 500 nm, which is the wavelength range of interest for ANTARES (see section 3.2.1), the refractive index of sea water is around 1.35 [Adrián-Martínez et al., 2012c]. For the neutrino energies of interest, $\beta \simeq 1$ and the light is emitted at an angle of about 42°.

The number of photons emitted per unit track length x and per unit wavelength is [Beringer et al., 2012]:

$$\frac{\mathrm{d}^2 N_\gamma}{\mathrm{d}x\mathrm{d}\lambda} = \frac{2\pi\alpha Z^2}{\lambda^2}\left(1 - \frac{1}{\beta^2 n^2(\lambda)}\right), \tag{3.7}$$

where α is the fine structure constant. Although the emission of photons constitutes a form of energy loss for the muon, it is small compared to ionisation and radiative processes [Allison and Wright, 1984]. Between 400 and 500 nm, about 100 photons are emitted per centimetre of track length.

The path of the muon yields a long lever arm, so the direction of the muon can in principle be well reconstructed. Furthermore, the

muon direction is effectively the same as the neutrino direction above energies of about 100 TeV, see figure 3.4. Below about 10 TeV the angular resolution is dominated by the angle between the muon and the neutrino in the neutrino interaction [Amram et al., 1999].

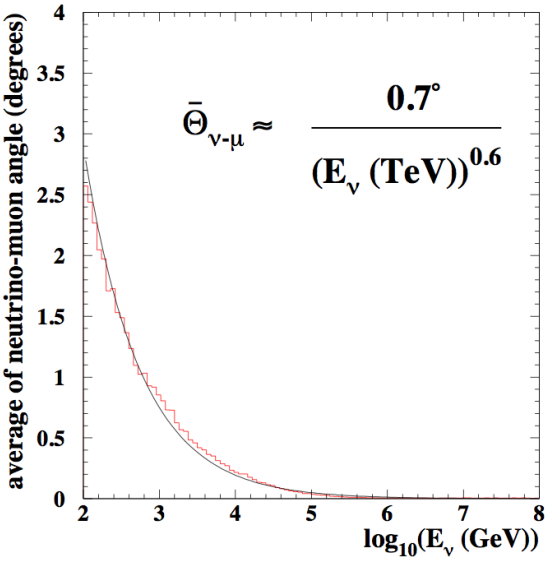

Figure 3.4: The average angle between the directions of the neutrino and the muon. Figure reproduced from [Amram et al., 1999].

The propagation of Čerenkov light through the sea water is affected by absorption and scattering. The intensity of the emitted light as a function of distance can be written as [Aguilar et al., 2005]:

$$I(s,\lambda) = I_0\, e^{-s/\lambda_{\text{att}}^{\text{eff}}(\lambda)}, \tag{3.8}$$

where I_0 is the intensity of the emitted light, s is the optical path length and $\lambda_{\text{att}}^{\text{eff}}(\lambda)$ is the effective attenuation length given by:

$$\frac{1}{\lambda_{\text{att}}^{\text{eff}}(\lambda)} = \frac{1}{\lambda_{\text{abs}}(\lambda)} + \frac{1}{\lambda_{\text{scat}}^{\text{eff}}(\lambda)}, \tag{3.9}$$

where $\lambda_{\text{abs}}(\lambda)$ is the absorption length and $\lambda_{\text{scat}}^{\text{eff}}(\lambda)$ is the effective scattering length, which is given by:

$$\lambda_{\text{scat}}^{\text{eff}} = \frac{\lambda_{\text{scat}}}{1 - \langle \cos\theta_{\text{scat}} \rangle}, \tag{3.10}$$

with $\langle \cos\theta_{\text{scat}} \rangle$ the average cosine of the scattering angle, which peaks in the forward direction and has a value of about 0.9. The

effective scattering length is a more useful quantity than the scattering length, since a photon that is scattered under a very small angle will only be delayed a little bit.

The absorption length of ice is longer than that of water, but the attenuation length is shorter, because the scattering length in ice is shorter. This leads to a worse angular resolution in ice, which is important for astronomy. More on the angular resolution can be found in chapter 4.

For ANTARES, the absorption length is about 60 m at a wavelength of 475 nm, while the effective scattering length is about 265 m [Aguilar et al., 2005].

Optical background

In addition to the Čerenkov photons produced by a muon, there are other sources of light in the deep sea. One of the sources is the decay of ^{40}K. This radioactive isotope of potassium has a very long half-life of $1.248 \cdot 10^9$ year and has a natural abundance of 0.012%; i. e. 120 out of one million potassium atoms will be ^{40}K. It can decay via all three channels:

$$\begin{aligned} {}^{40}\mathrm{K} &\rightarrow {}^{40}\mathrm{Ca} + \mathrm{e}^- + \overline{\nu}_\mathrm{e} && (89.28\%) \\ {}^{40}\mathrm{K} + \mathrm{e}^- &\rightarrow {}^{40}\mathrm{Ar} + \gamma + \nu_\mathrm{e} && (10.72\%) \\ {}^{40}\mathrm{K} &\rightarrow {}^{40}\mathrm{Ar} + \mathrm{e}^+ + \nu_\mathrm{e} && (\sim 0.001\%) \end{aligned} \tag{3.11}$$

The electron produced in the decay to ^{40}Ca has an energy up to 1.33 MeV, which is above the Čerenkov threshold for electrons in water (0.26 MeV) and produces up to 150 Čerenkov photons. The photon in the electron-capture process has an energy of 1.46 MeV and Čerenkov photons can be produced by electrons via Compton scattering of the photon.

Another source of light production is luminescence from organisms present in the water, so-called bioluminescence. The amount of light produced can be several orders higher than that produced by the ^{40}K-decay, but generally occurs in short bursts of light.

No radioactive ^{40}K or luminescent organisms are present in ice and the only (optical) background for a detector in ice is that created by the detector itself [Halzen and Klein, 2010].

3.2 THE ANTARES DETECTOR

The ANTARES neutrino telescope is located 40 km offshore from Toulon, France, see figure 3.5. Its coordinates are 42°48′ N, 6°10′ E.

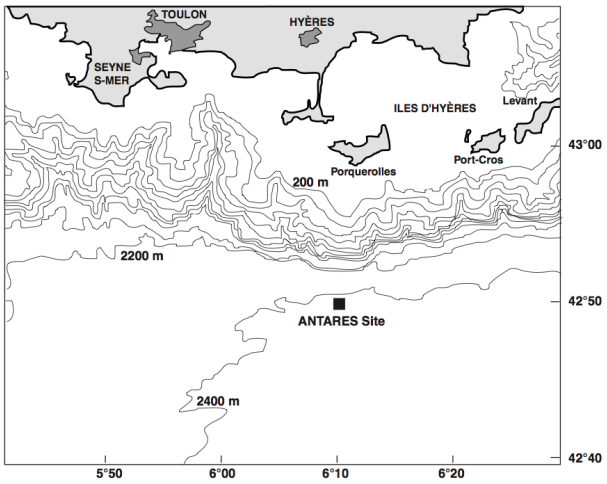

Figure 3.5: Map of the ANTARES site near Toulon. Figure reproduced from Amram et al. [1999].

The detector is located at a depth of 2475 m below sea level and consists of 12 lines. The first 11 lines consist of 25 storeys with a triplet of so-called Optical Modules (see below) and line number 12 consists of 20 storeys. The top part of this line contains acoustic detection devices.

Each line is divided in sectors, containing five storeys each, which have independent power distribution and data communication. This makes it possible to use part of the string in case of a failure. The different components of ANTARES will now be described in more detail; for a schematic overview of the detector, see figure 3.6.

3.2.1 *The optical module*

The photons are detected by PhotoMultiplier Tubes (PMTs), which are housed in a glass sphere called the Optical Module (OM). A PMT detects light using the photo-electric effect, whereby a photon liberates an electron from the photocathode, which is accelerated (and multiplied) in an electric field. It provides a current output proportional to the light intensity.

After considering several commercially available models, the 10″ Hamamatsu R7081-20 PMT was chosen, which is sensitive for light in the wavelength range of $300 - 600$ nm, with a maximum quantum efficiency of about 22% between 350 and 450 nm. The OM is the building block of the detector, which contains a total

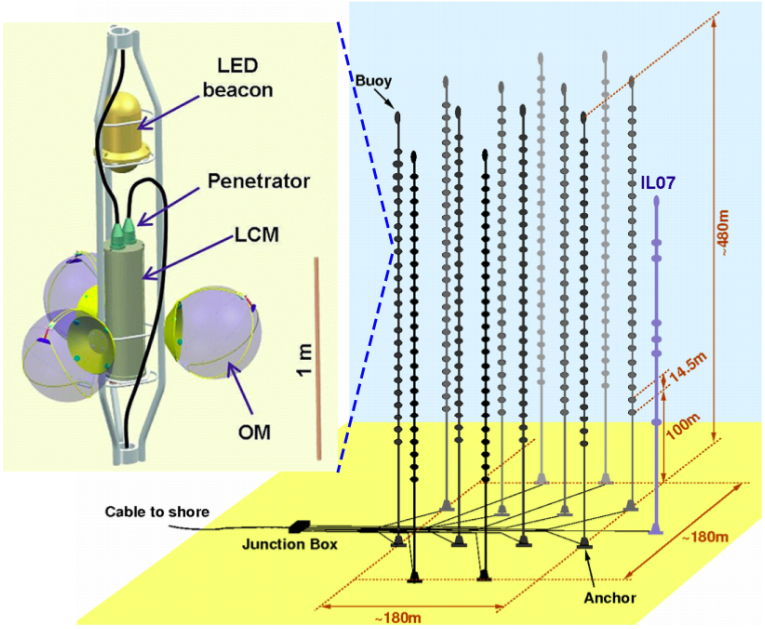

Figure 3.6: Schematic overview of the ANTARES detector, the inset shows a schematic view of a storey. Figure reproduced from Ageron et al. [2011].

of 885 OMs distributed over the 12 lines. The OMs look downward at an angle of 45° below the horizon in order to optimise the detection of light from upgoing muons. Figure 3.7 shows a schematic view and a photograph of an assembled OM.

A key parameter of the PMT is the Transit Time Spread (TTS). The transit time is the time it takes the photo-electron to traverse the PMT. It varies from electron to electron, which is summarised by the TTS, which is the standard deviation of the transit time distribution. From earlier studies it was found that a TTS of 1.5 ns is needed to obtain a sub-degree angular resolution. The chosen PMT has an average TTS of about 1.3 ns, which is conform the requirements [Amram et al., 2002].

The PMT is shielded against the Earth's magnetic field (~0.46 G locally) using a so-called μ-metal cage. Without this shielding, the TTS and charge amplification of the PMT would be significantly degraded. The PMT and the μ-metal cage are held in place in the OM with optical gel. The OM also contains an LED, which is used to monitor the internal timing of the OM (see section 3.2.5). The high voltage is generated by an electronics board mounted on the base, which is connected to an electronics container via a penetrator.

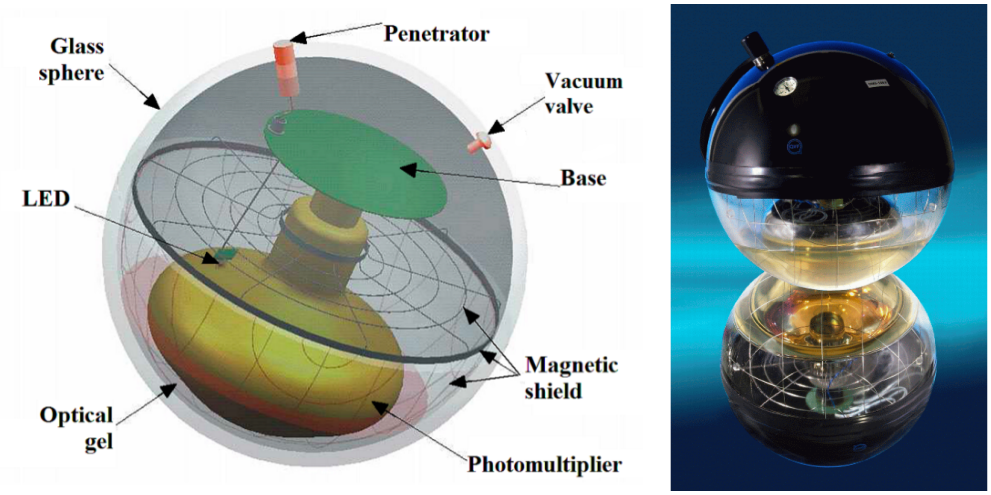

Figure 3.7: The ANTARES optical module. Figures reproduced from Ageron et al. [2011]. LEFT: schematic view. RIGHT: photograph.

An example of the output produced by a PMT is shown in figure 3.8, in which the counting rate is shown versus time. The base line in the counting rate, shown as a red dashed line, can be attributed to potassium decay and dark noise produced by the PMT. A typical value for the base line is 60 kHz (see also figure 4.4), but in this case it is just above 40 kHz. This difference can be attributed to the different quantum efficiencies of the PMTs. The short term bursts (lasting up to tens of seconds) are caused by bioluminescence.

3.2.2 *Detector layout*

In addition to three OMs, a storey also contains an electronics container, referred to as the Local Control Module (LCM), which houses the offshore electronics; see the inset in figure 3.6. The distance between storeys is 14.5 m, with the first storey being located about 100 m above the sea floor. The line is anchored by the Bottom String Socket (BSS) and held vertical by a buoy. The BSS consists of a dead weight which acts as an anchor, and a recoverable part that can be disconnected using an acoustic release. Once released, the line will float to the surface and can be picked up by a boat. The BSS also contains the String Control Module (SCM), which contains additional electronics.

An interlink cable links each line to the Junction Box (JB), which in turn is connected to the shore station by the Main Electro-

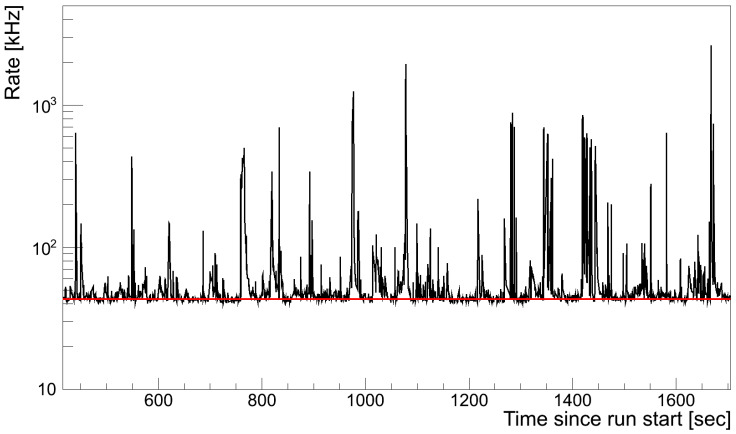

Figure 3.8: Example of the time dependence of the counting rate, the red line shows the base line.

Optical Cable (MEOC). After deployment of a line, an interlink cable is connected to the JB with a Remotely Operated underwater Vehicle (ROV). The MEOC is a standard telecommunications cable and provides the electrical power link and the optical data link between the detector and the shore station.

In addition to the twelve lines instrumented with OMs for the detection of neutrinos, there is a thirteenth line known as the Instrumentation Line (IL). This line contains several different instruments, including an acoustic detection system, instruments to monitor the speed and direction of the sea current, a sound velocimeter and cameras to record images of bioluminescent organisms.

Detector History

Construction of the detector commenced in 2001 with the installation of the MEOC, followed by the JB in December 2002. In March 2006, the first detector line was installed, followed by the second one in July 2006 and three more on January 29th 2007. With the connection of these lines ANTARES became the largest detector on the Northern Hemisphere.

In December of 2007, five more lines were installed, effectively doubling the size of the detector. The detector was completed on May 28th 2008 with the connection of lines 11 and 12. The detector did not always run with all twelve lines, since for some periods one or more of the lines exhibited problems and had to be recovered and repaired. From June 25th 2008 to September 5th

2008 the detector did not take any data due to a problem with the MEOC.

The full ANTARES detector collects on average about 5 atmospheric muons per second and about 3 neutrino candidates per day [Bogazzi, 2014].

3.2.3 *Data acquisition*

p.e.: photon-equivalent, the output signal of the PMT corresponding to the detection of one photon.

All signals from the PMTs that pass a predefined voltage threshold (typically equivalent to 0.3 p.e.) are digitised by an Analogue Ring Sampler (ARS) chip located in the LCM. The analogue signal is integrated by an Amplitude to Voltage Converter (AVC) to obtain the charge. The arrival time of the hit is determined by a Time to Voltage Converter (TVC) using the signal of the local clock, which is synchronised to a 20 MHz onshore master clock. Each LCM contains two ARSs which are connected to work in a token-ring scheme, to minimise the dead time induced by the digitisation. In the token-ring scheme, the ARS holding the token will treat the incoming events. After the signal integration the token is passed over to the other ARS with a delay of about $10 - 20$ ns [Aguilar et al., 2010].

In each sector of five OMs, one of the LCMs is the Master Local Control Module (MLCM). It multiplexes the signals from the other four storeys via an optical connection. The MLCM passes these multiplexed signals to a Dense Wavelength Division Multiplexer (DWDM) which in turn sends the data, via the MEOC, to shore. As noted before, no filtering of the data is performed, and all data from the OMs are sent to shore. Each MLCM uses a laser with a specific frequency chosen in the range from 192.1 to 194.9 THz, so that the data from the five sectors in a string can be transmitted to shore via a single fibre.

3.2.4 *The shore station*

The onshore facilities consist of two separate buildings: the power hut and the shore station. The power hut is located close to the place where the MEOC arrives on land and provides the power for the detector. The shore station is located in La Seyne-sur-Mer and has several rooms dedicated to the operation of ANTARES; a picture of the shore station is shown in figure 3.9.

The computer room hosts racks with DWDM boards that receive the signals from the DWDM boards of the detector. It also hosts a PC farm that performs the filtering (triggering) and stor-

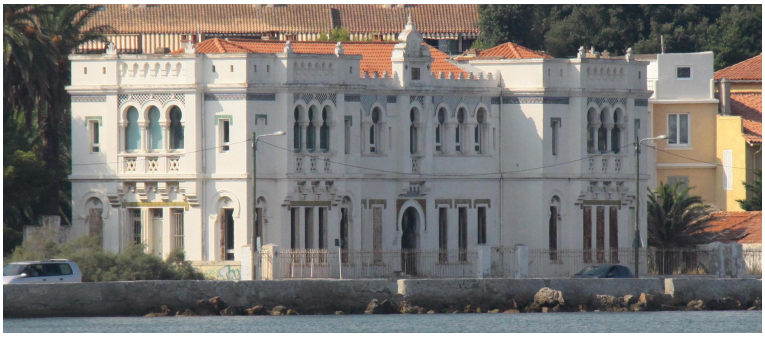

Figure 3.9: A photograph of the shore station in La Seyne-sur-Mer. Image credit Nicky, www.LaSeyne.Info.

age of the data. On average, the trigger reduces the data flow by a factor of about 10000. The filtered data are written in the ROOT format [Antcheva et al., 2009], and are copied to the IN2P3 computing centre in Lyon overnight.

The control room contains several computers for the operation of the detector and on-site shifts are performed here. Most of the shifts are performed remotely however, by means of a Virtual Network Computing (VNC) application.

3.2.5 *Calibration*

An important aspect is the calibration of the detector. In order to achieve an angular resolution of the order of a few tenths of a degree, the position of the OMs and the timing of the signals has to be known to an accuracy of 10 cm and 1 ns respectively. The calibration of the integrated charge measured by the PMTs is also important. These calibrations will now be described in more detail.

Position calibration

The detector lines move in the sea currents, so it is important to monitor the (relative) positions of all the OMs. A High Frequency Long Base Line (HFLBL) acoustic system is used to monitor the positions of hydrophones on storeys 1, 8, 14, 19 and 25 of each line. The positions are obtained by triangulation using emitters in the BSS of each line and some extra emitters on the sea floor. This allows the position of each OM to be known with an accuracy of about 10 cm [Adrián-Martínez et al., 2012b]. The orientation of

the OMs is also required, which is measured with an accuracy of a few degrees using compasses and tiltmeters.

Time calibration

For time calibration, the master clock is used to measure time delays between the shore station and the LCMs. The internal LED from each OM (wavelength of 470 nm) is used to determine the time delay from the moment the PMT measures the photon to when the signal arrives at the electronics of the LCM. Furthermore, four LED beacons (wavelength of 472 nm) are placed on storeys 2, 9, 15 and 21 on each string for intra-line calibration and two laser beacons (wavelength of 532 nm) located in the BSSs of lines 7 and 8 for inter-line calibration. Using these systems, a relative time calibration between the detector elements of less than 1 ns can be achieved, which is sufficient to obtain the required angular resolution [Aguilar et al., 2011a].

Charge calibration

The integrated charge of the analogue pulse from the PMT has to be converted to the number of photo-electrons that created the pulse. This calibration is performed using dedicated runs in which the output signal of the PMT is digitised at random moments to obtain the so-called pedestal value. This is the output given by the electronics even when no signal is detected by the PMT. The Single Photo-Electron peak is then studied using minimum bias events, for which ^{40}K decays and bioluminescence can be used, since they produce primarily single photons. The knowledge of the location of the single photo-electron peak and the pedestal value can then be used to determine the charge conversion for the dynamic range of the ADC of about 20 photo-electrons.

It has been noticed that the charge measurements by the ADC are influenced by the time measurements by the TDC, an effect known as cross-talk. Using in situ measurements, this effect is corrected for.

4

SIMULATION, TRIGGERS AND RECONSTRUCTION

In this chapter the triggering of the data that are sent to shore and the subsequent reconstruction of the neutrino interaction from these triggered data are described.

Before going into triggers and reconstruction, the simulation packages used to simulate the response of the detector to neutrino interactions and muons are described in section 4.1. These simulations are needed to quantify the performance of the trigger algorithms and reconstruction strategies.

In section 4.2 the trigger scheme and the different triggers used in the ANTARES detector are described. In section 4.3 the reconstruction of the neutrino direction and energy determination are described. The part on reconstruction is focused on the so-called *track reconstruction*, which is used to determine the direction of the muon produced in a CC muon-neutrino interaction. Several algorithms are used within the ANTARES collaboration, which are described together with a new track reconstruction algorithm, called GRIDFIT. The goal of this new algorithm is to improve the reconstruction efficiency for low energy neutrinos.

4.1 SIMULATION TOOLS

The simulation chain used in ANTARES consists of several steps. First neutrinos and atmospheric muons are generated using the GENHEN [L'Abbate et al., 2004] and MUPAGE [Carminati et al., 2008] packages respectively. Then, the charged particles are propagated through the detector using the KM3 [Navas and Thompson, 1999] and GEASIM [Brunner, 2002] packages. Finally the detector response to the Čerenkov light is simulated using the TRIGGER-EFFICIENCY [de Jong, 2010] program. These different steps are described in more detail below.

4.1.1 *Neutrino generation*

The rate of neutrinos detected by a detector can be written as [Bailey, 2002]:

$$R = \int\int\int \mathrm{d}E_\nu \, \mathrm{d}\Omega \, \mathrm{d}\vec{x} \, \Phi_\nu(E_\nu, \theta, \phi) \, \rho(\vec{x}) \, N_\mathrm{A} \, \sigma_{\nu\mathrm{N}}(E_\nu) \cdot P_\mathrm{det}(E_\nu, \theta, \phi, \vec{x}) \, P_\oplus(E_\nu, \theta, \phi), \tag{4.1}$$

where Ω is the solid angle, $\vec{x}$ is the position of the neutrino interaction, θ and ϕ are the zenith and azimuth angle in local detector coordinates respectively, $\Phi_\nu(E_\nu, \theta, \phi)$ is the neutrino flux at the surface of the Earth, $\rho(\vec{x})$ is the density of the medium in which the neutrino interacts and N_A is Avogadro's constant.

Furthermore, there are two probability terms in equation 4.1. The first, $P_\mathrm{det}(E_\nu, \theta, \phi, \vec{x})$, represents the probability that the neutrino interaction is detected. This depends on a number of factors, such as the location of the interaction, the amount of light produced by the interaction products, the detector response and the trigger and reconstruction efficiencies. The other probability term, $P_\oplus(E_\nu, \theta, \phi)$, represents the probability for the neutrino to penetrate the Earth, and is given by:

$$P_\oplus(E_\nu, \theta, \phi) = e^{-N_\oplus(\theta,\phi) N_\mathrm{A} \sigma_{\nu\mathrm{N}}(E_\nu)}, \tag{4.2}$$

with

$$N_\oplus(\theta, \phi) = \int \mathrm{d}s \, \rho_\oplus(s), \tag{4.3}$$

the mass density per unit of area integrated along a line of sight through the Earth as seen from the detector (i. e. the column density), with s the integration variable and $\rho_\oplus(s)$ the matter density of the Earth.

GENHEN: GENerator of High Energy Neutrinos

Neutrino events are generated with the GENHEN package. For this purpose, a large cylinder is defined around the detector in which neutrino events are generated isotropically. The size of this cylinder is chosen in such a way that all neutrinos that are able to produce a detectable signal in the detector are simulated. It has a typical radius and height of 25 km.

A second cylinder, called the *can* is defined, and only events that either have their vertex inside of this can (for CC electron-neutrino and NC interactions) or have a muon or tau reaching the can (for CC muon- and tau-neutrino interactions) are taken into account. Events for which the muon (or tau) direction is such that it does not intercept the can are discarded. The can typically

extends 3 light attenuation lengths beyond the instrumented volume and muons passing outside of it are too far away to produce a detectable signal in the PMTs. Typical values for the radius and height of the can are 300 m and 650 m respectively. The CTEQ6-DIS parton distribution functions [Pumplin et al., 2002] are used to calculate the cross sections and the Preliminary Reference Earth Model [Dziewonski and Anderson, 1981] is used to calculate the neutrino attenuation in the Earth.

To evaluate the triple integral in equation 4.1, GENHEN makes use of Monte Carlo (MC) integration[18], which is a mathematical technique in which an integral is approximated by evaluating the integrand at a number of randomly chosen points in the phase space. Equation 4.1 can then be written as:

$$R = \frac{V_{\text{gen}} I_\phi I_\theta I_E}{N_{\text{gen}}} \sum_{i=1}^{N_{\text{gen}}} \Phi_\nu(E_{\nu,i}, \theta_i, \phi_i)\, \rho(\vec{x}_i)\, N_A\, \sigma_{\nu N}(E_{\nu,i}) \cdot P_\oplus(E_{\nu,i}, \theta_i, \phi_i)\, P_{\text{det,i}}\, E_{\nu,i}^{\alpha}, \tag{4.4}$$

where V_{gen} is the generation volume, N_{gen} the number of generated events (typically of the order of 10^{10}) and α the spectral index of the generation spectrum. The events are generally not generated uniformly in the neutrino energy (i. e. $\alpha = 0$), but rather according to a power law spectrum. This is done to generate roughly the same number of events for each decade of neutrino energy. The value of α is typically around 1.4.

The three phase space factors I_ϕ, I_θ and I_E in equation 4.4 are given by:

$$I_\phi = \int_{\phi_{\min}}^{\phi_{\max}} \mathrm{d}\phi = \phi_{\max} - \phi_{\min}, \tag{4.5}$$

$$I_\theta = \int_{\theta_{\min}}^{\theta_{\max}} \mathrm{d}\theta\ \sin\theta = \cos(\theta_{\min}) - \cos(\theta_{\max}), \tag{4.6}$$

$$I_E = \int_{E_{\nu,\min}}^{E_{\nu,\max}} \mathrm{d}E_\nu\ E_\nu^{-\alpha} = \begin{cases} \frac{E_{\nu,\max}^{1-\alpha} - E_{\nu,\min}^{1-\alpha}}{1-\alpha} & \alpha \neq 1 \\ \ln \frac{E_{\nu,\max}}{E_{\nu,\min}} & \alpha = 1 \end{cases} \tag{4.7}$$

Finally, the term representing the probability that the neutrino interaction is detected ($P_{\text{det,i}}$ in equation 4.4) is now a binary variable, which is 1 if the event is triggered, reconstructed, etc. and 0 if not.

[18] *The method is named by physicist John von Neumann (*1903; †1957), who worked together with Stanislaw Ulam (*1909; †1984) on the Manhattan Project, where the technique was used. Since the project was secret, a code name was required and Von Neumann chose the name Monte Carlo, after the Monte Carlo casino in Monaco where Ulam's uncle used to gamble.*

By defining the so-called *event weight*, which captures the whole interaction and detection process:

$$w_i \equiv V_{\text{gen}}\, I_\Phi\, I_\theta\, I_E\, \rho(\vec{x}_i)\, N_A\, \sigma_{\nu N}(E_{\nu,i})\, P_\oplus(E_{\nu,i},\, \theta_i,\, \phi_i)\, P_{\text{det,i}}\, E_{\nu,i}^{\alpha}, \tag{4.8}$$

equation 4.4 can be written as:

$$R = \frac{1}{N_{\text{gen}}} \sum_{i=1}^{N_{\text{gen}}} w_i\, \Phi_\nu(E_{\nu,i},\, \theta_i,\, \phi_i), \tag{4.9}$$

and event rates for different neutrino fluxes can easily be calculated by multiplying the event weight by the required flux on an event by event basis.

4.1.2 *Atmospheric muon generation*

MUPAGE: atmospheric MUons from PArametric formulas: a fast GEnerator for neutrino telescopes

Atmospheric muon events are generated using the MUPAGE package. Instead of using a full MC simulation as for the neutrino generation, MUPAGE uses a set of parametric formulas to reproduce the energy and angular distribution of muon bundles of any multiplicity (typically up to 100) on the surface of the can. For MUPAGE the generated number of events corresponds to the livetime specified by the user.

4.1.3 *Propagation of muons, light and other secondaries*

The muons are propagated through the can using the KM3 package, which simulates the energy losses of the muon and generates photons along the muon track. The created photons are also propagated through the sea water, taking into account both absorption and scattering. Since tracking all photons is too computationally intensive, tables are used that contain the average number of photons arriving at a PMT with a given orientation and at a given distance from the muon track.

GEANT: GEometry ANd Tracking

All other particles are propagated using the GEASIM package, which is based on the GEANT package [Agostinelli, 2003] and performs a full tracking of all particles. Light scattering is not considered in GEASIM, and for this reason a new version of KM3 has recently been created, which performs the light creation and propagation for all particles [James, 2012].

4.1.4 *Detector simulation*

The final step involves the simulation of the detector response to the photons arriving at the PMTs. For this the TRIGGEREFFICIENCY program is used. This program simulates the response of the PMTs and the data acquisition system, and also adds optical background (see section 3.2.1).

The true number of signal photons is used to determine the integrated hit charge, which is smeared according to a Gaussian distribution with $\sigma = 0.3$ p.e. The time of the hit is smeared using a Gaussian with a width given by the TTS.

In addition to these signal hits, noise hits are added. These hits are generated according to a Poisson distribution, using the observed background rate of each PMT. After-pulses[19] are also added at this point. The charges of the background hits are generated according to the observed distributions of after-pulses and normal background hits.

The output at this stage is compatible with what is sent to shore by the detector and to which the trigger algorithms are applied, see section 4.2. These triggers are also simulated by the TRIGGEREFFICIENCY program.

[19] *There is a finite probability that a signal (or background) pulse is followed by a second pulse (called after-pulse), which is caused by the ionisation of residual gas in the PMT.*

4.1.5 *MC productions*

For the physics analyses, the so-called run-by-run (RBR) simulation has been developed [Riviére, 2012]. In this simulation, separate MC files are generated for each data run, and the observed background rates and detector conditions (such as which PMTs are operational and which triggers are active) are used. The software versions used for the RBR simulation are summarised in table 4.1. Muon bundles with multiplicities between 1 and 200 are simulated with MUPAGE, with the livetime of the simulation limited to one-third of the duration of the data run for computational reasons.

Since the rates and detector conditions vary in the RBR simulation, it is not well suited for the development of new reconstruction strategies, or for the comparison of two different ones. For these kinds of studies, a well defined background rate and a nominal detector are better suited. For this reason, a dedicated MC production is made (called fixed-conditions (FXC) simulation), with a fully working detector and the background rate fixed at 60 kHz. This production is used in the rest of this chapter. Slightly different versions of the MC programs are used than for the RBR simulation, as can be seen from table 4.1. In the FXC

PROGRAM	RBR VERSION	FXC VERSION
GENHEN	v6r10	v6r9
MUPAGE	v3r5	v3r4
KM3	v4r2	v4r4
GEASIM	v4r13	v4r13
TRIGGEREFFICIENCY	v2011-12-19	v2011-12-19

Table 4.1: The MC software versions used in the run-by-run (RBR) and fixed-conditions (FXC) simulations.

simulation, muon bundles with multiplicities up to 1000 are simulated with MUPAGE and only upgoing neutrino events ($\theta > 90^\circ$) are considered.

4.2 TRIGGERING

All PMT signals passing the ARS threshold of 0.3 p.e. are digitised and all digital data are sent to shore. These data are referred to as L0 hits and are used as input for the trigger algorithms running on the PCs in the shore station. Most of these hits are due to background however, so a pre-trigger is applied to reduce the input for the trigger algorithms [de Jong, 2005]. Hereby it is used that the optical background hits are uncorrelated and have primarily a charge equivalent to 1 p.e. To this end, hits on different PMTs on the same storey within 20 ns or hits with a high charge (typically above 3 p.e.) are selected. These hits are called L1 hits and are used as input for the different trigger algorithms.

The default run setup consists of using both the so-called 3N and 2T3 triggers, and the data taken with this run setup corresponds to what is used in most data analyses. When data taking conditions are favourable the so-called TQ trigger is also enabled, which has an improved efficiency for low energy neutrinos. These trigger algorithms are described first, after which the advantage of including TQ triggered events is assessed. Only a general overview will be given of the various trigger algorithms, for a more in depth description see the master thesis of Bakker [2011].

4.2.1 *The 3N trigger algorithm*

The general purpose ("standard") muon trigger is called the 3N trigger, which uses the fact that photons originating from the same muon are causally related in space and time.

When no muon direction is assumed, the causality criterion reads:

$$|t_i - t_j| \leqslant r_{ij} \frac{n_g}{c}, \tag{4.10}$$

where t_i and t_j are the times of a hit on PMT i and j respectively, n_g is the group refractive index and r_{ij} is the distance between PMT i and j.

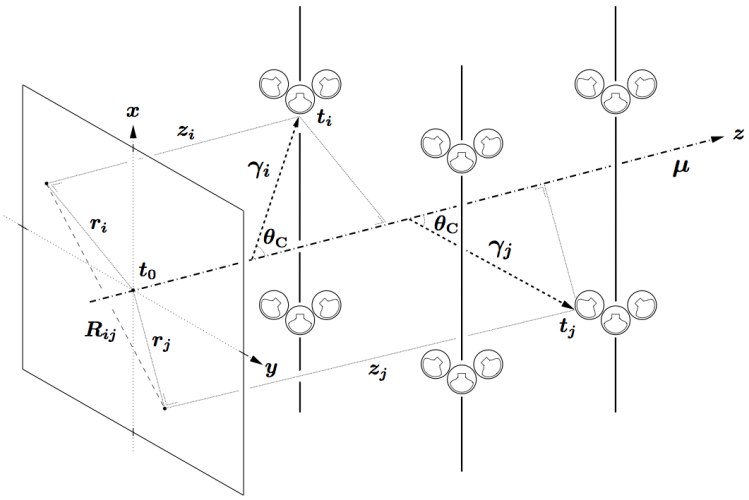

Figure 4.1: Schematic view of a muon traversing the ANTARES detector. Figure reproduced from Lim [2011].

When a muon direction is known, the causality criterion can be made more stringent. This can be seen from figure 4.1 in which the muon is chosen to travel along the z-axis. The time of a hit on PMT i can then be written as:

$$t_i = t_0 + \frac{1}{c}\left(z_i - \frac{r_i}{\tan(\theta_c)}\right) + \frac{n_g}{c}\frac{r_i}{\sin(\theta_c)}, \tag{4.11}$$

where t_0 is defined as the time when the muon is at $z = 0$, z_i is the position of PMT i along the muon track and r_i is the distance of closest approach of the muon to PMT i.

The difference in hit times of PMT i and PMT j can then be written as:

$$t_i - t_j = \frac{z_i - z_j}{c} + \frac{r_i - r_j}{c}\left(n_g \frac{1}{\sin(\theta_c)} - \frac{1}{\tan(\theta_c)}\right), \quad (4.12)$$

$$= \frac{z_i - z_j}{c} + \frac{r_i - r_j}{c}\tan(\theta_c), \quad (4.13)$$

where in the second step it has been assumed that $n_g = n$.

When the direction of the muon is assumed, the position of the track relative to PMTs i and j is still free. The minimum time difference is obtained when $r_i = r_j$, and the maximum time difference when either r_i or r_j is 0, so that the causality criterion can be written as:

$$\frac{z_i - z_j}{c} - \frac{R_{ij}}{c}\tan(\theta_c) \leqslant t_i - t_j \leqslant \frac{z_i - z_j}{c} + \frac{R_{ij}}{c}\tan(\theta_c), \quad (4.14)$$

where R_{ij} is the distance between PMT i and j in the plane perpendicular to the muon direction (see also figure 4.1).

The 3N trigger first uses the causality criterion of equation 4.10, where the allowed time difference is increased by 20 ns in order to account for (forward) scattered photons and uncertainties due to calibration. A set of L1 hits that satisfies this causality criterion is called a cluster. When a cluster of at least 5 L1 hits has been found, it is selected for the next step.

The L1 hits in each of the clusters are checked against the directional causality criterion of equation 4.14, where the allowed time difference is again increased by 20 ns. Since the direction of the muon is not known, an isotropic grid of 210 directions is defined on the full sky (with an average spacing between directions of about 14°) and the causality criterion is applied to each of these directions. A sky-map (using azimuth and elevation as coordinates) with the chosen directions is shown in figure 4.2. For the evaluation of the causality criterion, the decreasing intensity of the Čerenkov radiation with distance is taken into account by only using L1 hits with a maximum transverse distance of 90 m. If the cluster still has at least 5 L1 hits (that are compatible with the more stringent directional causality criterion), it is selected.

All selected clusters are saved to disk, together with all L0 hits from 2.2 µs before the first hit to 2.2 µs after the last hit in the selected cluster. A value of 2.2 µs is chosen, since it corresponds to the time a muon needs to traverse the whole detector. The collection of hits is called an *event* and is the input for the reconstruction strategies described in section 4.3.

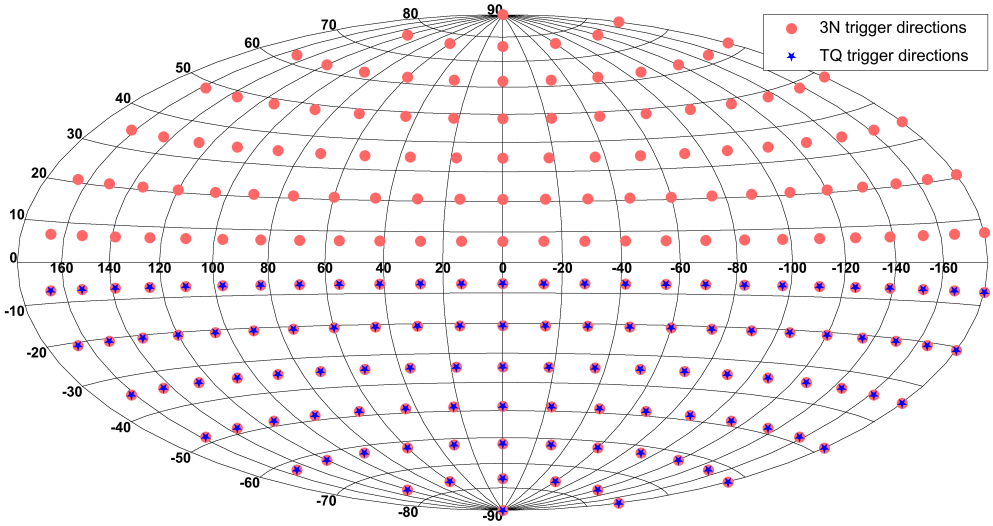

Figure 4.2: Sky-map with the directions used for the directional causality criterion in the 3N trigger and in the TQ trigger.

4.2.2 *The 2T3 trigger algorithm*

The requirement of the 3N trigger to have at least 5 L1 hits in the detector works well for neutrinos of high energy, since the created muon will produce a lot of light, but less so for lower energy neutrinos. For this reason another trigger algorithm has been developed, which is called the 2T3 trigger [Carr et al., 2007]. It is based on the T3 cluster trigger algorithm, which seeks a time coincidence between two L1 hits in adjacent storeys within 100 ns, or in next-to-adjacent storeys within 200 ns. The 2T3 trigger looks for a time coincidence between two of these T3 clusters in the whole detector within 2.2 µs. The algorithm requires a minimum of 3 L1 hits when the two T3 clusters are on the same line and at least 4 L1's otherwise. This gives an improved efficiency for lower energy neutrinos [Escoffier, 2008].

4.2.3 *The directional trigger algorithm*

Besides the general purpose trigger algorithms that look for neutrinos coming from any direction, there are also dedicated directional trigger algorithms. The 1D trigger algorithm uses only L1 hits as input and the mixed (MX) trigger algorithm also uses L0 data.

The directional trigger can be used to track a (hypothesised) neutrino source, which is done by for example the GC trigger which uses the MX trigger algorithm to follow the Galactic Centre. The TQ trigger also uses the MX trigger algorithm, but instead of following a specific source, it uses the directional trigger for a large set of directions. The TQ trigger will be described in the next section.

The first step in the directional trigger algorithms is to check all hits (in the case of the MX trigger L0 and L1) against the directional causality criterion of equation 4.14, for which a prespecified direction is used. The decreasing intensity of the Čerenkov radiation with distance is taken into account again by only considering L0 hits with a maximum transverse distance of 85 m and L1 hits with a maximum of 35 m. The largest set of hits that satisfies the causality relation and includes at least 1 L1 hit is called a cluster. Each cluster which additionally has at least 5 L0 hits is selected.

To reduce the number of accidentally selected clusters, those clusters with at most 10 hits are subjected to a track fit procedure. In general, 5 parameters are needed to parameterise a muon track: the time at a given position along the track, 2 positional parameters and 2 directional parameters. By assuming the muon direction, only 3 parameters are needed, which leads to a linearisation of the track fit problem [de Jong, 2007a]. Using $r_i = \sqrt{(x_i - x_0)^2 + (y_i - y_0)^2}$ and the assumption that $n_g = n$, equation 4.11 can be written as:

$$t_i = t_0 + \frac{z_i}{c} + \tan(\theta_c)\frac{\sqrt{(x_i - x_0)^2 + (y_i - y_0)^2}}{c}, \tag{4.15}$$

and using $t_0^* = t_0\, c / \tan(\theta_c)$ and $t_i^* = t_i\, c / \tan(\theta_c) - z_i / \tan(\theta_c)$:

$$t_i^* - t_0^* = \sqrt{(x_i - x_0)^2 + (y_i - y_0)^2}, \tag{4.16}$$

in which the fit parameter t_0^* appears in a linear way, but the parameters x_0 and y_0 do not. By squaring both sides of equation 4.16 and taking the difference with the same equation for a different hit (j), an equation is found in which all three fit parameters appear in a linear way:

$$(t_j^*)^2 - (t_i^*)^2 - 2(t_j^* - t_i^*)t_0^* = x_j^2 - x_i^2 - 2(x_j - x_i)x_0 + y_j^2 - y_i^2 - 2(y_j - y_i)y_0. \tag{4.17}$$

The problem can thus be formulated in matrix form by considering all pairs of consecutive hits:

$$\mathbb{H}\vec{\theta} = \vec{y}, \tag{4.18}$$

with (for a cluster of n hits):

$$\mathbb{H} = \begin{pmatrix} 2(x_2 - x_1) & 2(y_2 - y_1) & -2(t_2^* - t_1^*) \\ 2(x_3 - x_2) & 2(y_3 - y_2) & -2(t_3^* - t_2^*) \\ \vdots & \vdots & \vdots \\ 2(x_1 - x_n) & 2(y_1 - y_n) & -2(t_1^* - t_n^*) \end{pmatrix}, \tag{4.19}$$

$$\vec{y} = \begin{pmatrix} x_2^2 - x_1^2 + y_2^2 - y_1^2 - (t_2^*)^2 + (t_1^*)^2 \\ x_3^2 - x_2^2 + y_3^2 - y_2^2 - (t_3^*)^2 + (t_2^*)^2 \\ \vdots \\ x_1^2 - x_n^2 + y_1^2 - y_n^2 - (t_1^*)^2 + (t_n^*)^2 \end{pmatrix}, \tag{4.20}$$

$$\vec{\theta} = \begin{pmatrix} x_0 \\ y_0 \\ t_0^* \end{pmatrix}. \tag{4.21}$$

There is no exact analytical solution to equation 4.18, since the system of equations is over-determined (the minimum cluster size is 6). However, the optimal solution can be obtained by minimising the χ^2 given by:

$$\chi^2 = (\vec{y} - \mathbb{H}\vec{\theta})^{\mathrm{T}} \mathbb{V}^{-1} (\vec{y} - \mathbb{H}\vec{\theta}), \tag{4.22}$$

with $\mathbb{V}$ the covariance matrix. It is assumed this matrix is diagonal and that the uncertainties in time and position for each hit are the same. A value of 10 ns is assigned for this uncertainty.

The solution to equation 4.18 is given by:

$$\vec{\theta} = (\mathbb{H}^{\mathrm{T}} \mathbb{V}^{-1} \mathbb{H})^{-1} \mathbb{H}^{\mathrm{T}} \mathbb{V}^{-1} \vec{y}, \tag{4.23}$$

and the quality of the fit can be assessed by calculating the χ^2 probability [Metzger, 2002]. The cluster is selected if this probability is higher than 1%.

To reduce the number of accidental clusters due to the optical background even further, a quantity called the surface density of the hits is used [de Jong, 2007b]. The surface density corresponds to the number of hits per unit area and can be calculated by projecting the hits on the plane perpendicular to the muon track. The hits from the muon are then expected to be concentrated around the muon track, whereas the random background hits will be spread over a larger area.

The surface density is then normalised by dividing by a factor $n_{\min}/(0.25\pi R_{\max}^2)$, where $n_{\min} = 6$ is the minimum number of hits required by the MX trigger (so 1 L1 and 5 L0's) and $R_{\max}$ is equal to the maximum transverse distance considered for L0 hits (85 m). Furthermore this normalised surface density is multiplied by the total charge of all hits, exploiting the fact that optical background hits have on average a lower charge than hits from a muon. The resulting parameter is called ρ. By requiring a ρ value of at least 6 the amount of accidental clusters is reduced by a factor of 100.

Since the MX trigger only requires 1 L1 hit, and in addition at least 5 L0 hits, it is more efficient for low neutrino energies. Compared to the 3N trigger, the effiency is almost a factor of 2 higher at 1 TeV, increasing to a factor of about 20 at 10 GeV [Lim, 2011].

4.2.4 *The TQ trigger algorithm*

The TQ trigger applies the MX trigger to an isotropic grid of 105 directions, which coincide with those directions of the 3N trigger that have a negative elevation, see also figure 4.2. The trigger thus only looks for upgoing neutrino-induced muons and not for downgoing muons. Slightly different parameters are used for the MX trigger in this case. At least 2 L1 hits are required and at least 4 additional L0 hits. Also, the minimum ρ value is slightly relaxed; all clusters with $\rho \geqslant 5$ are kept.

Since the TQ trigger applies the loose MX trigger to 105 directions, the trigger rates will rise fast when the optical background increases and this trigger is thus only enabled when the conditions are favourable (i. e. the optical background rates not too high). This can be seen from figure 4.3 which shows the average base line of the PMT counting rate versus the (data) run number, with the runs for which the TQ trigger was enabled in red. It can be seen that when the rates are too high, which generally happens in spring, the TQ trigger is not enabled.

Data from run number 25682 (taken on January 29th 2007) to run number 68170 (taken on November 30th 2012) are used in this work. The first run coincides with the installation of the fifth detetection line (see section 3.2.2) and is the first data run used for physics analyses. The final run is the last data run used in the data analysis as described in the next chapter.

Calculating the fraction of time the TQ trigger is enabled to the total time the detector is running, shows that the TQ trigger is only enabled for 18.8% of the time. This is not a fair comparison

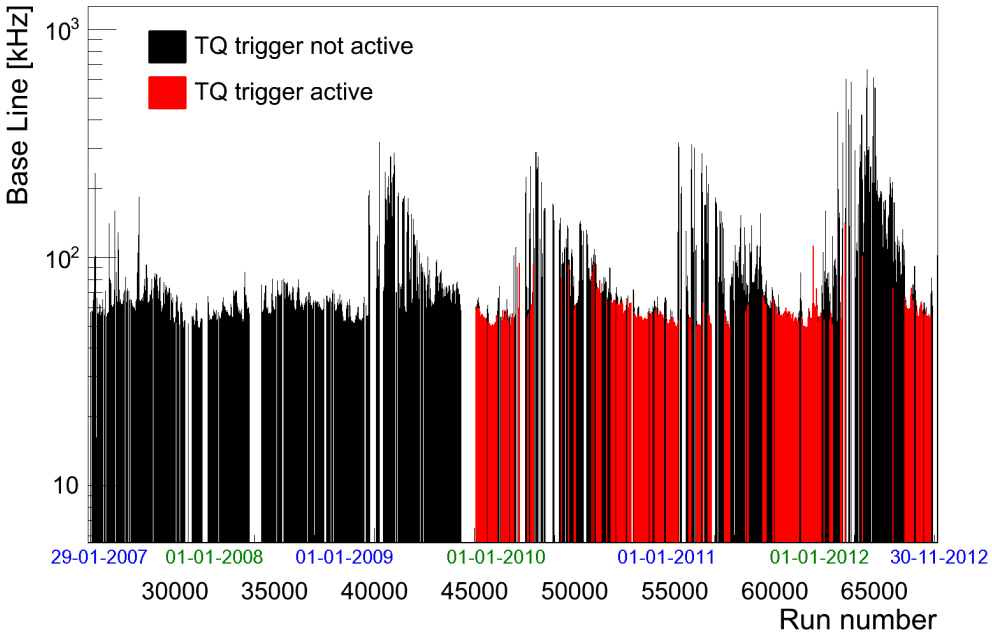

Figure 4.3: The average base line of the PMT counting rate versus data-run number, showing when the TQ trigger is active.

though, since the first data run for which the TQ trigger was available is run 45098, which was taken on December 11th 2009. Recalculating the fraction starting from when the TQ trigger was first available, gives 33.8%.

It should be noted that this fraction could be higher, since there is a subset of runs where the conditions are good, but the TQ trigger has not been enabled. This can be seen from figure 4.4, which shows the distribution of the average base line for all runs in black and those runs for which the TQ trigger is enabled in red, taking only runs after the TQ trigger has first been used. The figure confirms the statement that the TQ trigger is only active when the conditions are favourable; 90% of the TQ trigger runs have an average base line below 60 kHz. However, in only 71% of the total number of runs with an average base line below 60 kHz the TQ trigger has been enabled. If the TQ trigger would have been enabled also in the other 29% of these runs, the trigger would have been active for almost 50% of the total data taking time.

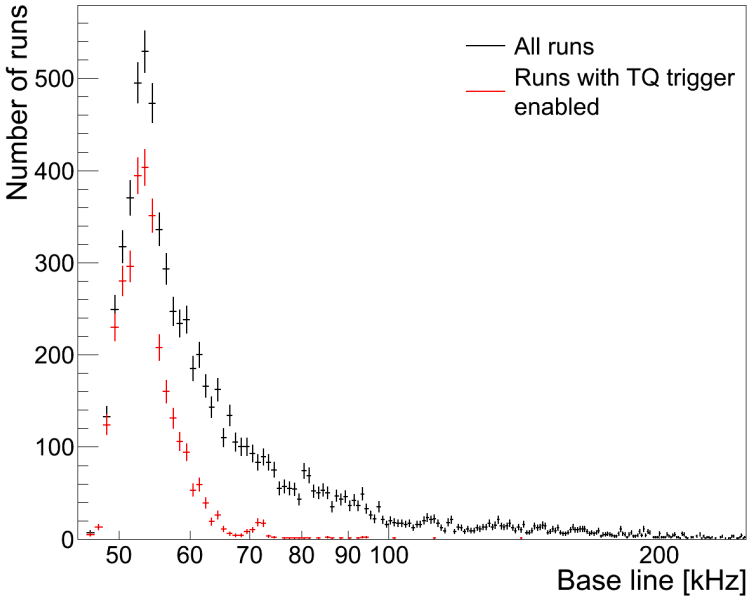

Figure 4.4: Distributions of the average base line.

TQ trigger performance

To quantify the increase in efficiency when using the TQ trigger (compared to the standard 3N and 2T3 triggers), the so-called effective area will be used. The effective area is an important quantity in (neutrino) astronomy and is the area with which the neutrino flux must be multiplied in order to obtain the event rate:

$$R = \int\int \mathrm{d}E_\nu \, \mathrm{d}\Omega \, \Phi_\nu(E_\nu, \theta, \phi) \, A_{\mathrm{eff}}(E_\nu, \theta, \phi), \tag{4.24}$$

with $A_{\mathrm{eff}}(E_\nu, \theta, \phi)$ given by (see equation 4.1):

$$A_{\mathrm{eff}}(E_\nu, \theta, \phi) = \int \mathrm{d}\vec{x} \, \rho(\vec{x}) \, N_{\mathrm{A}} \, \sigma_{\nu\mathrm{N}}(E_\nu) P_\oplus(E_\nu, \theta, \phi) \cdot P_{\mathrm{det}}(E_\nu, \theta, \phi, \vec{x}). \tag{4.25}$$

Using the FXC simulation, the effective area for both the default trigger setup (3N + 2T3 triggers) and for the one with the addition of the TQ trigger (3N + 2T3 + TQ) can be calculated. The effective area as a function of neutrino energy is shown in the left plot of figure 4.5, where the average has been taken for neutrinos and anti-neutrinos. It can be seen that the gain by using the TQ trigger is highest at low neutrino energies, rising to a factor of 2 below

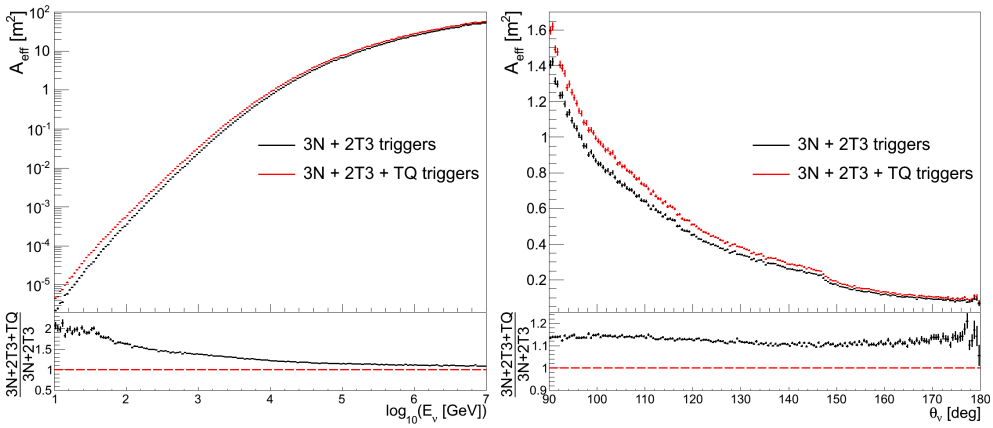

Figure 4.5: Effective area for the default 3N + 2T3 triggers and the default triggers with the TQ trigger added. The average is taken for neutrinos and anti-neutrinos. LEFT: versus energy. RIGHT: versus zenith.

about 30 GeV. Also at higher neutrino energies it is beneficial to use the TQ trigger; the gain being about 20% at 10 TeV.

The right plot in the figure shows the effective areas versus the zenith angle and it can be seen that the total gain by adding the TQ trigger is about 12%, independent of zenith angle.

The gain in terms of event rate depends on the energy spectrum of the neutrinos; the gain will be higher for a softer spectrum than for a harder one, as can be inferred from the left plot of figure 4.5. To quantify this, the cumulative event rates above energies of 100 GeV and 10 TeV are calculated for three different energy spectra: a typical point source spectrum ($\sim E_\nu^{-2}$), the diffuse Galactic spectrum ($\sim E_\nu^{-2.6}$) and the atmospheric neutrino spectrum ($\sim E_\nu^{-3.7}$). Table 4.2 shows the results of these calculations.

ENERGY SPECTRUM	GAIN ABOVE 100 GEV	GAIN ABOVE 10 TEV
Point source ($\sim E_\nu^{-2}$)	21%	16%
Diffuse Galactic ($\sim E_\nu^{-2.6}$)	33%	18%
Atmospheric ($\sim E_\nu^{-3.7}$)	49%	20%

Table 4.2: Gain in terms of event rate by using the 3N + 2T3 + TQ triggers compared to using the default triggers (3N + 2T3).

The gains shown in the table are for when the TQ trigger would be operational 100% of the time. Since the TQ trigger is only active in 18.8% of the runs used for the data analysis, the expected gain in signal for the diffuse Galactic neutrino flux is about 6% when using the TQ trigger. It should be noted however, that the background (atmospheric neutrinos) then also increases by about 9%.

4.3 RECONSTRUCTION

After the trigger algorithms have selected the interesting events, the neutrino direction and energy have to be reconstructed from the hit information. To accomplish this, several reconstruction strategies have been developed which are optimised for a specific neutrino signature.

For neutrino astronomy, the main objective is the reconstruction of the muon direction from the CC interaction of muon neutrinos. Several reconstruction strategies are used in the ANTARES collaboration, of which BBFIT and AAFIT are the most commonly used and are described first in sections 4.3.1 and 4.3.2 respectively. The goal of these reconstruction strategies is to determine the most likely values of the 5 parameters describing the muon track. BBFIT uses a χ^2 approach, while AAFIT maximises a likelihood function.

Within this work, a new track reconstruction strategy has been created, which is optimised to reconstruct low energy neutrinos. This strategy is called GRIDFIT and is described in detail in section 4.3.3. The performance of this new track reconstruction strategy is evaluated by comparing it to AAFIT and BBFIT.

Besides the reconstruction of the direction of the neutrino, the second important parameter that has to be reconstructed is its energy. As discussed in section 2.4.2, the neutrino energy can be used to distinguish the diffuse Galactic signal from the atmospheric neutrino background. The available strategies for the reconstruction of the neutrino energy are described in section 4.3.4.

The reconstruction of NC interactions and of CC electron- and tau-neutrino interactions requires a different approach, since an electromagnetic and/or hadronic shower is created in these interactions, but no muon. The reconstruction of these interactions is called *shower reconstruction*, a brief description of which is given in section 4.3.5.

All plots in this section are based on events which are triggered by the 3N trigger and/or the 2T3 trigger.

4.3.1 *BBFIT*

The BBFIT strategy is developed to provide a fast and robust reconstruction of the muons created in muon-neutrino interactions. BBFIT requires a factor of about 10 less computing time than the full likelihood fit (AAFIT, see next section) [Aguilar et al., 2011c] and is used in online applications like triggering optical follow-up observations or other multi-messenger studies. Since the efficiency for the reconstruction of low energy neutrinos by BBFIT is higher than AAFIT, it is also used for analyses involving, for instance, atmospheric neutrinos [Adrián-Martínez et al., 2012d].

The BBFIT concept is based on the principle that most of the Čerenkov light is seen around the point of closest approach of the muon track to a detector line [Brunner, 2009]. Since the algorithm is designed to run online, the orientations of the OMs are not used. Instead, only time and position information is used, resulting in a simplified geometry. Each storey is considered as a single space point, and hits on OMs on the same storey are combined.

The reconstruction procedure starts with a hit selection; only hits that are selected are used in the subsequent fitting procedure. For the simplified geometry, the hits of the three OMs on a storey are merged if they are closer in time than 20 ns. The time of the earlier hit is taken as the time for the merged hit and the charges of the single hits are added. When hits from different OMs are merged, a bonus charge of 1.5 p.e. is assigned to the merged hit (but only once per merged hit).

Analogously to the L1 hits and T3 clusters used in the triggers, all merged hits with a charge bigger than 2.5 p.e. are called "L1" hits. A "T3" is then defined as the coincidence of two of these "L1" hits within 80 ns for adjacent, and within 160 ns for next-to-adjacent floors (i. e. slightly tighter than used for the 2T3 trigger). Using these "T3" hits as roots, additional hits are searched for in adjacent and next-to-adjacent floors, which are compatible in time with a linear extrapolation of the "T3" hit times along the line. If, for instance, two hits are selected on floors i and $i+1$, with times t_i and t_{i+1} respectively, then the hit time of a hit on floor $i+2$ is assumed to be:

$$t_{i+2} = t_{i+1} + (t_{i+1} - t_i). \tag{4.26}$$

A hit on floor $i+2$ is added to the already selected hits, if it occured in a time window ranging from 10 ns before the time given by equation 4.26 to 10 ns after. If no new hit can be found, neither

in the adjacent nor in the next-to-adjacent floor, the procedure stops and the next "T3" root is considered. Only events with at least 5 hits are selected for the fit.

The hypothesis for the fit is that the selected hits are caused by a muon following a straight trajectory and moving with the speed of light. To build a fit function, three variables have to be calculated. These are the expected arrival time t_{exp} of a Čerenkov photon at a given position along the detector line, its corresponding travel path d_γ and its inclination with respect to the line $\cos\theta_\gamma$. These variables can be calculated from the parameters describing the track, see Aguilar et al. [2011c].

The reconstruction is then based on the minimisation of a quality function given by:

$$Q = \sum_{i=1}^{N_{\text{hit}}} \left[\frac{(t_i - t_{\text{exp}})^2}{\sigma_i^2} + \frac{A(a_i)D(d_\gamma)}{\langle a \rangle d_0} \right], \tag{4.27}$$

which consists of two terms. The standard χ^2 term contains the difference between the measured time of hit i, t_i, and the expected time of this hit, divided by the error on the hit time σ_i. The second term penalises hits with a large charge a_i at large distances from the assumed track. For σ_i a value of 10 ns is taken for hits with a charge higher than 2.5 p.e., and 20 ns otherwise.

The penalty term is not written as a difference between measured and expected amplitude to avoid penalties from hits with a large expected amplitude. Instead, a penalty is given to the combination of high amplitude at large distance, given by the product $A(a_i)D(d_\gamma)$, where:

$$A(a_i) = \frac{a_0 \tilde{a}_i}{\sqrt{a_0^2 + \tilde{a}_i^2}}, \tag{4.28}$$

is the amplitude of the hit corrected for the angular acceptance through:

$$\tilde{a}_i = \frac{2a_i}{\cos\theta_\gamma + 1}, \tag{4.29}$$

and $a_0 = 10$ p.e. is the saturation value, which is obtained when $\tilde{a}_i \gg a_0$. This protects $A(a_i)$ against extreme values of the charge a_i.

A similar method is used for the photon travel distance:

$$D(d_\gamma) = \sqrt{d_1^2 + d_\gamma^2}, \tag{4.30}$$

where $d_1 = 5\,\mathrm{m}$ is the minimum photon travel path, which avoids too strong a pull of the fit to the detector line.

The penalty is divided by the average amplitude $\langle a \rangle$, given by:

$$\langle a \rangle = \frac{1}{N_{\mathrm{hit}}} \sum_{i=1}^{N_{\mathrm{hit}}} \tilde{a}_i, \tag{4.31}$$

to correct for the fact that tracks with a higher energy will produce more light. The factor $d_0 = 50\,\mathrm{m}$ normalises the penalty term and balances it with the χ^2 term.

Depending on the number of lines involved in the hit selection (i. e. the number of lines with at least one "T3"), either a single-line or a multi-line fit procedure is started. For the single-line fits, the azimuth angle of the muon track cannot be determined, since the track geometry is invariant under rotations around the detector line.

When only 2 lines are used for the fit, there always exists an alternative solution that has the same zenith and Q value, but a different azimuth value. To break this degeneracy, a temporary hit selection is performed, where only hits for which the absolute value of the time residual $(t_i - t_{\mathrm{exp}})$ is smaller than 20 ns are selected. The track with the highest weighted charge A_{tot} is then chosen, where:

$$A_{\mathrm{tot}} = \sum_{i=1}^{N_{\mathrm{hit}}} a_i f_{\mathrm{ang}}(\theta_\gamma), \tag{4.32}$$

where $f_{\mathrm{ang}}(\theta_\gamma)$ is the angular acceptance of the PMT, which can be approximated by $\frac{\cos\theta_\gamma + 1}{2}$ (as done in equation 4.29) [Galatà, 2010].

To select well reconstructed events and to discriminate misreconstructed atmospheric muons from neutrinos, the $\tilde{Q}$ parameter can be used, which is defined as:

$$\tilde{Q} = \frac{Q}{N_{\mathrm{dof}}}, \tag{4.33}$$

where N_{dof} is the number of degrees of freedom (the number of hits used in the fit minus the number of fit parameters). Figure 4.6 shows the distribution of $\tilde{Q}$ for both atmospheric neutrinos and misreconstructed atmospheric muons, using only events that are reconstructed as upgoing. It can be seen that by only selecting events with $\tilde{Q} < \tilde{Q}_{\mathrm{cut}}$, a sample can be created of predominantly neutrinos.

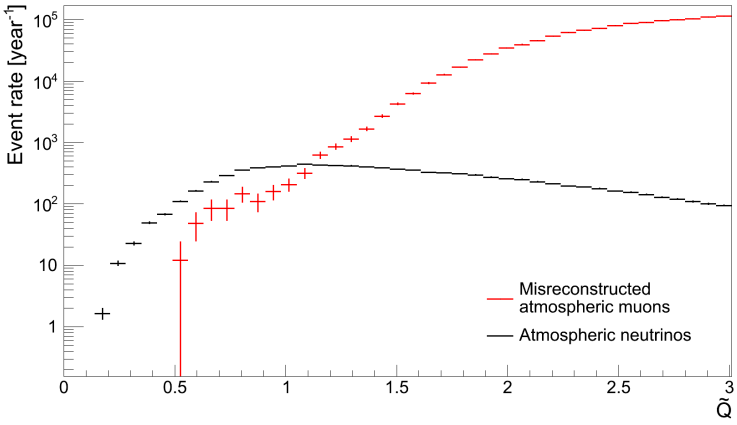

Figure 4.6: Distributions of the $\tilde{Q}$ variable for events reconstructed as upgoing.

To improve the accuracy of the result, an additional fit step is performed for multi-line fits, using the track found by BBFIT as a prefit. A new hit selection is performed, selecting all hits with a time residual smaller than 20 ns with respect to the BBFIT track. These hits are then used to minimise the function:

$$M = \sum_{i=1}^{N_{\text{hit}}} \left[2\sqrt{1 + \frac{(t_i - t_{\text{exp}})^2}{2\sigma^2}} - 2 \right], \tag{4.34}$$

called an M-estimator, which combines the properties of χ^2 and absolute-value minimisation. For small values of the time residual its behaviour is like the χ^2 estimator (see the first term of the sum in equation 4.27), but it becomes linear for large time residuals. This property makes the fit less sensitive to background hits that survive the hit selection, but show large time residuals. For σ a value of 1 ns is chosen, but this value has little impact on the angular resolution [Aguilar et al., 2011c].

The improvement in angular resolution when using the M-estimator can be seen from the distributions shown in figure 4.7. The left plot in the figure shows the distribution of the space-angle error for atmospheric neutrinos. The space-angle error is the angle between the reconstructed (rec) direction and the true (MC) direction of the muon:

$$\begin{aligned}\Delta\alpha \equiv |\alpha_{\text{rec}} - \alpha_{\text{MC}}| = \cos^{-1}(&\sin\theta_{\text{MC}}\cos\phi_{\text{MC}}\sin\theta_{\text{rec}}\cos\phi_{\text{rec}} + \\ &\sin\theta_{\text{MC}}\sin\phi_{\text{MC}}\sin\theta_{\text{rec}}\sin\phi_{\text{rec}} + \cos\theta_{\text{MC}}\cos\theta_{\text{rec}})\end{aligned} \tag{4.35}$$

where θ_i and ϕ_i are the zenith and azimuth of the (reconstructed or MC) track respectively. Only events for which the M-estimator

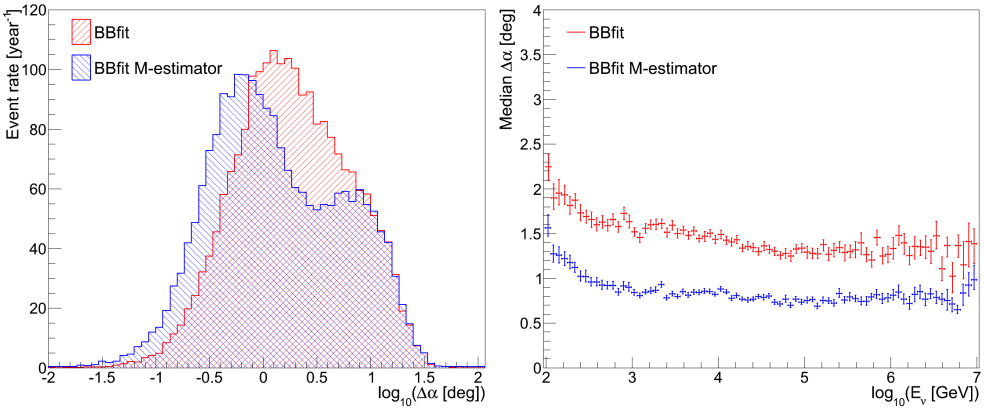

Figure 4.7: LEFT: distributions of the space angle error for atmospheric neutrinos. RIGHT: angular resolution versus neutrino energy.

has been applied (i. e. at least 2 detector lines are used for the reconstruction) are shown in the figure; badly reconstructed tracks are removed by selecting events for which $\tilde{Q} < 1.4$.

The angular resolution is defined as the median of this distribution. The angular resolution is shown versus neutrino energy in the right plot in figure 4.7. Above 1 TeV, the angular resolution is almost independent of energy and improves from about 1.4° for the standard fit to about 0.8° for the M-estimator fit.

Besides a track fit, a bright point fit is also performed, in which the hypothesis of a light source emitting a single flash of light at a given position and time is used. When this fit is applied to hadronic and electromagnetic showers it yields the interaction vertex of the neutrino, see section 4.3.5.

4.3.2 *AAFIT*

The AAFIT reconstruction strategy uses a full likelihood fit to determine the parameters of the muon track and consists of four fit steps [Heijboer, 2004]. The purpose of the first steps is to provide start values for the final likelihood fit that are sufficiently close to the right values.

Like for BBFIT, the reconstruction starts with a hit selection. All hits with an amplitude higher than 3 p.e. and hits in local coincidence are used. A local coincidence is defined as two or more hits on the same storey within 25 ns. Note that this selection

corresponds to the L1 hits, but with a different coincidence time window.

The first fit stage is a linear fit through the positions of the hits. The distance of the muon track to each OM with a hit is estimated using the orientation of the PMT and the amplitude of the hit. It can be expected that an OM recording a high amplitude hit is more likely to be close to the muon track. To obtain a linear relation between the positions of the hits and the track parameters, it is assumed that the hits occur on points along the muon track. The problem can then be formulated in matrix-vector form[20] analogously to equation 4.18:

[20] *Note that the linearisation comes from the assumption that all hits lie on a straight line (the muon track) in this case, while for equation 4.18 the linearisation comes from the assumption on the direction of the muon.*

$$\mathbb{H}\vec{\theta} = \vec{y}, \tag{4.36}$$

with the matrix and vectors given by:

$$\mathbb{H} = \begin{pmatrix} 1 & ct_1 & 0 & 0 & 0 & 0 \\ 0 & 0 & 1 & ct_1 & 0 & 0 \\ 0 & 0 & 0 & 0 & 1 & ct_1 \\ 1 & ct_2 & 0 & 0 & 0 & 0 \\ 0 & 0 & 1 & ct_2 & 0 & 0 \\ 0 & 0 & 0 & 0 & 1 & ct_2 \\ \vdots & \vdots & \vdots & \vdots & \vdots & \vdots \\ 0 & 0 & 0 & 0 & 1 & ct_n \end{pmatrix}, \tag{4.37}$$

$$\vec{y} = (x_1, y_1, z_1, x_2, y_2, z_2, \ldots, z_n)^{\mathrm{T}}, \tag{4.38}$$

$$\vec{\theta} = (p_x, d_x, p_y, d_y, p_z, d_z)^{\mathrm{T}}, \tag{4.39}$$

with p_i and d_i the position and the direction of the track.

The optimal solution to equation 4.36 is given by equation 4.23, which can be found by minimising the χ^2 given by equation 4.22. The covariance matrix contains only the error estimates on the hit positions (which are assumed equal for the x, y and z components); the uncertainties on the hit times are neglected.

The prefit result is only a crude estimate of the track parameters (the median space angle error is about 20°), but it is sufficient as a starting point for the following steps.

To improve the accuracy of the prefit, an M-estimator fit is performed, which is shown to improve the angular resolution (see figure 4.7 for BBFIT). The function that is minimised is:

$$G = \sum_{i=1}^{N_{\text{hit}}} \left[2\kappa \sqrt{1 + a_i (t_i - t_{\text{exp}})^2 / 2} + (1 - \kappa) f_{\text{ang}}(\theta_\gamma) \right], \quad (4.40)$$

where the relative contribution of both terms (the amplitude weighted time residuals and the angular acceptance) is determined by the parameter κ for which the value 0.05 is used.

The sum in equation 4.40 runs over all hits that have a time residual with respect to the prefit between -150 ns and $+150$ ns and are located at most 100 m away from this track. All hits with an amplitude larger than 2.3 p.e. are also selected. The M-estimator fit is only performed when at least 15 hits are selected. The M-estimator greatly improves the angular resolution compared to the prefit; the median space angle error is of the order of a few degrees.

The third step is a Maximum Likelihood (ML) fit, for which the result of the M-estimator fit is used. Hits that have a time residual within[21] $-0.5\,T_{\text{RMS}}$ and $+T_{\text{RMS}}$, where T_{RMS} is the root mean square of the residuals used for the M-estimator fit, are selected; as well as hits with an amplitude above 2.5 p.e. For each set of parameters describing the muon track, the probability to obtain the selected hits can be calculated. This probability is called the likelihood of the event. Assuming the hits are uncorrelated, the likelihood of the event is the product of the likelihood of the hits:

$$L \equiv P(\text{event}|\,\text{track}) = \prod_{i=1}^{N_{\text{hit}}} P(t_i|\,t_{\text{exp}},\, \cos\theta_\gamma,\, d_\gamma,\, a_i), \quad (4.41)$$

in which only the probability of the time of the hits is taken into account. The term in the product is called a PDF.

For the third step a simplified version of the PDF is used, in which the dependence on $\cos\theta_\gamma$, d_γ and a_i is neglected, and the PDF is expressed in terms of only the time residual of the hits. Also the contribution of the optical background hits is not included in this case. The ML estimate of the track is given by the set of track parameters that maximises the likelihood[22].

The last two steps are repeated another 8 times, by rotating and translating the track found by the prefit, to increase the chance of finding the global maximum. Four additional starting points are obtained by rotating the prefit track by 25° around the point on the track closest to the centre of gravity of the hits. By translating

[21] *The interval is not fixed as in the M-estimator hit selection, but rather depends on how close the M-estimator and true tracks are.*

PDF: Probability Density Function

[22] *In practice the maximum value of L is found by minimising $-\log L$, where the logarithm converts the product into a sum.*

the prefit track by $\pm 50\,\mathrm{m}$ in the vertical direction (i. e. straight up and down) and by $\pm 50\,\mathrm{m}$ in the direction perpendicular to both the vertical direction and the direction of the track, four more starting points are obtained. The track with the best reduced likelihood (the likelihood divided by the number of degrees of freedom) is selected as an input for the final reconstruction step. The number of tracks that give the same track direction to within 1° compared to the selected track is called N_{comp} and is used later on for a quality assessment of the track fit.

The track selected in the previous step is used as an input for another ML fit using an improved PDF, which takes the optical background into account and uses the amplitude information of the hits:

$$P(t_i|\, t_{\mathrm{exp}},\, \cos\theta_\gamma,\, d_\gamma,\, a_i) = \frac{1}{N_{\mathrm{tot}}(\cos\theta_\gamma,\, d_\gamma,\, a_i)} \left[P^{\mathrm{sig}}(t_i|\, t_{\mathrm{exp}},\, a_i) N^{\mathrm{sig}}(\cos\theta_\gamma,\, d_\gamma,\, a_i) + R^{\mathrm{bg}}(a_i) \right], \tag{4.42}$$

where $P^{\mathrm{sig}}(t_i|\, t_{\mathrm{exp}},\, a_i)$ is the signal PDF, $N^{\mathrm{sig}}(\cos\theta_\gamma,\, d_\gamma,\, a_i)$ is the expected number of signal hits and $R^{\mathrm{bg}}(a_i)$ is the background rate. The factor $N_{\mathrm{tot}}(\cos\theta_\gamma,\, d_\gamma,\, a_i)$ normalises the PDF and is given by:

$$N_{\mathrm{tot}}(\cos\theta_\gamma,\, d_\gamma,\, a_i) = N^{\mathrm{sig}}(\cos\theta_\gamma,\, d_\gamma,\, a_i) + R^{\mathrm{bg}}(a_i) T, \tag{4.43}$$

where T is the time window in which hits are selected. For the hit selection, all hits with time residuals between $-250\,\mathrm{ns}$ and $+250\,\mathrm{ns}$ with respect to the first ML fit are taken, so $T = 500\,\mathrm{ns}$. All hits with an amplitude larger than 2.5 p.e. are also selected.

Like the $\tilde{Q}$ parameter used in BBFIT to reject the badly reconstructed events, the likelihood of the final ML fit (L^{max}) can be used in AAFIT, since it is expected that events with a higher value of L are better reconstructed. Also N_{comp} can be used, since badly reconstructed events typically have $N_{\mathrm{comp}} = 1$ [Heijboer, 2004]. These two variables are combined to form the Λ-parameter:

$$\Lambda = \frac{\log L^{\mathrm{max}}}{N_{\mathrm{hit}} - 5} + 0.1(N_{\mathrm{comp}} - 1). \tag{4.44}$$

Besides estimates of the track parameters, the fit procedure also provides error estimates. Assuming that the likelihood function follows a Gaussian distribution for all the variables, the (co-)variances can be obtained from the second derivatives of the likelihood function near the maximum. In particular, the esti-

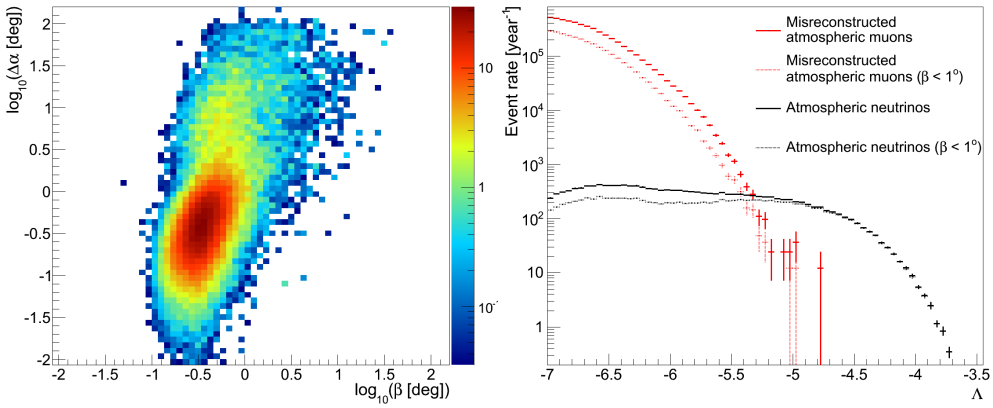

Figure 4.8: LEFT: event rate of atmospheric neutrinos in units of year^{-1} versus β and space angle error, for events with $\Lambda > -5.2$. RIGHT: distributions of the Λ variable for events reconstructed as upgoing.

mated error on the zenith and azimuth angles of the track can be obtained from:

$$\frac{1}{\hat{\sigma}_\theta^2} = -\left.\frac{\partial^2 \log L}{\partial \theta^2}\right|_{L=L^{\max}}, \tag{4.45}$$

$$\frac{1}{\hat{\sigma}_\phi^2} = -\left.\frac{\partial^2 \log L}{\partial \phi^2}\right|_{L=L^{\max}}, \tag{4.46}$$

with the "hat" signifying an estimate[23]. The estimated zenith and azimuth angle errors are combined in the β variable [Heijboer, 2004]:

$$\beta = \sqrt{\sin^2(\hat{\theta})\,\hat{\sigma}_\phi^2 + \hat{\sigma}_\theta^2}, \tag{4.47}$$

which is correlated to the space angle error. This can be seen from the left plot in figure 4.8, which shows the distribution of β versus $\Delta\alpha$ for atmospheric neutrinos, using only events with $\Lambda > -5.2$.

Analogously to figure 4.6 for BBFIT, the distribution of Λ for both atmospheric neutrinos and misreconstructed atmospheric muons, using only events that are reconstructed as upgoing, is shown in the right plot of figure 4.8. It can be seen that Λ can be used to distinguish misreconstructed muons from neutrinos. The β variable can also be used, since applying a cut of $\beta < 1°$ reduces the amount of misreconstructed muons, while the number of well reconstructed neutrinos (i. e. having a high Λ value) is practically unchanged.

[23] *The reconstructed zenith angle is thus denoted by* $\hat{\theta}$.

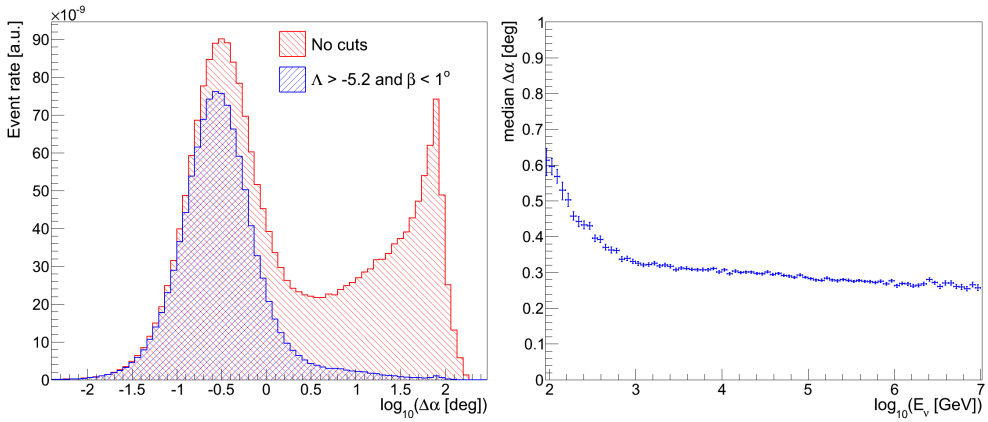

Figure 4.9: LEFT: distributions of the space angle error for E_ν^{-2} neutrinos. RIGHT: angular resolution versus neutrino energy for events passing the point source cuts.

The space angle error distributions are shown in the left plot of figure 4.9. Distributions are shown for all events and events for which $\beta < 1^\circ$ and $\Lambda > -5.2$, which are the cuts applied for the standard point source analysis [Adrián-Martínez et al., 2012a] (which will be referred to as the *point source cuts*). The events are weighted with an E_ν^{-2} spectrum for this figure, since AAFIT is optimised for point source searches for which an E_ν^{-2} spectrum is expected. The angular resolution is shown in the right plot; only for events passing the point source cuts. Above 1 TeV it is nearly independent of energy and is about 0.3°, which corresponds to the intrinsic detector resolution.

4.3.3 *GRIDFIT*

The GRIDFIT strategy is a reconstruction chain developed as part of this work to improve the reconstruction efficiency for low energy neutrinos. Like AAFIT it consists of several fitting steps; three in this case. The first two steps serve to find good starting values of the parameters describing the track, which are necessary for the final likelihood fit. The algorithm will be described first, after which a comparison is made with the existing reconstruction strategies BBFIT and AAFIT.

The algorithm

Like the other reconstruction strategies, also GRIDFIT starts with a hit selection. For GRIDFIT, the Cluster Hit Selection is used [Motz,

2011]. This hit selection is tuned to have a good performance for low energy events. As for the triggers, hits are selected that are close in time and distance. For each hit, a cluster is made of hits that are within a given maximum time and distance window. If the number of hits in such a cluster is larger than a chosen size, the slopes in the $z - t$-plane (with z chosen along the detector line) are calculated between the hit and all other hits that are selected. If the hits are caused by a passing muon, these slopes are expected to be similar (see also [Aguilar et al., 2011c]). Hits for which the slope differs too much from the others are removed until the standard deviation of the slope distribution is below a given value. If the number of hits in the selection is sufficient after the hit removal, the remaining hits are marked for the next step in the hit selection. Besides these hits, hits are also selected if they have a charge larger than a given minimum charge (as is also done in the hit selections for AAFIT and BBFIT).

Three different sub-selections are made, in order to utilise correlations on different scales (see [Motz, 2011] for more details). If a hit is both selected as part of a cluster and exceeds the charge threshold or is selected as part of a cluster in at least two sub-selections, it is selected by the Cluster Hit Selection.

In addition to these hits, all hits are selected that have a charge corresponding to at least 2.5 p.e., which is found to improve the reconstruction accuracy (especially at higher neutrino energies).

After the hit selection, a prefit is performed using the FilteringFit package [Kopper and Samtleben, 2012]. This prefit is based on scanning the whole sky using a given number of isotropically distributed directions. Since a direction is assumed, the track fit problem can be linearised, as is also done for the directional trigger.

The grid of directions is different than that used for the triggers (figure 4.2). It is generated by an algorithm that generates (a, b)-tuples, with $a, b \in [0, 1]$. The zenith and azimuth values are then generated using:

$$\theta = \cos^{-1}(1 - 2a), \tag{4.48}$$

$$\phi = 2\pi b. \tag{4.49}$$

There are different options to generate the (a, b)-tuples, for instance using the scheme from the ANTARES trigger or using a quasi-random generator. Here the (a, b)-tuples are generated by such a generator using the algorithm from Niederreiter [1988]; the other options are found to give comparable results.

For each of the directions a second hit selection is performed using equation 4.14, where the time difference is increased by 5 ns

(as opposed to 20 ns in the trigger) and the maximum transverse distance between the hits is 120 m. The number of hits selected for direction i is called $N_{\text{hits},i}$, which has a minimum value of 4 (since 3 parameters are used for the fitting).

The optimal track is found using equation 4.23 and the χ^2 value is calculated using equation 4.22. For the matrix $\mathbb{H}$ in these equations only the time residuals are used, with the hits ordered in time in such a way as to obtain the largest differences between them. The uncertainty on the hit times is arbitrarily set to 2 ns. The covariance matrix $\mathbb{V}$ is again assumed to be diagonal.

For the FilteringFit prefit 5000 directions are used and the best 9 of these are selected to provide multiple starting points for the final likelihood fit, as is also done in AAFIT. The best directions are selected according to the quality parameter Q:

$$Q = N_{\text{hits}} - w\frac{\chi^2}{N_{\text{hits}} - 3}, \tag{4.50}$$

where w is a weighting factor which determines the relative importance of the number of hits and reduced χ^2 terms. This quality parameter favours solutions which have a large number of clustered hits over solutions with a good reduced χ^2 value, but with a low number of hits. The optimal value of w has been found to be 0.5.

The selection of the best 9 tracks can further be improved by looking at the fraction of hits that can be clustered in the true direction. It has been found that this number is almost always a high fraction of the maximum number of hits found in the grid. At an energy of about 400 GeV, the true direction has at least 80% of the maximum number of hits in ~93% of the events; at an energy of about 200 TeV this is the case in ~80% of the events. So, in the determination of the best 9 tracks, only directions that have at least 80% of the maximum number of hits found are selected.

Since a grid of 5000 directions is used for the prefit, the execution time per event is rather large. It takes on average around 300 ms [Visser and Wagner, 2013] to perform the prefit step per event. For this reason it has been decided to filter out atmospheric muons and only reconstruct those events which are likely neutrino candidates. For this purpose a grid of 500 directions is used to evaluate the GridFit Ratio (R_{GF}) variable, which is defined as:

$$R_{\text{GF}} = \frac{\sum_{\text{UP}} N_{\text{hits},i}}{\sum_{\text{DOWN}} N_{\text{hits},i}}, \tag{4.51}$$

where $\sum_{\text{UP}}$ is performed over all directions with a negative elevation (i. e. directions for which the track is UPgoing) and $\sum_{\text{DOWN}}$ over all directions with a positive elevation.

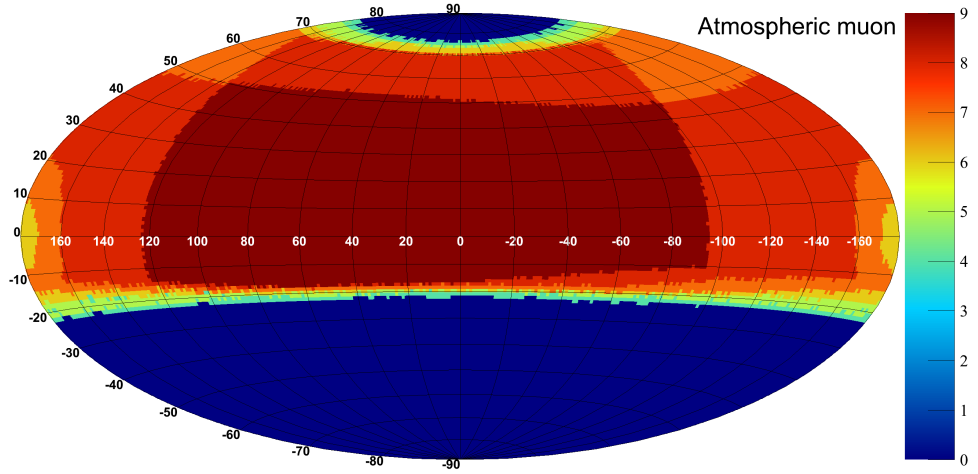

Figure 4.10: Sky-map with the N_{hits} grid for an atmospheric muon.

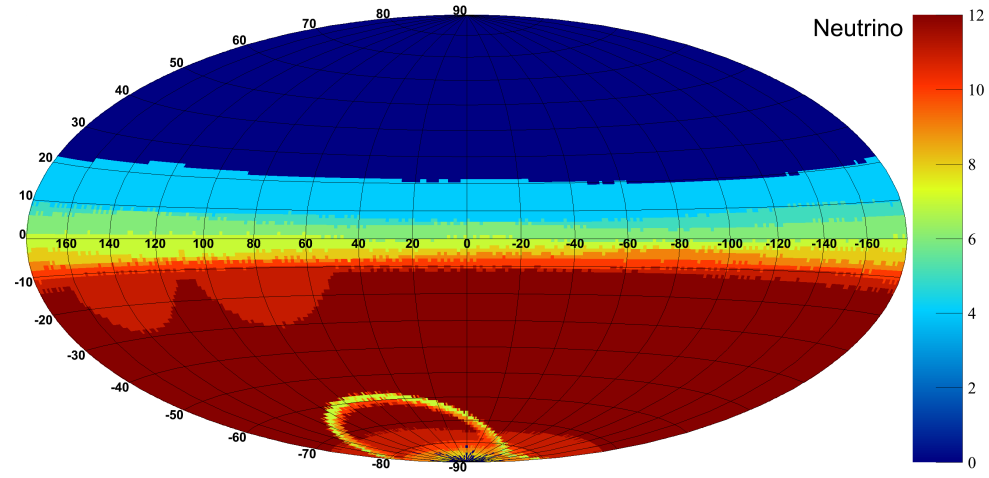

Figure 4.11: Sky-map with the N_{hits} grid for an upgoing neutrino.

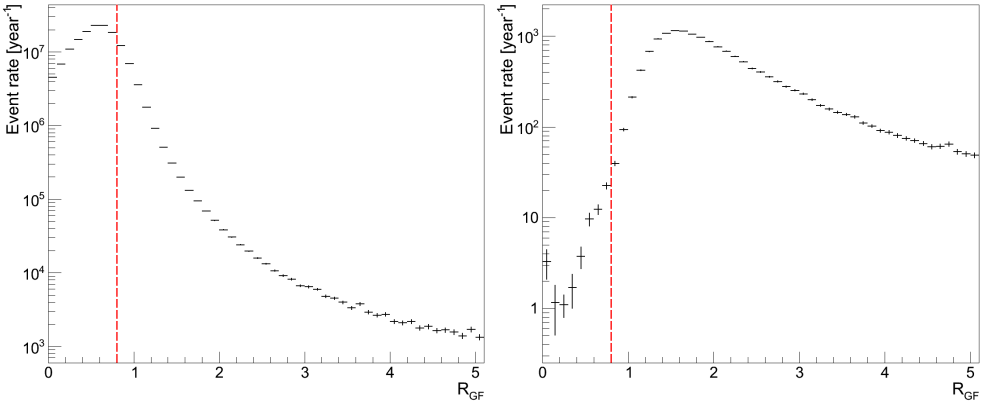

Figure 4.12: Distribution of R_{GF}, the red dashed line indicates the cut value of 0.8. LEFT: for atmospheric muons. RIGHT: for atmospheric neutrinos.

The plots in figures 4.10 and 4.11 show sky-maps of the N_{hits} grid (using azimuth and elevation, as done in figure 4.2) for an atmospheric muon and an upgoing neutrino respectively. It can be seen that for the muon, the number of hits for DOWNgoing directions is higher than for UPgoing directions, which is expected since atmospheric muons are downgoing. For the neutrino it is the other way around; the number of hits for UPgoing directions is higher than for DOWNgoing directions. This information is summarised in the R_{GF} variable: for muons the value is expected to be smaller than 1, while for neutrinos it is expected to be bigger than 1. For the events shown in figures 4.10 and 4.11, $R_{GF} = 0.36$ for the muon and $R_{GF} = 6.77$ for the neutrino.

To filter out atmospheric muons, the R_{GF} variable is used and the reconstruction is performed only for events with $R_{GF} > 0.8$. Figure 4.12 shows the distribution of R_{GF} for both atmospheric muons and neutrinos. The effect of only accepting events with $R_{GF} > 0.8$, is that 81.3% of the atmospheric muons are filtered out and only 0.32% (1.05%) of the atmospheric (E_ν^{-2}) neutrinos.

The angular resolution of the prefits is limited to a couple of degrees, because the points are separated by about 3° in a grid of 5000 points. To improve the angular resolution of this prefit, an M-estimator fit is performed for each of them, as is done in AAFIT and BBFIT. The implementation is identical to the implementation in AAFIT. First a hit selection is performed, selecting all hits that have an absolute time residual smaller than 150 ns with respect to the prefit and are at most 100 m away from it. In addition all hits with an amplitude of at least 2.3 p.e. are

kept. Like in AAFIT, the M-estimator fit is only performed if at least 15 hits are selected.

The effect on the space angle error can be seen from figure 4.13, in which the distribution of the space angle error is shown for the different fit steps. For this, the chosen final track (and corresponding prefit) is used. Since the same M-estimator (and PDF, see below) are used as in AAFIT, the events are again weighted with an E_ν^{-2} spectrum. From the figure it can be seen that using the M-estimator is beneficial, since it improves the angular resolution of the prefit substantially.

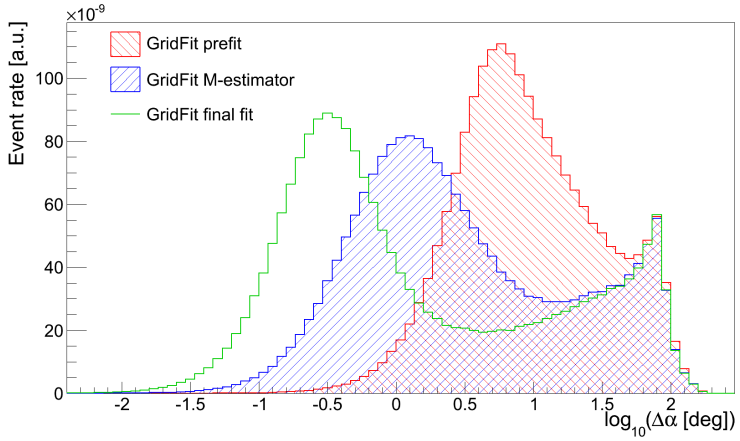

Figure 4.13: Distributions of the space angle error for the chosen final track for E_ν^{-2} neutrinos.

The results of the prefit are used for a final likelihood fit, for which the same PDF is used as in AAFIT (see equation 4.42). It should be noted that only one likelihood fit step is performed here, unlike in AAFIT where two PDF fit steps are performed. In GRIDFIT the first PDF fit step is not performed and the M-estimator results are immediately used for the final likelihood fit. The hit selection is also different than in AAFIT and similar to that of the M-estimator fit. All hits that have an absolute time residual smaller than 150 ns and a maximum distance of 120 m are selected. Since the 9 best tracks from the FilteringFit prefit are chosen, this gives 9 hit selections. These hit selection are merged into one final hit selection. Then, for each prefit the final likelihood fit is performed, using the parameters from the prefit as starting values. The improvement in the space angle error can be seen in figure 4.13.

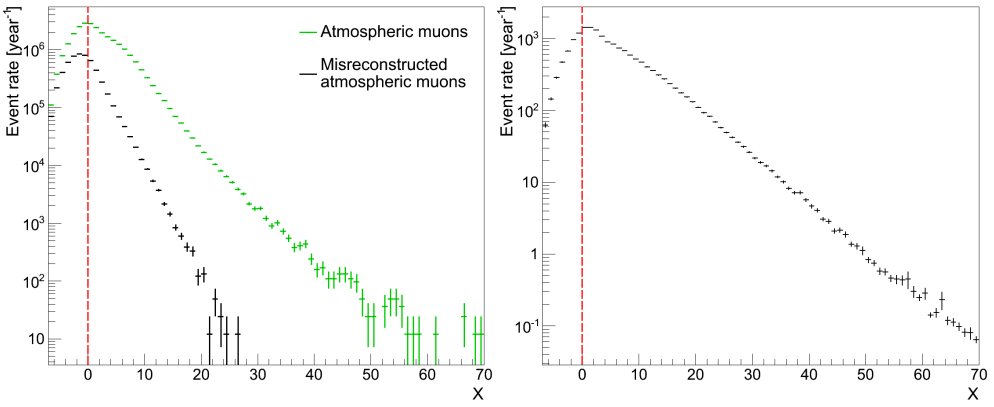

Figure 4.14: Distribution of X, the red dashed line indicates the cut value of 0. LEFT: for atmospheric muons. RIGHT: for atmospheric neutrinos.

Out of the 9 PDF fits, the track with the highest value of X is selected as the final fit result, where X is defined as:

$$X = N_{\text{hits, ff}} + w_x \frac{\log L^{\max}}{N_{\text{hit}} - 5}. \tag{4.52}$$

This selection criterion is similar to the quality parameter Q used in FilteringFit (see equation 4.50) and was found to give good results in selecting the track with the smallest space angle error with respect to the true direction.

Like w in equation 4.50, the weighting factor w_x determines the relative factor between the number of hits close to the final track ($N_{\text{hits, ff}}$) and the reduced log-likelihood (which is the same as in equation 4.44)[24]. The optimal value for the parameter w_x is found to be 1.1, although it should be pointed out that the quality of the reconstruction is stable under small variations [Visser and Wagner, 2013].

[24] *Note that the reduced log-likelihood is negative, hence the '+' in front of the term.*

The number of hits close to the final track in equation 4.52 is determined as follows. Starting with the hits used as input to the final likelihood fits, those hits are selected that have an absolute time residual smaller than 5 ns and a maximum distance of 70 m. This hit selection is very tight and serves to select only those hits that are consistent with the track hypothesis; any background hits that might have been in the hit selection and any hits not consistent with the found track, are thus filtered out.

From equation 4.52 it can be seen that the value of X can become negative. This mostly happens when only a few hits are found to be close to the track. All events for which the value of

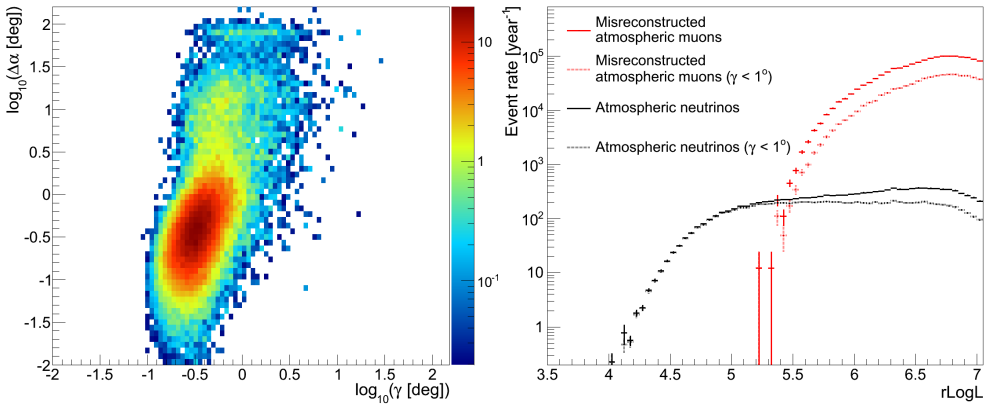

Figure 4.15: LEFT: event rate of atmospheric neutrinos in units of year^{-1} versus γ and space angle error, for events with rLogL > 5.4. RIGHT: distributions of the rLogL variable for events reconstructed as upgoing.

X is negative for all 9 fits, are rejected, since these events were found to be mostly misreconstructed. This can be seen from figure 4.14, which shows the distribution of X for (misreconstructed) atmospheric muons on the left and for atmospheric neutrinos on the right.

By rejecting events with a negative value of X, 22.6% of the atmospheric neutrinos are rejected (4.8% for an E_ν^{-2} flux), 39.0% of the atmospheric muons and 67.2% of the misreconstructed atmospheric muons. It should be pointed out that almost all the events that are rejected by this cut on the X-parameter would also have been cut away when applying quality cuts.

Rejecting misreconstructed muons

Just like the Λ parameter for AAFIT and the $\tilde{Q}$ parameter for BBFIT, the rLogL parameter (which is defined to be minus the reduced log-likelihood from equation 4.52 and so is positive) can be used in GRIDFIT to reject the badly reconstructed events. This can be seen from the right plot in figure 4.15, in which the distribution of rLogL for atmospheric neutrinos and misreconstructed atmospheric muons is shown.

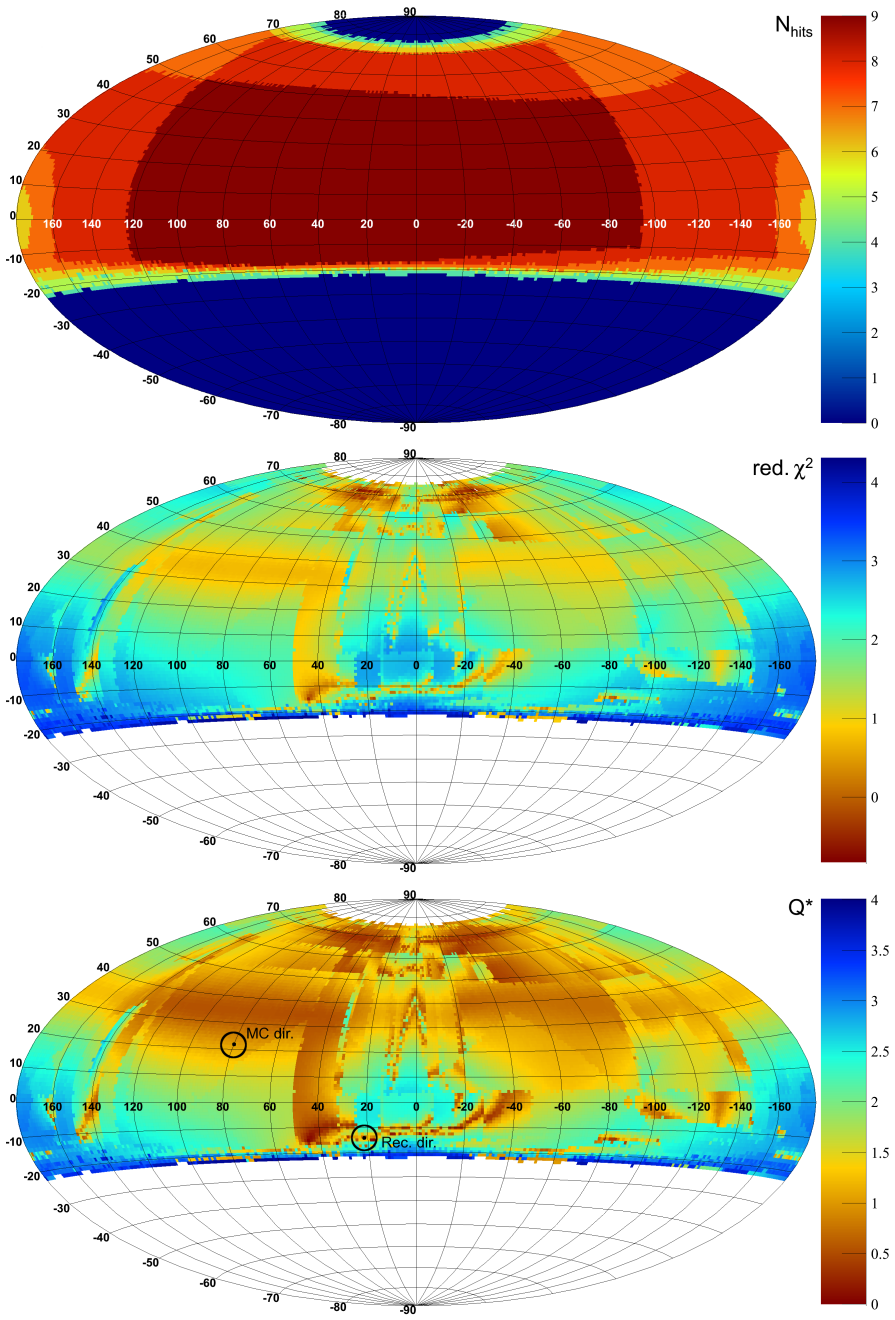

Figure 4.16: Sky-maps for a misreconstructed muon. TOP: N_{hits}. MIDDLE: $\log_{10}$ of the reduced χ^2. BOTTOM: $\log_{10}$ of $Q^* = -Q + C$, where C is the maximum found value of Q plus 1. This is done so that the Q^*-scale always starts at 1.

The estimated error on the zenith and azimuth angles of the track is also calculated in GRIDFIT. Unlike AAFIT this is done by determining the ellipse in the two dimensions of the track directions where the log-likelihood value is 1/2 lower than the found maximum value of the likelihood (which gives the 1σ confidence interval on the directions). This ellipse is determined by defining a new coordinate system, in which the track direction points to the direction with $\theta = 90^\circ$ and $\phi = 0^\circ$, where the distortion of the angles is minimal and the coordinates can be considered Cartesian. Using a Gaussian approximation, the likelihood landscape around the maximum can be considered a paraboloid. The parameters of this paraboloid are fitted using an analytic χ^2 minimisation and used to determine the zenith and azimuth angle errors. See the paper by Neunhöffer [2006] for more information.

The estimated zenith and azimuth angle errors are combined in the γ variable:

$$\gamma = \sqrt{\hat{\sigma}_\phi^2 + \hat{\sigma}_\theta^2}, \tag{4.53}$$

where the fact has been used that the coordinates are almost Cartesian. This variable is very similar to β from AAFIT, and is correlated to the space angle error, as can be seen in the left plot in figure 4.15. For this plot, only events are used for which rLogL > 5.4 (see also the corresponding plot in figure 4.8).

In addition to the rLogL and γ variables, also the R_{GF} variable can be used to reject misreconstructed muons. For this, the same atmospheric muon event as in figure 4.10 is considered. The sky-map of the number of hits found for each direction is shown again in figure 4.16, together with sky-maps of the corresponding reduced χ^2 and Quality grids. Although this is an atmospheric muon event, the reconstructed direction is found in the UPgoing part and the event should thus be classified as misreconstructed. It turns out that, besides filtering out atmospheric muon events, the R_{GF} variable can also be used to reject misreconstructed atmospheric muons. This can also be seen when looking at the distribution of this variable for neutrinos compared to misreconstructed atmospheric muons, which is shown in the left plot of figure 4.17. By taking only events with $R_{\mathrm{GF}} > 1.5$ for instance, 92.2% of the surviving misreconstructed muons is rejected and only 20.0% of the (atmospheric) neutrinos. Note that the R_{GF} variable by itself is not sufficient to get rid of all the misreconstructed muons. It has to be used in combination with the other two parameters (rLogL and γ) described previously.

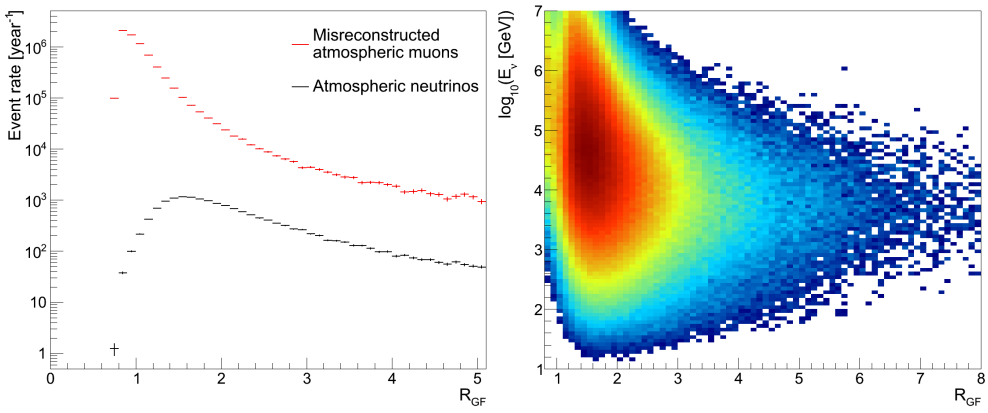

Figure 4.17: LEFT: distributions of R_{GF}. RIGHT: distribution of the event rate of neutrinos (in arbitrary units) versus R_{GF} and neutrino energy.

Although a naive application of R_{GF} works quite well, there is more to gain by looking at its energy and zenith dependence. The right plot in figure 4.17 shows the distribution of R_{GF} versus the true energy of the neutrinos. It can be seen that for higher energies the distribution is more centred around 1.0, while for lower energies there is a large tail towards large values of R_{GF} present. The explanation for this is that the neutrino-induced muons produce more hits at higher energies, so that more hits can be clustered both for upgoing as downgoing directions. Since both the numerator and denominator in equation 4.51 are larger in this case, the value of R_{GF} will be close to 1.0. This effect implies that the R_{GF} variable is not very efficient at high neutrino energies.

To compensate, the cut on R_{GF} can be made dependent on the number of hits used for the final fit, which is a (albeit rudimentary) measure for the energy of the particle in the event. Analogously to how the $\tilde{Q}$ variable of BBFIT is adapted to recover high energy events [Aguilar et al., 2011c], the R_{GF} variable can be adapted as well to make it more efficient for higher energies:

$$R_{\#} = R_{GF} + [0.02 \cdot (N_{\text{hits, ff}} - 5)]^2 , \tag{4.54}$$

for $N_{\text{hits, ff}} > 4$. The effect of this cut can be seen in figure 4.18, in which the event rate distributions versus R_{GF} and $N_{\text{hits, ff}}$ are shown for atmospheric neutrinos and misreconstructed atmospheric muons. For the figure $R_{\#} > R_{\#,\text{cut}} = 1.4$ has been chosen. It can be seen that most of the misreconstructed atmospheric muons are rejected, while most of the neutrino events are kept.

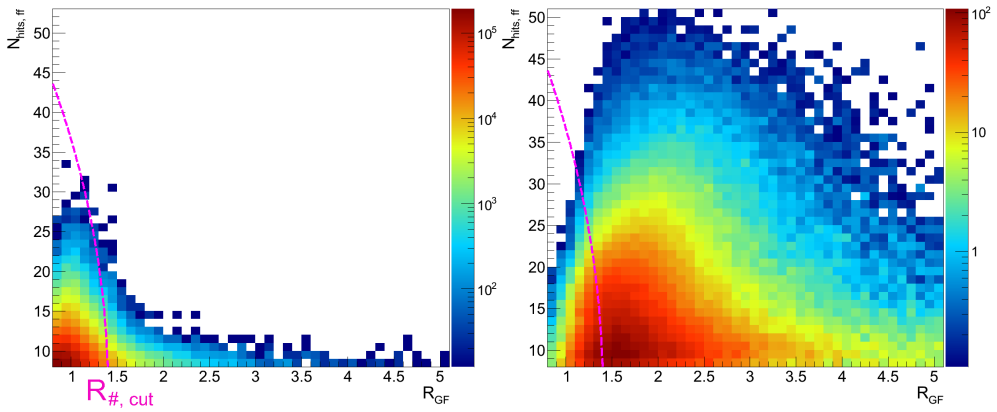

Figure 4.18: Event rate in units of year^{-1} versus R_{GF} and $N_{\text{hits,ff}}$. The purple dashed line represents the cut at $R_{\#} > 1.4$. Note that the colour scales are different for both plots. LEFT: for misreconstructed atmospheric muons. RIGHT: for atmospheric neutrinos.

Figure 4.19 shows the event rate distributions versus R_{GF} and the reconstructed zenith angle. By comparing the left plot (for misreconstructed atmospheric muons) with the right plot (for atmospheric neutrinos), it can be seen that the value of R_{GF} is higher for events that are reconstructed more vertical. This can be understood by the fact that it is more difficult to cluster hits in a downgoing direction if the event is straight upgoing, than it would be when the event would be more horizontal. By adapting the R_{GF} variable, this feature can be utilised:

$$R_\theta = R_{\text{GF}} - R_{\text{diff}} \frac{\hat{\theta}\,[\text{deg}] - 90^\circ}{90^\circ}, \tag{4.55}$$

where R_{diff} determines the slope in the R_{GF}-$\hat{\theta}$-plane. A value of about 1.5 is found to be optimal. Only events with a reconstructed zenith angle of at least 90° are considered, since the focus lies on neutrino events. The effect of adjusting R_{GF} like this is illustrated in figure 4.19, where $R_\theta > R_{\theta,\text{cut}} = 1.0$ has been chosen.

In the following sections, GRIDFIT is compared to BBFIT and AAFIT, and the R_{GF} variable will be used in addition to rLogL and γ to reject misreconstructed atmospheric muons.

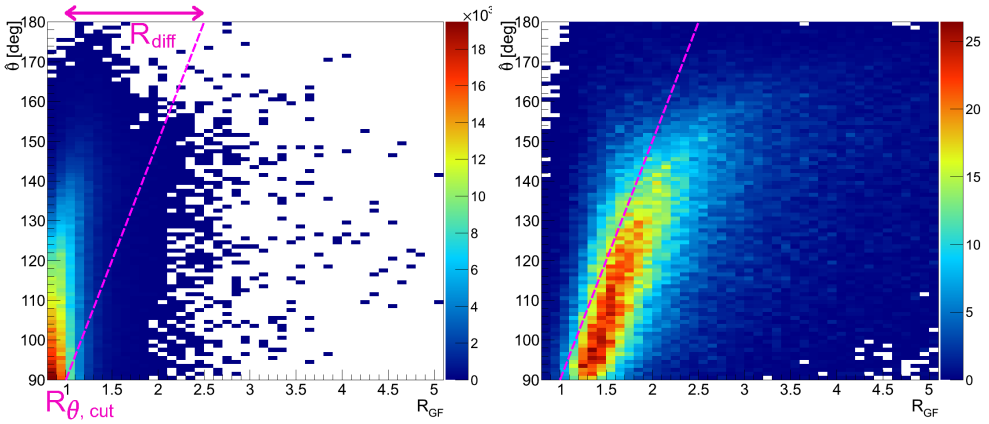

Figure 4.19: Event rate in units of year^{-1} versus R_{GF} and reconstructed zenith angle. The purple dashed line represents the cut at $R_\theta > 1.0$. Note that the colour scales are different for both plots. LEFT: for misreconstructed atmospheric muons. RIGHT: for atmospheric neutrinos.

Comparing reconstruction strategies

In order to compare reconstruction strategies, the cuts on the variables are tuned in such a way as to obtain the same purity. The purity is defined as the percentage of neutrinos in the obtained event sample, which contains both neutrinos (atmospheric neutrinos, neutrinos from for instance point sources, or from some other signal) and atmospheric muons:

$$\mathcal{P} = \frac{N_{\nu_\mu+\overline{\nu}_\mu}}{N_{\nu_\mu+\overline{\nu}_\mu} + N_\mu} \cdot 100\%, \tag{4.56}$$

where $N_{\nu_\mu+\overline{\nu}_\mu}$ is the number of muon-neutrinos plus anti-neutrinos surviving the cuts and N_μ is the number of atmospheric muons surviving. If multiple cut combinations result in the same purity, the combination yielding the largest number of neutrinos is taken.

It is straightforward to obtain the number of atmospheric (anti-) neutrinos from the MC simulation by simply counting the number of events that survive the cuts. Determining the number of atmospheric muons is more tricky, since generally only a few of them will survive the applied cuts. The low statistics of the final sample of atmospheric muons results in a relatively large statistical error. It is also possible that no muon event survives the applied cuts at all. In order to still get an estimate of the number of atmospheric muons and reduce the error in case only a few survive, the following approach is taken. All cuts are applied,

except the cut on the track quality parameter (rLogL for GRIDFIT, $\tilde{Q}$ for BBFIT and Λ for AAFIT). The tail of the cumulative distribution of the track quality parameter is then fitted with an exponential function[25]:

$$N_\mu = 10^{C_1 + q\,C_2}, \tag{4.57}$$

where C_1 and C_2 are fit parameters and q is the track quality parameter. The number of atmospheric muons can then be obtained by inserting the chosen cut value of the track quality parameter in equation 4.57. The error on the number of atmospheric muons can also be determined and is given by:

$$\delta N_\mu = N_\mu \cdot \ln 10 \cdot \sqrt{(\delta C_1)^2 + (q\,\delta C_2)^2 + 2\,\rho\,q\,\delta C_1 \delta C_2}, \tag{4.58}$$

where δC_i is the error on parameter i and ρ is the correlation coefficient, which are all obtained from the fit. Examples can be found in figures 4.20, 4.22 and 4.25.

The strategies are then compared using two figures of merit. These are the effective area (equation 4.25), for which the average is taken for neutrinos and anti-neutrinos and the angular resolution (equation 4.35).

[25] *It should be pointed out that the tail of the distribution can sometimes also be well fitted with a Gaussian function, which falls off faster and would thus result in a lower number of muons. However, the exponential function will give a more conservative result and will always be used.*

Comparison with BBFIT

In the ANTARES collaboration, the BBFIT strategy is used for analyses focusing on low energy neutrinos, such as the neutrino oscillation analysis [Adrián-Martínez et al., 2012d]. The cuts used in the neutrino oscillation analysis are used here for BBFIT, which will be referred to as the *oscillation cuts*:

- $\cos\hat{\theta} < -0.15$
- For single-line events:
  - $N_{\text{hit}} > 7$
  - $\tilde{Q} < 0.95$
- For multi-line events:
  - $N_{\text{hit}} > 5$
  - $\tilde{Q} < 1.3$ (4.59)

Atmospheric neutrinos are used as signal for the oscillation analysis, so all plots in this section are made for atmospheric neutrinos. In the analysis only the standard BBFIT reconstruction is used; the M-estimator fit is not applied.

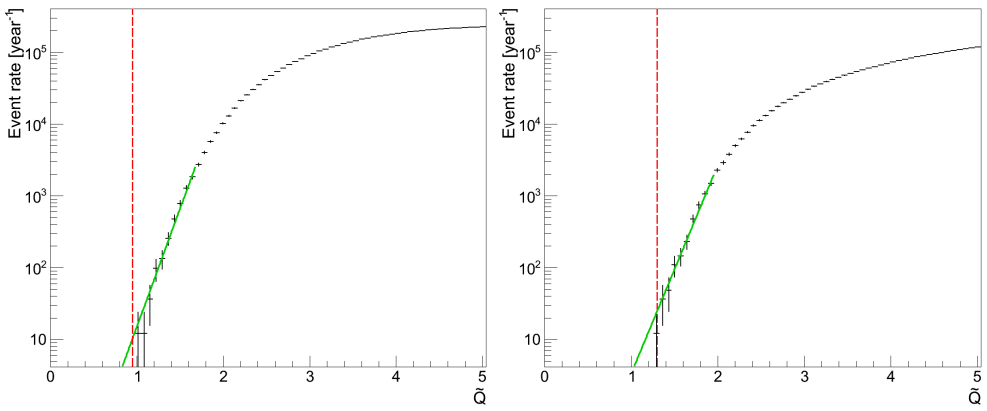

Figure 4.20: Cumulative event rate distribution of the BBFIT $\tilde{Q}$ variable for atmospheric muons. The red dashed line represents the cut. LEFT: for single-line events. RIGHT: for multi-line events.

Using the oscillation cuts, 2110 ± 10 atmospheric neutrinos survive per year (447 ± 7 single-line events and 1660 ± 10 multi-line events). The cumulative muon event rates are shown in figure 4.20. Using the result of the fit, 14 ± 2 single-line events survive per year and 25 ± 5 multi-line events. This gives a purity of $\mathcal{P} = 98.4 \pm 0.3\%$. The effective area is shown in figure 4.21, in which also the contributions of the single-line and multi-line events are shown. It can be seen that the single-line events contribute mostly at low energy, while the multi-line events contribute mostly at high energy.

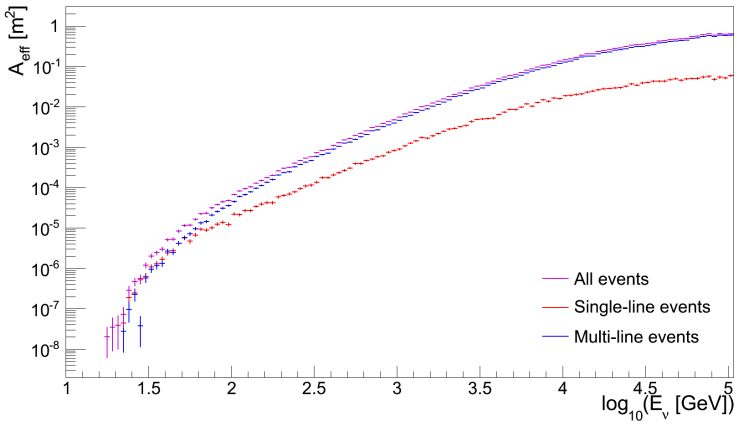

Figure 4.21: Effective area of BBFIT for events passing the oscillation cuts.

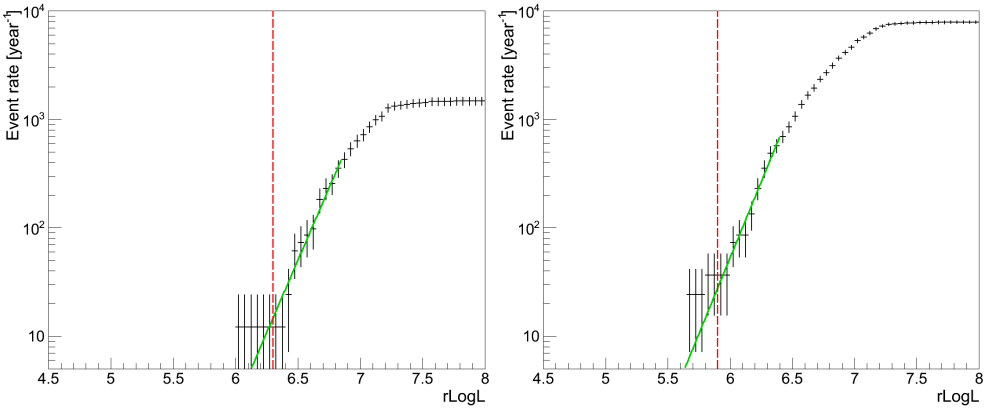

Figure 4.22: Cumulative event rate distribution of the GRIDFIT rLogL variable for atmospheric muons. The red dashed line represents the cut. LEFT: for events passing the Low Energy cuts. RIGHT: for events passing the Recovery cuts.

To obtain the same purity for GRIDFIT and in addition a good efficiency at low energies, a tight cut on R_{GF} will be used, since this variable has been shown to work well for rejecting misreconstructed muons and simultaneously keeping low energy neutrino events. The value of the cut on R_{GF} is varied, after which the rLogL parameter is tuned to obtain a purity similar to BBFIT. It is found that the following cut combination gives good results, which will be referred to as the *Low Energy cuts*:

- $\cos\hat{\theta} < 0$
- rLogL < 6.3
- $\gamma < 20.0^{\circ}$
- $R_{\mathrm{GF}} > 3.5$ (4.60)

As remarked before, the R_{GF} variable works well at low energies, so a tight cut can be placed on it. For low energy events the rLogL value is not that good in general, so it is best to keep this cut as loose as possible. The γ cut is very loose, since the angular resolution is not expected to be important at low energies. Still, this cut is beneficial, since it reduces the amount of misreconstructed atmospheric muons. Applying these cuts, there are 573 ± 9 atmospheric neutrinos surviving per year and 15 ± 2 misreconstructed atmospheric muons (see also the left plot in figure 4.22, in which the cumulative muon event rates are shown for GRIDFIT).

Although the Low Energy cuts work very well at the lowest energies, the efficiency is quite low for higher energy events. This can be seen in figure 4.23, which shows the effective area for events passing the Low Energy cuts in orange. The reason for this is the very strict cut on R_{GF}. To recover the higher energy events, also events passing the following cut combination are kept (this will be referred to as the *Recovery cuts*):

- $\cos\hat{\theta} < 0$
- rLogL < 5.9
- $\gamma < 20.0^{\circ}$
- $R_{\#} > 2.0$ (4.61)

where the value of the cut on rLogL is chosen such that the purity of GRIDFIT is the same as obtained for BBFIT.

This gives an additional 1940 ± 10 atmospheric neutrinos per year and an extra 28 ± 3 misreconstructed atmospheric muons (see also the right plot in figure 4.22). From figure 4.23 it can be seen that this cut does indeed recover the higher energy events.

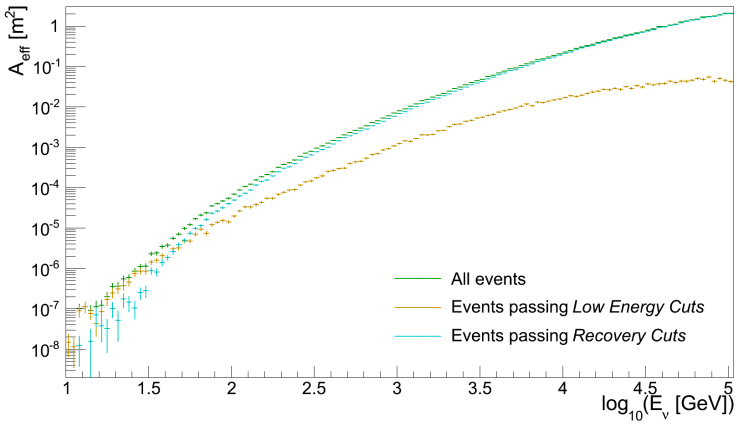

Figure 4.23: Effective area of GRIDFIT for events passing the Low Energy Optimised cuts.

The combination of the Low Energy cuts and the Recovery cuts will be called the *Low Energy Optimised cuts*. For these cuts, the total rate of atmospheric neutrino events is 2510 ± 10 per year and the total rate of misreconstructed atmospheric muons is 43 ± 3 per year. This gives a purity of $\mathcal{P} = 98.3 \pm 0.1\%$. When comparing the number of neutrinos reconstructed by GRIDFIT to the amount reconstructed by BBFIT, it can be seen that GRIDFIT

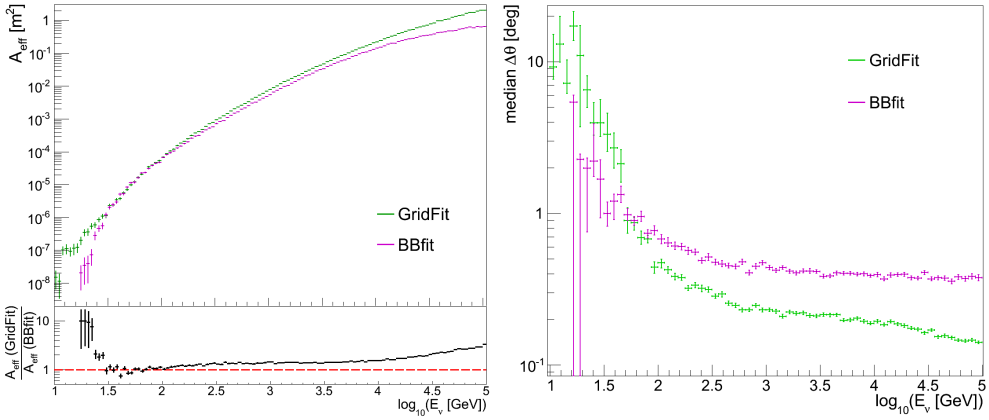

Figure 4.24: Comparison between BBFIT and GRIDFIT. LEFT: effective area versus neutrino energy. RIGHT: zenith resolution versus neutrino energy.

reconstructs almost 20% more neutrinos for the same purity of the final sample.

A more detailed comparison shows that GRIDFIT outperforms BBFIT over almost the whole energy range, with the biggest increase in effective area reached at the lowest energies. It is also important to note that events with energies as low as 10 GeV are reconstructable, although the event rates will of course be limited. This can be seen from the left plot in figure 4.24, which shows the effective areas for both reconstruction strategies together. The effective area of GRIDFIT is comparable to the one for BBFIT in the region from ~35 GeV to ~65 GeV, which is the overlap region of both cut combinations (see also figure 4.23).

The zenith angle resolution[26] is shown for both strategies in the right plot of figure 4.24. For energies above ~50 GeV the zenith resolution of GRIDFIT is better than for BBFIT . For lower energies the zenith resolution of BBFIT is slightly better. The reason for this is the loose cuts on the reconstruction quality and angular resolution estimate, which are required to boost the effiency at these energies. More neutrinos survive in the final event sample, but their direction is not reconstructed as well. It should be noted that the angular resolution is not expected to be important for these low energies. Furthermore, the events reconstructed by GRIDFIT have some azimuth angle information, whereas the single-line events from BBFIT do not. The azimuth resolution is quite poor at the lowest energies, but it is better than a random guess [Visser and Wagner, 2013].

[26] *The zenith angle resolution is compared here instead of the angular resolution, since the single-line events from BBFIT do not have any azimuth information.*

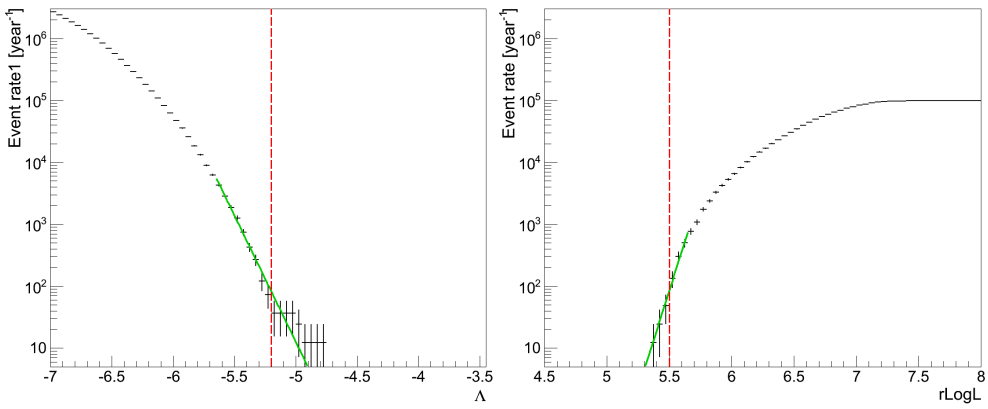

Figure 4.25: Cumulative event rate distribution for atmospheric muons. The red dashed line represents the cut. LEFT: Λ for AAFIT. RIGHT: rLogL for GRIDFIT.

Comparison with AAFIT

Even though GRIDFIT has been optimised for low energies, it is interesting to see how its performance compares to AAFIT. Again, the cuts of both reconstruction strategies are tuned in such a way as to obtain the same purity and after that the effective area and angular resolution are compared.

For AAFIT the point source cuts are used:

- $\cos\hat{\theta} < 0$
- $\Lambda > -5.2$
- $\beta < 1.0^\circ$ (4.62)

In this analysis the assumed signal consists of E_ν^{-2} neutrinos, so all plots are made for neutrinos following this energy spectrum.

Using these cuts 2610 ± 10 atmospheric neutrinos survive per year and 83 ± 9 atmospheric muons, see the left plot in figure 4.25, in which the cumulative muon event rates are shown. This gives a purity of $\mathcal{P} = 96.9 \pm 0.4\%$. The purity obtained here differs from the one given in the paper [Adrián-Martínez et al., 2012a], where it is found to be about 87%. This difference can be explained by the fact that here a perfect detector is considered with 60 kHz background, whereas in the paper more realistic conditions are considered.

To obtain the same purity for GRIDFIT, different combinations of γ and R_{GF} are considered, after which the rLogL cut is tuned in such a way that the purity of GRIDFIT is the same as that ob-

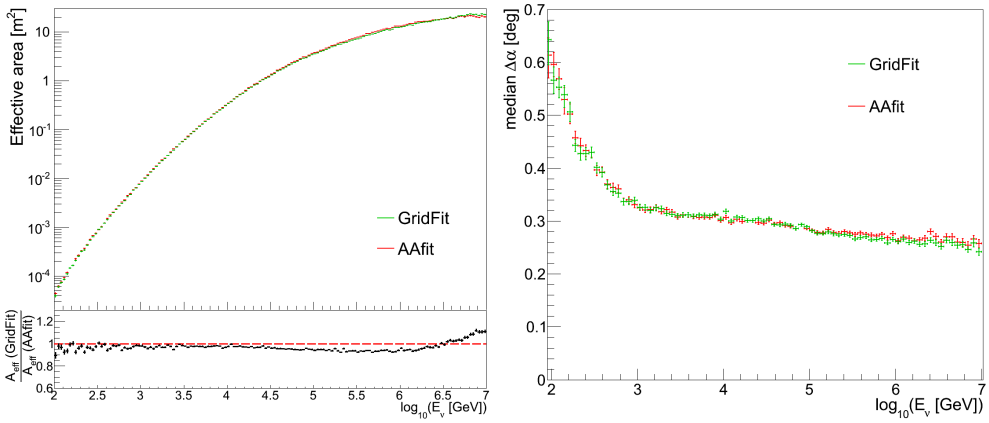

Figure 4.26: Comparison between AAFIT and GRIDFIT. LEFT: effective area versus neutrino energy. RIGHT: angular resolution versus neutrino energy.

tained for AAFIT. In the end it was determined that the following combination gives the best results:

- $\cos\hat{\theta} < 0$
- rLogL < 5.5
- $\gamma < 1.0^{\circ}$
- $R_{\#,\theta} > 0.95$ (4.63)

where R_{GF} is made dependent on both the number of hits used for the final fit and the reconstructed zenith angle (called $R_{\#,\theta}$).

This leaves 2490 ± 10 atmospheric neutrinos and 85 ± 9 misreconstructed atmospheric muons per year (see the right plot in figure 4.25), giving a purity of $\mathcal{P} = 96.7 \pm 0.4\%$.

The left plot in figure 4.26 shows the effective areas for AAFIT (in red) and GRIDFIT (in green). It can be seen that AAFIT and GRIDFIT perform equally well up to 30 TeV; the effective area of AAFIT is about 3% higher. Between 30 TeV and 1.5 PeV the effective area of GRIDFIT is about 7% lower. At the very highest energies, above about 3 PeV, GRIDFIT performs better than AAFIT, yielding an increase in effective area of about 10% at 10 PeV. From the right plot in the figure it can be seen that the angular resolution is essentially the same for both strategies.

It is interesting to point out that not all events found by using GRIDFIT are also found by using AAFIT, and vice versa. For the cut combinations given above, about 7.5% of the triggered events are reconstructed by GRIDFIT and pass the applied cuts, but are not selected by AAFIT. Vice versa, about 9.5% of the triggered

events are selected by AAFIT but not by GRIDFIT. This information could potentially be used to increase the total amount of reconstructed neutrinos or to improve AAFIT, but this possibility has not been pursued any further.

Discussion

GRIDFIT is a reconstruction algorithm with a good efficiency for low energy neutrinos ($\lesssim 100\,\text{GeV}$). The cut combinations can be optimised such that the number of reconstructed neutrinos is increased by about 20% compared to BBFIT, which is the reconstruction algorithm used in current analyses focusing on low energy neutrinos. In addition, GRIDFIT provides some information on the azimuth angle, which is not the case for single-line BBFIT events.

Even though it was set out to be efficient at low energies, the performance at high energies is also good. The efficiency is almost as good as AAFIT in most of the energy range and better than AAFIT for the highest energies ($\gtrsim 3\,\text{PeV}$). The angular resolution is similar to that of AAFIT.

For the analysis of diffuse Galactic neutrinos, which is the focus of this work, the energy range of interest is from about 100 GeV to about 100 TeV, see section 5.4. In this energy range, AAFIT outperforms GRIDFIT by 3% to 7%, so AAFIT will be used as the reconstruction strategy for the analysis.

It has been shown that the R_{GF} variable can be used to distinguish neutrinos from misreconstructed atmospheric muons. The use of this variable is not limited to GRIDFIT and can also be used with other reconstruction strategies. It can be used to increase the efficiency of, for instance, AAFIT, whilst keeping the same purity.

4.3.4 *Energy reconstruction*

After the direction of the neutrino has been reconstructed, there is still one other parameter that has to be determined: the energy. This is the purpose of the energy estimators, for which two basic approaches are used. The energy is either obtained by fitting a distribution of a parameter that is correlated with the energy, or energy-loss patterns are modelled explicitly. The main estimators that are used are the dE/dX estimator, which falls in the former category, and the ANNERGY estimator, which falls in the latter. Besides these two, which will be described in some more detail

ANN: Artificial Neural Network

below, other estimators also exist, see the paper by Schnabel [2013b] for an overview.

As noted previously, the muon loses energy by ionisation and radiative processes when it traverses matter. The ionisation losses are nearly independent of muon energy and can safely be considered a continuous process. The radiative processes cause electromagnetic and hadronic showers along the muon track and are stochastic in nature, so the energy losses are subject to large fluctuations. Above the critical energy, which is several hundred GeV for muons, the radiative processes become dominant and their contribution to the energy loss rises linearly with muon energy. The total energy loss of the muon can be expressed as [Beringer et al., 2012]:

$$-\frac{dE_\mu}{dx} = a(E_\mu) + b(E_\mu)E_\mu, \tag{4.64}$$

with x the amount of matter traversed and $a(E_\mu)$ and $b(E_\mu)$ as in equation 3.5.

From equation 4.64 it can be seen that at low energies, the track length of the muon can be used to get an estimate of its energy. For muons with an energy above the critical energy, the photons produced by the radiative processes can be used for the energy determination. However, due to the stochastic nature, the uncertainty on the energy of the muon is rather large.

The dE/dX estimator [Schüssler, 2012] uses the total number of photons created by the muon to determine its energy loss and from that its energy. The total muon energy loss is approximated by ρ:

$$\frac{dE_\mu}{dx} \approx \rho = \frac{\sum_{i=1}^{N_{\text{hit}}} a_i}{L_\mu \varepsilon}, \tag{4.65}$$

with N_{hit} the number of hits used by the track reconstruction strategy, L_μ the path length of the muon in the detector and ε a factor correcting for the detector efficiency:

$$\varepsilon = \sum_{i=1}^{N_{\text{PMT}}} \frac{e^{-d_i/\lambda_{\text{att}}^{\text{eff}}} f_{\text{ang}}(\theta_{\gamma,i})}{d_i}, \tag{4.66}$$

where the sum runs over all active PMTs and with d_i the distance between the PMT and the reconstructed muon track.

To convert the obtained value of ρ to an energy estimate for the muon, or the neutrino that induced the muon, calibration tables are used that have been created from MC simulations. The

obtained energy resolution is about 0.45 in the logarithm of the energy for well reconstructed muons at 1 TeV energy.

The ANNERGY estimator [Schnabel, 2012] uses a machine learning algorithm to derive the dependence between a set of observables and the energy estimate. In the case of the ANNERGY estimator, an Artifial Neural Network is used, which can be seen as a representation of the PDF describing the relation between the observables and the energy estimate. The list of observables include the number of hits used for the track reconstruction, the total charge of the hits and their average time residual. The obtained energy resolution is just below 0.4 in the logarithm of the energy for well reconstructed muons at 1 TeV energy.

For the analysis of diffuse Galactic neutrinos, the energy reconstructed by the ANNERGY estimator (E_{rec}) will be used to distinguish atmospheric neutrinos and signal neutrinos. The ANNERGY estimator is chosen since the energy resolution is slightly better than that of the dE/dX estimator. It has been verified that using the dE/dX estimator gives comparable results [Visser, 2014].

4.3.5 *Shower reconstruction*

For completeness, some words have to be said about the shower reconstruction strategies. These strategies deal with the reconstruction of the NC interaction of all neutrino flavours, the CC electron-neutrino interactions and most of the tau-neutrino interactions. Instead of a muon, a particle shower is created in these interactions, which is observed as a point source of light.

The first step in the reconstruction is to identify the location of the interaction vertex and the time of the interaction. The bright point fit of BBFIT is one approach used for this, which makes use of a χ^2 fit.

Another shower reconstruction strategy, called DUSJ [Folger, 2013], performs a maximum likelihood fit to determine the vertex time and position. After this step a second maximum likelihood fit is performed, using the information from the vertex fit, to determine the direction and energy of the neutrino that caused the interaction. For the reconstruction of the neutrino direction, it is used that the light is not emitted isotropically, but that the highest light intensity is expected at the Čerenkov angle. The total charge measured by the PMTs can be used to give an estimate of the neutrino energy.

5

CONSTRAINTS ON THE DIFFUSE GALACTIC NEUTRINO FLUX FROM ANTARES

Now that the signal flux has been described, and the detector used to perform a measurement of this flux is introduced, the stage is set to describe the analysis of the ANTARES data. This is the main focus of this chapter. The obtained results are also shown and discussed.

The analysis consists of comparing the number of events from the *on-source* region, with the number of events from the *off-source* region. The on-source region, also called the *signal region*, is a rectangular area encompassing the Galactic plane, where the highest signal is expected. The optimal size of the signal region depends on the angular distribution of the diffuse Galactic neutrino flux. The statistical tools used to determine this optimal size are described in section 5.1.

The off-source region will consist of a number of regions (also called *background regions*), which have the same size and detector coverage as the signal region, but are centred on directions where the expected signal is low. The background regions are constructed in such a way that the number of background events expected in each of them is the same as that expected in the signal region. The method used to construct these background regions is also described in section 5.1.

After the signal and background regions are defined, it has been verified that the background regions are equivalent. The checks that have been performed are described in section 5.2. The data are also compared to the predictions from a MC simulation for events coming from these background regions. A reasonable agreement between data and MC is required, since the MC is used to optimise the cut values of the variables introduced in the previous chapter (Λ, β, E_{rec} and R_{GF}) and to convert the measured number of events into a flux limit.

The cut variables are used to create a final event sample with a high purity. The background (atmospheric muons and atmospheric neutrinos) should then be reduced as much as possible. The same statistical tools as used to determine the optimal size of the signal region are used for this optimisation, which is described in section 5.3.

After the final event sample has been obtained, the sensitivity of ANTARES to the diffuse Galactic neutrino flux can be determined. This is explained in section 5.4, and a comparison is presented with the sensitivity of the AMANDA-II experiment. The influence of the cosmic neutrino signal measured by IceCube is discussed in more detail in this section as well.

The final step is to count the number of events in the signal region and compare it to the number of events from the background regions. The event numbers are used to set flux limits, which are shown and discussed in section 5.5.

5.1 DETERMINING THE OPTIMAL SIGNAL REGION SIZE

The advantage of using an off-source region to perform a measurement of the background, is that no modelling of the background is required for the analysis. In this way, the analysis is in principle not affected by any systematic uncertainties on the background. A MC simulation is still used to optimise the size of the signal region and the cuts on the quality variables, as well as to estimate the number of signal events expected from the diffuse Galactic neutrino flux. In case the MC simulation does not fully describe the data, this could lead to non-optimal values for the parameters or a wrong estimate of the expected number of signal events. The influence of the MC simulation on the measurement is reduced however, since it is not used to estimate the background.

The goal of the analysis is to produce a flux limit, so the parameters are optimised for the best sensitivity. This is explained in more detail below, together with the statistical tools required for this.

5.1.1 *Statistical tools*

In counting experiments, testing for the presence of a signal is based on the determination of the probability that the observed number of events is caused by fluctuations of the background alone. The probability to measure n_{obs} events when μ_{b} are expected from the background is given by Poisson statistics:

$$P(n_{\text{obs}}|\,\mu_{\text{b}}) = \text{Pois}(n_{\text{obs}}|\,\mu_{\text{b}}) = \frac{\mu_{\text{b}}^{n_{\text{obs}}} e^{-\mu_{\text{b}}}}{n_{\text{obs}}!}, \tag{5.1}$$

where the probability is conditional (i. e. the probability to measure n_{obs} given μ_{b}).

For equation 5.1 it is assumed that the expected number of background events is exactly known (or the uncertainty on it can be neglected). When the expected number of background events has a non-neglible uncertainty, things become more complicated. This is the case when using an off-source region to determine the number of background events from the data. The advantage of not having to rely on any modelling of the background outweighs this additional complexity: the measurement is not affected by systematic errors on the background. This method is therefore commonly used in both astronomy and high-energy physics. In the former, the measurement of the background consists of pointing the telescope in a source-free direction, whereas in the latter so-called *sidebands* are used[27]. In ANTARES, the Fermi bubble analysis [Adrián-Martínez et al., 2014a] has made use of on- and off-source regions.

[27] *A sample of events which is near the signal region in the measured parameter, for instance around an expected mass peak of some hypothesised new particle.*

When the uncertainty on the background is non-neglible, the probability given by equation 5.1 has to be modified to include the additional measurement. This subsidiary measurement can also be described using a Poissonian [Cousins et al., 2008; Li and Ma, 1983], in which n_{bg} events are measured in the off-source region where μ_{bg} are expected. The off-source region does not need to have the same size as the on-source region, and is often chosen to be bigger to reduce the statistical uncertainty on n_{bg}. The ratio of off-source to on-source region is called τ, which is usually known and given by:

$$\tau = \frac{\mu_{\mathrm{bg}}}{\mu_{\mathrm{b}}}. \tag{5.2}$$

Since the two measurements are independent, the probability to measure n_{obs} when $\mu_{\mathrm{obs}} (= \mu_{\mathrm{b}} + \mu_{\mathrm{s}})$ are expected, and n_{bg} events when μ_{bg} are expected, can be written as:

$$P(n_{\mathrm{obs}}, n_{\mathrm{bg}} | \mu_{\mathrm{b}}, \mu_{\mathrm{s}}; \tau) = \mathrm{Pois}(n_{\mathrm{obs}} | \mu_{\mathrm{b}} + \mu_{\mathrm{s}}) \mathrm{Pois}(n_{\mathrm{bg}} | \tau \mu_{\mathrm{b}}), \tag{5.3}$$

where μ_{s} is the expected number of signal events.

After performing a measurement of both n_{bg} and n_{obs}, a confidence interval $[\mu_{\mathrm{low}}, \mu_{\mathrm{up}}]$ can be constructed for μ_{s} at a certain confidence level α (for instance 90%). Using frequentist statistics, this means that the interval contains the fixed unknown value of the number of signal events in a fraction α of the experiments:

$$P(\mu_{\mathrm{s}} \in [\mu_{\mathrm{low}}, \mu_{\mathrm{up}}]) = \alpha. \tag{5.4}$$

Using Bayesian statistics, one rather speaks of a credibility interval, and using a 'confidence' level of α means in this case that the

probability that the true value of the number of signal events is within the interval is α [Metzger, 2002].

If the confidence interval is constructed according to equation 5.4, it is said to *cover* that parameter at the stated confidence level. In case $P(\mu_s \in [\mu_{low}, \mu_{up}]) < \alpha$ the interval is said to undercover the parameter, and when $P(\mu_s \in [\mu_{low}, \mu_{up}]) > \alpha$ it is said to overcover[28]. Although overcoverage is generally considered not to be such a big problem as undercoverage, it is still undesirable since the interval is larger than it should be.

[28] *The interval is in this case also called conservative.*

Depending on the measurement, two types of results can be expected from an experiment. Either an experiment shows a new source of signal events and a discovery can be claimed, or, when the measurement is consistent with the background-only hypothesis, an upper limit can be reported on the assumed signal flux. Both results require a different optimisation, as described for instance in the paper by Hill et al. [2005]. For ANTARES the optimisation will be done to set the best upper limit (i. e. the upper part of a confidence interval), for KM3NeT also the optimisation for a discovery will be used, see section 6.2.1.

MRF: Model Rejection Factor

In order to optimise for the best upper limit, the MRF technique is used. The MRF technique is often used in neutrino astronomy as an unbiased method to optimise the experiment for the best sensitivity [Hill and Rawlins, 2003]. The method yields the cuts that minimise the average expected upper limit, under the assumption there is no true signal present.

Since the actual upper limit is not known before the measurement, the average upper limit can be determined that would be obtained when repeating the experiment a large number of times. This average upper limit is the sum of the upper limits for all possible values of n_{obs} and n_{bg}, weighted with their Poisson probabilities of occuring:

$$\overline{\mu}^{\alpha}(n_{obs}, n_{bg}) = \sum_{n_{obs}=0}^{\infty} \sum_{n_{bg}=0}^{\infty} \mu^{\alpha}(n_{obs}, n_{bg}) \frac{\mu_b^{n_{obs}} e^{-\mu_b}}{n_{obs}!} \frac{(\tau\,\mu_b)^{n_{bg}} e^{-\tau\,\mu_b}}{n_{bg}!}, \quad (5.5)$$

where $\mu^{\alpha}(n_{obs}, n_{bg})$ is the event upper limit at a confidence level of α (i. e. μ_{up} in equation 5.4).

The MRF is then defined as the average upper limit divided by the expected signal:

$$\mathrm{MRF} = \frac{\overline{\mu}^{\alpha}(n_{obs}, n_{bg})}{\mu_s}. \quad (5.6)$$

The MRF shows how much the sensitivity of the experiment is above (or below) the signal flux model (so an MRF of 10 means that the experiment is sensitive to fluxes at least 10 times higher than the assumed signal flux model). By optimising the cuts to get the lowest MRF, the sensitivity of the experiment is maximised.

To determine the event upper limits, the profile likelihood method is used. In this method, the multi-dimensional likelihood function is reduced to a function that only depends on the parameter of prime interest. In the case at hand, the likelihood function is given by:

$$\mathcal{L}(\mu_b, \mu_s | n_{obs}, n_{bg}) = P(n_{obs}, n_{bg} | \mu_b, \mu_s; \tau), \tag{5.7}$$

and the parameter of prime interest is the expected number of signal events (for which the upper limit is determined). The expected number of background events is a so-called nuisance parameter. By fixing μ_s and maximising the likelihood over μ_b alone, the maximum-likelihood estimator of μ_b (denoted by $\hat{\mu}_b$) is obtained as a function of μ_s:

$$\hat{\mu}_b(\mu_s) = \frac{n_{obs} + n_{bg} - (1+\tau)\mu_s + \sqrt{[n_{obs} + n_{bg} - (1+\tau)\mu_s]^2 + 4(1+\tau)\mu_s}}{2(1+\tau)}. \tag{5.8}$$

The profile likelihood is then given by:

$$\lambda(\mu_s | n_{obs}, n_{bg}) = \frac{\mathcal{L}(\hat{\mu}_b(\mu_s), \mu_s | n_{obs}, n_{bg})}{\mathcal{L}(\hat{\hat{\mu}}_b, \hat{\hat{\mu}}_s | n_{obs}, n_{bg})}, \tag{5.9}$$

which is only a function of μ_s and where $\hat{\hat{\mu}}_b = \frac{n_{bg}}{\tau}$ and $\hat{\hat{\mu}}_s = n_{obs} - \frac{n_{bg}}{\tau}$ are the maximum-likelihood estimators of μ_b and μ_s respectively (maximising the overall likelihood).

The profile likelihood method is widely used in high energy physics and gamma-ray astronomy (where it is popularised by Li and Ma [1983]) and it provides a very good approximation in the parameter space of interest [Cousins et al., 2008]. The profile likelihood method is implemented in ROOT in the TROLKE class. This method is a fully frequentist implementation and uses a likelihood ratio test to determine the signal upper and lower limits. To speed up the calculations, it makes use of the fact that $-2\log\left(\lambda(\mu_s | n_{obs}, n_{bg})\right)$ has an approximate χ^2 distribution with 1 degree of freedom [Rolke et al., 2005].

This frequentist approach is compared to a Bayesian method (using the same profile likelihood) with a flat prior in the left plot

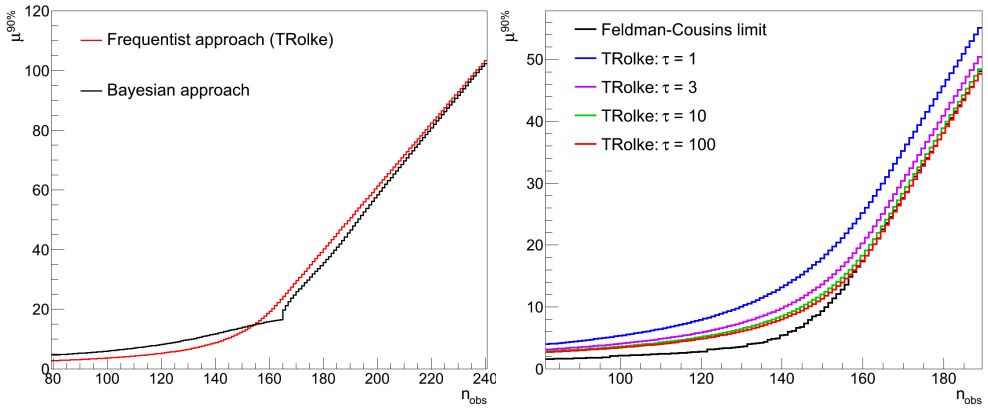

Figure 5.1: 90% CL event upper limit versus number of observed events. LEFT: comparison between frequentist and Bayesian approach for $n_b = 166$ and $\tau = 8$. RIGHT: for $n_b = 166$ for different values of τ.

of figure 5.1 for $\tau = 8$ and $n_b \equiv \frac{n_{bg}}{\tau} = 166$ (which are the number of used background regions and the measured average number of background events per region respectively). The plot shows the 90% confidence level event upper limit as a function of the number of observed events. It can be seen that the obtained event upper limits are different for the two approaches, which can be expected. The differences are not that big however. For this work, the frequentist method as implemented in ROOT is used.

The effect of τ on the event upper limit is shown in the right plot of figure 5.1, for $n_b = 166$ and $\alpha = 90\%$. The higher the value of τ, the better the limit becomes, which is expected since the uncertainty on the background becomes less for increasing values of τ. Also shown is the signal upper limit obtained with the Feldman-Cousins (FC) method, which assumes that the expected number of background events is known exactly [Feldman and Cousins, 1998]. When choosing a high value for τ, for instance 100, so that the uncertainty on the background measurement becomes negligible, it is expected that the limit from the TROLKE method becomes similar to that from the FC method. It can be seen that this is the case when $n_{obs} > n_b$, but not for smaller values of n_{obs}. The upper limit obtained with the TROLKE method is slightly higher for those cases, which is because the method overcovers [Rolke et al., 2005]. This is no problem however, since care must be taken in interpreting the limit anyway in the case that the number of observed events is lower than what is expected from background.

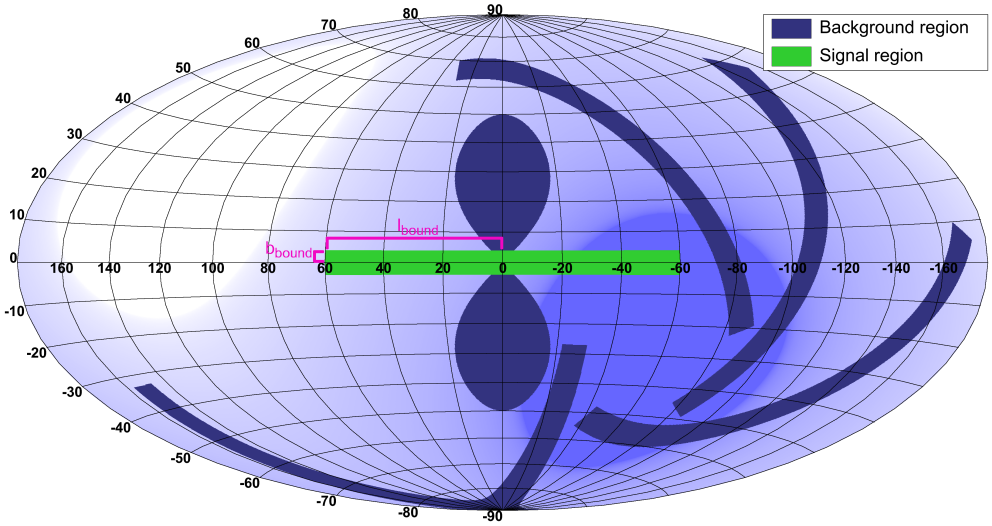

Figure 5.2: Signal and background regions overlaid on the ANTARES visibility for $l_{\text{bound}} = 60^\circ$ and $b_{\text{bound}} = 4^\circ$. Also shown is the signal region used in the Fermi bubble analysis.

5.1.2 *Construction of the background regions*

The analysis method, using an on-source (signal) and an off-source region region, is applied as follows. First, a signal region of a specific size is chosen, which is centred at the Galactic centre. The signal region can be characterised by two parameters, l_{bound} and b_{bound}, which denote the extension in longitude and latitude respectively. For example, a region with $l_{\text{bound}} = 60^\circ$ and $b_{\text{bound}} = 4^\circ$ will extend from a Galactic longitude of -60° to $+60^\circ$ and from a Galactic latitude of -4° to $+4^\circ$, see also figure 5.2 (another example can be found in figure 5.5).

Then, the signal region is converted to local detector coordinates (zenith and azimuth) at an arbitrary time t. The signal region is subsequently converted back to Galactic coordinates at a later time t_1. The time t_1 is thereby chosen such, that the time-shifted region does not overlap with the signal region. Using the fact that a given point in Galactic coordinates follows the same path in detector coordinates every sidereal day, this time-shifted region (background region 1) will follow the exact same path in detector coordinates as the signal region, but with some time offset $\delta t_1 = t_1 - t$. In one sidereal day the expected number of background events is then the same in both regions.

The process is repeated and a second background region is created in the same way, which again follows the same path in de-

tector coordinates, but with a time offset of $\delta t_2 = t_2 - t$ compared to the signal region. This second time offset is chosen such that background region 2 does not overlap with background region 1 to avoid double counting of events. The process is repeated until $t_n = t + T$, where $T = 23.9345\,\text{day}$ corresponds to one sidereal day. As a result $N = n - 1$ background regions are created. This can be summarised as:

$$\delta t_i = i \cdot T/(N+1), \tag{5.10}$$

which shows the time offset of region i compared to the signal region. The value of N depends on the size of the signal region (compare figures 5.2 and 5.5). Figure 5.3 shows the possible number of background regions for different values of the l_{bound} and b_{bound} parameters.

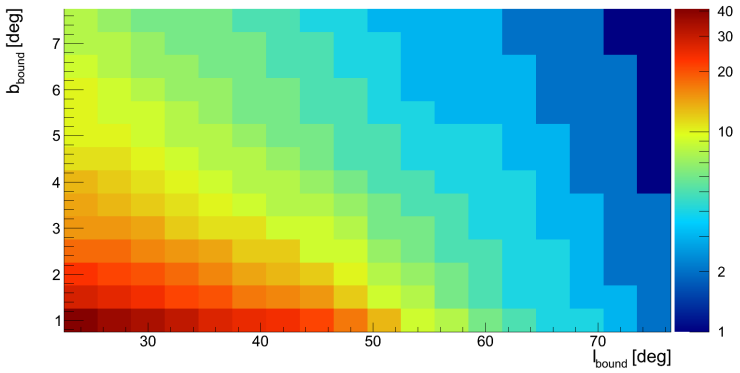

Figure 5.3: Number of background regions as a function of l_{bound} and b_{bound}.

In order to do a proper background measurement with the generated background regions, no significant signal must be present in those regions. For this reason, the background regions which overlap with the signal region used in the Fermi bubble analysis are skipped. The regions which partly overlap with the Galactic plane are not skipped, since no significant signal is expected where these regions cross the Galactic plane.

The advantage of defining the background regions in this way is that most systematic effects cancel out. Since the detector response to each of the background regions should be identical by construction, the number of events can be compared to check for any remaining systematic biases. This is presented in section 5.2.

5.1.3 *Signal region optimisation*

In total there are 6 parameters to optimise (2 parameters for the size of the signal region and 4 cut parameters). Since optimising all 6 parameters at the same time is extremely time consuming, the optimisation is split into two parts. First the size of the signal region is optimised for fixed values of the cut parameters and then the values of the 4 cut parameters are optimised. By factorising the problem, it is possible that the obtained combination of parameters is not optimal. This is investigated by checking the stability of the optimal size of the signal region when using different combinations of the quality cuts.

The optimisation of the size of the signal region is performed for different cut combinations using the MRF method. In this, the MRF is always calculated at 90% confidence level. As input, the expected number of signal and background events is required, which are obtained from the run-by-run (RBR) MC (see section 4.1.5), using only events that have a reconstructed direction falling in the signal region. The amount of atmospheric muons is again evaluated using equation 4.57.

β-CUT	Λ-CUT	PURITY
1.0°	−5.1	~94%
1.0°	−5.3	~78%
1.0°	−5.4	~63%
2.0°	−5.0	~92%
2.0°	−5.2	~75%
2.0°	−5.3	~60%

Table 5.1: The different cut combinations considered for the optimisation of the signal region size.

For the optimisation, the longitude bound is varied from 24° to 75° in steps of 3° and the latitude bound from 1° to 7.5° in steps of 0.5°. For each combination of longitude and latitude bound the MRF value is calculated. Since the quality cut optimisation is made after choosing the signal region, different sets of cuts with different values for the purity (equation 4.56) are investigated. Only events which are reconstructed as upgoing (i. e. $\cos\hat{\theta} < 0$) are considered and only cuts on the track quality parameters Λ and β are used to check the effect of the purity. In table 5.1 the various cuts are summarised.

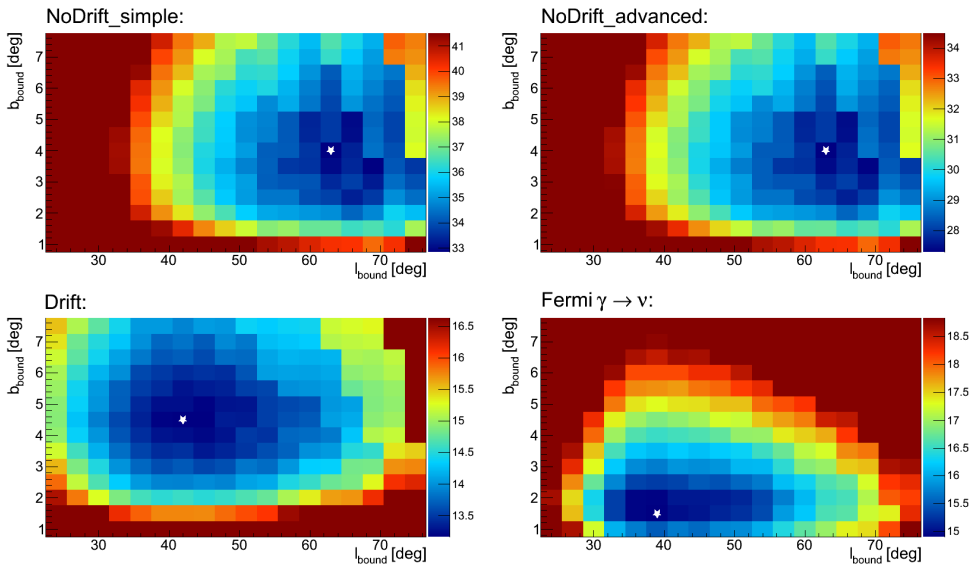

Figure 5.4: MRF versus longitude and latitude bound for an event selection with $\beta < 1.0^\circ$ and $\Lambda > -5.1$. The white star marks the location of the minimum.

Figure 5.4 shows the MRF as a function of longitude bound and latitude bound for an event selection with $\beta < 1.0^\circ$ and $\Lambda > -5.1$ for the four signal flux models. The colour scale shows the value of the MRF and has been chosen such that the blue part of the scale corresponds to the bottom 10% of the MRF values for each signal model. Note that the colour scales are different for each model.

It can be seen that a lower MRF is obtained for the Drift model compared to the NoDrift models, which is expected since the number of signal events is higher in the Drift model. The MRF is also lower for the Fermi $\gamma \to \nu$ model than for the NoDrift models.

With this particular cut combination, the lowest MRF is found at $l_{\text{bound}} = 63^\circ$ and $b_{\text{bound}} = 4^\circ$ for both NoDrift models, at $l_{\text{bound}} = 42^\circ$ and $b_{\text{bound}} = 4.5^\circ$ for the Drift model and at $l_{\text{bound}} = 39^\circ$ and $b_{\text{bound}} = 1.5^\circ$ for the Fermi $\gamma \to \nu$ model. It should be noted however that the minimum is quite shallow for each of the models.

The different values of the longitude and latitude bounds obtained for the various signal models are caused by the differences in the predicted angular profile of the flux. By choosing a longitude and latitude bound that is optimal for one model, the

sensitivity to the other models is slightly worse. Since the Drift model is more optimistic and the corresponding optimal signal region is in between the optimal regions for the other models, the Drift model will be used for the further optimisation. By choosing this region, the sensitivity to both the NoDrift models and the Fermi $\gamma \rightarrow \nu$ model is about 13% worse than specifically choosing the region that is found optimal for each model.

To check the influence of the uncertainty on the atmospheric neutrino flux, the MRF optimisation is also performed with an increased (25% higher) and decreased (25% lower) atmospheric neutrino flux. The MRF results for the Drift model are summarised in table 5.2. The results for the other models are not shown, since they are not used for the optimisation, but the main conclusions which apply to the Drift model also apply to the other three models.

It can be seen that a looser cut on Λ gives more signal and more background and that for both β cuts the middle Λ cut gives the lowest MRF. This is expected, since cutting too hard on Λ not only removes a lot of misreconstructed atmospheric muons, but also removes a lot of signal. On the other hand, too loose a cut leaves more signal but also more background. The optimal signal region is not very dependent on the purity of the final event sample; for both β cuts the same size of the signal region is found to within a few degrees for the different Λ cuts.

The optimal signal region size has a small dependency on β. When comparing the cut of $\beta < 1.0^\circ$, $\Lambda > -5.1$ with $\beta < 2.0^\circ$, $\Lambda > -5.0$ (which have a comparable purity), it can be seen that the former results in a better MRF value. This is caused by the fact that a harder Λ cut is required in order to get the same purity for a looser β cut. To compensate for the loss in signal, the signal region has to be made bigger which also gives more background. It means that the optimisation of the signal region size and the cuts are correlated: for a more optimal set of cuts (i. e. a set of cuts resulting in a lower sensitivity), a smaller signal region is found to be optimal. The effect is however quite small.

The effect of using a cut on E_{rec} has also been checked, but the optimal size of the signal region does not change [Visser, 2014]. The effect of using the R_{GF} cut has not been checked explicitly, but since it is expected that using it in combination with Λ and β will increase the neutrino efficiency, it is reasonable to assume a slightly smaller optimal size of the signal region will be found

CUT COMBINATION	ATMOSPHERIC ν-FLUX	OPTIMAL VALUES l_{bound}	b_{bound}	MRF	μ_s	μ_b
$\beta < 1.0°, \Lambda > -5.1$	Default	42°	4.5°	13.17	1.34	78.4
	25% increased	42°	4.5°	14.59	1.34	97.2
	25% decreased	45°	5°	11.56	1.46	70.4
$\beta < 1.0°, \Lambda > -5.3$	Default	39°	4.5°	12.99	1.64	118
	25% increased	39°	4.5°	14.23	1.64	143
	25% decreased	39°	4.5°	11.63	1.64	93.5
$\beta < 1.0°, \Lambda > -5.4$	Default	39°	4.5°	13.89	1.81	167
	25% increased	39°	4.5°	15.02	1.81	195
	25% decreased	39°	4.5°	12.69	1.81	138
$\beta < 2.0°, \Lambda > -5.0$	Default	45°	5°	14.03	1.30	82.1
	25% increased	45°	5°	15.48	1.30	101
	25% decreased	51°	5°	12.39	1.38	71.1
$\beta < 2.0°, \Lambda > -5.2$	Default	45°	5°	13.88	1.57	122
	25% increased	51°	5°	15.13	1.87	201
	25% decreased	51°	5°	12.55	1.87	137
$\beta < 2.0°, \Lambda > -5.3$	Default	51°	5°	14.76	2.12	247
	25% increased	48°	4°	15.77	1.84	217
	25% decreased	48°	4°	13.62	1.84	160

Table 5.2: Optimal longitude and latitude bounds and obtained MRF value for the Drift model for the considered cuts.

when used. Again, the effect is expected to be small[29].

The effect of an increased/decreased atmospheric neutrino background is only an increase/decrease in the MRF; (almost) the same size of the signal region is found to be optimal when varying the atmospheric neutrino flux. For an increased background a slightly smaller region seems optimal for some cut combinations, but the effect is negligible.

From the information in the table it can be concluded that a region with $l_{\text{bound}} = 39°$ and $b_{\text{bound}} = 4.5°$ is optimal. The signal region has a size of 0.21 sr, and 8 background regions can be used. The signal and background regions are shown in figure 5.5.

[29] *The signal region optimisation has been repeated with the optimal cuts (equation 5.19) to check this explicitly, resulting in the same optimal size of* $l_{bound} = 39°$ *and* $b_{bound} = 4.5°$.

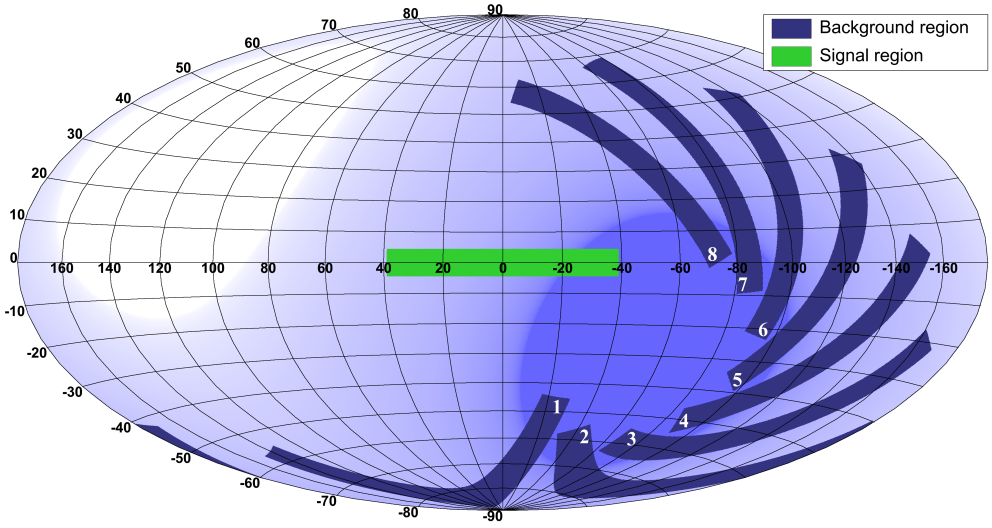

Figure 5.5: Signal and background regions for the optimised signal region ($l_{\text{bound}} = 39^\circ$ and $b_{\text{bound}} = 4.5^\circ$) overlaid on the ANTARES visibility. The numbering of the background regions is also shown.

5.2 CHECKS ON THE BACKGROUND REGIONS

Now that the optimal signal region has been determined and the background regions defined, some checks can be performed on the background regions. It can be seen from figure 5.5 that each background region has the same visibility. However, systematic biases can arise, because data taking is not continuous. There is for instance a small amount of time between two data runs in which no data are taken, and also no physics data are taken during calibration of the detector. In addition, not all physics data runs are suitable for analyses (see section 5.2.1). The gaps in data taking can result in some regions having a higher/lower visibility than others, so that the background regions are no longer identical.

In order to check for this possibility, the effective visibility is calculated and presented in section 5.2.2 and a check for any systematic bias is made and presented in section 5.2.3.

Finally, a comparison between the data and the MC simulation is made and presented in section 5.2.4. A good agreement between data and MC is required, since the MC is used to optimise the quality cuts and to convert the measured number of events into a flux limit.

5.2.1 *Data selection*

For this analysis, the data from January 29th 2007 (run 25682) to November 30th 2012 (run 68170) are used. In this period, a total of 15982 data runs are taken, in which either the 3N, the 2T3 or the TQ trigger were active (or a combination of them). From these data runs, only those runs are used that are suitable for data analysis. For this, the run duration has to be more than one second and there should not be any serious problems. In addition, all SCAN runs and all SPARKING runs are excluded. SCAN runs are runs which are used to test new calibrations or detector settings. SPARKING runs contain events which are caused by a sparking PMT. Finally, the reconstruction algorithms (AAFIT, GRIDFIT) should have been applied to the data and there should be matching run-by-run MC files.

SELECTION STEP	NUMBER OF DATA RUNS THAT PASS
Total number of physics data runs	15982
+ Suitable for data analysis	15172
+ Is not a SCAN run	13529
+ Is not a SPARKING run	13481
+ Reconstruction applied	13223
+ RBR MC files exist	12377

Table 5.3: The number of data runs selected after applying selection criterea.

After these selection criteria, a total of 12377 runs are selected, which have a combined total livetime of 1288 days (3.53 years). Table 5.3 lists the number of data runs selected by applying the selection criterea. From the selected runs, all events that are either triggered by the 3N, the 2T3 or the TQ trigger are used.

5.2.2 *Effective visibility*

The visibility of ANTARES is shown in figure 2.29 (and in figure 5.5). It is calculated by taking a given direction in Galactic coordinates and checking for which fraction of a sidereal day it is visible (i. e. has a zenith angle above 90°). This is the theoretical visibility, in that it would be obtained if the ANTARES detector would measure continuously for a sidereal day, or any integer multiple of it. In reality however, the data taking is not contin-

uous, so there are parts of a sidereal day for which no data are taken. This affects the visibility and can lead to systematic biases. This can best be illustrated by an example.

Consider a total livetime of exactly 10 sidereal days and a specific direction (in the signal region) which is visible during 80% of a sidereal day. If data taking is continuous over the whole livetime, the visibility of this direction is just $\mathcal{V} = 80\%$ (equation 2.63). Now consider that a calibration run of 2 hours is taken on one of the days, during a time in which the direction can be observed (i. e. it is visible). For the sidereal day in which this calibration run is done, the direction is only seen during 78.2% of the time when physics data are taken (so excluding the calibration run). The effective visibility of the direction is averaged over the whole livetime and is defined as:

$$\mathcal{V}_{\text{eff}} = \frac{\int_{T_{\text{start}}}^{T_{\text{stop}}} \mathrm{d}t \; v(l,\, b,\, t) A(t)}{\int_{T_{\text{start}}}^{T_{\text{stop}}} \mathrm{d}t \; A(t)}, \tag{5.11}$$

where $v(l,\, b,\, t)$ is as defined in equation 2.64, T_{start} and T_{stop} are the time when data taking starts and stops respectively and with:

$$A(t) = \begin{cases} 1 & \text{If 'good' physics data are taken} \\ 0 & \text{Otherwise} \end{cases} \tag{5.12}$$

Using equation 5.11 gives $\mathcal{V}_{\text{eff}} = 79.8\%$ in the example above. Note that the effective visibility is defined such that it is unaffected if the calibration run would last exactly one sidereal day.

Consider now a second direction (e. g. from one of the background regions), that should by construction have the same visibility as the direction considered above (80%). However, during the time the calibration run is performed, this direction is above the horizon and so is not visible, giving $\mathcal{V}_{\text{eff}} = 80.7\%$. The fact that the effective visibilities are different for both directions results in a systematic bias. The same number of events is expected from each of the directions within the statistical uncertainty, but a different number of events is actually measured.

Using again the fact that a given direction in Galactic coordinates has the same local detector coordinates after one sidereal day has passed, the effective visibility can be rewritten as:

$$\mathcal{V}_{\text{eff}} = \int_0^T \mathrm{d}t \; w(t)\, v(l,\, b,\, t), \tag{5.13}$$

where $w(t)$ is the sidereal day weight, which represents in which fraction of the livetime data are taken at that time of the sidereal

day. In case of continuous data taking, $w(t)$ would have a value of $1/T$ and the effective visibility (equation 5.13) would be identical to the theoretical visibility (equation 2.63). If, on the other hand, only during the first 3 hours of the sidereal day data would be taken, the value of $w(t)$ would be $1/(3\,\text{hour})$ for the first 3 hours and 0 for the rest of the day. By dividing the sidereal day in 1657 bins of 52 s each, the integral in equation 5.13 becomes a sum, and the value of $w(t)$ would be $1/1657$ for each bin in case of continuous data taking.

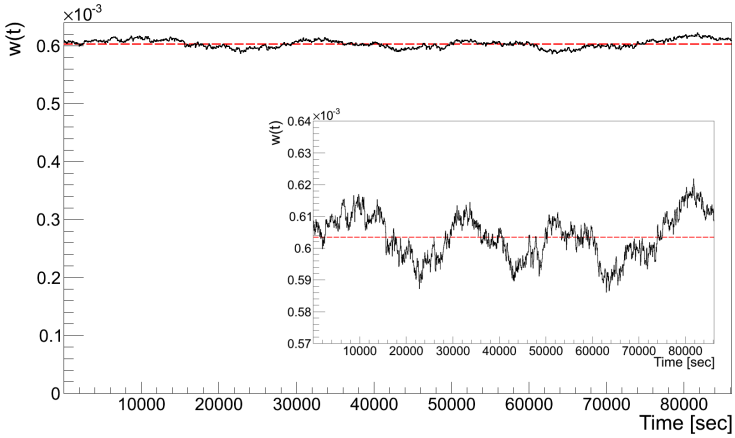

Figure 5.6: Sidereal day weight $w(t)$ versus time for the 12377 selected data runs. The red line indicates the theoretical value assuming there is continuous data taking. The same results are shown in the inset, but focused around the average weight.

The distribution of $w(t)$ for the 12377 data runs that are selected is shown in figure 5.6. For each data run that is selected, the start and stop times are taken and converted to sidereal time. The bins corresponding to the time period between start and stop times are filled with a value of 1. The histogram is then normalised. The red dashed line shows the fraction obtained when data taking would be continuous over the whole sidereal day.

From the inset in the figure, the effect of the data run selection can be more appreciated. The discontinuity of the data taking results in a higher fraction of the data runs being taken during certain parts of a sidereal day than for others. The differences compared to the red line are about 3%.

Since different parts of the sidereal day get a different weight, the effective visibility is expected to look different from the theoretical visibility. By eye however, the effective visibility looks

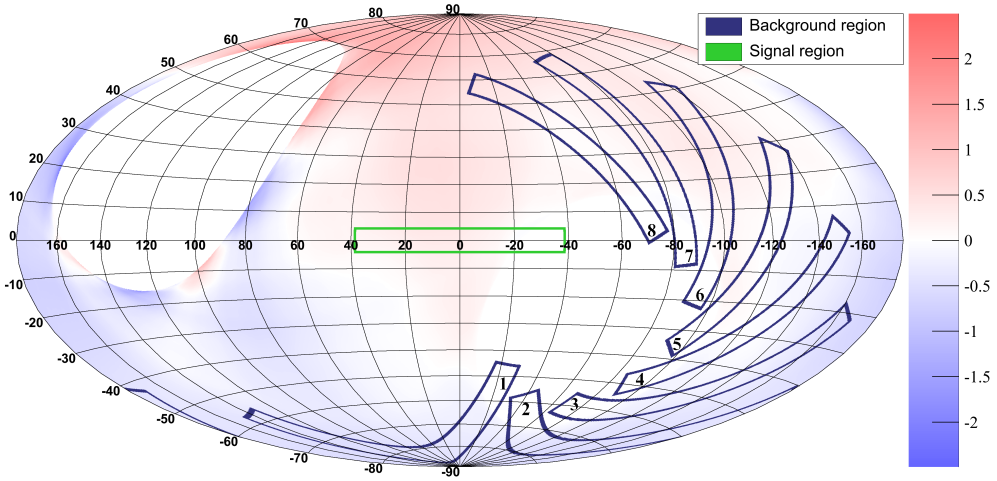

Figure 5.7: The percentual differences between the effective and the theoretical visibility.

the same as the theoretical visibility. The small differences can be visualised by calculating the percentual differences between the effective and the theoretical visibility:

$$\Delta\mathcal{V} = \frac{\mathcal{V}_{\text{eff}} - \mathcal{V}}{\mathcal{V}} \cdot 100\%. \tag{5.14}$$

The sky-map of $\Delta\mathcal{V}$ is shown in figure 5.7.

From the figure it can be seen that the visibility is unchanged in the two parts of the sky that are either never or always visible, as is expected. For the other directions there are some small differences; for most of the directions the difference is around 5‰. The maximum differences are found near the region which is never visible and are about 2.5%. Since the visibility of these directions is low, the impact of these differences is small.

The borders of the signal and background regions are also shown in the figure. It can be seen that part of regions 1, 2, 3 and to a lesser extent 4, lies in the blue part, so slightly less events are expected in those regions. Part of regions 6, 7 and 8, as well as part of the signal region, lies in the red part and slightly more events are expected in those regions. Region 5 lies mostly in the white part, so is unchanged as to the expectation from the theoretical visibility. However, since only a part of the regions lies in the blue/red part, and the differences in the regions are less than a percent, no significant differences are expected between the regions.

5.2.3 *Checking for systematic biases*

On the basis of the effective visibility, it is found that the same number of events is expected in the signal and background regions to within one percent. To check for remaining systematic biases, the number of data events in each of the 8 background regions is counted and compared to each other. In order to reject badly reconstructed events and keep sufficient statistics, only upgoing events with $\Lambda > -6.0$ and $\beta < 1.75^\circ$ are considered. Table 5.4 shows the number of events surviving this cut for each of the 8 regions; for the numbering of the regions see figure 5.5.

BACKGROUND REGION	NUMBER OF EVENTS	BACKGROUND REGION	NUMBER OF EVENTS
1	8920 ± 94	5	9000 ± 95
2	8945 ± 95	6	8881 ± 94
3	9022 ± 95	7	8934 ± 95
4	8983 ± 95	8	8826 ± 94

Table 5.4: Number of events reconstructed as upgoing (with $\Lambda > -6.0$ and $\beta < 1.75^\circ$) in each of the 8 background regions. The error on the number of events is the statistical uncertainty.

The numbers of events obtained from the 8 regions are consistent within the statistical uncertainties. It can thus be concluded that there are no big systematic biases. To carry out a more thorough check, the number of events surviving in each region is subdivided into multiple 'measurements', by defining several cut regions.

In order to make these comparisons, a certain cut combination is applied and the surviving events are counted, giving n_i events for region i. This number of events is then compared to the average number of events from the other 7 regions, n_{av}, giving an event-ratio:

$$R_i = \frac{n_i}{n_{\text{av}}}, \tag{5.15}$$

with an error of:

$$\delta R_i = R_i \cdot \sqrt{\left(\frac{\delta n_i}{n_i}\right)^2 + \left(\frac{\delta n_{\text{av}}}{n_{\text{av}}}\right)^2}, \tag{5.16}$$

where δn_i and δn_{av} are the statistical uncertainties on n_i and n_{av} respectively.

NUMBER	CUT COMBINATION	NUMBER	CUT COMBINATION
1	$\beta \leqslant 1.0°$, $-6 \leqslant \Lambda < -5.99$	19	$\beta \leqslant 1.0°$, $-5.59 \leqslant \Lambda < -5.45$
2	$\beta \leqslant 1.0°$, $-5.99 \leqslant \Lambda < -5.98$	20	$\beta \leqslant 1.0°$, $\Lambda \geqslant -5.45$
3	$\beta \leqslant 1.0°$, $-5.98 \leqslant \Lambda < -5.97$	21	$1.0° < \beta \leqslant 1.05°$, $\Lambda \geqslant -6.0$
4	$\beta \leqslant 1.0°$, $-5.97 \leqslant \Lambda < -5.96$	22	$1.05° < \beta \leqslant 1.1°$, $\Lambda \geqslant -6.0$
5	$\beta \leqslant 1.0°$, $-5.96 \leqslant \Lambda < -5.95$	23	$1.1° < \beta \leqslant 1.15°$, $\Lambda \geqslant -6.0$
6	$\beta \leqslant 1.0°$, $-5.95 \leqslant \Lambda < -5.93$	24	$1.15° < \beta \leqslant 1.2°$, $\Lambda \geqslant -6.0$
7	$\beta \leqslant 1.0°$, $-5.93 \leqslant \Lambda < -5.92$	25	$1.2° < \beta \leqslant 1.25°$, $\Lambda \geqslant -6.0$
8	$\beta \leqslant 1.0°$, $-5.92 \leqslant \Lambda < -5.91$	26	$1.25° < \beta \leqslant 1.3°$, $\Lambda \geqslant -6.0$
9	$\beta \leqslant 1.0°$, $-5.91 \leqslant \Lambda < -5.89$	27	$1.3° < \beta \leqslant 1.35°$, $\Lambda \geqslant -6.0$
10	$\beta \leqslant 1.0°$, $-5.89 \leqslant \Lambda < -5.87$	28	$1.35° < \beta \leqslant 1.4°$, $\Lambda \geqslant -6.0$
11	$\beta \leqslant 1.0°$, $-5.87 \leqslant \Lambda < -5.85$	29	$1.4° < \beta \leqslant 1.45°$, $\Lambda \geqslant -6.0$
12	$\beta \leqslant 1.0°$, $-5.85 \leqslant \Lambda < -5.83$	30	$1.45° < \beta \leqslant 1.5°$, $\Lambda \geqslant -6.0$
13	$\beta \leqslant 1.0°$, $-5.83 \leqslant \Lambda < -5.81$	31	$1.5° < \beta \leqslant 1.55°$, $\Lambda \geqslant -6.0$
14	$\beta \leqslant 1.0°$, $-5.81 \leqslant \Lambda < -5.78$	32	$1.55° < \beta \leqslant 1.6°$, $\Lambda \geqslant -6.0$
15	$\beta \leqslant 1.0°$, $-5.78 \leqslant \Lambda < -5.75$	33	$1.6° < \beta \leqslant 1.65°$, $\Lambda \geqslant -6.0$
16	$\beta \leqslant 1.0°$, $-5.75 \leqslant \Lambda < -5.71$	34	$1.65° < \beta \leqslant 1.7°$, $\Lambda \geqslant -6.0$
17	$\beta \leqslant 1.0°$, $-5.71 \leqslant \Lambda < -5.66$	35	$1.7° < \beta \leqslant 1.75°$, $\Lambda \geqslant -6.0$
18	$\beta \leqslant 1.0°$, $-5.66 \leqslant \Lambda < -5.59$		

Table 5.5: The 35 cut regions that are used for determining the event-ratios from the ANTARES data.

If no systematic bias is present, the distribution of the calculated event-ratios will be a Gaussian centred at 1 with a width corresponding to the total number of events. In case a systematic bias is present, the mean of the Gaussian will be offset from 1. The method has been tested by giving one of the regions a systematic bias of $\pm x\%$ which is then noticed as a shift in the central value equal to the same percentage [Visser, 2014].

For the application to data, a total of 35 measurements are defined, which are summarised in table 5.5. The cuts are chosen such, that the total number of events is more or less evenly distributed over the measurements. It should be noted that except for the $\beta \leqslant 1.0°$, $\Lambda \geqslant -5.45$ cut (which has a purity of about $60 \pm 1\%$), the measurements are dominated by atmospheric muons.

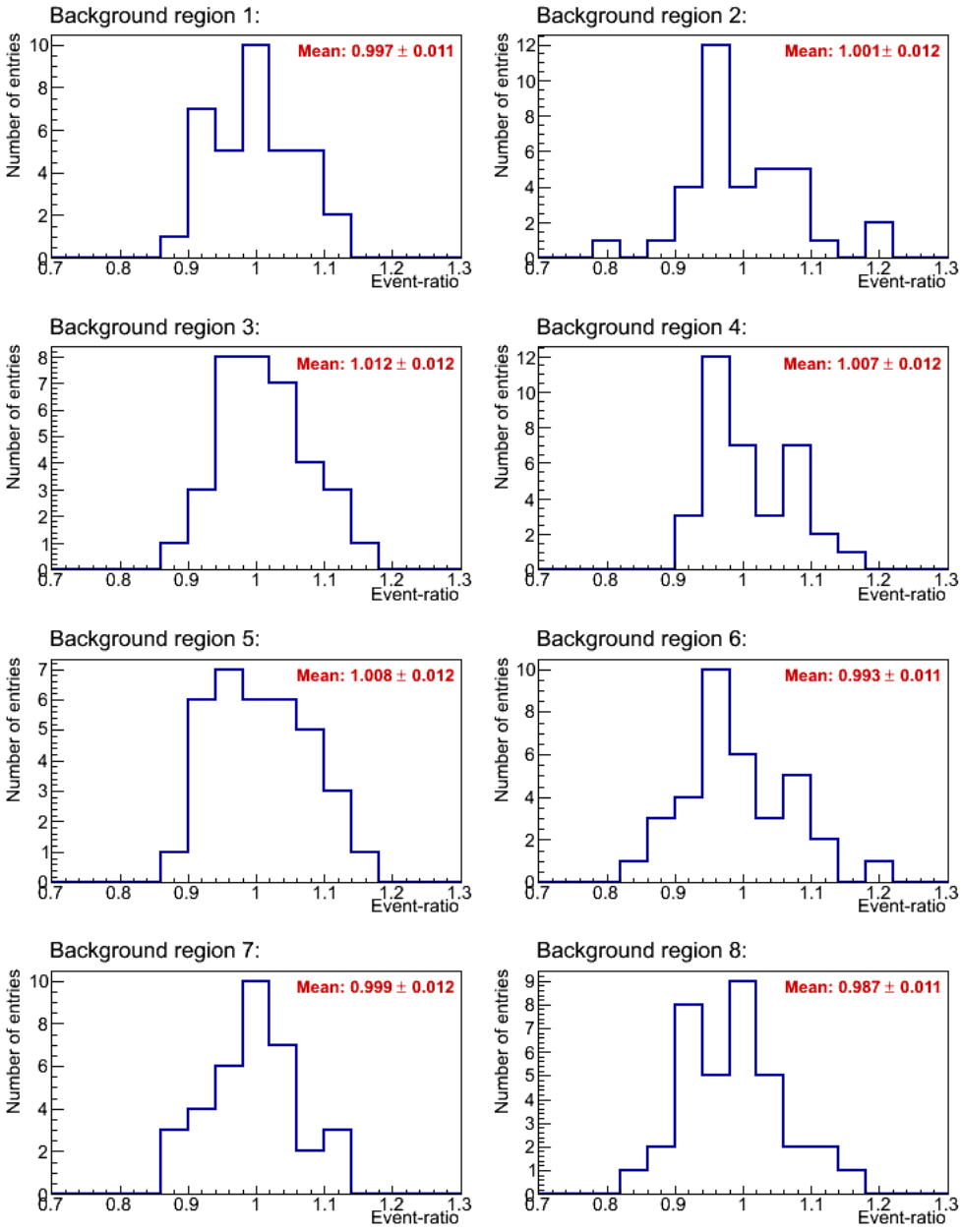

Figure 5.8: Event-ratio distributions for the ANTARES data for the different background regions.

The event-ratio distributions for the ANTARES data are shown in figure 5.8 for the different background regions. The mean of the distribution (i. e. the average event-ratio for that background region) is shown in red in the plot. The error on the mean is also shown, which has been calculated from the error on the event-ratio (equation 5.16) using error propagation. It can be seen that the mean of the event-ratio distribution for each background region is compatible with 1 within the uncertainty. The remaining systematic biases are then limited to about 1%.

5.2.4 *Data-MC comparison*

Finally, the agreement between data and the run-by-run MC simulation is checked for all events that are reconstructed in the background regions. Data-MC comparison plots are made for the 6 key parameters, which are the reconstructed zenith and azimuth angles ($\hat{\theta}$ and $\hat{\phi}$ respectively) and the four cut parameters: Λ, β, E_{rec} and R_{GF}.

For the plots, the following cuts are applied:

- $\cos\hat{\theta} < 0$
- $\Lambda > -5.8$
- $\beta < 10.0^{\circ}$
- $\log_{10}(E_{\mathrm{rec}}) > 2.0$
- $R_{\mathrm{GF}} > 1.35$ (5.17)

which corresponds to the loosest combination of cuts considered in the optimisation (see section 5.3.3).

The plots are shown in figure 5.9. In the plots, the data (in black) are compared to the atmospheric muon simulation (in red) and the atmospheric CC muon-(anti-)neutrino simulation (in purple). For each of the plots all cuts shown in equation 5.17 are applied, except the cut on the variable that is plotted (if applicable). The cut is represented by the dashed dark blue line. In addition, the ratio of data to the sum of both MC contributions is calculated and shown below the corresponding figure; the red line in this plot denotes a ratio of 1.

The agreement between data and MC is reasonable for all variables, but a few remarks must be made. As also found in other analyses, the data exceeds the atmospheric neutrino flux prediction, which can be seen most clearly in the Λ distribution (for $\Lambda > -5$, where the atmospheric muon contribution is small). This is important for the optimisation of the cuts, since a higher

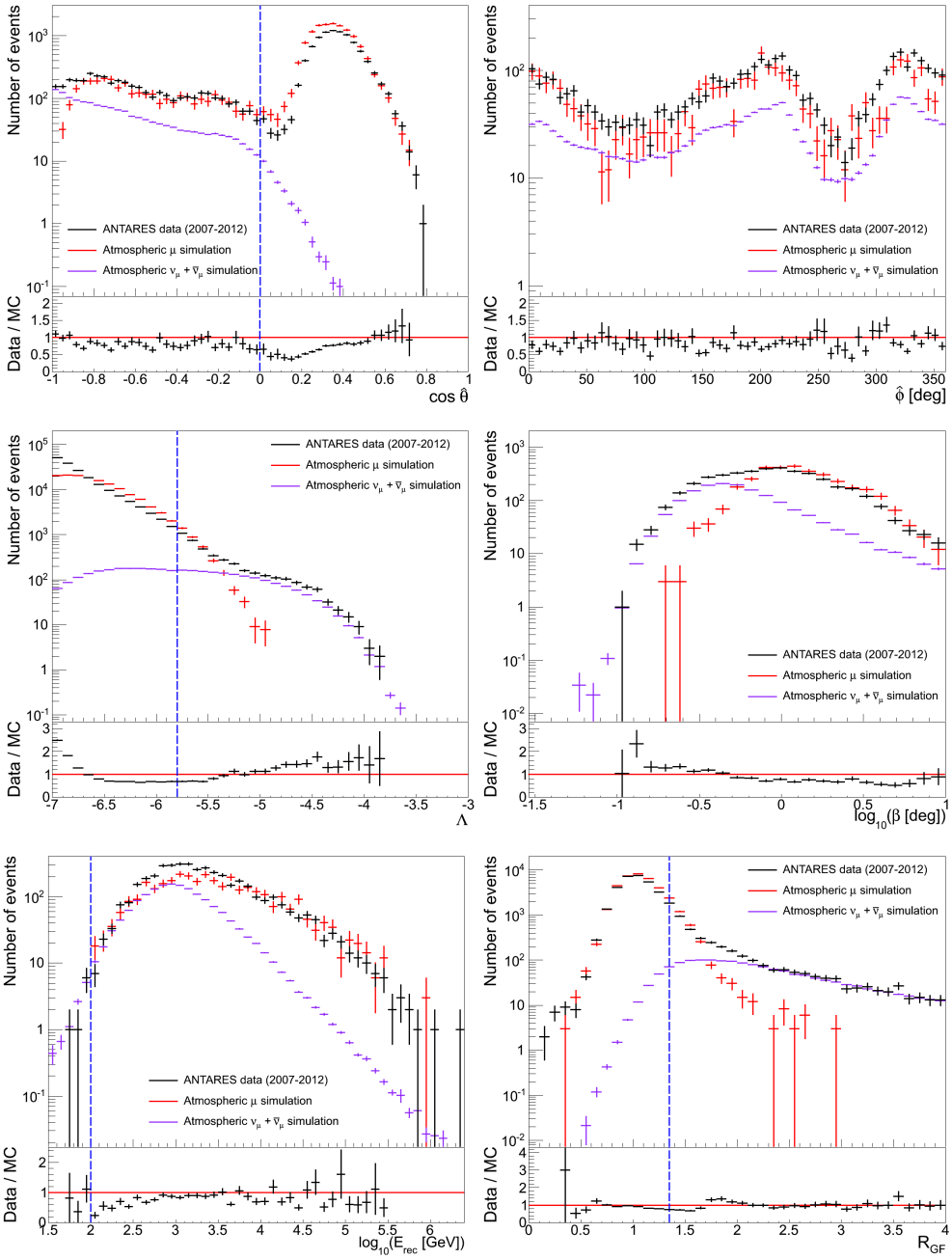

Figure 5.9: Data-MC comparison plots for events from the background regions. TOP LEFT: $\cos\hat{\theta}$ distribution. TOP RIGHT: reconstructed azimuth angle distribution. MIDDLE LEFT: Λ distribution. MIDDLE RIGHT: β distribution. BOTTOM LEFT: $\log_{10}(E_{\mathrm{rec}})$ distribution. BOTTOM RIGHT: R_{GF} distribution.

atmospheric neutrino background might affect the optimal cut values. Instead of an ad hoc scaling of the MC to match the data, the optimisation is repeated for an increased and decreased atmospheric neutrino background. In this way, the influence of the normalisation of the atmospheric neutrino flux can be quantified.

Furthermore, there are some apparent features in the Λ and $\cos\hat{\theta}$ distributions. In the former, the shape of the muon MC is different than the data for low values, while for the latter the shapes are different for downgoing events. These differences are thought to be caused by high optical background [Bogazzi, 2014]. Since the applied cuts avoid these features and the shape of the data is reasonably well described for the regions of interest, this should not be a problem for this analysis.

5.3 EVENT SELECTION

After optimising the size of the signal region and checking for systematic biases, the last step is the optimisation of the cut parameters: Λ, β, E_{rec} and R_{GF}. Since the optimisation problem is 4 dimensional, the process is split into three steps. First the cut on R_{GF} is not applied and the optimal combination of the other three parameters is found; then the same is done for β. This gives an idea about where to look in the cut space, so that the full 4D optimisation can be performed more efficiently.

In the following sections, all events triggered either by the 3N, the 2T3 or the TQ trigger are used and the same cuts are applied regardless of the trigger algorithm. In addition, only events that are reconstructed as upgoing are used. The effect of variable cuts is checked in section 5.3.4. In the following sections, the cut on $\log_{10}(E_{\text{rec}})$ is varied between 2.0 and 3.0 in steps of 0.05. The ranges and step sizes used for Λ, β and R_{GF} vary and are given below.

5.3.1 *Optimisation without R_{GF}*

The MRF is calculated in the same way as for the optimisation of the size of the signal region. The quality cuts are applied, the number of signal and background events is obtained from the run-by-run MC and the MRF is calculated using formula 5.6.

To visualise the 3D cut space, a 2D grid of the MRF versus the applied Λ and $\log_{10}(E_{\text{rec}})$ cuts is made for a fixed value of β, and the minimum is obtained. Examples can be found in figure 5.10.

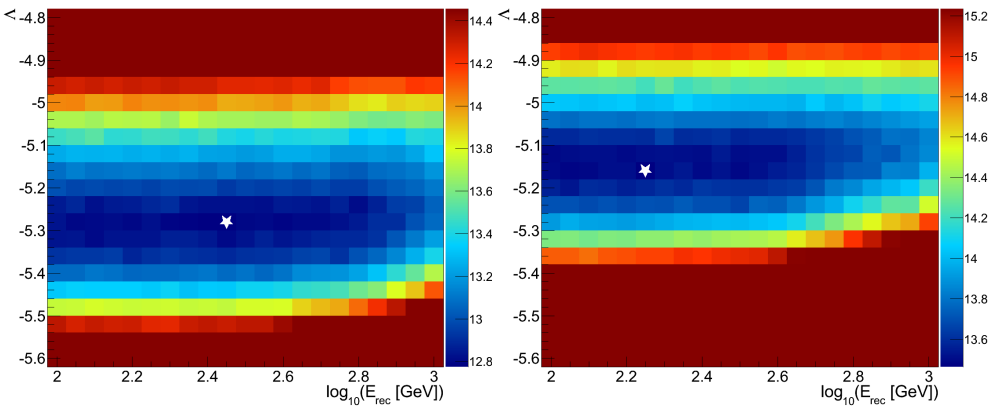

Figure 5.10: MRF versus Λ and $\log_{10}(E_{\text{rec}})$; no R_{GF} cut is applied. The white star marks the location of the minimum. LEFT: for $\beta < 0.7^\circ$. RIGHT: for $\beta < 1.4^\circ$.

This process is repeated for other β values to find the global minimum. The cut on Λ is varied between -5.6 and -4.8 in steps of 0.04 and the cut on β between 0.4° and 1.5° in steps of 0.1°.

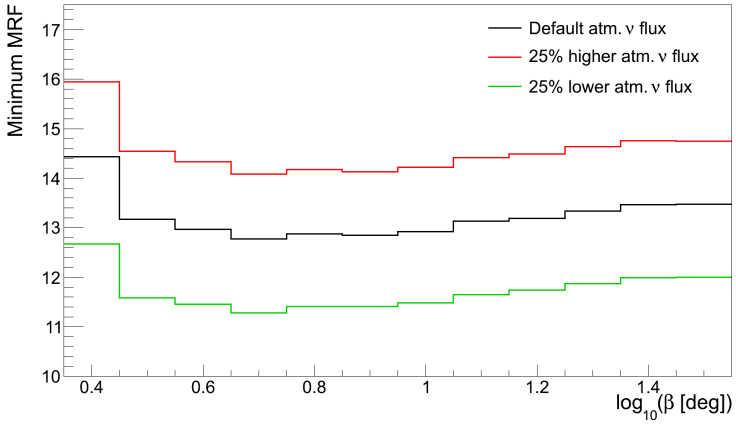

Figure 5.11: Minimum MRF versus β without applying a R_{GF} cut. For each β cut, the Λ and $\log_{10}(E_{\text{rec}})$ cuts have been optimised.

The results of the optimisation are shown in table 5.6 and the minimum MRF is plotted versus β in figure 5.11. It can be seen that the optimal β cut is found at 0.7°, although the minimum is quite shallow. The same β cut is found to be optimal for the increased/decreased atmospheric neutrino flux. Also the energy cut is found to be stable under variation of the atmospheric neutrino flux. The Λ cut does vary however; a looser cut is

ATM. ν FLUX	OPTIMAL CUT VALUES Λ	β	$\log_{10}(E_{\text{rec}})$	MIN. MRF	μ_s	μ_b	PURITY
Default	-5.28	0.7°	2.45 ($= 282\,\text{GeV}$)	12.77	1.47	90.7	92.1%
25% incr.	-5.32	0.7°	2.5 ($= 316\,\text{GeV}$)	14.09	1.52	119	91.3%
25% decr.	-5.24	0.7°	2.45 ($= 282\,\text{GeV}$)	11.28	1.41	64.3	90.0%

Table 5.6: Optimal cuts and obtained MRF value for the optimisation without R_{GF}.

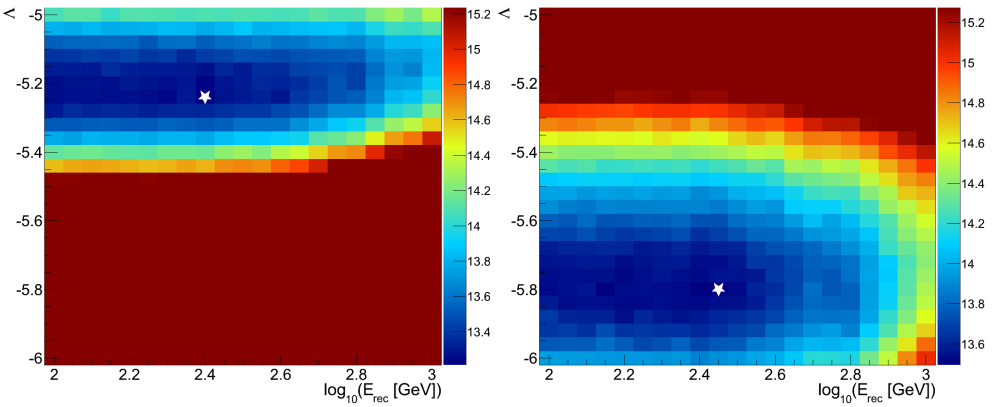

Figure 5.12: MRF versus Λ and $\log_{10}(E_{\text{rec}})$; no β cut is applied. The white star marks the location of the minimum. LEFT: for $R_{\text{GF}} > 1.2$. RIGHT: for $R_{\text{GF}} > 1.8$.

optimal when the atmospheric neutrino background is higher and vice versa. In general, a purity of the final event sample of around 90% is optimal. For a higher atmospheric neutrino flux, more misreconstructed atmospheric muons are allowed in the sample, leading to a looser cut on Λ.

5.3.2 *Optimisation without β*

The same procedure is now applied to determine the optimal cut values without application of the β cut. For this, the cut on Λ is varied between -6.0 and -5.0 in steps of 0.04 and the cut on R_{GF} between 1.0 and 2.0 in steps of 0.1. The Λ-$\log_{10}(E_{\text{rec}})$ grids for two R_{GF} cuts are shown in figure 5.12. It can be seen that the stricter the cut on the R_{GF} parameter is, the looser the Λ cut can be.

The results for the optimisation are shown in table 5.7 and the minimum MRF is plotted versus R_{GF} in figure 5.13. A R_{GF} cut

ATM. ν FLUX	OPTIMAL CUT VALUES Λ	R_{GF}	$\log_{10}(E_{rec})$	MIN. MRF	μ_s	μ_b	PURITY
Default	−5.6	1.6	2.55 (= 355 GeV)	12.65	1.79	134	90.1%
25% incr.	−5.64	1.6	2.55 (= 355 GeV)	13.93	1.84	174	90.3%
25% decr.	−5.52	1.6	2.55 (= 355 GeV)	11.18	1.68	90.8	91.1%

Table 5.7: Optimal cuts and obtained MRF value for the optimisation without β.

of 1.6 is found to be optimal, with a Λ cut of −5.6. This value corresponds to a much looser cut compared to when using a cut on β instead of a cut on R_{GF}. It can thus be concluded that the R_{GF} variable is more powerful than β to reject misreconstructed atmospheric muons.

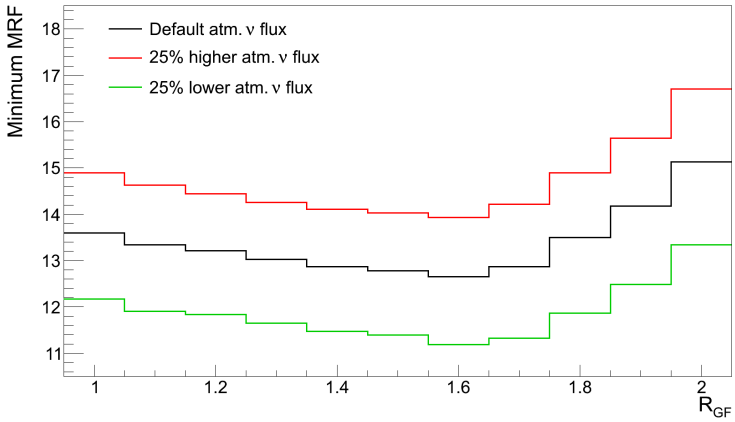

Figure 5.13: Minimum MRF versus R_{GF} without applying a β cut. For each R_{GF} cut, the Λ and $\log_{10}(E_{rec})$ cuts have been optimised.

An increase or decrease of the atmospheric neutrino background yields the same conclusions as before. The R_{GF} and reconstructed energy cuts are not affected, and a looser Λ cut is found to be optimal for an increased atmospheric neutrino background.

5.3.3 *Full optimisation*

After performing the 3D optimisations, the full 4D optimisation is performed. Using the results from the previous sections, the cut parameters are varied as follows. The cut on Λ is varied between

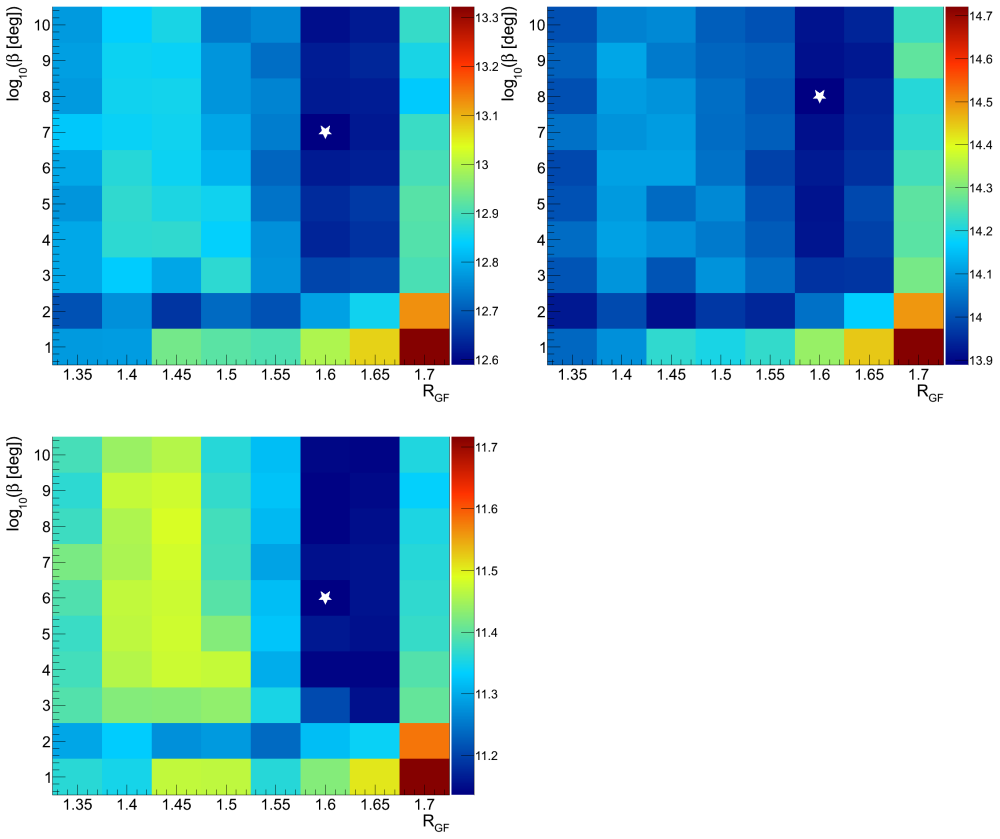

Figure 5.14: Minimum MRF versus R_{GF} and β. For each R_{GF}-β cut combination, the Λ and $\log_{10}(E_{rec})$ cuts have been optimised. The white star marks the location of the minimum. TOP LEFT: for the default atmospheric neutrino background. TOP RIGHT: for a 25% higher atmospheric neutrino background. BOTTOM LEFT: for a 25% lower atmospheric neutrino background.

-5.8 and -5.2 in steps of 0.04, the cut on R_{GF} between 1.35 and 1.7 in steps of 0.05 and the cut on β between 1.0° and 10.0° in steps of 1.0°.

Like before, the minimum MRF is obtained for fixed R_{GF} and β cuts by finding the minimum in the Λ-$\log_{10}(E_{rec})$ grid. The results are summarised in table 5.8 and the minimum MRF is plotted versus β and R_{GF} in figure 5.14 for the default atmospheric neutrino flux as well as for the increased/decreased flux.

The same R_{GF} and Λ cut values which were found to be optimal in the previous section are also found to be optimal now, but using the β cut in addition is beneficial, since a slightly lower MRF value is found. The required β cut is quite loose, which

ATM. ν FLUX	OPTIMAL CUT VALUES Λ	R_{GF}	β	$\log_{10}(E_{rec})$	MIN. MRF	μ_s	μ_b	PURITY
Default	-5.6	1.6	7.0°	2.55 (= 355 GeV)	12.59	1.77	131	91.1%
25% incr.	-5.64	1.6	8.0°	2.55 (= 355 GeV)	13.89	1.83	171	91.1%
25% decr.	-5.52	1.6	6.0°	2.55 (= 355 GeV)	11.14	1.67	88.7	92.1%

Table 5.8: Optimal cuts and obtained MRF value for the full optimisation.

can be expected since both Λ and R_{GF} are powerful in removing misreconstructed muons. The results for the increased and decreased atmospheric neutrino background are almost identical to the result for the default atmospheric neutrino flux. As found before, a slightly looser (stricter) cut on Λ is better for a higher (lower) neutrino background. The same holds true for the cut on β, a looser cut on this parameter is better for a higher neutrino background and vice versa.

Since the number of atmospheric neutrinos seems to be higher in data than predicted from the MC (see section 5.2.4), the cut combination corresponding to the increased atmospheric neutrino flux is chosen. The optimal cut combination obtained is then:

- $\cos\hat{\theta} < 0$
- $\Lambda > -5.64$
- $\beta < 8.0^\circ$
- $\log_{10}(E_{rec}) > 2.55$
- $R_{GF} > 1.6$ (5.18)

It is interesting to compare the MRF obtained by additionally using the R_{GF} parameter to that obtained when only using the standard cut variables (Λ, β and reconstructed energy). When comparing the results from section 5.3.1 to the results obtained in this section (for the increased atmospheric neutrino background) it is found that the MRF is 1.4% better when additionally using the R_{GF} parameter. In addition, the expected number of signal events (from the Drift model) increases from 1.52 to 1.83 (i. e. a 20% increase).

5.3.4 *Additional optimisation*

In the cut optimisation described in the last sections, two simplifications have been used: the cut on the reconstructed zenith angle

ATM. ν FLUX	$\hat{\theta}$-CUT	OPTIMAL CUT VALUES Λ	$\log_{10}(E_{\text{rec}})$	MIN. MRF	μ_s	μ_b	PURITY
Default	90°	−5.59	2.55 (= 355 GeV)	12.60	1.76	129	91.5%
	87°	−5.62	2.55 (= 355 GeV)	12.64	1.81	137	89.4%
	84°	−5.58	2.55 (= 355 GeV)	12.63	1.75	129	91.2%
	81°	−5.53	2.55 (= 355 GeV)	12.95	1.69	126	88.7%
25% incr.	90°	−5.62	2.55 (= 355 GeV)	13.87	1.80	166	92.0%
	87°	−5.66	2.55 (= 355 GeV)	13.94	1.86	178	89.7%
	84°	−5.62	2.55 (= 355 GeV)	13.94	1.81	168	91.4%
	81°	−5.62	2.7 (= 501 GeV)	14.21	1.71	157	87.3%
25% decr.	90°	−5.55	2.6 (= 398 GeV)	11.12	1.69	91.1	90.7%
	87°	−5.55	2.55 (= 355 GeV)	11.19	1.71	94.8	90.0%
	84°	−5.52	2.55 (= 355 GeV)	11.18	1.67	90.4	91.3%
	81°	−5.53	2.55 (= 355 GeV)	11.51	1.69	97.8	85.4%

Table 5.9: Optimal cuts and obtained MRF value for the different cuts on the reconstructed zenith angle.

is fixed to 90° and the same cuts are applied regardless of which trigger algorithm selected the event. In this section the effect of these simplifications is investigated.

Relaxing the cut on the reconstructed zenith angle

In the standard optimisation, only events which are reconstructed as upgoing are considered. It could be beneficial to extend the zenith cut somewhat. The visibility of the Galactic centre (from where the highest signal is expected) is about 68% when considering only upgoing events (i. e. with $\hat{\theta} > 90°$). However, extending the cut on the reconstructed zenith to 81° for instance, the visibility rises to 77%.

From the $\cos\hat{\theta}$ distribution in figure 5.9 it can be seen that the atmospheric muon background remains constant until about $\cos\hat{\theta} = 0.15$ (which corresponds to $\hat{\theta} \simeq 81°$), so by retuning the Λ cut, it is possible that a better sensitivity is obtained.

In order to check this, the R_{GF} and β cuts are fixed at the values found in the previous section and zenith cuts of 81°, 84°, 87° and 90° are tested. In each case the $\log_{10}(E_{\text{rec}})$ and Λ cuts are optimised, where the cut on Λ is varied between −5.7 and −5.45 in steps of 0.01. Note that the step size in Λ is now 4 times as fine as before.

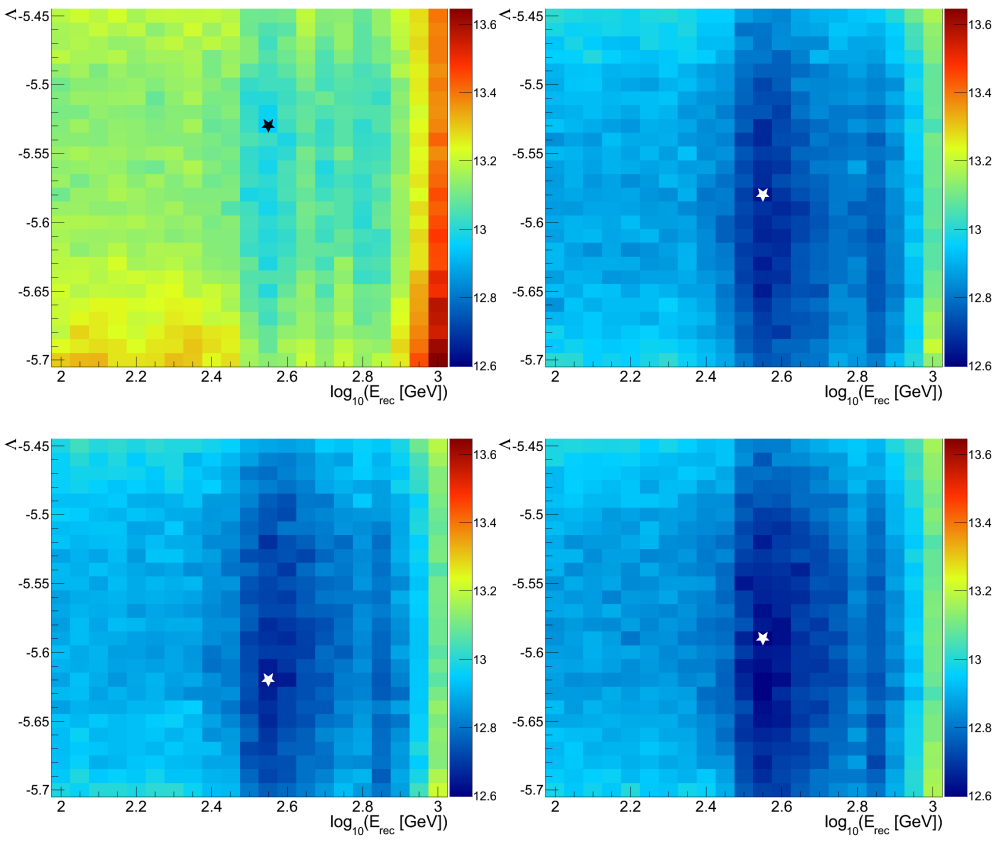

Figure 5.15: MRF versus Λ and $\log_{10}(E_{\text{rec}})$. The white (black) star marks the location of the minimum. TOP LEFT: for $\hat{\theta} > 81^{\circ}$. TOP RIGHT: for $\hat{\theta} > 84^{\circ}$. BOTTOM LEFT: for $\hat{\theta} > 87^{\circ}$. BOTTOM RIGHT: for $\hat{\theta} > 90^{\circ}$.

The results are summarised in table 5.9 and the MRF is plotted versus Λ and $\log_{10}(E_{\text{rec}})$ for each of the $\hat{\theta}$ cuts in figure 5.15. It can be seen that relaxing the cut on the reconstructed zenith angle does not result in a much better value for the MRF. Relaxing the zenith cut to 87° increases the signal a bit, but the background increases also, due to the slightly looser Λ cut found to be optimal in this case. The resulting purity of the final event sample is then lower, and a worse MRF value is found compared to a zenith cut of 90°. Relaxing the zenith cut to 84° gives almost the same results as for the zenith cut at 90°. The signal is slightly lower in this case, again resulting in a slightly higher MRF value. When relaxing the zenith cut to 81°, the MRF gets significantly worse.

In conclusion, relaxing the zenith cut is not beneficial, so the default cut ($\hat{\theta} > 90°$) is kept. Since a finer step size is used for the Λ parameter, a slightly different optimal value is found for this parameter. This value will be used instead of the one found in the standard optimisation. As before, the cuts obtained for the increased atmospheric neutrino background are chosen, resulting in the same cuts as listed in equation 5.18, with the difference that $\Lambda > -5.62$ instead.

Retuning the cuts for events only triggered by the TQ trigger

Finally, it is checked if separately optimising the cuts for events triggered only by the TQ trigger is beneficial. This concerns events that are triggered exclusively by the TQ trigger and not by the 3N or 2T3 triggers. These events will be referred to as *TQonly* events. Until now the same cuts have been applied to all events. For the optimal cut combination, the TQ trigger adds about 1% more neutrinos, and by retuning the cuts on the TQonly events this percentage might increase.

To check this, the cuts on the events triggered by the 3N and/or 2T3 triggers are kept fixed at the values found in the previous section and the cuts for events only triggered by the TQ trigger are varied. In this, only the Λ and $\log_{10}(E_{\text{rec}})$ cuts are varied; the β and R_{GF} cuts are kept fixed. The cut on the logarithm of the reconstructed energy is, as before, varied between 2.0 and 3.0 in steps of 0.05 and the cut on Λ is varied between -5.7 and -5.45 in steps of 0.01.

The results for varying the cuts on the TQonly events and keeping them fixed to the cuts found in the last section are summarised in table 5.10. The MRF versus Λ and $\log_{10}(E_{\text{rec}})$

ATM. ν FLUX	TQONLY CUTS	OPTIMAL CUT VALUES Λ	OPTIMAL CUT VALUES $\log_{10}(E_{\text{rec}})$	MIN. MRF	μ_s	μ_b	PURITY
Default	Fixed	-5.62	2.55 (= 355 GeV)	12.60	1.80	135	90.2%
	Varied	-5.47	2.35 (= 224 GeV)	12.54	1.80	134	90.6%
25% incr.	Fixed	-5.62	2.55 (= 355 GeV)	13.87	1.80	166	92.0%
	Varied	-5.57	2.4 (= 251 GeV)	13.84	1.80	165	92.4%
25% decr.	Fixed	-5.62	2.55 (= 355 GeV)	11.18	1.80	105	87.3%
	Varied	-5.46	2.2 (= 158 GeV)	11.09	1.80	104	87.9%

Table 5.10: Optimal cuts and obtained MRF value when retuning the cuts on TQonly events.

for an increased atmospheric neutrino background is shown in figure 5.16. Note that the maximum MRF value in the plot is only 2.5% higher than the minimum, so the variations are very small. The MRF improves slightly by retuning the cuts for the TQonly events, which is caused by an increase of the purity of the sample. The table confirms the main conclusion. The sample of events exclusively triggered by the TQ trigger has a slightly higher contamination of misreconstructed atmospheric muons, so by applying a slightly stricter Λ cut on these events, the signal is kept constant while the background is decreased. The effect is small because the livetime of the TQ trigger is 0.66 year compared to the total livetime of 3.53 year.

Even though the effect of applying different cuts to the TQonly events is small, it does provide a lower MRF value and the expected background decreases by about 1 event. So, for the final event selection, all events are selected that pass the following set of cuts:

- $\cos\hat{\theta} < 0$
- $\beta < 8.0^\circ$
- $R_{\mathrm{GF}} > 1.6$
- For 3N or 2T3 triggered events:
  - $\Lambda > -5.62$
  - $\log_{10}(E_{\mathrm{rec}}) > 2.55$
- For TQonly triggered events:
  - $\Lambda > -5.57$
  - $\log_{10}(E_{\mathrm{rec}}) > 2.4$ (5.19)

To check the effect of including events triggered by the TQ trigger, the results obtained above are compared to the results obtained when only using the events triggered by the 3N and/or the 2T3 trigger. Not including the TQonly events[30] gives $\mu_{\mathrm{s}} = 1.74$ and $\mu_{\mathrm{b}} = 156$, resulting in a MRF of 13.92. Comparing these numbers to the results obtained above shows that that the MRF improves by 0.6% when including the TQ triggered events and 3% more signal events are expected from the Drift model.

[30] *The cuts are re-optimised for the sample without the TQ triggered events, resulting in:* $R_{GF} > 1.6$, $\beta < 8.0^\circ$, $\Lambda > -5.63$, $log_{10}(E_{rec}) > 2.65$.

The increase in the signal of 3% can be compared with the expected gain for the diffuse Galactic neutrino flux of 6%, as calculated in section 4.2.4. The quoted gain of 6% is at trigger level however, whereas not all of the extra neutrinos are reconstructable and/or pass the applied quality cuts, which explains the difference. In addition, since the background increases as

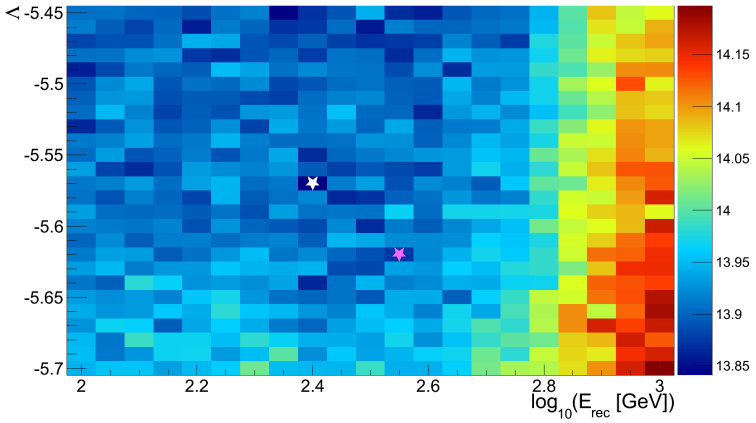

Figure 5.16: MRF versus Λ and $\log_{10}(E_{\mathrm{rec}})$ for an increased atmospheric neutrino background. The white star marks the location of the minimum when retuning the cuts on the TQonly triggered events; the purple star marks the location of the minimum when keeping the cuts fixed to the optimal values found in the previous section.

well, the improvement in sensitivity is only 0.6%. Nevertheless, using the TQ trigger is beneficial.

5.4 ANTARES SENSITIVITY

After the final event sample has been obtained, the sensitivity of ANTARES to the diffuse Galactic neutrino flux can be determined. For this, the data from the background regions are used. The number of events surviving the cuts in each of the 8 background regions is presented in table 5.11. The distribution of the events is shown in figure 5.19; for the numbering of the regions see figure 5.5.

The background measurement gives an expected background of $n_{\mathrm{b}} = 166 \pm 5$, which can be used to calculate the MRF for the four signal models. Since the background measurement has been performed, the average signal upper limit is calculated slightly different than given by equation 5.5, since no averaging has to be performed over the possible values of n_{bg} and n_{b} will be used instead of μ_{b}:

$$\overline{\mu}^{\alpha}(n_{\mathrm{obs}}, n_{\mathrm{bg}}) = \sum_{n_{\mathrm{obs}}=0}^{\infty} \mu^{\alpha}(n_{\mathrm{obs}}, n_{\mathrm{bg}}) \frac{n_{\mathrm{b}}^{n_{\mathrm{obs}}} e^{-n_{\mathrm{b}}}}{n_{\mathrm{obs}}!}, \tag{5.20}$$

which will be used in equation 5.6.

BACKGROUND REGION	NUMBER OF EVENTS 3N + 2T3	TQONLY	TOTAL
1	161 ± 13	2 ± 2	163 ± 13
2	165 ± 13	2 ± 2	167 ± 13
3	174 ± 13	3 ± 2	177 ± 14
4	147 ± 12	2 ± 2	149 ± 12
5	141 ± 12	3 ± 2	144 ± 12
6	162 ± 13	1 ± 1	163 ± 13
7	177 ± 13	3 ± 2	180 ± 13
8	178 ± 13	3 ± 2	181 ± 13
Sum	1305 ± 36	19 ± 4	1324 ± 36

Table 5.11: Number of events measured per background region. The error on the number of events is the statistical uncertainty.

Table 5.12 summarises the expected signal and average MRF values for the four signal models. Also shown is the energy validity range of the average upper limit, which is defined to be the energy interval containing the central 90% of the detected signal[31].

[31] *The energy validity range is determined using the MC simulation.*

MODEL NAME	μ_s	MRF	ENERGY VALIDITY RANGE
NoDrift_simple	0.90	27.57	0.17 TeV – 61 TeV
NoDrift_advanced	1.12	22.11	0.15 TeV – 45 TeV
Drift	1.80	13.77	0.18 TeV – 66 TeV
Fermi $\gamma \rightarrow \nu$	1.41	17.65	0.18 TeV – 71 TeV

Table 5.12: Expected signal, MRF and energy validity range for the signal models.

For the Drift model, the obtained MRF is 13.77, which is slightly lower than the MRF obtained for this cut combination in the previous chapter. This is caused by the different way of calculating the average signal upper limit.

The signal predictions for the other three models are lower, resulting in a higher MRF value. Also the energy validity ranges are slightly different, which is caused by a different predicted spectral index of the signal, see also table 2.3.

The sensitivity can also be presented in a model independent way, by starting with an isotropic flux with a given spectral index γ and an arbitrary normalisation given by the flux constant $\mathcal{F}_\gamma$:

$$\Phi_{\nu_\mu+\overline{\nu}_\mu} = \mathcal{F}_\gamma \cdot E_\nu^{-\gamma}\,\mathrm{GeV}^{-1}\,\mathrm{m}^{-2}\,\mathrm{sr}^{-1}\,\mathrm{s}^{-1}, \tag{5.21}$$

and calculating the average expected flux upper limit $\overline{\mathcal{F}}_\gamma^{90\%}$ (at a confidence level of 90%). The advantage of presenting the sensitivity in this way, is that it is more general, and not just applicable to a single signal model.

SPECTRAL INDEX	$\overline{\mathcal{F}}_\gamma^{90\%}$	ENERGY VALIDITY RANGE
2.5	$1.4\,\mathrm{GeV}^{1.5}\,\mathrm{m}^{-2}\,\mathrm{sr}^{-1}\,\mathrm{s}^{-1}$	$0.24\,\mathrm{TeV} - 96\,\mathrm{TeV}$
2.6	$3.2\,\mathrm{GeV}^{1.6}\,\mathrm{m}^{-2}\,\mathrm{sr}^{-1}\,\mathrm{s}^{-1}$	$0.18\,\mathrm{TeV} - 71\,\mathrm{TeV}$
2.7	$7.1\,\mathrm{GeV}^{1.7}\,\mathrm{m}^{-2}\,\mathrm{sr}^{-1}\,\mathrm{s}^{-1}$	$0.15\,\mathrm{TeV} - 52\,\mathrm{TeV}$

Table 5.13: The average limit on the flux constant for different values of γ.

The spectral indices predicted by the signal models are in the range from 2.6 and 2.7, so the sensitivity is calculated for these two values of γ. Besides these values, the sensitivity is also calculated for $\gamma = 2.5$. The results are shown in table 5.13.

The sensitivity for $\gamma = 2.7$ can be compared to the flux upper limit as set by the AMANDA-II experiment:

$$\Phi_{\nu_\mu+\overline{\nu}_\mu} < 4.8\,E_\nu^{-2.7}\,\mathrm{GeV}^{-1}\,\mathrm{m}^{-2}\,\mathrm{sr}^{-1}\,\mathrm{s}^{-1}, \tag{5.22}$$

with E_ν in GeV, which is valid in the energy range from 0.2 TeV to 40 TeV [Kelley et al., 2005]. By comparing the normalisation factor to the corresponding result in table 5.13 it can be seen that the ANTARES sensitivity is about 50% worse than this limit.

However for a fair comparison the ANTARES sensitivity should be compared to the AMANDA-II sensitivity. In the AMANDA-II analysis 283.3 background events were expected, but the data in the signal region underfluctuated and only 272 events were observed. Using the expected number of background events gives a sensitivity of $7.8\,\mathrm{GeV}^{1.7}\,\mathrm{m}^{-2}\,\mathrm{sr}^{-1}\,\mathrm{s}^{-1}$, which is 10% worse than the ANTARES sensitivity. Also the energy validity range of the AMANDA-II limit is slightly smaller.

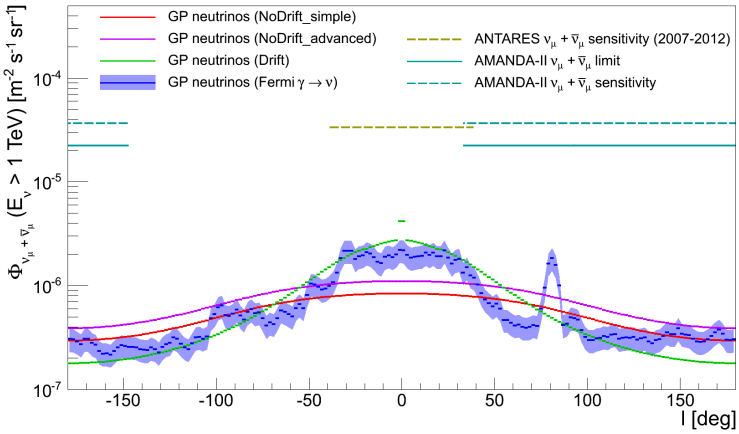

Figure 5.17: Sensitivities and AMANDA-II limit versus Galactic longitude together with the average signal fluxes ($|b| < 4.5°$) above 1 TeV.

The AMANDA-II limit and the sensitivities for both experiments are shown versus Galactic longitude in figure 5.17, together with the average signal fluxes from the four models (as already shown on a linear scale in figure 2.25). This plot shows a more important difference between the two experiments. A different region has been used as signal region by the AMANDA-II experiment: $33° < l < 213°$ and $-4.4° < b < 4.4°$. While the latitudinal extension of this signal region has been optimised using the MRF method, the longitudinal extension has been chosen simply because this is the range of longitude values AMANDA-II can observe (around $b = 0°$), see also figure 2.28. The size of the signal region used by AMANDA-II is 0.48 sr, which is a factor of about 2.3 bigger than that used in the ANTARES analysis. Since a bigger region is used by AMANDA-II, the sensitivity will be lower. To really compare the sensitivities, one should consider how they compare to the expected signal fluxes in both regions. The average fluxes in the signal region used by AMANDA-II are on average a factor of about three lower than the fluxes in the signal region used in the ANTARES analysis (see also table 2.3), making the ANTARES sensitivity a factor of three more stringent.

5.4.1 *The cosmic neutrino flux measured by IceCube*

As mentioned already in the introduction, the IceCube experiment has recently measured a flux of cosmic neutrinos. At the time of writing, the flux seems isotropic. The most recent pub-

lication by IceCube [Aartsen et al., 2015] gives the following parameterisation of the flux (per neutrino flavour):

$$\Phi_{\nu+\bar{\nu}} = 2.06^{+0.4}_{-0.3} \cdot 10^{-14} \left(\frac{E_\nu}{10^5\,\mathrm{GeV}}\right)^{-2.46\pm0.12} \mathrm{GeV}^{-1}\,\mathrm{m}^{-2}\,\mathrm{sr}^{-1}\,\mathrm{s}^{-1}. \tag{5.23}$$

Using the best-fit results (i. e. the mean of the two fit parameters) for the flux given by equation 5.23 and assuming the flux is truly diffuse, 1.0 event is expected from this flux in the signal region for the livetime considered here. In case of a diffuse flux, the same number of events is expected also in each of the background regions, so the sensitivity to an additional flux of neutrinos from the Galactic plane is not affected (since the background is measured from data). If however, the flux is Galactic in origin (or has a significant Galactic component), there will be an additional contribution to the number of events in the signal region, which could show up as an excess.

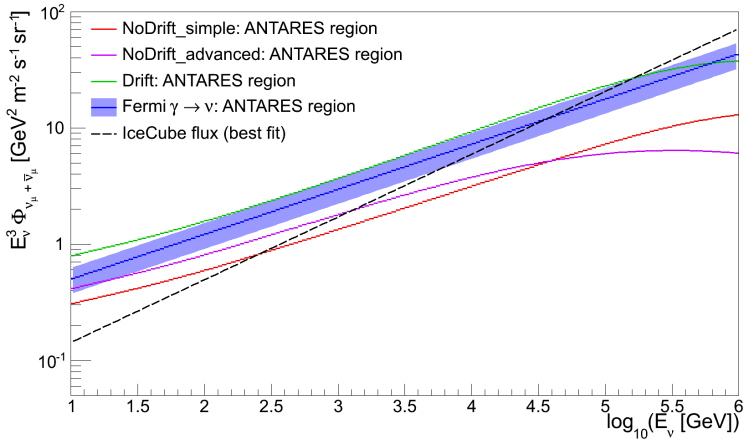

Figure 5.18: Average diffuse Galactic neutrino fluxes in the ANTARES signal region together with the best-fit to the flux measured by IceCube versus neutrino energy.

It is interesting that the number of events expected in the signal region is of the same order as the signal predicted by the four diffuse Galactic neutrino flux models that are used (which ranges from 0.9 to 1.8). This is not surprising, since the IceCube flux is comparable in size to the average fluxes predicted in the signal region, as can be seen from figure 5.18 in which the fluxes are plotted versus neutrino energy. In addition, the best-fit value for the spectral index is 2.46, which is close to the spectral indices predicted by the models (2.6 to 2.7).

From figure 5.18 it seems that the neutrino flux measured by IceCube could be explained as being from cosmic rays interacting in our Galaxy. However, one should keep in mind that the diffuse Galactic neutrino fluxes that are shown in the figure are the average fluxes in the ANTARES signal region, while the IceCube flux is an isotropic flux. Assuming that the fluxes are isotropic and comparing the neutrino fluxes integrated over the full sky leads to the conclusion that the flux observed by IceCube is between one and two orders of magnitude higher. This means that the flux measured by IceCube cannot be explained as originating solely from cosmic ray interactions with interstellar matter in our Galaxy.

5.5 RESULTS

The background measurement described earlier gives an expected background of $n_b = 166 \pm 5$. In the signal region a total of $n_{obs} = 177 \pm 13$ events are measured. This number consists of 176 events triggered by the 3N and/or 2T3 triggers and 1 event triggered exclusively by the TQ trigger. A sky-map of the event distribution is shown in figure 5.19.

Figures 5.20 and 5.21 show Data-MC comparison plots for the reconstructed zenith and azimuth angles ($\hat{\theta}$ and $\hat{\phi}$ respectively) and the four quality parameters: Λ, β, E_{rec} and R_{GF}. The left plots in these figures show the distributions for events that are reconstructed in the background regions; the right plots show the same for events reconstructed in the signal region. Like in figure 5.9, the data (in black) is compared to the atmospheric muon simulation (in red) and the atmospheric CC muon (anti-) neutrino simulation (in purple); in addition the fluxes predicted by the Drift and Fermi $\gamma \rightarrow \nu$ models are shown. For each of the plots all cuts shown in equation 5.19 are applied, except the cut on the variable that is plotted (if applicable)[32]. The cut is represented by the dashed dark blue line. In addition, the ratio of data to the sum of the MC contributions is calculated and shown below the corresponding figure; the red line in this plot denotes a ratio of 1.

When comparing the distributions for signal and background regions, it can be seen that the shape is the same. The data and atmospheric neutrino fluxes are about 8 times as high in the background regions, whereas the signal predicted by the Drift and Fermi $\gamma \rightarrow \nu$ models is higher in the signal region. This is expected, since the signal region is defined to maximise the sensitivity and there are 8 background regions.

[32] *Since different Λ and $\log_{10}(E_{rec})$ cuts are obtained for events triggered by the 3N and/or 2T3 triggers as for TQonly events, the cuts on these parameters are not shown.*

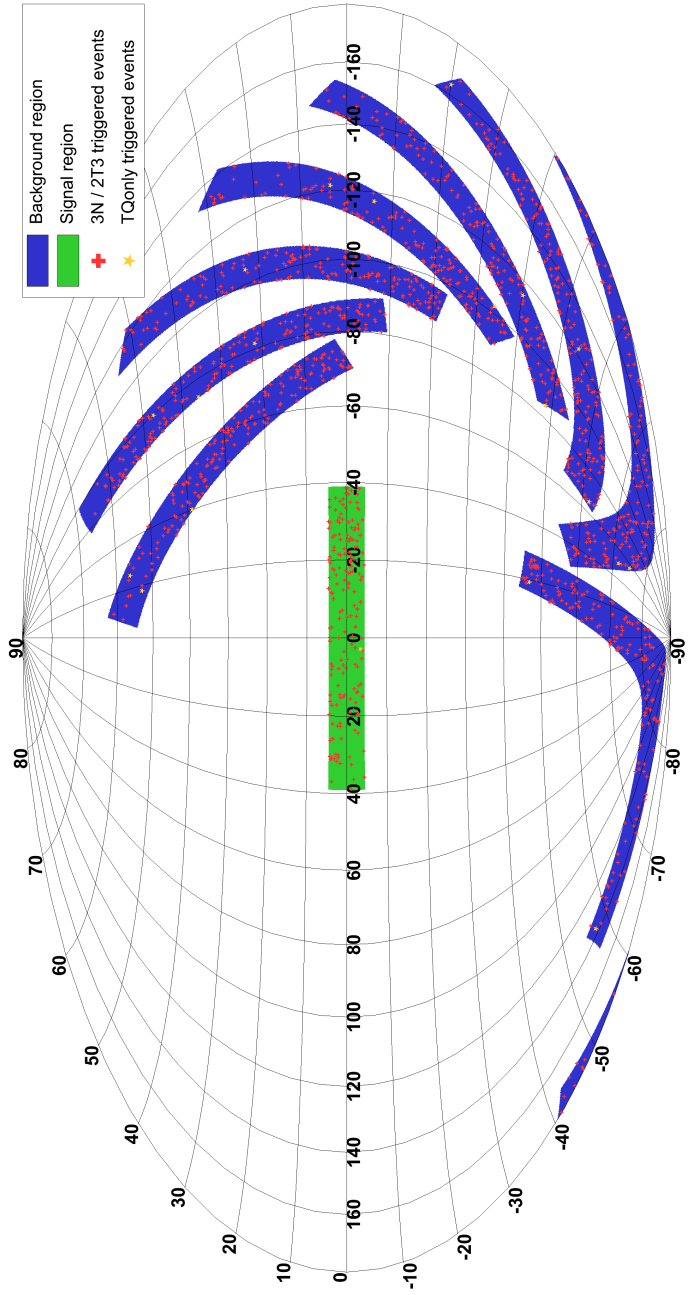

Figure 5.19: The distribution of the events in the signal region and the 8 background regions.

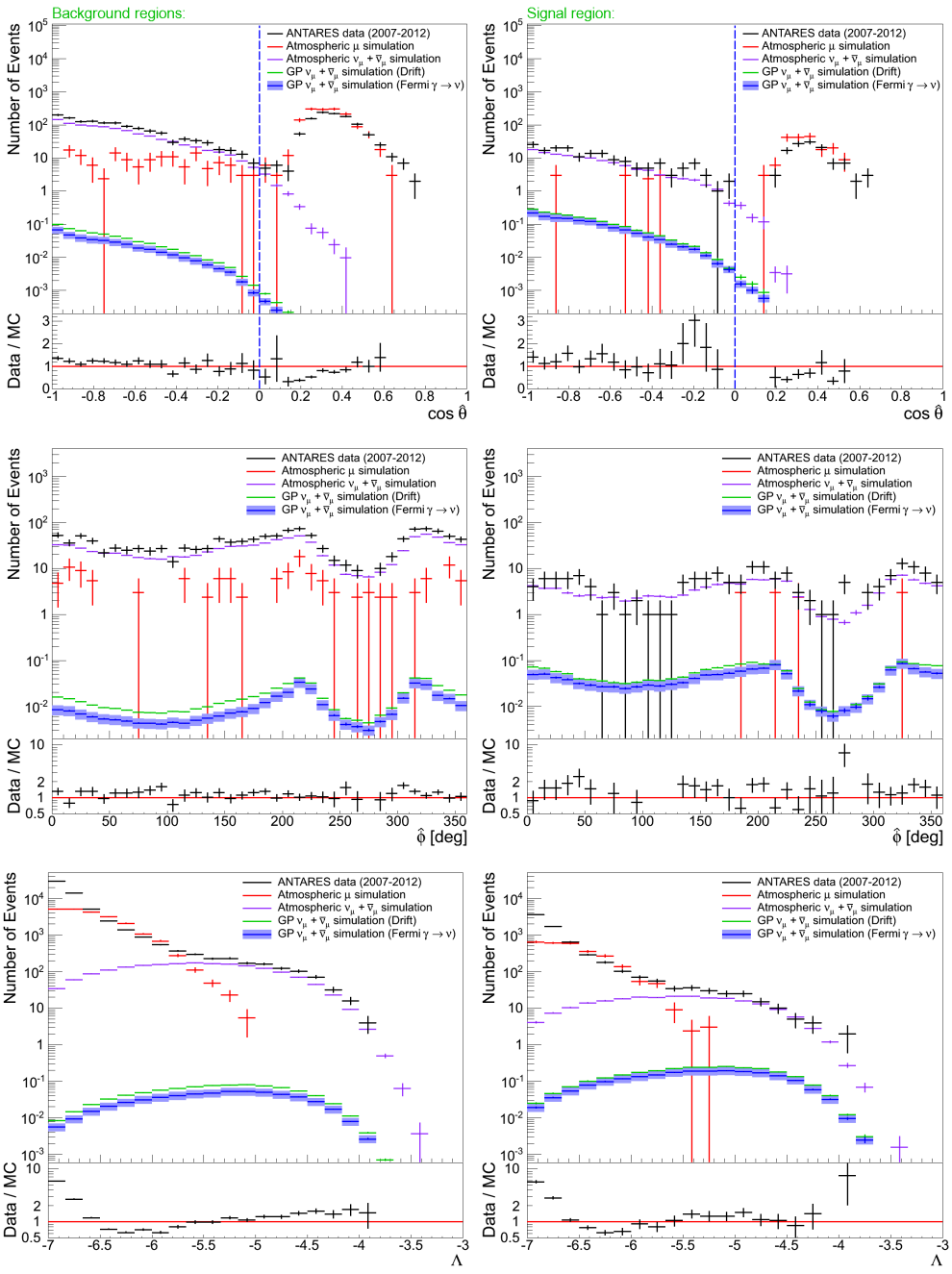

Figure 5.20: Data-MC comparison plots for events from the background regions (left plots) and from the signal region (right plots). TOP ROW: $\cos\hat{\theta}$ distributions. MIDDLE ROW: reconstructed azimuth angle distributions. BOTTOM ROW: Λ distributions.

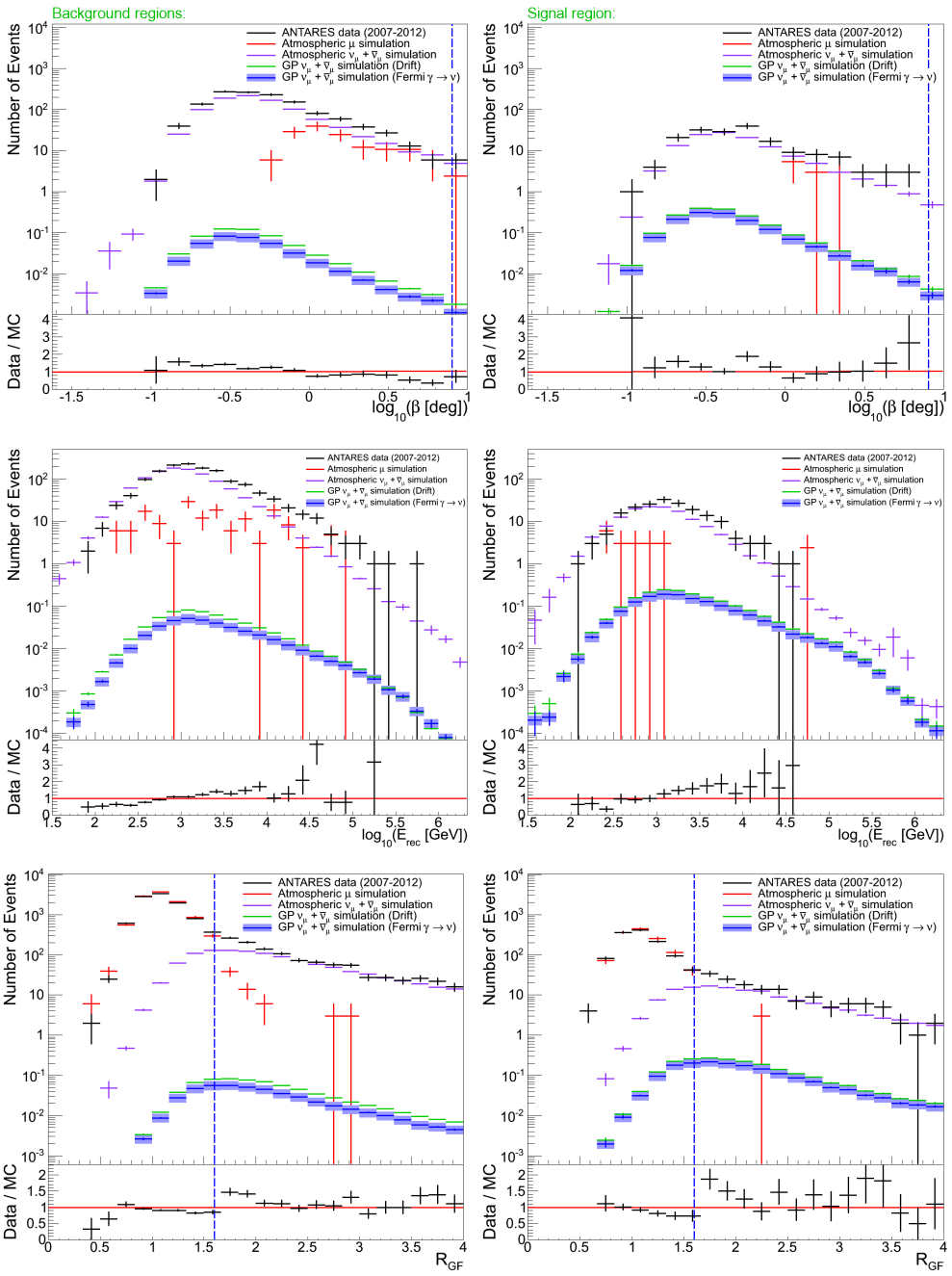

Figure 5.21: Data-MC comparison plots for events from the background regions (left plots) and from the signal region (right plots). TOP ROW: β distributions. MIDDLE ROW: $\log_{10}(E_{\text{rec}})$ distributions. BOTTOM ROW: R_{GF} distributions.

The measured number of events corresponds to a slight over-fluctuation, with a significance given by [Li and Ma, 1983]:

$$S = \sqrt{2n_{\mathrm{obs}} \ln\left[(\tau+1)\frac{n_{\mathrm{obs}}}{n_{\mathrm{obs}}+\tau\, n_{\mathrm{b}}}\right] + 2\tau\, n_{\mathrm{b}} \ln\left[(\tau+1)\frac{n_{\mathrm{b}}}{n_{\mathrm{obs}}+\tau\, n_{\mathrm{b}}}\right]}, \tag{5.24}$$

which gives $S = 0.8\sigma$. From this it can be concluded that the excess is not significant and the measurement is compatible with the background expectation.

SPECTRAL INDEX	$\mathcal{F}_\gamma^{90\%}$	ENERGY VALIDITY RANGE
2.5	$2.0\,\mathrm{GeV}^{1.5}\,\mathrm{m}^{-2}\,\mathrm{sr}^{-1}\,\mathrm{s}^{-1}$	0.24 TeV – 96 TeV
2.6	$4.6\,\mathrm{GeV}^{1.6}\,\mathrm{m}^{-2}\,\mathrm{sr}^{-1}\,\mathrm{s}^{-1}$	0.18 TeV – 71 TeV
2.7	$10\,\mathrm{GeV}^{1.7}\,\mathrm{m}^{-2}\,\mathrm{sr}^{-1}\,\mathrm{s}^{-1}$	0.15 TeV – 52 TeV

Table 5.14: The obtained limit on the flux constant for different values of γ.

Since no significant excess has been observed, the observed number of events can be converted into a flux upper limit. The limits that can be set are shown in table 5.14. These limits are above the sensitivities shown in table 5.13 since more events are measured in the signal region than expected from the background-only hypothesis.

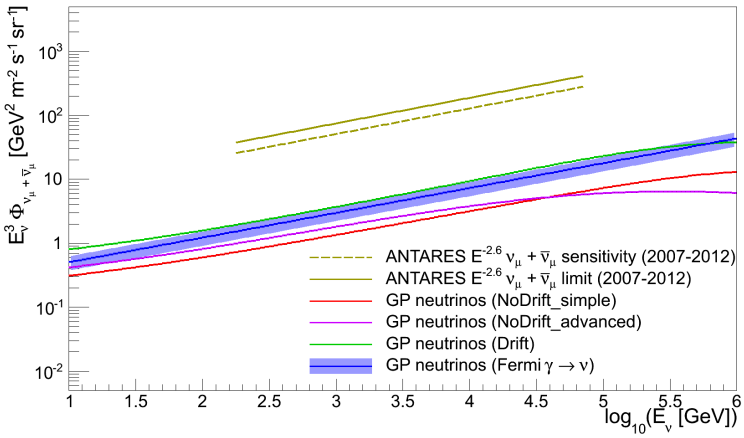

Figure 5.22: ANTARES limit and sensitivity versus neutrino energy for $\gamma = 2.6$ together with the average fluxes from the four signal models.

The flux upper limit, for a spectral index of $\gamma = 2.6$ is shown versus neutrino energy in figure 5.22, together with the sensitivity and the average signal fluxes from the four models. The flux upper limit is a factor of about 20 above the flux predicted by the Drift model and a factor of about 25 above the Fermi $\gamma \to \nu$ model predictions.

The flux upper limit versus Galactic longitude is shown in figure 5.23, where the limit and sensitivity are shown for a spectral index of $\gamma = 2.7$. The ANTARES limit is a factor of 2.1 above the limit set by AMANDA-II. As explained in the previous section, this is caused by an underfluctuation in the AMANDA-II measurement and an overfluctuation in the ANTARES measurement. It should be stressed however, that different signal regions are used, and that the limit obtained here is the first of its kind covering the inner Galactic plane region.

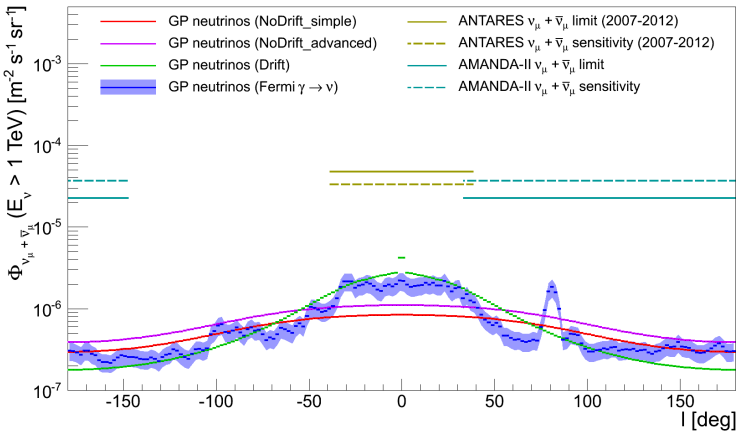

Figure 5.23: Sensitivities and limits versus Galactic longitude together with the average signal fluxes ($|b| < 4.5^\circ$) above 1 TeV.

Even though the expected fluxes in the signal region are higher and the sensitivity of ANTARES is better than that of AMANDA-II, the sensitivity is still more than a factor of 10 higher than even the most optimistic signal flux model. From this it can be concluded that a bigger neutrino telescope, like KM3NeT, is needed to constrain the models further and learn more about the diffuse Galactic neutrino flux. The sensitivity of KM3NeT will be assessed in the next chapter.

Before turning to KM3NeT, some more information is extracted from the flux upper limits, which can also be used to say something about the origin of the flux measured by IceCube. One can test the hypothesis that all the events measured by

IceCube originate from the signal region used in this analysis ($-39^\circ \leqslant l \leqslant +39^\circ$ and $-4.5^\circ \leqslant b \leqslant +4.5^\circ$). Since the signal region takes up only 1.7% of the total sky, the flux from this region has to be a factor of about 60 more intense than the diffuse flux from equation 5.23 to result in the same number of observed events for IceCube [Spurio, 2014]:

$$\Phi_{\nu+\overline{\nu}} = 3.8^{+0.7}_{-0.6}\, E_\nu^{-2.5}\,\mathrm{GeV}^{-1}\,\mathrm{m}^{-2}\,\mathrm{sr}^{-1}\,\mathrm{s}^{-1}, \tag{5.25}$$

for a spectral index of 2.5 and with E_ν in GeV.

Comparing this flux to the ANTARES 90% confidence level flux upper limit for the same spectral index shows that the limit is a factor of about 1.9 lower than this flux. The hypothesis that all events measured by IceCube originate from the signal region can thus be rejected. Furthermore, the limit indicates that at most about 50% of the flux measured by IceCube could originate from the signal region considered here.

6 DETECTION POTENTIAL OF KM3NET FOR THE DIFFUSE GALACTIC NEUTRINO FLUX

From the sensitivities and limits obtained with the ANTARES detector it can be concluded that a much bigger neutrino telescope is needed to probe the diffuse Galactic neutrino flux. The level of the flux that can be probed with ANTARES is more than a factor of 10 above the predicted fluxes.

The KM3NeT detector, which is the next generation neutrino telescope in the Mediterranean, is well suited to perform a measurement of the diffuse Galactic neutrino flux. Like ANTARES, its location in the Mediterranean Sea yields a high visibility of the region from which the highest signal is expected. Furthermore, the effective area is expected to be about two orders of magnitude bigger than that of ANTARES. A brief description of KM3NeT is given in section 6.1.

The analysis for KM3NeT is based on that developed for ANTARES. The number of events from the signal region is compared to the number of events from the background regions. These signal and background regions are constructed in the same way as done for ANTARES. The optimal size of the signal region for KM3NeT could be different than obtained for ANTARES. This potential difference is addressed in section 6.2. In section 6.3, the resulting sensitivity of KM3NeT is presented and compared to the limits and sensitivities obtained with ANTARES.

In addition to calculating the flux sensitivity of KM3NeT, the discovery potential is also assessed. This is described in more detail in section 6.4.

6.1 KM3NET

The KM3NeT detector will consist of neutrino telescopes at three sites in the Mediterranean Sea. The sites have been chosen after long-term site characterisation by the ANTARES, NEMO [Riccobene et al., 2005] and NESTOR [Belias et al., 2007] collaborations, and are selected according to several criteria. A suitable site should have a sufficient depth in order to provide shielding against atmospheric muons and at the same time be close to the coast, to ease deployment and reduce the costs of power and signal connections to shore. Furthermore, the optical properties of

NEMO: NEutrino Mediterranean Observatory

NESTOR: Neutrino Extended Submarine Telescope with Oceanographic Research

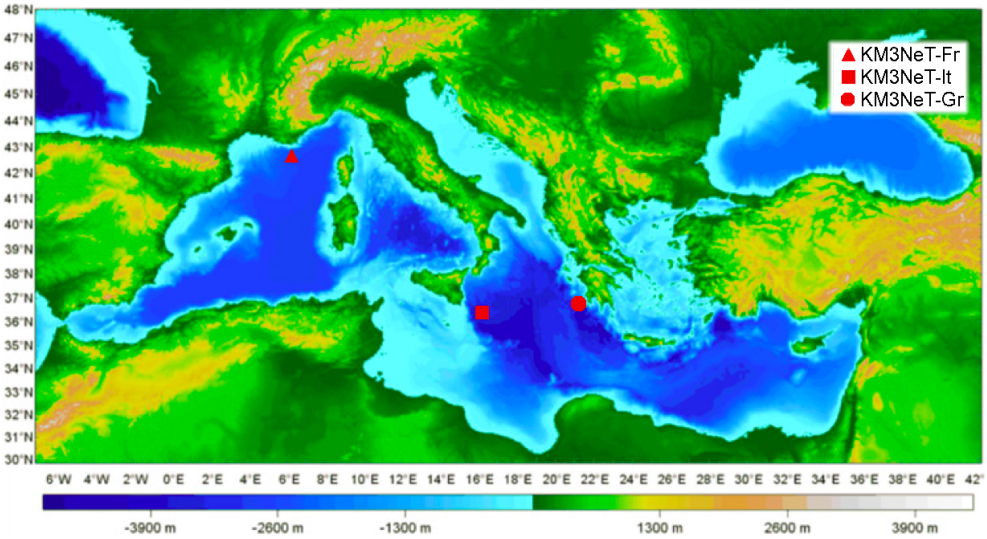

Figure 6.1: Bathymetry map of the Mediterranean Sea with the three site locations of KM3NeT marked. Figure reproduced from Margiotta [2013].

the water should be good (i. e. absorption and scattering lengths close to those of pure sea water) and the level of bioluminescence should be low.

The sites are indicated in figure 6.1, which shows a bathymetry[33] map of the Mediterranean Sea. The site off the coast of Toulon, France is referred to as KM3NeT-Fr, and is close to where the ANTARES detector is located. The KM3NeT-It site is located off the coast of Portopalo di Capo Passero, Sicily, Italy. The third site, KM3NeT-Gr, is located off the coast of Pylos, Peloponnese, Greece.

[33] *Bathymetry is the study of underwater depth of lake or ocean floors. The name comes from the Greek words βαθός (meaning deep) and μέτρον (meaning measure).*

The detection principle of KM3NeT is the same as that of ANTARES. One key difference is that the Optical Modules (OMs) in KM3NeT will contain 31 small PMTs of 3″ diameter instead of one large PMT, see also figure 6.2. The main advantages are a 4π coverage, a very large photocathode surface and insensitivity to the Earth's magnetic field [Margiotta, 2013]. Segmenting the photocathode also helps in rejecting the background.

A prototype of the KM3NeT optical module has been attached to the instrumentation line of ANTARES, and was deployed on April 16th 2013. Data taking commenced the same day, the results of which can be found in the paper by Adrián-Martínez et al. [2014b].

Figure 6.2: Photo of the recently completed KM3NeT string. The Multi-PMT optical modules can also be seen.

Just like in ANTARES, the OMs will be attached to vertical lines that are anchored on the sea floor and held upright by buoys. A line contains 18 storeys, each containing one OM. The vertical distance between two storeys is 36 m and the first storey is located about 100 m above the sea floor. The first string has recently been completed, see the picture in figure 6.2. To facilitate the distribution over different sites, the total detector will be built up of so-called building blocks. One building block consists of 115 strings with about 90 m spacing. This number of strings and the spacing between OMs has been found to give the best detection efficiency for candidate Galactic neutrino sources while keeping the total number of optical modules constant.

The KM3NeT detector will be built in several phases. For phase 1, strings will be deployed in the Italian and French sites, and the resulting instrumented volume will be about 3 times that of ANTARES. Phase 1.5 will consist of 2 building blocks and is planned to perform an independent measurement of the neutrino

flux discovered by IceCube. The full phase 2 KM3NeT detector will consist of 6 building blocks.

More information about the technology can be found in the technical design report [Ageron et al., 2010].

6.1.1 *Muon track reconstruction*

Since the KM3NeT detector consists of different optical modules from ANTARES, new reconstruction strategies have been developed. In the following sections, the so-called RECOLNS strategy is used [Trovato, 2013]. This reconstruction strategy is based on AAFIT, which has been modified to utilise the OM properties. For example, a different hit selection is used and the charge information is substituted by the multiplicity of hits.

The first step of the reconstruction strategy is a hit selection. Each hit is assigned a score, which depends on how many other hits are in coincidence with it, and how these hits are distributed. For instance, an L1 hit (which is defined as two hits on different PMTs on the same OM within 10 ns) gets a score of 2^0, while an L3 hit (defined as a coincidence between 4 or more PMTs on the same OM within 10 ns) gets a score of 2^5. In total 6 different hit patterns are defined. The hit with the highest score, which is in 99.6% of the cases a hit caused by a passing muon, is taken as the reference hit.

After this hit selection, a causality filter is applied to remove background hits. The same causality relation as used by the 3N trigger is used for this, i. e. equation 4.10, where the allowed time difference is increased by 20 ns. Additionally, hits are required to fulfil:

$$\left| |t_i - t_j| - \frac{r_{ij}}{c} \right| < 500\,\text{ns}, \tag{6.1}$$

where r_{ij} is the distance between PMT i and j. This relation takes into account that light absorption does not allow the Čerenkov light to move far from the muon track.

The hits are then used for a linear prefit similar to that performed in AAFIT. After a first track estimate has been obtained, the angle of incidence of the photon on the PMT is determined for each hit. If this angle is larger than 60° (with 0° being a head-on hit), the hit is discarded. This improves the purity of the hit selection to about 90% [Trovato, 2013].

The result of the prefit is used as an input for an M-estimator fit, for which the function given in equation 4.34 is used. For this fit, all hits that have a time residual with respect to the prefit

between −150 ns and +150 ns and are located at most 100 m away from this track are selected. In addition, all L3 hits are selected[34].

[34] This corresponds to how hits with an amplitude larger than 2.3 p.e. are selected at ANTARES.

The third step is a Maximum Likelihood fit using the same PDF as used for AAFIT. As input all hits are selected that are at most 300 m from the M-estimator track and that have a time residual within $-0.5\,T_{\mathrm{RMS}}$ and $+T_{\mathrm{RMS}}$, where T_{RMS} is the root mean square of the residuals used for the M-estimator fit. All L3 hits are also selected again.

Step two and three are done 7200 times, by rotating the prefit track in steps of 3° and using the new track as starting point. Out of these tracks the best track is chosen according to:

$$Q = N_{\mathrm{hit}} + w\frac{\log L^{\max}}{N_{\mathrm{hit}} - 5}, \tag{6.2}$$

where N_{hit} is the number of hits used to perform the likelihood fit and $\frac{\log L^{\max}}{N_{\mathrm{hit}}-5}$ is the reduced log-likelihood (rLogL). The optimal value for the weighting factor is found to be 1.

Finally, the track with the highest value of Q is used for another Maximum Likelihood fit using the AAFIT PDF which takes the background hits into account (equation 4.42). As input, all hits with time residuals with respect to the chosen track between −150 ns and +150 ns and that are at most 100 m away from this track are selected. Again, the L3 hits are added.

Analogously to AAFIT, the angular error estimate β is defined (see equation 4.47). This parameter can be used together with the reduced log-likelihood value of the final track, to reject badly reconstructed events and misreconstructed atmospheric muons.

Although the reconstruction strategy does not perform an estimate of the muon energy, the N_{hit} parameter can be used as a rudimentary energy estimator. For instance, selecting events with $N_{\mathrm{hit}} > 30$ will select mainly events above 1 TeV; only 3% of the events below 1 TeV pass this cut [Trovato, 2013].

KM3NeT effective area

To determine the effective area for KM3NeT, the same simulation tools as described in section 4.1 are used. Background from potassium decays and the dark noise produced by the PMTs are simulated using an uncorrelated background rate of 5 kHz per PMT and a time-correlated (L1) rate of 500 Hz per optical

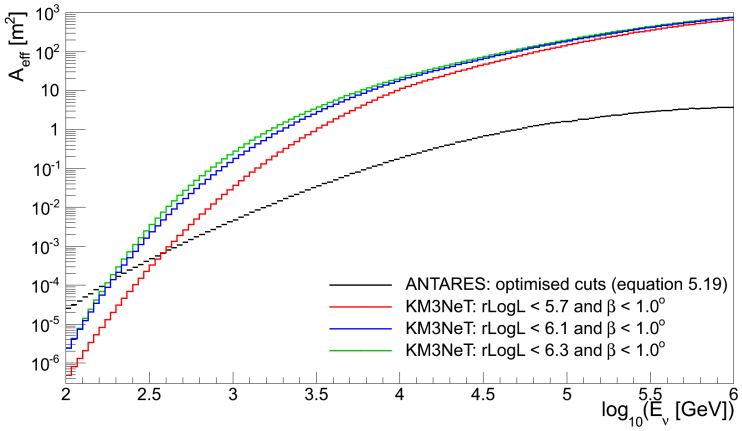

Figure 6.3: Effective area of KM3NeT phase 2 using the RECOLNS strategy for different cut combinations. Also shown is the ANTARES effective area corresponding to the event selection from equation 5.19. The average is taken for neutrinos and anti-neutrinos.

module[35].

The effective area has been determined using equation 4.25 and is shown versus neutrino energy for different cut combinations in figure 6.3. The effective area shown here is for the full phase 2 detector and the average is taken for neutrinos and anti-neutrinos. As reference, the ANTARES effective area corresponding to the event selection from equation 5.19 is shown.

[35] *This has to be added, since a KM3NeT OM consists of multiple PMTs which are situated close together, so that it is possible that the decay of ^{40}K produces a coincidence between two PMTs.*

6.2 DETERMINING THE OPTIMAL SIGNAL REGION SIZE

The detection potential of the KM3NeT detector for the diffuse Galactic neutrino flux is now assessed using the same type of analysis as used for ANTARES. Signal and background regions are defined and the corresponding numbers of events are compared. Besides optimising to obtain the best sensitivity, as is done for ANTARES, the optimisation is also done to obtain the highest probability for a discovery. This is explained in more detail below first, after which the optimisation of the size of the signal region is described in section 6.2.2.

6.2.1 *Statistical tools*

For ANTARES the optimisation of the size of the signal region has been carried out using the MRF technique, which results

in the best limit. The MRF is used, because ANTARES is too small to claim a discovery of a diffuse Galactic neutrino flux. For KM3NeT, the MDP technique is also used, which optimises the cuts for the highest probability for a discovery [Hill et al., 2005].

MDP: Model Discovery Potential

Using frequentist statistics, a discovery can be claimed if the observation is very unlikely to be caused by a background fluctuation. It is generally accepted that when this probability is smaller than $5.73 \cdot 10^{-7}$ (which is the area in the 5σ tails in a two-sided Gaussian distribution) a discovery can be claimed. When the probability is smaller than $2.7 \cdot 10^{-3}$ (the area in the 3σ tails in a two-sided Gaussian distribution) the experiment can report evidence for a new signal.

The critical number of events n^{α}_{crit} can then be defined, so that

$$P(n_{\text{obs}} \geqslant n^{\alpha}_{\text{crit}} | \, \mu_{\text{b}}) < \alpha, \tag{6.3}$$

where α is called the significance level (not to be confused with the confidence level from the MRF case), which is $5.73 \cdot 10^{-7}$ for a discovery. The critical number of events is the minimum number of events needed for an observation with a significance level of α.

If a real signal is also present, the probability to measure at least n_{crit} events is given by:

$$P(n_{\text{obs}} \geqslant n^{\alpha}_{\text{crit}} | \, \mu_{\text{b}} + \mu_{\text{s}}) = 1 - \beta, \tag{6.4}$$

where $1 - \beta$ is called the discovery potential. If for instance $1 - \beta = 0.9$, an observation of at least n_{crit} events is expected in 90% of the experiments. The least detectable signal μ_{lds} is defined to be the lowest value of μ_{s} for which the equality in equation 6.4 is satisfied. The MDP is then defined as:

$$\text{MDP} = \frac{\mu_{\text{lds}}}{\mu_{\text{s}}}, \tag{6.5}$$

and shows what level of flux the experiment can discover. By optimising the cuts to get the best MDP, the probability to make an observation at significance level α in a fraction of $1 - \beta$ experiments, is maximised.

Figure 6.4 shows the least detectable signal[36] for a 5σ observation with 50% probability as a function of the expected number of background events for different values of τ (the ratio of off-source to on-source region, see equation 5.2) and for the case with no uncertainty on the background. The same conclusion as drawn from the right plot of figure 5.1 is also valid here; the higher the value of τ (and the lower the uncertainty on the background), the lower the value of the least detectable signal.

[36] *The least detectable signal is again calculated with the profile likelihood method implemented in the* TROLKE *class in* ROOT.

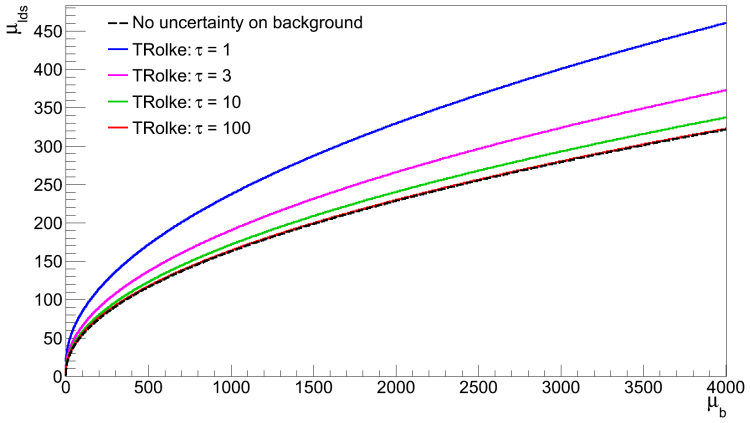

Figure 6.4: Least detectable signal for a 5σ observation with 50% probability versus number of background events for several different values of τ.

6.2.2 *Signal region optimisation*

The optimisation of the size of the signal region is again performed for different cut combinations. As before, the MRF is always calculated at 90% confidence level, whereas the MDP is calculated for a 5σ observation with 50% probability. Both the MRF and the MDP are calculated for 2 years of livetime of phase 2.

rLogL-CUT	β-CUT	N_{hit}-CUT	PURITY
5.7	1.0°	—	$> 99\%$
5.7	2.0°	—	$> 99\%$
6.1	1.0°	—	~97%
6.2	1.0°	—	~88%
6.2	2.0°	—	~88%
6.2	—	27	~86%
6.3	1.0°	—	~64%

Table 6.1: The different cut combinations considered for the signal region optimisation.

As input, the expected number of signal and background events is required, which are obtained from the effective area using equation 4.24. The flux $\Phi_\nu(E_\nu, \theta, \phi)$ is calculated by transforming the fluxes from Galactic coordinates to local coordinates and averaging over a full sidereal day.

For the optimisation, the longitude bound is again varied from 24° to 75° in steps of 3° and the latitude bound from 1° to 7.5° in steps of 0.5° and the MRF and MDP values are calculated for each combination. Several cut combinations are used for the optimisation, which are shown in table 6.1. As before, only events that are reconstructed as upgoing are considered.

MRF optimisation

Figure 6.5 shows the MRF as a function of longitude bound and latitude bound for an event selection with rLogL < 6.1 and $\beta < 1.0°$ for all four of the signal flux models. The colour scale shows the value of the MRF, with the blue part of the scale corresponding to the bottom 10% of the MRF values.

With this particular cut combination, the lowest MRF is found at $l_{\text{bound}} = 66°$ and $b_{\text{bound}} = 2.5°$ for both NoDrift models, at $l_{\text{bound}} = 42°$ and $b_{\text{bound}} = 4°$ for the Drift model and at $l_{\text{bound}} = 39°$ and $b_{\text{bound}} = 1.5°$ for the Fermi $\gamma \to \nu$ model. As before, the minimum is quite shallow, so varying the longitude or latitude bound will result in only a slightly worse MRF value.

As found in the optimisation for ANTARES, the optimal region is different for the NoDrift and the other two models, which is due to the angular distribution of the flux. Choosing the region that is optimal for the Drift model gives a 12% worse result for the NoDrift models and a 17% worse result for the Fermi $\gamma \to \nu$ model.

The influence of the cuts on the optimal region size is small, as can be seen from table 6.2, in which the MRF results for the Drift model are summarised. The influence of the atmospheric neutrino flux uncertainty is also small, resulting in the same optimal region for nearly all cut combinations. In the table, only the results for the default atmospheric neutrino flux are shown.

Concerning the event selection, the lowest MRF is obtained for rLogL < 6.1 and $\beta < 1.0°$, so this cut combination is used to assess the sensitivity of KM3NeT to the diffuse Galactic neutrino flux. It is possible to optimise the cuts further, as is done for

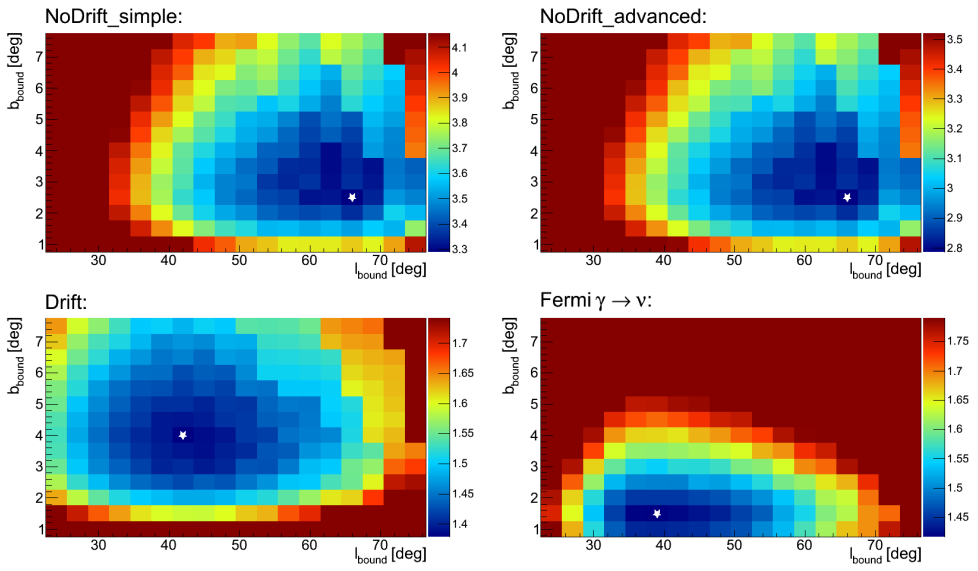

Figure 6.5: MRF versus longitude and latitude bound for an event selection with rLogL < 6.1 and $\beta < 1.0°$. The white star marks the location of the minimum.

CUT COMBINATION	OPTIMAL VALUES l_{bound}	b_{bound}	MRF	μ_s	μ_b
rLogL < 5.7, $\beta < 1.0°$	45°	3.5°	1.57	29.2	576
rLogL < 5.7, $\beta < 2.0°$	42°	4°	1.58	30.3	624
rLogL < 6.1, $\beta < 1.0°$	42°	4°	1.38	59.3	1860
rLogL < 6.2, $\beta < 1.0°$	42°	4°	1.41	66.1	2420
rLogL < 6.2, $\beta < 2.0°$	42°	4°	1.39	67.4	2460
rLogL < 6.2, $N_{\text{hit}} > 27$	42°	4°	1.40	66.3	2380
rLogL < 6.3, $\beta < 1.0°$	45°	3.5°	1.61	71.1	3670

Table 6.2: Optimal longitude and latitude bounds and obtained MRF values for the considered cuts for the Drift model.

ANTARES, but this is beyond the scope of this work. It should be noted that it is possible to improve the senstivities shown in section 6.3.

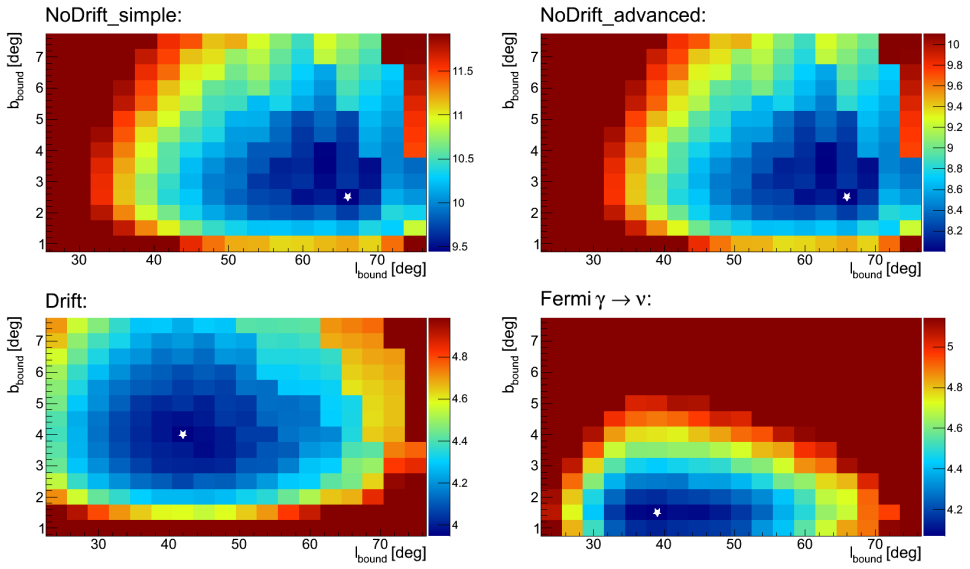

Figure 6.6: MDP versus longitude and latitude bound for rLogL < 6.1 and $\beta < 1.0^\circ$. The white star marks the location of the minimum.

MDP optimisation

The results for the MDP optimisation are shown in figure 6.6 for an event selection with rLogL < 6.1 and $\beta < 1.0^\circ$. This figure shows the MDP, calculated according to equation 6.5, versus longitude and latitude bound. The colour scale again shows the value of the MDP, with the blue part of the scale corresponding to the bottom 10% of the values. With the applied cuts, the lowest MDP is found at $l_{\text{bound}} = 66^\circ$ and $b_{\text{bound}} = 2.5^\circ$ for both NoDrift models, at $l_{\text{bound}} = 42^\circ$ and $b_{\text{bound}} = 4^\circ$ for the Drift model and at $l_{\text{bound}} = 39^\circ$ and $b_{\text{bound}} = 1.5^\circ$ for the Fermi $\gamma \to \nu$ model.

Upon comparison with figure 6.5, it can be seen that the plots are basically identical, except that the MDP values are higher than the MRF values. This means that a higher flux is needed to claim a discovery than to set a limit (for the chosen confidence level and discovery potential).

The MDP results for three of the cut combinations are shown in table 6.3 for each of the four signal models. As with the MRF case, the influence of the cuts on the optimal size of the signal region is small. The effect of the atmospheric neutrino flux uncertainty is also small, resulting in almost the same optimal size for the signal region as that found for the default atmospheric neutrino flux.

MODEL NAME	CUT COMBINATION	OPTIMAL VALUES l_{bound}	b_{bound}	MDP	μ_s	μ_b
NoDrift_simple	rLogL < 6.1, $\beta < 1.0°$	66°	2.5°	9.44	25.8	1800
	rLogL < 6.2, $\beta < 1.0°$	66°	2.5°	9.60	28.8	2340
	rLogL < 6.2, $N_{\text{hit}} > 27$	66°	2.5°	9.51	28.9	2300
NoDrift_advanced	rLogL < 6.1, $\beta < 1.0°$	66°	2.5°	8.00	30.5	1800
	rLogL < 6.2, $\beta < 1.0°$	66°	2.5°	8.08	34.3	2340
	rLogL < 6.2, $N_{\text{hit}} > 27$	66°	2.5°	8.02	34.2	2300
Drift	rLogL < 6.1, $\beta < 1.0°$	42°	4°	3.95	59.3	1860
	rLogL < 6.2, $\beta < 1.0°$	42°	4°	4.03	66.1	2420
	rLogL < 6.2, $N_{\text{hit}} > 27$	42°	4°	3.99	66.3	2380
Fermi $\gamma \to \nu$	rLogL < 6.1, $\beta < 1.0°$	39°	1.5°	4.07	33.3	648
	rLogL < 6.2, $\beta < 1.0°$	36°	1.5°	4.15	35.6	778
	rLogL < 6.2, $N_{\text{hit}} > 27$	36°	1.5°	4.11	35.7	765

Table 6.3: Optimal longitude and latitude bounds and obtained MDP value for the considered cuts for each of the signal models.

Also in this case, choosing the region that is optimal for one model, gives worse results for the others. For instance, choosing the optimal region for the Drift model, yields a 12% worse MDP for the NoDrift models and a 17% worse result for the Fermi $\gamma \to \nu$ model (which are similar percentages as found in the MRF optimisation). Since the goal is to assess the discovery potential of KM3NeT, the region that is optimal for a given model is used as signal region to assess the discovery potential of that model. For the Drift model $l_{\text{bound}} = 42°$ and $b_{\text{bound}} = 4°$ is used, for which 8 background regions can be defined and for the Fermi $\gamma \to \nu$ model $l_{\text{bound}} = 39°$ and $b_{\text{bound}} = 1.5°$ is used, for which 17 background regions can be defined. The NoDrift models are not used in assessing the discovery potential of KM3NeT, since many simplifying assumptions are made in these two models.

Again, the best results are obtained for rLogL < 6.1 and $\beta < 1.0°$, so this cut combination is also used for the discovery potential calculations. Again it should be kept in mind that the cuts can be further optimised. Furthermore, the use of an energy estimator will improve the probability of a discovery over the simple cut-and-count analysis used here. The excess of events from the diffuse Galactic neutrino flux is expected at high ener-

gies (see also figure 2.27), so taking only events above a minimum reconstructed energy value into account will improve the signal-to-background ratio. This is beyond the scope of this work and is not investigated further.

6.3 KM3NET SENSITIVITY

The sensitivity of KM3NeT to the diffuse Galactic neutrino flux has been evaluated in a model independent way using the same method as used for ANTARES. Starting from equation 5.21, the average flux upper limit is calculated for spectral indices of 2.5, 2.6 and 2.7. The energy ranges which contain the central 90% of the signal are shown in table 6.4. Comparing these results to those for ANTARES (table 5.13), it can be seen that the energy ranges are shifted towards higher energies for KM3NeT. This is due to the difference between the effective areas, which for KM3NeT rises more, but at higher energies, as can be seen from figure 6.3.

SPECTRAL INDEX	ENERGY VALIDITY RANGE
2.5	1.1 TeV − 180 TeV
2.6	0.96 TeV − 130 TeV
2.7	0.89 TeV − 96 TeV

Table 6.4: The energy validity range for the sensitivity of KM3NeT for different values of γ.

The KM3NeT sensitivities for $\gamma = 2.6$ for 1 and 10 years of livetime are shown in figure 6.7 versus neutrino energy, together with the limit and sensitivity of ANTARES. From the figure it can be seen that even with 1 year of data of the full KM3NeT detector, the obtained sensitivity is more than a factor of 7 better than that of ANTARES. Between 3 to 4 years of data taking with the full KM3NeT detector is required to reach sensitivities comparable to the fluxes predicted by the Drift model.

The same conclusion can be drawn from figure 6.8, which shows the KM3NeT sensitivity for $\gamma = 2.7$ versus Galactic longitude. In this case, 1 year of data from KM3NeT gives a sensitivity that is about 6.6 times better than the ANTARES sensitivity and a factor of about 4.4 better than the AMANDA-II limit. The reason that the improvement of the KM3NeT sensitivity to the ANTARES sensitivity is slightly smaller in this case is due to the assumed softer energy spectrum.

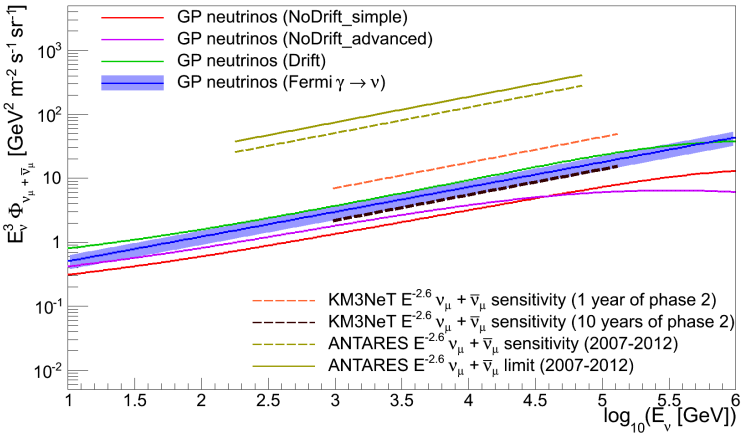

Figure 6.7: KM3NeT sensitivity versus neutrino energy for $\gamma = 2.6$ together with the average fluxes from the four signal models and the ANTARES limit and sensitivity.

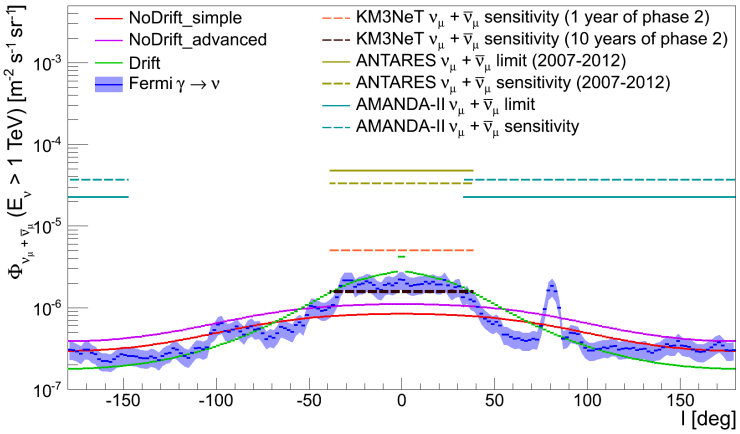

Figure 6.8: Sensitivities and limits versus Galactic longitude together with the average signal fluxes ($|b| < 4.5°$) above 1 TeV.

The evolution of the sensitivity with the number of years of data is shown in figure 6.9. The grey band represents the uncertainty on the atmospheric neutrino flux (i. e. $\pm 25\%$). The left plot shows the average upper limit that can be set on the flux constant for a spectrum with a spectral index of $\gamma = 2.6$. The right plot in the figure shows the upper limit for a spectral index of $\gamma = 2.7$. The results from the ANTARES experiment (from tables 5.13 and 5.14) and the AMANDA-II limit (equation 5.22) are also shown.

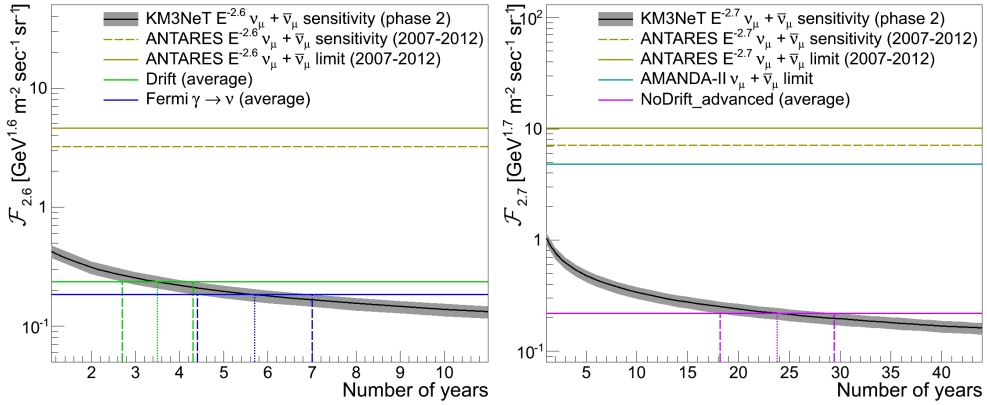

Figure 6.9: KM3NeT sensitivity versus number of years of livetime. The vertical lines denote the number of years required for the sensitivity to reach the model prediction with the same colour. LEFT: for $\gamma = 2.6$. RIGHT: for $\gamma = 2.7$.

In order to compare the KM3NeT sensitivity to the predictions from the theoretical models, a fit has been performed to the average fluxes in the signal region ($l_{\text{bound}} = 39^\circ$ and $b_{\text{bound}} = 4.5^\circ$) in order to determine the predicted flux constants. The resulting flux constants for the Drift and Fermi $\gamma \to \nu$ models are shown in the left plot and the flux constant for the NoDrift_advanced model is shown in the right plot. The spectral index predicted by the models is not exactly 2.6 (or 2.7), see table 2.3, so the fit has been performed by fixing the spectral index[37] to the value used in the plot.

The vertical lines in the figure show the number of years it takes for the sensitivity to reach the level of the flux predicted by the model. Depending on the normalisation of the atmospheric neutrino flux, this is about 2.7 to 4.3 years for the Drift model and about 4.4 to 7.0 years for the Fermi $\gamma \to \nu$ model. For the NoDrift_advanced model it would take more than 20 years to reach the level of the predicted flux. However, as remarked before, this model is not realistic.

Even though the number of years needed for KM3NeT to reach the flux predictions of the Drift and Fermi $\gamma \to \nu$ models is significant, the calculations here show that it is possible to constrain the diffuse Galactic neutrino flux. It should be noted that the sensitivity is calculated using only track-like events (i. e. from CC muon-neutrino interactions) and no real cut optimisation has been performed. Further improvements are thus possible, which are discussed in the next section.

[37] *The result for the NoDrift_simple model is not shown in either of the plots since the spectral index of 2.63 is in between the two chosen spectral indices.*

6.4 KM3NET DISCOVERY POTENTIAL

The results of the discovery potential calculation for KM3NeT are shown in figure 6.10. In the plot the significance (in number of σ) is shown versus number of years of data taken with KM3NeT. As in the MDP optimisation, the results are shown for an observation with 50% probability.

Considering the results for the most optimistic model (the Drift model), it can be seen that it takes about 30 years to reach a significance of 5σ for the claim of a discovery for this particular model. The evidence for a new signal, i. e. a significance of 3σ, takes about 11 years. The results for the Fermi $\gamma \rightarrow \nu$ model are very similar; it takes about 11 (32) years to have a significance of 3σ (5σ).

From these results it is clear that observing the diffuse Galactic neutrino flux is difficult, even for KM3NeT. However, as remarked at the end of the previous section, no real optimisation has been performed for the results presented here. In addition, only track-like events, originating from CC muon-(anti-)neutrino interactions, are considered. The sensitivity[38] can be improved in multiple ways, including:

A. Inclusion of shower-like events;

B. Flavour identification (ν_τ);

C. Using an energy estimator;

D. Optimisation of the quality cuts.

[38] *It may seem confusing that the word 'sensitivity' is used here while the discovery potential is assessed, but a 2 times lower sensitivity just means that twice as many signal events are observed for the same number of background events.*

The biggest improvement of the sensitivity is expected from the inclusion of the shower-like events. To get an estimate of the expected improvement, the results from the diffuse flux analyses in ANTARES can be used. The sensitivity of the track analysis (using only CC muon-(anti-)neutrino interactions) for 885 days of livetime is [Schnabel, 2013a]:

$$\Phi_{\nu_\mu+\overline{\nu}_\mu} < 4.70 \cdot 10^{-4}\, E_\nu^{-2}\, \mathrm{GeV}^{-1}\, \mathrm{m}^{-2}\, \mathrm{sr}^{-1}\, \mathrm{s}^{-1}, \tag{6.6}$$

with E_ν in GeV, while the sensitivity of the shower analysis for 1247 days of livetime is [Folger, 2014]:

$$\Phi_{\nu+\overline{\nu}} < 2.21 \cdot 10^{-4}\, E_\nu^{-2}\, \mathrm{GeV}^{-1}\, \mathrm{m}^{-2}\, \mathrm{sr}^{-1}\, \mathrm{s}^{-1}, \tag{6.7}$$

which is per neutrino flavour and has been calculated using the Feldman-Cousins method. Part of the improvement in sensitivity is due to the larger livetime of the data sample that is used.

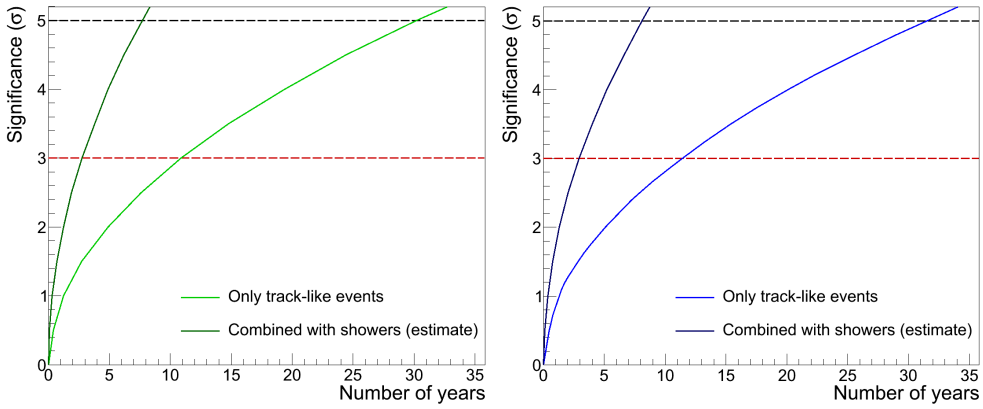

Figure 6.10: Significance obtained in 50% of the experiments versus number of years of livetime of KM3NeT. LEFT: for the Drift model. RIGHT: for the Fermi $\gamma \rightarrow \nu$ model.

Scaling the sensitivity of the showers to 885 days of livetime gives:

$$\Phi_{\nu+\overline{\nu}} < 2.81 \cdot 10^{-4} \, E_{\nu}^{-2} \, \mathrm{GeV}^{-1} \, \mathrm{m}^{-2} \, \mathrm{sr}^{-1} \, \mathrm{s}^{-1}, \tag{6.8}$$

which is an improvement of about 70% compared to the analysis using track-like events. It should be noted that this improvement is obtained by using shower-like events *instead* of track-like events. A combination of both will improve the sensitivity even further. From these considerations, a sensitivity improvement of a factor of 2 compared to that obtained here seems realistic.

The curves for the significance versus number of years when including shower-like events (i. e. a sensitivity improvement of a factor 2) are also shown in the plots in figure 6.10. It can be seen that a significance of 3σ is reached for the Drift model after only 2.8 years of data taking and a significance of 5σ after about 7.7. Again, the results for the Fermi $\gamma \rightarrow \nu$ model are similar; it takes 2.9 (8.1) years of taking data to reach a significance of 3σ (5σ).

Optimisation of the quality cuts, flavour identification of the neutrinos and usage of an energy estimator could result in further improvements, reducing the amount of time needed for a discovery.

A complication in assessing the discovery potential is the neutrino flux measured by IceCube. Since the origin of this flux is not known at the time of writing, it is not known how it will affect the analysis of the diffuse Galactic neutrino flux. As described in section 5.4.1, if the flux is truly diffuse, the same number of events are expected in the signal region and each of the background

regions. In this case, the flux measured by IceCube constitutes an additional background. If, however, the flux is Galactic in origin (or at least has a strong Galactic component), the number of events in the signal region will be higher and this will enhance the obtained significance. The two flux contributions then have to be disentangled, which requires a better modelling of the diffuse Galactic neutrino flux.

In summary, it is difficult to predict how many years of data of KM3NeT are required for a discovery. It is clear, however, that the measurement of the diffuse Galactic neutrino flux requires a combined track and shower analysis. The presented results show that with KM3NeT it should be possible to study the diffuse Galactic neutrino flux after about 3 years of operation.

7

CONCLUSIONS AND OUTLOOK

When cosmic rays interact with the interstellar matter in our Galaxy, one of the particles that may be produced is the neutrino. Although the environmental conditions are very different, this is similar to how neutrinos are produced when cosmic rays interact with the atmosphere of the Earth. Not much is known yet about the Galactic neutrino signal and the only published result so far is a limit set by the AMANDA-II experiment [Kelley et al., 2005].

The ANTARES neutrino telescope is at a suitable location to perform a measurement of this neutrino flux, since it offers a good visibility of the region from where the highest signal is expected: the Galactic plane. The average flux in the region of interest for ANTARES is about a factor of 3 higher than in the region visible by AMANDA-II.

The analysis performed for this work consists of defining a signal region and a number of background regions. The background regions are used to determine the background from the data. Hence, no modelling is needed to estimate the background and the measurement is not affected by systematic uncertainties on the background. The background regions are constructed to have the same size and detector response as the signal region, so that the same number of background events is expected in each region.

Since the expected signal is too low compared to the background to make a discovery with ANTARES, the Model Rejection Factor (MRF) technique is used. The optimal signal region that is found in this way extends from a Galactic longitude of -39° to $+39^\circ$ and from a Galactic latitude of -4.5° to $+4.5^\circ$. It should be noted that the optimal size of the signal region depends on the angular distribution of the flux predicted by the models. Since the minimum of the MRF is quite shallow, fixing the optimal region found for a specific model makes the results for the other models slightly worse.

For the size of the signal region that is found to be optimal, 8 background regions can be defined, which are shown in Galactic coordinates in figure 5.5. Since the data taking of ANTARES is not continuous, the background regions may no longer be equivalent. To check for any biases, the effective visibility has been determined and compared to the theoretical visibility. It is found that

the differences between the signal and background regions are at the level of 5‰. The compatibility of the background regions is verified by defining 35 cut intervals yielding 35 independent measurements per region. By comparing the number of events in each of these intervals for the 8 background regions, it is found that no systematic biases are present to within the statistical error of about 1%.

To enhance the sensitivity of ANTARES compared to other analyses performed so far, the TQ trigger is used in addition to the standard 3N + 2T3 triggers (see section 4.2). The TQ trigger applies looser selection criteria and improves the detection efficiency for low energy neutrinos. The gain is about a factor of 2 below 30 GeV. It is also beneficial to use the TQ trigger at higher neutrino energies; the gain is about 20% compared to the standard triggers at 10 TeV.

However, since the TQ trigger only became operational at the end of 2009 and was only enabled when the conditions are suitable (i. e. the optical background is not too high), it is only active in 18.8% of the runs used for the data analysis. It should be noted that this fraction could be higher, since there is a subset of runs where the conditions are good, but the TQ trigger has not been enabled. If the TQ trigger would have been enabled, it would have been active in 27.8% of the runs. The expected gain for the diffuse Galactic neutrino flux is about 6% at trigger level when using the TQ trigger.

To further enhance the sensitivity, the R_{GF} parameter from GridFit is used to reject misreconstructed atmospheric muons. The GridFit reconstruction chain has been developed to improve the efficiency for low energy neutrinos ($\lesssim 100$ GeV). After optimising the quality cuts, the number of reconstructed neutrinos can be increased by about 20% compared to BBFit, which is a reconstruction strategy used in current analyses focusing on low energy neutrinos (see section 4.3.1). In addition, GridFit provides some information on the azimuth angle, which is not the case for single line BBFit events. This is for example beneficial when trying to detect neutrinos from dark matter annihilations in the Sun.

Even though it was set out to be efficient at low energies, the performance at high energies is also good. The efficiency is almost as good as AAFit (which is a reconstruction strategy used in analyses focusing on high energy neutrinos, see section 4.3.2) in most of the energy range, and better than AAFit for the highest energies ($\gtrsim 3$ PeV), with an identical angular resolution. In the energy range of interest for this work, AAFit outperforms Grid-

FIT by 3% to 7%. Therefore, AAFIT is used as the reconstruction strategy.

The R_{GF} parameter from GRIDFIT, which is related to the clustering of the hits, has proven to be effective in distinguishing upgoing neutrinos from misreconstructed atmospheric muons and can also be used in combination with other reconstruction strategies. It is most effective for low energy neutrinos. By taking the number of hits into account, the efficiency for high energy neutrinos can be increased as well, making it also suitable for a point source analysis.

After optimising the quality cuts, it is found that using the R_{GF} parameter increases the expected number of signal events from the Drift model by 21% compared to using the standard quality parameters (Λ, β and the reconstructed energy). This results in an improvement of the MRF by 1.4%. Using the TQ trigger in addition to the default 3N + 2T3 triggers gives a 3% increase of the number of signal events expected from the Drift model, resulting in an improvement of the MRF of 0.6%.

After optimising the quality cuts (see equation 5.19), a total of 1324 events are found in the 8 background regions, 19 of which are triggered exclusively by the TQ trigger. This results in a background estimate for the signal region of 166 ± 5 and gives a (model independent) sensitivity of:

$$\Phi_{\nu_\mu+\overline{\nu}_\mu} = 3.2\, E_\nu^{-2.6}\,\mathrm{GeV}^{-1}\,\mathrm{m}^{-2}\,\mathrm{sr}^{-1}\,\mathrm{s}^{-1}, \tag{7.1}$$

in the energy range from 0.18 TeV to 71 TeV. In this and the following equations, E_ν has units of GeV.

In the signal region a total of 177 ± 13 events are measured, of which 1 is triggered exclusively by the TQ trigger. This corresponds to a slight overfluctuation with a significance of $S = 0.8\sigma$. The measurement is thus compatible with the background-only hypothesis. The flux upper limits that can be set are:

$$\Phi_{\nu_\mu+\overline{\nu}_\mu} < 4.6\, E_\nu^{-2.6}\,\mathrm{GeV}^{-1}\,\mathrm{m}^{-2}\,\mathrm{sr}^{-1}\,\mathrm{s}^{-1}, \tag{7.2}$$

for a spectral index of 2.6 and:

$$\Phi_{\nu_\mu+\overline{\nu}_\mu} < 10\, E_\nu^{-2.7}\,\mathrm{GeV}^{-1}\,\mathrm{m}^{-2}\,\mathrm{sr}^{-1}\,\mathrm{s}^{-1}, \tag{7.3}$$

for a spectral index of 2.7, in the energy range from 0.15 TeV to 52 TeV.

The latter limit can be compared to the flux upper limit set by the AMANDA-II experiment, which is:

$$\Phi_{\nu_\mu+\overline{\nu}_\mu} < 4.8\, E_\nu^{-2.7}\,\mathrm{GeV}^{-1}\,\mathrm{m}^{-2}\,\mathrm{sr}^{-1}\,\mathrm{s}^{-1}. \tag{7.4}$$

in the energy range from 0.2 TeV to 40 TeV.

The results can be found in figure 5.23, which shows the sensitivities and limits versus Galactic longitude. It can be seen that the ANTARES limit is a factor of 2.1 above the AMANDA-II limit. However, it should be pointed out that the sensitivity of ANTARES is 10% better than that of AMANDA-II. The difference in the limits is primarily caused by a combination of an overfluctuation measured by ANTARES and an underfluctuation measured by AMANDA-II.

Furthermore, it is important to note that a different region has been used as signal region by the AMANDA-II experiment: $33^\circ < l < 213^\circ$ and $-4.4^\circ < b < 4.4^\circ$, for which only the latitudinal extension has been optimised. The longitudinal extension has been chosen simply because this is the range of longitude values AMANDA-II can observe (around $b = 0^\circ$). Since the size of the signal region used by AMANDA-II is a factor of about 2.3 bigger than that used in the ANTARES analysis, the AMANDA-II limit and sensitivity are lower. To really compare the results from both experiments, they should be compared to the expected signal fluxes in both regions. The average fluxes in the signal region used by AMANDA-II are on average a factor of about three lower than the fluxes in the signal region used in the ANTARES analysis, making the ANTARES limit, which specifically covers the inner Galactic plane region, the more stringent one.

The limits obtained here can also be used to say something about the origin of the flux measured by IceCube. Assuming a spectral index of 2.5, the hypothesis that all events measured by IceCube originate from the signal region can be rejected, since the required flux is a factor of about 1.9 higher than the obtained limit. Furthermore, the limit indicates that at most about 50% of the flux measured by IceCube can originate from the signal region considered here.

The current sensitivity is still more than a factor of 10 higher than the most optimistic model. Various options to improve the sensitivity of ANTARES (compared to standard analyses) have been investigated and when effective also implemented. A further possibility is to include the shower-like events created from electron- and tau-neutrino interactions and NC muon-neutrino interactions. Since the neutrino fluxes for all flavours are expected to be (nearly) the same due to oscillations, the useful signal could

potentially be tripled (depending on the shower reconstruction efficiency). The worse angular resolution of shower events compared to track events is not a problem for this analysis, since the signal and background regions are large compared to the expected angular resolution.

With the inclusion of showers, the ANTARES neutrino telescope is still too small to detect a diffuse Galactic neutrino flux and a bigger neutrino telescope is required. The KM3NeT neutrino telescope is well suited for this measurement, since it offers the same high visibility of the region from where the highest signal is expected, but it is much larger than ANTARES.

The detection potential of KM3NeT is determined by using the same type of analysis as for ANTARES. The optimal size of the signal region is determined for KM3NeT using both the MRF and MDP techniques and is found to be almost identical to that found for ANTARES. For the calculation of the sensitivity, the same signal region is used so that the results can be directly compared.

The resulting sensitivity for 1 and 10 years of data taking with the full KM3NeT phase 2 detector is shown in figure 6.8. From the figure it can be seen that 1 year of data gives a sensitivity that is about 6.6 times better than the ANTARES sensitivity and a factor of about 4.4 better than the AMANDA-II limit.

Depending on the normalisation of the atmospheric neutrino flux, it takes about 2.7 to 4.3 years for KM3NeT to reach the level of the flux of the Drift model (see section 2.2) and about 4.4 to 7.0 years to reach that of the Fermi $\gamma \rightarrow \nu$ model (see section 2.3).

In addition to the sensitivity, the discovery potential of KM3NeT is determined. It is found that about 30 years are needed to reach a significance of 5σ (with 50% probability) for the claim of a discovery of the Drift model. Evidence for a new signal, i. e. a significance of 3σ, takes about 11 years. The results for the Fermi $\gamma \rightarrow \nu$ model are very similar; it takes about 11 (32) years to reach a significance of 3σ (5σ).

Considering the results of the diffuse flux analyses performed in ANTARES shows that including shower-like events can result in a sensitivity improvement of a factor of 2 compared to using only track-like events. In this case a significance of 3σ is reached for the Drift model after only 2.8 years of data taking of KM3NeT and a significance of 5σ after about 7.7. Again, the results for the Fermi $\gamma \rightarrow \nu$ model are similar; it takes 2.9 (8.1) years of taking data to reach a significance of 3σ (5σ). Further optimisation of the quality cuts, flavour identification of the neutrinos and usage of an energy estimator could potentially result in a further improvement.

It can be concluded that the measurement of the diffuse Galactic neutrino flux requires a combined track and shower analysis. Only then can the diffuse Galactic neutrino flux be seriously constrained after about 3 years of operation of the KM3NeT neutrino telescope.

BIBLIOGRAPHY

M.G. Aartsen et al. First observation of PeV-energy neutrinos with IceCube. *Phys. Rev. Lett.*, 111(021103), 2013a.

M.G. Aartsen et al. Evidence for High-Energy Extraterrestrial Neutrinos at the IceCube Detector. *Science*, 342:947, 2013b.

M.G. Aartsen et al. Observation of High-Energy Astrophysical Neutrinos in Three Years of IceCube Data. *Phys. Rev. Lett.*, 113 (101101), 2014.

M.G. Aartsen et al. Atmospheric and astrophysical neutrinos above 1 TeV interacting in IceCube. *Phys. Rev. D*, 91(022001), 2015.

A.A. Abdo et al. Discovery of TeV Gamma-Ray Emission from the Cygnus Region of the Galaxy. *ApJ*, 658:L33–L36, 2007.

J. Abraham et al. Properties and performance of the prototype instrument for the Pierre Auger Observatory. *Nucl. Inst. Meth. Phys. Res. A*, 523:50–95, 2004.

M. Ackermann et al. The cosmic-ray and gas content of the Cygnus region as measured in gamma rays by the *Fermi* Large Area Telescope. *A&A*, 538(A71), 2012a.

M. Ackermann et al. *Fermi*-LAT Observations of the Diffuse γ-ray Emission: Implications for Cosmic Rays and the Interstellar Medium. *ApJ*, 750(3), 2012b.

M. Ackermann et al. The *Fermi* Large Area Telescope On Orbit: Event Classification, Instrument Response Functions, and Calibration. *ApJS*, 203(4), 2012c.

M. Ackermann et al. Detection of the Characteristic Pion-decay Signature in Supernova Remnants. *Science*, 339:807–811, 2013.

S. Adrián-Martínez et al. Search for Cosmic Neutrino Point Sources with Four Years of Data from the ANTARES Telescope. *ApJ*, 760(53), 2012a.

S. Adrián-Martínez et al. The positioning system of the ANTARES Neutrino Telescope. *JINST*, 7(T08002), 2012b.

S. Adrián-Martínez et al. Measurement of the group velocity of light in sea water at the ANTARES site. *Astropart. Phys.*, 35: 552–557, 2012c.

S. Adrián-Martínez et al. Measurement of atmospheric neutrino oscillations with the ANTARES neutrino telescope. *Phys. Lett. B*, 714:224–230, 2012d.

S. Adrián-Martínez et al. A search for neutrino emission from the Fermi bubbles with the ANTARES telescope. *Eur. Phys. J. C*, 74(2701), 2014a.

S. Adrián-Martínez et al. Deep sea tests of a protoype of the KM3NeT digital optical module. *Eur. Phys. J. C*, 74(3056), 2014b.

M. Ageron et al. KM3NeT Technical Design Report, 2010. Available at www.km3net.org/TDR/TDRKM3NeT.pdf.

M. Ageron et al. ANTARES: the first undersea neutrino telescope. *Nucl. Inst. Meth. Phys. Res. A*, 656:11–38, 2011.

S. Agostinelli. GEANT4 - a simulation toolkit. *Nucl. Inst. Meth. Phys. Res. A*, 506:250–303, 2003.

J.A. Aguilar et al. Transmission of light in deep sea water at the site of the ANTARES neutrino telescope. *Astropart. Phys.*, 23: 131–155, 2005.

J.A. Aguilar et al. Performance of the front-end electronics of the ANTARES neutrino telescope. *Nucl. Inst. Meth. Phys. Res. A*, 622:59–73, 2010.

J.A. Aguilar et al. Time Calibration of the ANTARES Neutrino Telescope. *Astropart. Phys.*, 34:539–549, 2011a.

J.A. Aguilar et al. Search for a diffuse flux of high-energy ν_μ with the ANTARES neutrino telescope. *Phys. Lett. B*, 696:16–22, 2011b.

J.A. Aguilar et al. A Fast Algorithm for Muon Track Reconstruction and its Application to the ANTARES Neutrino Telescope. *Astropart. Phys.*, 34:652–662, 2011c.

M. Ahlers, J. Kersten, and A. Ringwald. Long-lived staus at neutrino telescopes. *JCAP*, 2006(005), 2006.

J. Aleksić et al. Discovery of very high energy γ-ray emission from the blazar 1ES $0033 + 595$ by the MAGIC telescopes. *MNRAS*, 446:217–225, 2015.

W.W.M. Allison and P.R.S. Wright. The Physics of Charged Particle Identification: dE/dx, Cerenkov and Transition Radiation. *Formulae and Methods in Experimental Data Evaluation*, 2, 1984.

P. Amram et al. A Deep Sea Telescope for High Energy Neutrinos. *Preprint astro-ph/9907432*, 1999.

P. Amram et al. The ANTARES Optical Module. *Nucl. Inst. Meth. Phys. Res. A*, 484:369–383, 2002.

L. Anchordoqui, T. Paul, S. Reucroft, and J. Swain. Ultrahigh Energy Cosmic Rays: The state of the art before the Auger Observatory. *Int. J. Mod. Phys. A.*, 18:2229–2366, 2003.

L.A. Anchordoqui et al. Cosmic Neutrino Pevatrons: A Brand New Pathway to Astronomy, Astrophysics, and Particle Physics. *JHEAp*, pages 1–30, 2014.

E. Andres et al. The AMANDA neutrino telescope: principle of operation and first results. *Astropart. Phys.*, 13:1–20, 2000.

I. Antcheva et al. ROOT - A C++ framework for petabyte data storage, statistical analysis and visualization. *Comput. Phys. Commun.*, 180:2499–2512, 2009. Available at `root.cern.ch/drupal`.

M. Arneodo and M. Diehl. Diffraction for non-believers. *Preprint hep-ph/0511047*, 2005. Contributed to the Proceedings of the Workshop on HERA and the LHC, DESY and CERN, 2004-2005.

W.D. Arnett and J.L. Rosner. Neutrino Mass Limits from SN1987A. *Phys. Rev. Lett.*, 58:1906–1909, 1987.

P. Auger, P. Ehrenfest, R. Maze, J. Daudin, and R.A. Fréon. Extensive Cosmic-Ray Showers. *Rev. Mod. Phys.*, 11:288–291, 1939.

A. Avrorin et al. The Gigaton Volume Detector in Lake Baikal. *Nucl. Inst. Meth. Phys. Res. A*, 639:30–32, 2011.

W.I. Axford, E. Leer, and G. Skadron. The acceleration of cosmic rays by shock waves. *Proceedings of the 15th ICRC*, 11:132–137, 1978.

V. Aynutdinov et al. The Baikal Neutrino Telescope: From NT200 to NT200+. *Czechoslovak Journal of Physics*, 56:A349–A360, 2006.

D.J.L. Bailey. *Monte Carlo tools and analysis methods for understanding the ANTARES experiment and predicting the sensitivity to Dark Matter*. PhD thesis, University of Oxford, 2002.

B. Bakker. Trigger studies for the Antares and KM3NeT neutrino telescopes. Master thesis, Universiteit van Amsterdam, 2011.

M.G. Baring. Diffusive Shock Acceleration: The Fermi Mechanism. *Invited review in the Proceedings of the XXXIInd Rencontres de Moriond*, pages 97–106, 1997.

G.D. Barr, T.K. Gaisser, P. Lipari, S. Robbins, and T. Stanev. Three-dimensional calculation of atmospheric neutrinos. *Phys. Rev. D*, 70(023006), 2004.

R. Beck. Galactic and Extragalactic Magnetic Fields. *AIP Conference Proceedings*, 1085:83–96, 2008.

A. Belias et al. NESTOR. *Proceedings of the First Workshop on Exotic Physics with Neutrino Telescopes, EPNT06*, pages 94–98, 2007.

V.S. Berezinsky, T.K. Gaisser, F. Halzen, and T. Stanev. Diffuse radiation from cosmic ray interactions in the galaxy. *Astropart. Phys.*, 1:281–287, 1993.

J. Beringer et al. Review of Particle Physics. *Phys. Rev. D*, 86 (010001), 2012.

R.M. Bienta et al. Observation of a Neutrino Burst in Coincidence with Supernova 1987A in the Large Magellanic Cloud. *Phys. Rev. Lett.*, 58:1494–1496, 1987.

C. Bogazzi. *Search for cosmic neutrinos with ANTARES*. PhD thesis, Universiteit Leiden, 2014.

J.C. Brown. The Magnetic field of the Milky Way Galaxy. *ASP Conference Series*, 438:216–228, 2011.

J. Brunner. Cherenkov light from HE electromagnetic and hadronic showers. Internal Note, 2002.

J. Brunner. The BBfit Reconstruction algorithm. Internal Note, 2009.

B.F. Burke and F. Graham-Smith. *An Introduction to Radio Astronomy*. Cambridge University Press, 3rd edition, 2010.

M. Bustamante et al. High-energy cosmic-ray acceleration. *Proceedings of the 5th CERN - Latin-American School of High-Energy Physics*, pages 533–540, 2009.

J. Candia. Detectable neutrino fluxes due to enhanced cosmic ray densities in the Galactic Center region. *JCAP*, 2005(002), 2005.

J. Candia and E. Roulet. Rigidity dependent knee and cosmic ray induced high energy neutrino fluxes. *JCAP*, 2003(005), 2003.

G. Carminati, M. Bazzotti, A. Margiotta, and M. Spurio. Atmospheric MUons from PArametric formulas: a fast GEnerator for neutrino telescopes (MUPAGE). *Comput. Phys. Commun.*, 179: 925–923, 2008.

J. Carr, S. Escoffier, and D. Zaborov. Proposition for an alternative trigger based on the T3 cluster trigger. Internal Note, 2007.

G. Case and D. Bhattacharya. Revisiting the galactic supernova remnant distribution. *A&A Suppl. Ser.*, 120:437–440, 1996.

A. Connolly, R.S. Thorne, and D. Waters. Calculation of High Energy Neutrino-Nucleon Cross Sections and Uncertainties Using the MSTW Parton Distribution Functions and Implications for Future Experiments. *Phys. Rev. D*, 83(113009), 2011.

J.M. Cordes, J.M. Weisberg, D.A. Frail, S.R. Spangler, and M. Ryan. The galactic distribution of free electrons. *Nature*, 354:121–124, 1991.

R.D. Cousins, J.T. Linneman, and J. Tucker. Evaluation of three methods for calculating statistical significance when incorporating a systematic uncertainty into a test of the background-only hypothesis for a Poisson process. *Nucl. Inst. Meth. Phys. Res. A*, 595:480–501, 2008.

M. de Jong. The ANTARES Trigger Software. Internal Note, 2005.

M. de Jong. Partial linearisation of the track fit problem. Internal Note, 2007a.

M. de Jong. The Convex Hull of a Point Set. Internal Note, 2007b.

M. de Jong. The TRIGGEREFFICIENCY program. Internal Note, 2010.

A.M. Dziewonski and D.L. Anderson. Preliminary reference Earth model. *Phys. Earth Planet. Inter.*, 25:297–356, 1981.

R. Enberg, M.H. Reno, and I. Sarcevic. Prompt neutrino fluxes from atmospheric charm. *Phys. Rev. D*, 78(043005), 2008.

R. Engel. High Energy Cosmic Ray Interactions - Lecture 2: Intermediate energy physics, 2008. Available at www.physics.adelaide.edu.au/~jbellido/cosmicraysschool/Charlas/RalphEngel/EngelLecture2.pdf.

S. Escoffier. Performance of the T3 Triggers on MC Data. Internal Note, 2008.

C. Evoli, D. Grasso, and L. Maccione. Diffuse Neutrino and Gamma-ray Emissions of the Galaxy above the TeV. *JCAP*, 2007 (003), 2007.

H.I. Ewen and E.M. Purcell. Observation of a Line in the Galactic Radio Spectrum: Radiation from Galactic Hydrogen at 1,420 Mc./sec. *Nature*, 168:356, 1951.

G.J. Feldman and R.D. Cousins. Unified approach to the classical statistical analysis of small signals. *Phys. Rev. D*, 57:3873–3889, 1998.

E. Fermi. On the Origin of the Cosmic Radiation. *Phys. Rev. Lett.*, 75:1169–1174, 1949.

Ferrière. The Interstellar Environment of our Galaxy. *Rev. Mod. Phys.*, 73:1031–1066, 2001.

F. Folger. The Dusj shower reconstruction project. Internal Note, 2013.

F. Folger. *Search for a diffuse cosmic neutrino flux using shower events in the ANTARES neutrino telescope*. PhD thesis, Friedrich-Alexander-Universität Erlangen-Nürnberg, 2014.

J.A. Formaggio and G.P. Zeller. From eV to EeV: Neutrino Cross-Sections Across Energy Scales. *Rev. Mod. Phys.*, 84:1307–1353, 2013.

S. Galatà. The BBFIT reconstruction with full detector geometry in Seatray. Internal Note, 2010.

M. Galeazzi et al. The origin of the local 1/4-keV X-ray flux in both charge exchange and a hot bubble. *Nature*, 512:171–173, 2014.

I.S. Glass. *Handbook of Infrared Astronomy*. Cambridge University Press, 1999.

S.C.O. Glover and M.-M. Mac Low. On the relationship between molecular hydrogen and carbon monoxide abundances in molecular clouds. *MNRAS*, 412:337–350, 2011.

A. Goobar and B. Leibundgut. Supernova cosmology: legacy and future. *Annu. Rev. Nucl. Part. Sci.*, 61:251–279, 2011.

C. Grupen. *Astroparticle Physics*. Springer, 2005.

J.S. Hall. Observations of the Polarized Light From Stars. *Science*, 109:166–167, 1949.

F. Halzen and S.R. Klein. IceCube: An instrument for neutrino astronomy. *Rev. Sci. Instrum.*, 81(081101), 2010.

H. Hanada et al. A Highly Sensitive Optical Detector for a Use in Deep Underwater. *Nucl. Inst. Meth. Phys. Res. A*, 408:425–437, 1998.

M. Haverkorn. Magnetic Fields in the Milky Way. *Preprint astro-ph/1406.0283*, 2014. To appear in "Magnetic Fields in Diffuse Media".

A.J. Heijboer. *Track Reconstruction and Point Source Searches with ANTARES*. PhD thesis, Universiteit van Amsterdam, 2004.

V.F. Hess. Über Beobachtungen der durchdringenden Strahlung bei sieben Freiballonfahrten. *Phys. Zeitschr.*, 13:1084–1091, 1912.

G.C. Hill and K. Rawlins. Unbiased cut selection for optimal upper limits in neutrino detectors: the model rejection potential technique. *Astropart. Phys.*, 19:393–402, 2003.

G.C. Hill, J. Hodges, B. Hughey, A. Karle, and M. Stamatikos. Examining the balance between optimising an analysis for best limit setting and best discovery potential. *PHYSTAT*05 *Conference Proceedings*, pages 108–111, 2005.

W.A. Hiltner. Polarization of Light From Distant Stars by Interstellar Medium. *Science*, 109:165, 1949.

K. Hirata et al. Observation of a Neutrino Burst from the Supernova SN1987A. *Phys. Rev. Lett.*, 58:1490–1493, 1987.

M. Honda, T. Kajita, K. Kasahara, S. Midorikawa, and T. Sanuki. Calculation of atmospheric neutrino flux using the interaction model calibrated with atmospheric muon data. *Phys. Rev. D*, 75(043006), 2007.

C.-Y. Huang and M. Pohl. Production of neutrinos and secondary electrons in cosmic sources. *Astropart. Phys.*, 29:282–289, 2008.

E.P. Hubble. Extra-galactic nebulae. *ApJ*, 64:321–369, 1926.

G. Ingelman and M. Thunman. Particle Production in the Interstellar Medium. *Preprint hep-ph/9604286*, 1996.

C.W. James. km3 release v4r4. Internal Note, 2012.

K.G. Jansky. Radio Waves from Outside the Solar System. *Nature*, 132:66, 1933.

R. Jansson and G.R. Farrar. The Galactic Magnetic Field. *ApJ*, 761 (L11), 2012a.

R. Jansson and G.R. Farrar. A New Model of the Galactic Magnetic Field. *ApJ*, 757(14), 2012b.

M.H. Jones and R.J.A. Lambourne. *An Introduction to Galaxies and Cosmology*. Cambridge University Press, 2004.

J.C. Joshi, W. Winter, and N. Gupta. How many of the observed neutrino events can be described by cosmic ray interactions in the Milky Way? *MNRAS*, 439:3414–3419, 2014.

F. Jouvenot. *Sensibilité du télescope Antares au flux diffus de neutrinos Galactiques*. PhD thesis, Université Paris VII, 2005.

M. Kachelrieß and S. Ostapchenko. Neutrino yield from Galactic cosmic rays. *Preprint astro-ph/1405.3797*, 2014.

T. Kamae, T. Abe, and T. Koi. Diffractive Interaction and Scaling Violation in pp $\rightarrow \pi^0$ Interaction and GeV Excess in Galactic Diffuse Gamma-Ray Spectrum of EGRET. *ApJ*, 620:244–256, 2005.

B. Kambič. *Viewing the Constallations with Binoculars*. Springer, 2010.

J.L. Kelley et al. A Search for High-energy Muon Neutrinos from the Galactic Plane with AMANDA-II. *Proceedings of the 29th ICRC*, 5:127–130, 2005.

C. Kopper and D. Samtleben. Track reconstruction on a grid - Filteringfit. Internal Note, 2012.

A. L'Abbate, T. Montaruli, and I. Sokalski. GENHEN v6: ANTARES neutrino generator extension to all neutrino flavors and inclusion of propagation through the Earth. Internal Note, 2004.

M. Lemoine, E. Vangioni-Flam, and M. Cassé. Galactic Cosmic Rays and the Evolution of Light Elements. *ApJ*, 499:735–745, 1998.

T. Li and Y. Ma. Analysis methods for results in gamma-ray astronomy. *ApJ*, 272:317–324, 1983.

G.M.A. Lim. *Searching for Dark Matter with the Antares Neutrino Telescope*. PhD thesis, Universiteit van Amsterdam, 2011.

D.R. Lorimer, A.J. Faulkner, A.G. Lyne, R.N. Manchester, M. Kramer, M.A. McLaughlin, G. Hobbs, A. Possenti, I.H. Stairs, F. Camilo, M. Burgay, N.D. Amico, A. Corongiu, and F. Crawford. The Parkes Multibeam Pulsar Survey – VI. Discovery and timing of 142 pulsars and a Galactic population analysis. *MNRAS*, 372:777–800, 2006.

C. Lunardini, S. Razzaque, T. Theodoseau, and L. Yang. Neutrino Events at IceCube and the Fermi Bubbles. *Preprint astro-ph/1311.7188*, 2013.

A. Margiotta. The KM3NeT project: status and perspectives. *Geosci. Instrum. Method. Data Syst.*, 2:35–40, 2013.

A.D. Martin, M.G. Ryskin, and A.M. Stasto. Prompt neutrinos from atmospheric $c\bar{c}$ and $b\bar{b}$ production and the gluon at very small x. *Acta Phys. Polon*, B34:3273–3304, 2003.

B.R. Martin and G. Shaw. *Particle Physics*. Wiley, 3rd edition, 2008.

D. McCammon and W.T. Sanders. The soft X-ray background and its origins. *ARA&A*, 28:657–688, 1990.

K. McFarland. Neutrino Interactions. *Preprint hep-ex/0804.3899*, 2008.

W.J. Metzger. *Stastical Methods in Data Analysis*. Katholieke Universiteit Nijmegen, 2002.

I.V. Moskalenko, T.A. Porter, and A.W. Strong. Attenuation of Very High Energy Gamma Rays by the Milky Way Interstellar Radiation Field. *ApJ*, 640:L155–L158, 2006.

I.V. Moskalenko, S.W. Digel, G. Jóhannesson, E. Orlando, T.A. Porter, R. Ruiz de Austri, A.W. Strong, R. Trotta, and A.E. Vladimirov. GALPROP Code for Galactic Cosmic Ray Propagation and Associated Photon Emissions. *Proceedings of the 32nd ICRC*, 6:279–282, 2011.

H.M. Motz. *Dark Matter Search with ANTARES*. PhD thesis, Friedrich-Alexander-Universität Erlangen-Nürnberg, 2011.

C.A. Muller and J.H. Oort. Observation of a Line in the Galactic Radio Spectrum: The Interstellar Hydrogen Line at 1,420 Mc./sec., and an Estimate of Galactic Rotation. *Nature*, 168: 357–358, 1951.

S. Navas and L. Thompson. KM3 User Guide and Reference Manual. Internal Note, 1999.

A. Neronov, D. Semikoz, and C. Tchernin. PeV Neutrinos from interactions of cosmic rays with the interstellar medium in the Galaxy. *Phys. Rev. D*, 89(103002), 2014.

T. Neunhöffer. Estimating the angular resolution of tracks in neutrino telescopes based on a likelihood analysis. *Astropart. Phys.*, 25:220–225, 2006.

H. Niederreiter. Low-Discrepancy and Low-Dispersion Sequences. *J. Number Theor.*, 30:51–70, 1988.

D. Palioselitis. *Measurement of the atmospheric neutrino energy spectrum*. PhD thesis, Universiteit van Amsterdam, 2012.

J.M. Pasachoff. *Astronomy: From the Earth to the Universe*. WB Saunders Co., 1st edition, 1979.

E.A. Paschos. Precise Ratios for Neutrino-Nucleon and Neutrino-Nucleus Interactions. *Preprint hep-ph/0204090*, 2002.

R.W. Pogge. Lecture notes from the Astronomy 871 course, taught at the Ohio State University, 2011. Available at www.astronomy.ohio-state.edu/~pogge/Ast871.

M. Prouza and Šmída. The Galactic magnetic field and propagation of ultra-high energy cosmic rays. *A&A*, 410:1–10, 2003.

V. Ptuskin. Propagation of galactic cosmic rays. *Astropart. Phys.*, 39–40:44–51, 2012.

J. Pumplin, D.R. Stump, H.-L. Lai, P. Nadolsky, and W.-K. Tung. New Generation of Parton Distributions with Uncertainties from Global QCD Analysis. *JHEP*, 2002(012), 2002.

G. Riccobene et al. On-line monitoring of underwater acoustic background at 2000 m depth. *Proceedings of the 29th ICRC*, 9: 287–290, 2005.

C. Riviére. Run-by-run Monte Carlo simulation for ANTARES: v2. Internal Note, 2012.

W.A. Rolke, A.M. López, and J. Conrad. Limits and Confidence Intervals in the Presence of Nuisance Parameters. *Nucl. Inst. Meth. Phys. Res. A*, 551:493–503, 2005.

J. Schnabel. The ANNergy estimator. Internal Note, 2012.

J. Schnabel. Search for a diffuse flux of cosmic neutrinos with ANTARES, 2013a. Presentation at the TAUP conference in Asilomar, California.

J. Schnabel. Muon energy reconstruction in the ANTARES detector. *Nucl. Inst. Meth. Phys. Res. A*, 725:106–109, 2013b.

F. Schüssler. Energy reconstruction of Antares events: the $\mathrm{d}E/\mathrm{d}X$ energy estimator. Internal Note, 2012.

T. Sjöstrand, S. Mrenna, and P. Skands. A Brief Introduction to PYTHIA 8.1. *Comput. Phys. Commun.*, 178:852–867, 2008. Available at http://home.thep.lu.se/~torbjorn/Pythia.html.

S.L. Snowden, M.J. Freyberg, P.P. Plucinsky, J.H.M.M. Schmitt, J. Trümper, W. Voges, R.J. Edgar, D. McCammon, and W.T. Sanders. First Maps of the Soft X-Ray Diffuse Background from the ROSAT XRT/PSPC All-Sky Survey. *ApJ*, 454:643–653, 1995.

M. Spurio. Constraints to a Galactic component of the Ice Cube cosmic neutrino flux from ANTARES. *Phys. Rev. D*, 90(103004), 2014.

A.W. Strong, I.V. Moskalenko, and V.S. Ptuskin. Cosmic-ray propagation and interactions in the Galaxy. *Annu. Rev. Nucl. Part. Sci.*, 57:285–327, 2007.

M. Su, T.R. Slatyer, and D.P. Finkbeiner. Giant Gamma-ray Bubbles from *Fermi*-LAT: AGN Activity or Bipolar Galactic Wind. *ApJ*, 724:1044–1082, 2010.

A.M. Taylor, S. Gabici, R.J. White, S. Casanova, and F.A. Aharonian. Revisiting the diffuse neutrino flux from the inner Galaxy using new constraints from very high energy γ-ray observations. *Nucl. Inst. Meth. Phys. Res. A*, 602:113–116, 2009.

A.M. Taylor, S. Gabici, and F. Aharonian. A Galactic Halo Origin of the Neutrinos Detected by IceCube. *Preprint astro-ph/1403.3206*, 2014.

C. Tchernin, J.A. Aguilar, A. Neronov, and T. Montaruli. Neutrino signal from extended Galactic sources in IceCube. *A&A*, 560 (A67), 2013.

A. Trovato. *Development of reconstruction algorithms for large volume neutrino telescopes and their application to the KM3NeT detector*. PhD thesis, Università degli Studi di Catania, 2013.

H.C. van de Hulst. Radio Waves from Space: Origin of Radiowaves. *Ned. tijd. natuurkunde*, 11:210–221, 1945.

P.A. Čerenkov. Visible Radiation Produced by Electrons Moving in a Medium with Velocities Exceeding that of Light. *Phys. Rev. Lett.*, 52:378–379, 1937.

E. Visser. Neutrino Fluxes from Cosmic Ray Interactions in the Galactic Plane. Internal Note, 2013.

E. Visser. Sensitivity of Antares to Neutrinos from the Galactic Plane. Internal Note, 2014.

E. Visser and S. Wagner. Studies of the performance of different track reconstruction strategies using the FilteringFit track reconstruction. Internal Note, 2013.

W.H. Walter and P.W. Hodge. *Galaxies and the Cosmic Frontier*. Harvard University Press, 2003.

E. Waxman. IceCube's Neutrinos: The beginning of extra-Galactic neutrino astrophysics? *Preprint astro-ph/1312.0558*, 2014.

E. Waxman and Bahcall. High Energy Neutrinos from Astrophysical Sources: An Upper Bound. *Phys. Rev. D*, 59(023002), 1998.

T.J. Weiler. Oscillations and Mixing Among the Three Neutrino Flavors. *Preprint astro-ph/1308.1715*, 2013.

R. Wischnewski. The AMANDA-II neutrino telescope. *Nucl. Phys. B - Proceedings Supplements*, 110:510–512, 2002.

I. Yusifov and I. Küçük. Revisiting the radial distribution of pulsars in the Galaxy. *A&A*, 422:545–553, 2004.

SUMMARY

When you find yourself away from light pollution of cities and look up at the night sky, a dim "milky" band of light can be seen: the Milky Way. The best view is from the Southern Hemisphere, since the central part of the Milky Way is then visible at a higher position above the horizon. The milky band corresponds to the plane of our Galaxy and appears bright since it contains most of the stars.

Since ancient times the universe has been studied using light in the range of wavelengths that is visible to the human eye. Today, observations of the universe are also made using light at different wavelengths, ranging from low-energy radio waves to high-energy γ-rays. The Milky Way clearly stands out at these wavelengths as well. When observing high-energy γ-rays or infrared light, the Milky Way actually stands out even more, because the dust in our Galaxy does not absorb those photons as much as the photons in the visible range of wavelengths.

Following the discovery of cosmic rays by Victor Hess in 1912, a new way of observing the universe became possible, usually referred to as astroparticle physics. Cosmic rays are fully ionised atomic nuclei (like hydrogen and iron) which constantly bombard the Earth's atmosphere from all directions. The origin of cosmic rays is still unclear. Because cosmic rays are charged, they are deflected in the (extra-)Galactic magnetic fields. As a result, they no longer point back to their source by the time they arrive on Earth. One of the prime candidate sources for cosmic rays originating in our Galaxy are supernova remnants, which are the left-overs after a massive star goes supernova. Identifying the sources of cosmic rays is one of the main goals in astroparticle physics.

During their travel through our Galaxy, the cosmic rays interact with the interstellar matter. In these interactions, unstable particles are created which decay to other stable particles such as photons (i. e. γ-rays), electrons and neutrinos. These neutrinos are the main subject of this dissertation. Even though the corresponding flux of neutrinos is guaranteed, it has not yet been observed. The only published result so far is an upper limit of this flux of neutrinos set by the AMANDA-II collaboration which operated a neutrino telescope at the South Pole.

Neutrinos can be detected by looking at the products of an interaction of a neutrino with matter in the vicinity of the detector. The list of interaction products generally includes various charged particles. When the velocity of a charged particle exceeds that of the light in a medium, a kind of electro-magnetic shock wave is produced which is referred to as Čerenkov light (the effect is similar to the acoustic shock wave that is created when an airplane goes faster than the speed of sound). Neutrino telescopes are therefore built in transparent media like water or ice. The Čerenkov light can then be observed using a sparse array of light sensors. Because neutrinos only interact weakly with matter, a big instrumented volume of water or ice is required. A big advantage of neutrinos is the fact that they do not carry any charge, so that they are not deflected in the (extra-)Galactic magnetic fields. When cosmic rays interact in the vicinity of their source and thus produce neutrinos, the direction of the neutrinos will point to the source of the cosmic rays.

There exist three flavours of neutrinos: the electron-neutrino, the muon-neutrino and the tau-neutrino. Depending on the flavour of the neutrino, a different particle is produced in their interaction. Due to oscillations of neutrinos (a phenomenon in which a neutrino spontaneously changes flavour during its journey), neutrinos with all three flavours are expected to arrive on Earth. Traditionally, neutrino astronomy focuses on the muon-neutrino, since in its interaction a muon (a heavier version of the electron) is created. The advantage of detecting a muon is that the muon can travel a large distance through the medium before it stops. This provides for a long lever arm which in turn allows to determine the direction of the neutrino with good accuracy.

The main background for neutrino telescopes consists of muons which are created by the interactions of cosmic rays with the atmosphere of the Earth. To reduce this background, neutrino telescopes are located under a thick layer of sea or ice to provide for a natural shielding. Because neutrinos interact weakly with matter, neutrinos are the only particles that can pass through the entire Earth. So the field of view of a neutrino telescope is generally pointing downwards instead of upwards. By doing so, the atmospheric muon background can effectively be reduced to an acceptable level. Neutrinos, which are also created by the interactions of cosmic ray with the Earth's atmosphere, constitute an *a priori* irreducible background since they cannot be rejected in the same way.

As with γ-rays, the Milky Way is expected to stand out when neutrinos are observed. Since neutrino telescopes primarily look

through the Earth, a detector on the Northern Hemisphere is best suited to observe the signal (as opposed to looking for light). The ANTARES neutrino telescope, located about 40 km offshore from Toulon, France is at a prime location. The ANTARES detector is located at a depth of 2475 m and consists of a total of 885 light sensors, distributed along 12 vertical lines. All signals that are recorded by the light sensors are sent to shore, where the interesting signals are selected in a process called *triggering*. The triggered events are processed offline to determine the direction and energy of the neutrino that caused the interaction. Several different algorithms exist for the reconstruction of the direction of the neutrino. For this work a new algorithm (GRIDFIT) has been developed. Compared to previous algorithms, it provides for a 20% higher efficiency to reconstruct low-energy neutrinos.

To distinguish the signal neutrinos from the background of atmospheric neutrinos, two aspects can be used. First, the signal is expected to be strongest in the inner region of the Galactic plane, since the matter density is highest there. By using a simulation of the detector response to neutrinos, it is found that a region which extends 39° in longitude and 4.5° in latitude on either side of the Galactic Centre is optimal. Second, the energy of the neutrinos can be considered. The typical energy of the signal neutrinos is expected to be higher than that of atmospheric neutrinos. This difference is due to the lower matter density in the Galaxy compared to that in the Earth's atmosphere. Unstable particles produced in the Earth's atmosphere may interact before they decay whereas those produced in the Galaxy will all decay. Because the effective lifetime of the unstable particles increases with energy due to relativistic effects, the energy spectrum of the background neutrinos will be steeper than that of the signal neutrinos.

To detect an excess of neutrinos above the background, the measured number of neutrinos is compared to what is expected assuming only background. Usually, the background expectation is obtained from a model. To avoid a bias due to the uncertainties associated with the assumed model of the background, a measurement of the background is performed. For this purpose, eight additional regions are defined in which no signal is expected. These regions are chosen to have the same size and detector coverage as the signal region. Using the ANTARES data from the beginning of 2007 until the end of 2012, an average background of 166 events is found, whereas 177 events are measured in the signal region. The statistical significance of this excess is 0.8σ which is compatible with a fluctuation of the background (a dis-

covery of a new signal can only be claimed when an excess of 5σ or more has been observed).

Since no significant excess of events has been observed, upper limits can be placed on the neutrino flux. The obtained upper limits can be found in table 5.14. They are worse than those obtained by the AMANDA-II experiment. However, the present limits are focused on the inner region of the Galactic plane and are thus the most stringent.

The current flux upper limits are more than a factor of ten above the expected fluxes. Hence, a more powerful neutrino telescope is needed to detect the signal. The planned successor of ANTARES, the KM3NeT detector, is ideally suited for this. It will also be located in the Mediterrenean Sea, but it will be a factor of about 100 larger than the ANTARES detector. It is found that within one year of operation of KM3NeT, flux limits can be set which are almost a factor of seven better than those obtained with ANTARES. By using all three neutrino flavours and after about three years of operation of the KM3NeT detector, one can constrain the various neutrino flux models and possibly obtain the first evidence of the expected signal.

SAMENVATTING

Als je omhoog kijkt naar de nachtelijke hemel, en je bevindt je ver genoeg van de lichtvervuiling van steden, dan kun je een flauwe "melkachtige" band van licht zien: de Melkweg. De zichtbaarheid is het beste vanaf het zuidelijk halfrond, omdat het centrale deel van de Melkweg daar hoger boven de horizon zichtbaar is. De melkachtige band komt overeen met het vlak van onze Melkweg en is relatief helder omdat er zich het grootste deel van de sterren bevindt.

Sinds de oudheid is het heelal onderzocht met behulp van licht in het golflengtegebied dat zichtbaar is voor het menselijk oog. Tegenwoordig worden er ook waarnemingen verricht met behulp van licht van andere golflengtes, variërend van laag-energetische radiogolven tot hoog-energetische γ-stralen. Ook bij deze golflengtes is de Melkweg duidelijk zichtbaar. In waarnemingen met hoog-energetische γ-stralen of met infrarood licht is de Melkweg zelfs nog duidelijker te onderscheiden, omdat het stof in ons sterrenstelsel deze fotonen minder absorbeert dan de fotonen in het golflengtegebied van zichtbaar licht.

Met de ontdekking van kosmische stralen door Victor Hess in 1912 ontstond een nieuwe manier om het heelal waar te nemen: de astrodeeltjesfysica. Kosmische stralen zijn volledig geïoniseerde atoomkernen (van onder andere waterstof en ijzer) die vanuit alle richtingen de atmosfeer van de aarde bestoken. De oorsprong van kosmische stralen is nog onduidelijk. Aangezien kosmische stralen geladen zijn, worden ze in de (extra-)galactische magneetvelden afgebogen. Op het moment dat ze op de aarde aankomen wijzen ze dan niet meer terug naar hun bron. Eén van de belangrijkste kandidaten voor de bronnen van galactische kosmische stralen zijn supernovaresten, die overblijven nadat een zware ster via een supernova aan zijn einde is gekomen. Het identificeren van de bronnen van kosmische stralen is één van de belangrijkste doelen in de astrodeeltjesfysica.

Tijdens hun reis door de Melkweg gaan de kosmische stralen interactie aan met de interstellaire materie. In deze interacties worden instabiele deeltjes gecreëerd die vervallen naar andere stabiele deeltjes zoals fotonen (i. e. γ-stralen), elektronen en neutrino's. Deze neutrino's zijn het onderwerp van dit proefschrift. Ondanks dat deze flux van neutrino's gegarandeerd is, is hij nog niet waargenomen. Het enige resultaat dat tot nu is gepubliceerd,

is een bovengrens voor de flux van neutrino's geplaatst door de AMANDA-II collaboratie, welke een neutrinotelescoop op de Zuidpool bediende.

Neutrino's kunnen worden gedetecteerd door te kijken naar de deeltjes die vrijkomen bij een interactie van een neutrino met materie in de nabijheid van de detector. De lijst van interactieproducten omvat in het algemeen verschillende geladen deeltjes. Wanneer de snelheid van een geladen deeltje groter is dan die van het licht in een medium, ontstaat een soort elektromagnetische schokgolf, welke wordt aangeduid als Čerenkov licht (het effect is vergelijkbaar met de akoestische schokgolf die ontstaat wanneer een vliegtuig sneller gaat dan de geluidssnelheid). Neutrinotelescopen zijn daarom gebouwd in transparante media zoals water of ijs. Het Čerenkov licht kan dan worden waargenomen met behulp van een matrix van lichtsensoren. Omdat neutrino's slechts zwak reageren met materie, is een groot geïnstrumenteerd volume van water of ijs vereist. Een groot voordeel van neutrino's is dat ze geen lading hebben, zodat ze niet worden afgebogen in de (extra-)galactische magneetvelden. Wanneer kosmische stralen een interactie ondergaan in de nabijheid van hun bron en dus neutrino's produceren, zal de richting van het neutrino terugwijzen naar de bron van de kosmische stralen.

Er bestaan drie generaties (of smaken) neutrino's: het elektron-neutrino, het muon-neutrino en het tau-neutrino. Het deeltje dat wordt geproduceerd in de interactie van een neutrino is afhankelijk van de smaak van het neutrino. Omdat neutrino's tussen de generaties kunnen oscilleren (een verschijnsel waarbij een neutrino spontaan overgaat van de ene generatie naar de andere), zullen neutrino's van alle drie de smaken op aarde aankomen. Traditioneel richt de neutrino-astronomie zich op het muon-neutrino, omdat een interactie hiervan een muon (een zwaardere versie van het elektron) produceert. Het voordeel van het detecteren van een muon is dat deze een grote afstand kan afleggen in een medium voordat het stopt. Dit verschaft een lange hefboomarm, zodat de richting van het neutrino met goede nauwkeurigheid kan worden bepaald.

De belangrijkste achtergrond voor neutrinotelescopen bestaat uit muonen die worden gecreëerd in de interactie van kosmische stralen met moleculen in de atmosfeer van de aarde. Om deze achtergrond te verminderen, worden neutrinotelescopen onder een dikke laag van water of ijs gebouwd, wat zorgt voor een natuurlijke afscherming. Omdat neutrino's zo zwak met materie reageren, zijn neutrino's de enige deeltjes die door de hele aarde kunnen reizen. Het gezichtsveld van een neutrinotelescoop is dus

over het algemeen naar beneden gericht, in plaats van naar boven zoals bij een (foton)telescoop. Hierdoor kan de achtergrond van atmosferische muonen effectief gereduceerd worden tot een aanvaardbaar niveau. Neutrino's, die ook worden geproduceerd in de interactie van kosmische stralen in de atmosfeer van de aarde, vormen een *a priori* niet te verminderen achtergrond, omdat zij niet op dezelfde manier kunnen worden verworpen.

Zoals het geval is voor γ-stralen, zal de Melkweg naar verwachting ook duidelijk te onderscheiden zijn door het waarnemen van neutrino's. Omdat neutrinotelescopen vooral naar beneden kijken (door de aarde heen), zal een detector op het noordelijk halfrond het meest geschikt zijn om het signaal te observeren (in tegenstelling tot wanneer licht gebruikt zou worden). De ANTARES neutrinotelescoop, gelegen op ongeveer 40 km uit de kust van Toulon, Frankrijk ligt op een uitstekende locatie. De ANTARES detector bevindt zich op een diepte van 2475 m en bestaat uit in totaal 885 lichtsensoren, verdeeld over 12 verticale lijnen. Alle signalen die door de lichtsensoren worden waargenomen worden verstuurd naar land, alwaar de interessante signalen worden geselecteerd in een proces dat *triggering* wordt genoemd. De geselecteerde signalen worden offline verwerkt om de richting en de energie van het neutrino dat de interactie heeft veroorzaakt vast te stellen. Er bestaan diverse algoritmes voor de bepaling van de richting van het neutrino. Voor dit werk is een nieuw algoritme (GRIDFIT) ontwikkeld. Vergeleken met bestaande algoritmes biedt het een 20% hogere efficiëntie voor laag-energetische neutrino's.

Om het gewenste neutrinosignaal van de achtergrond van atmosferische neutrino's te onderscheiden, kunnen twee aspecten worden gebruikt. Ten eerste wordt het sterkste signaal verwacht in het binnenste gebied van het galactische vlak, omdat de materiedichtheid daar het hoogst is. Met behulp van een simulatie van de detectorreactie voor neutrino's, is gebleken dat het optimale gebied zich 39° in galactische lengtegraad en 4.5° in galactische breedtegraad uitstrekt aan weerszijden van het galactisch centrum. Als tweede onderscheidende aspect kan de energie van de neutrino's beschouwd worden. De typische energie van het neutrinosignaal zal naar verwachting hoger zijn dan dat van de achtergrond van atmosferische neutrino's. Dit verschil komt door de lagere materiedichtheid in de Melkweg vergeleken met die in de atmosfeer. De instabiele deeltjes die in de atmosfeer van de aarde worden geproduceerd kunnen met de atomen in de atmosfeer botsen voordat ze vervallen, terwijl de deeltjes die in de Melkweg geproduceerd worden allemaal zullen vervallen zonder

te botsen. Aangezien de effectieve levensduur van de instabiele deeltjes toeneemt met de energie vanwege relativistische effecten, zal het energiespectrum van de achtergrond steiler zijn dan dat van het signaal.

Door het gemeten aantal neutrino's te vergelijken met wat er verwacht wordt van alleen de achtergrond, kan bepaald worden of er een signaal aanwezig is. Meestal wordt de verwachting van de achtergrond verkregen met behulp van een model. Om te voorkomen dat het achtergrondmodel de werkelijkheid vertekend weergeeft, wordt in plaats hiervan een meting van de achtergrond uitgevoerd. Hiervoor zijn acht extra gebieden gedefinieerd, waarin geen signaal wordt verwacht. Deze gebieden zijn zo gekozen dat ze dezelfde grootte hebben als het signaalgebied, en dat de dekkingsgraad door de detector ook hetzelfde is. Met behulp van de meetgegevens van ANTARES vanaf het begin van 2007 tot het einde van 2012, is een gemiddelde achtergrond van 166 gebeurtenissen gevonden, terwijl er 177 gebeurtenissen zijn gemeten in het signaalgebied. De statistische significantie van dit overschot is 0.8σ, wat compatibel is met een fluctuatie van de achtergrond (de ontdekking van een nieuw signaal kan pas geclaimd worden als een overschot van 5σ of meer is waargenomen).

Aangezien er geen significant overschot van neutrino's is waargenomen, kunnen bovengrenzen voor de flux van neutrino's worden geplaatst. De verkregen bovengrenzen kunnen worden gevonden in tabel 5.14. Ze zijn slechter dan die verkregen door de AMANDA-II detector. De hier geplaatste bovengrenzen zijn echter voor het binnengebied van de Melkweg en zijn dus het meest strikt.

De huidige bovengrenzen voor de flux zijn meer dan een factor tien boven de verwachte flux. Daarom is een krachtigere neutrinotelescoop nodig om het signaal te kunnen waarnemen. De geplande opvolger van ANTARES, de KM3NeT detector, is hier bij uitstek geschikt voor. De detector zal zich ook in de Middellandse Zee bevinden, maar zal ongeveer een factor 100 groter zijn dan de ANTARES detector. Met meetgegevens verkregen binnen een jaar van gebruik van de KM3NeT detector, zijn de verwachte bovengrenzen die voor de flux verkregen kunnen worden bijna een factor zeven beter dan die verkregen met ANTARES. Door het gebruik van alle drie de neutrinosmaken en met meetgegevens van ongeveer drie jaar van gebruik van de KM3NeT detector, kan men de verschillende modellen voor de flux van neutrino's beperken en misschien zelfs een eerste bewijs verkrijgen voor het verwachte signaal.

ABOUT THE AUTHOR

I, Erwin Lourens Visser, was born on the 2nd of January 1987 in Hoorn, a small town in the Netherlands. I lived most of my life in the nearby town of Enkhuizen, in which I also attended high school at the *Regionale Scholengemeenschap*.

From the courses followed at high school, physics was by far my favourite and so the choice of studying physics at the Vrije Universiteit (VU) in Amsterdam was quickly made. When not following courses I could be found in AIK, the physics study association at the VU, for which I was also the treasurer for a year.

I performed my bachelor project in the LHCb group at the Nikhef Institute in Amsterdam, studying the forward-backward asymmetry in the decay of B^0 to $K^{*0} + \mu^+ + \mu^-$. After obtaining my bachelor degree cum laude in 2008, I chose to continue in the field of particle physics with the Particle and Astroparticle physics master. I also performed my master project in the LHCb group, with a more experimental subject this time: the preventing, monitoring and curing of the aeging in the LHCb Outer Tracker.

After obtaining my masters degree in 2010 (also cum laude), I decided to look around for a PhD position at Nikhef. Some of my friends and fellow students did their masters research in the ANTARES group at Nikhef, in the field of astroparticle physics. I applied for a position in the group and was accepted. I didn't apply for a specific position, so an analysis had to be thought up. A presentation in Paris by an IceCube scientist on the subject of neutrinos from cosmic ray interactions with the interstellar medium, lead to the question why ANTARES hadn't performed an analysis on this subject yet, and this became the subject of my dissertation.

Besides working on my analysis, I also did some hardware work for the future KM3NeT telescope, by testing PMTs and later (at the end of my time at Nikhef) full DOMs.

In addition to presenting my work at the numerous collaboration meetings in several European (and one African) cities, I also presented my analysis at the TeVPA conference in Amsterdam and the ECRS2014 conference in Kiel, Germany.

ACKNOWLEDGEMENTS

The work described in this dissertation was performed in the ANTARES group at the *Nationaal Instituut voor Subatomaire Fysica* (Nikhef) in Amsterdam. Although writing a disseration is something that you generally do by yourself, the end result wouldn't be the same without the help of a number of people.

First and foremost I would like to thank my supervisor, Dorothea Samtleben. She always made time to answer any questions I had and her suggestions were always very helpful. I am also grateful for her encouragement at those times that I lost my resolve.

My promotor, Maarten de Jong, also deserves my thanks for his useful advice. Thanks to his suggestions I was able to improve this dissertation and the associated propositions by a great amount.

My work at Nikhef was made enjoyable thanks to the people, past and present, of the ANTARES/KM3NeT group: Aart, Akis, Arjen, Bardo, Ching-Cheng, Claudio, Daan, Dimitris, Els, Jeroen, Karel, Maria, Martijn, Mieke, Paul, Robert, Ronald, Stephan, Tino and Tri. Thanks to all of you! A special thanks to Robert and Tino for being my office mates and for the always interesting discussions we had.

The Nikhef group is only one part of the larger ANTARES collaboration and I would also like to thank my colleagues abroad. Thanks in particular to Antoine Kouchner and Thierry Stolarczyk for their useful comments on my analysis during the unblinding process.

Thanks are also due to my parents for always supporting me in my choices and for their interest in my research, which they showed by attending the yearly *open dag* at Nikhef and listening to me explaining the status of neutrino detection.

Last, but definitely not least, I would like to thank Michelle Nicol for all her love and support, especially during the writing of this dissertation. I also owe her thanks for proof-reading my manuscript and correcting my English mistakes. Without her, this dissertation would not look the same.

Erwin Visser